

NUMERICAL STUDY OF INTERFACE BEHAVIOUR IN COMPOSITE SHCC-CONCRETE BEAMS

Samuel Budhi Setyanto



Rijksvastgoedbedrijf
Ministerie van Binnenlandse Zaken en
Koninkrijksrelaties

**TU Delft**

Master Thesis

NUMERICAL STUDY OF INTERFACE BEHAVIOUR IN COMPOSITE SHCC-CONCRETE BEAMS

by

Samuel Budhi Setyanto

In partial fulfilment of the requirements for the degree of

Master of Science

in Structural Engineering

at Delft University of Technology

to be defended publicly on 27 August 2021

Committee

Dr. ir. M. Lukovic (Chairperson)

Dr. ir. C.B.M. Blom (Daily Supervisor)

Dr. ir. M.A.N. Hendriks

Ir. J.W.G.M. Kraak, MSc (Company – Rijksvastgoedbedrijf)

PREFACE

This thesis marks the end of my master's study journey in TU Delft. For 2 years, a lot of knowledge and experiences have been gained through the courses and this graduation project despite of the challenging situation.

I can only reach this point because of all people who has support me until today. I want to express my gratitude to Mladena, Kees, and Max for every advice, comment, suggestion, and encouragement throughout this project. I also want to thank Jan for a lot of time that you spent with me to discuss so many things, to give me support when I got stuck, and to always remind me to keep the work-life balance every week. For Nuttapon, Zhuo, Yotrisno, Nick, Monic, and many others, I want to thank you for your support along my study and for believing that I can finish this thesis well. For Nuffic Neso Indonesia team, especially Bu Indy, Ka Bagus, and Ka Octa, I want to thank you for your support through the scholarship and many other things in the past 2.5 years.

More than everything, I want to thank God for Your grace that has abundantly flow in me throughout my life and for the hope that you always put in my heart throughout my lowest days. There is always a special place for my family, Papa, Mama, Ka Ika, Ka Dewi, and Ka Bonus, who always pray for me from far away and always be there for me in my good and bad days.

Finally, I hope this thesis can be beneficial for the future studies and development of the research of composite structures and related topics in the Netherlands.

Samuel Budhi Setyanto
Delft, August 2021

ABSTRACT

A parking garage of Eindhoven airport partially collapsed in 2017. It was caused by failure of the longitudinal joint (long-side) of the composite plank floor or *breedplaatvloer* on the roof level. Experimental and numerical research showed that the joint suffered high positive bending moment in its transverse direction. However, from the investigation results, there was not enough resistance at the concrete-to-concrete interface around the joint to transfer the tensile force from the precast to the cast-in-situ section, which led to delamination of the two layers of concrete and resulting in failure when the delamination crack reaches the end of the coupling reinforcements. As happened in that case, the concrete-to-concrete interface usually is the weakest link and has a critical role on behaviour of a composite concrete system, especially the one which has unreinforced interface (no stirrup near joint). Further studies have been conducted to understand the influence of various details around the joint on the interface behaviour. In this thesis, details in spacing between lap splices (coupling reinforcements in cast-in-situ layer and bottom reinforcements in precast layer), spacing between connecting reinforcements (stirrups crossing the interface near the joint), the role of connecting reinforcement, and the sensitivity of interface parameters were studied numerically using DIANA finite element analysis software. Since the spacings are in direction of the specimen's width, interface behaviour was analysed in both longitudinal and transverse directions. An additional study about compressive membrane action or arching was also conducted to understand the influence of lateral restraint, which usually occurs in composite plank floor systems used in buildings, including the one used in Eindhoven parking garage, to the capacity of the structure. This action was suspected of providing additional strength to the existing composite plank floor

Two composite SHCC-concrete beam specimens from the experimental research by Harrass [1] were used in this numerical study since the experiment had both unreinforced and reinforced interface specimens which were important for this study. The unreinforced interface beam (Sample 1) was suitable for the study of lap splice spacing and lateral restraint without any influence from reinforcement crossing the interface, while the reinforced interface beam (Sample 7) was suitable for the study of stirrups spacing. The specimens are solid beams (without weight-saving element) consisting of a SHCC (Strain Hardening Cementitious Concrete) precast layer with a joint in the mid-span, and a regular concrete cast-in-situ layer. By using DIANA 10.4 finite element analysis software, this study is able to simulate both specimens in 2D and 3D numerical models. The models represented Sample 1 failed with a horizontal crack along the interface and a flexural crack at the end of coupling reinforcement reaches the top of the cast-in-situ layer, while the models represented Sample 7 failed with a horizontal crack along the interface, a flexural crack at the end of coupling reinforcement, and a crack at the stirrup location in precast layer. From the verification study, the reinforcement bond-slip function (CEB-FIB 2010) was chosen not to be used for the rest of the study since it did not affect much the load capacity and the failure mechanism of the specimens. Consequently, pull-out failure of the stirrup is excluded for the rest of this study.

Prior to the main study, the influence of each interface parameter was studied in both unreinforced and reinforced interface models by varying the interface parameters. It was observed that interface tensile strength and stiffness are governing in the unreinforced interface model. Within the range of those parameters, the load capacity was increased and decreased by more than 50% in compared to the reference model verified by Sample 1. By adding a rectangular stirrup near the joint of unreinforced interface model, the model with reinforced interface has a different governing parameter, the cohesion, and the variability of the results decrease. Within the range of the cohesion, the load capacity was increased and decreased up to 30% in compared to the reference model verified by Sample 7. Since the interface parameters influence the capacity of both unreinforced and reinforced interface beams, two different interface types are used for the whole of the study. They are known as “smooth interface” which uses the parameters obtained from the verification with the experimental specimen, and “perfect bonded interface” which use rigid connection between the elements of the two concrete layers.

To study the influence of lap splices spacing, models with three lap splices setup from Harrass’ experiment (three coupling reinforcements and three bottom reinforcements) were compared to models with a single lap splice (one coupling reinforcement and one bottom reinforcement) with the same total reinforcement area. As a result, with perfect bonded interface, model with single lap splice has higher load capacity by more than 10% in compared to model with three lap splices though both models failed with the same failure mechanism which was the horizontal crack along coupling reinforcement and a flexural crack at the end of coupling reinforcement reaches the top of the cast-in-situ layer. Stress concentration around coupling reinforcements were observed in all models, especially in model with single coupling reinforcement. However, different horizontal crack propagation occurred in each models. Uniform horizontal crack propagation along the interface were observed in models with smooth interface, while more concentrated crack propagation around the coupling reinforcements were observed in models with perfect bonded interface, especially in model with single lap splice. This different crack propagation in models with perfect bonded interface could be the cause of different load capacity since more uncracked elements could provide more tensile force transfer from precast layer to cast-in-situ layer.

In the study of the influence of stirrups spacing, models with rectangular stirrup (two legs) setup were compared to models with a single leg vertical stirrup setup with the same total reinforcement area. In both cases the presence of the stirrup near the joint stopped the propagation of the horizontal crack. As a result, all models could reach yielding of the coupling reinforcement for both interface types although different structural stiffness is observed. The plausible cause for this difference in structural stiffness was the higher tensile stress in stirrups of model with two legs stirrups compared to model with single leg stirrup. This higher tensile stress might be resulted by the more distributed stirrups across the width of the beam.

In the additional study, models with full height lateral restraint at the support were compared with models with simple support. As a result, with perfect bonded interface, model with lateral restraint has higher load and displacement capacity by more than 14 and 2.5 times consecutively compared to the model without lateral restraint. In compared to the collapse load, the numerical result of model with lateral restraint has higher load capacity by almost 4 times. With smooth interface, model with lateral restraint has higher load and displacement capacity by more than 10 and 5.5 times consecutively compared to the model without lateral restraint. In compared to the collapse load, the numerical result of model with lateral restraint has higher load capacity by more than 2 times. These increases are in accordance with a research by Ockleston [2] which found a considerable increase of load capacity on concrete slab with lateral restraint compared to the yield line theory. Part of the increase of capacity was resulted by the fix boundary action due to bending moment at support. However, it was observed that compressive membrane action started to develop after the first flexural crack as the horizontal force at support rapidly increased after that crack. Although the models with lateral restraint of both interface types had a different failure mechanism compared to the models without lateral restraint, they have a similar final stage of the failure mechanism, which is the flexural crack at the end of coupling

reinforcement. This flexural crack propagation can be prevented from occurring earlier due to the high compressive stress at the top part of the cast-in-situ layer. When the concrete crushed at the support due to limited rotation capacity of the concrete, the compressive stress dropped causing the flexural crack at the end of coupling reinforcement to develop.

In conclusion, there was an influence of the interface behaviour to the failure and the capacity of composite SHCC-concrete beam. However, the influence was varied, depending on the coupling reinforcement spacing, presence of stirrup crossing the interface near the joint, spacing of stirrup, and interface type. It is also concluded that compressive membrane action in addition to flex bending action, which occurred due to the lateral restraint, increased the capacity of the structure. This increase depended on the interface type and rotation capacity of the concrete. A wider range of the influencing parameters are needed in future studies to get a more robust results which are beneficial for a more general conclusions. However, the series of experimental research based on this study are essential to provide a verification on the results of this numerical study.

Keywords: Interface behaviour, SHCC-concrete beam, lap splice, connecting reinforcement, interface parameters, lateral restraint, compressive membrane action, stress concentration, horizontal crack propagation

TABLE OF CONTENT

PREFACE.....	iii
ABSTRACT.....	v
TABLE OF CONTENT.....	ix
LIST OF FIGURES.....	xii
LIST OF TABLES.....	xix
 1 INTRODUCTION.....	1
1.1. Background.....	1
1.2. Problem description and statement.....	1
1.3. Research objectives and questions.....	3
1.4. Research methodology.....	4
1.5. Thesis outline.....	5
 2 LITERATURE REVIEW.....	7
2.1. Concrete-to-concrete interface.....	7
2.1.1. <i>fib</i> model code for concrete structures 2010.....	7
2.1.2. Eurocode NEN-EN 1992-1-1+C2:2011.....	9
2.1.3. Research by Croes.....	9
2.2. Reinforcement bond transfer.....	10
2.2.1. Ultimate bond stress.....	10
2.2.2. Anchorage length.....	11
2.2.3. Bar spacing.....	11
2.2.4. Bond-slip.....	12
2.3. Lap splice.....	12
2.3.1. Lap length.....	13
2.3.2. Transverse reinforcement.....	13
2.4. Membrane action.....	14
2.4.1. Compressive membrane action.....	14
2.4.2. Tensile membrane action.....	16
2.5. Composite plank floor.....	16
2.5.1. Interface of composite plank floor.....	18
2.5.2. Non-contact lap splice.....	19
2.5.3. Connecting reinforcement.....	20
2.5.4. Failure mechanisms.....	22
2.5.5. Numerical models.....	22
2.6. Summary.....	26
 3 NUMERICAL MODEL SETUP.....	28
3.1. Experimental reference.....	28
3.1.1. Test specimens.....	28

3.1.2.	Experimental result of Sample 1.....	30
3.1.3.	Experimental result of Sample 7.....	32
3.2.	Numerical setup	34
3.2.1.	Finite element types.....	36
3.2.2.	Material properties and constitutive models	37
3.2.3.	Load, boundary, and symmetry conditions.....	40
3.2.4.	Mesh size	42
3.2.5.	Iterative scheme.....	42
3.3.	Verification of numerical models.....	43
3.3.1.	Unreinforced interface beams.....	43
3.3.2.	Reinforced interface beams.....	44
3.4.	Interface parameters in codes and other research	47
3.5.	Summary.....	47
 4 	SENSITIVITY STUDY OF INTERFACE PARAMETERS.....	49
4.1.	Unreinforced interface beams	49
4.1.1.	Interface stiffness	49
4.1.2.	Interface tensile strength.....	51
4.1.3.	Cohesion	52
4.1.4.	Friction angle	53
4.2.	Reinforced interface beams.....	54
4.2.1.	Interface stiffness	55
4.2.2.	Interface tensile strength.....	55
4.2.3.	Cohesion	56
4.2.4.	Friction angle	57
4.3.	Summary.....	58
 5 	NUMERICAL RESULTS AND DISCUSSIONS.....	62
5.1.	Unreinforced interface beams	62
5.1.1.	Experimental lap splices setup.....	62
5.1.2.	Single lap splice setup	70
5.2.	Reinforced interface beams.....	82
5.2.1.	Rectangular stirrup setup.....	82
5.2.2.	Single leg stirrup setup	92
5.3.	Laterally restrained beams.....	100
5.3.1.	Perfect bonded interface	100
5.3.2.	Smooth interface	104
 6 	CONCLUDING REMARKS.....	109
6.1.	Conclusions.....	109
6.2.	Recommendation.....	112
	REFERENCES.....	114
 A1 	MODEL VARIATIONS	116
 A2 	ANALYTICAL SOLUTIONS.....	120
 A3 	CONVERGENCE BEHAVIOUR OF REFERENCE MODELS.....	122

LIST OF FIGURES

Figure 1.1 – Critical detail at composite plank floor joint [3].....	1
Figure 1.2 – Spacing between coupling reinforcements (modified from [4] and [10])	2
Figure 1.3 – Spacing between connecting reinforcement (modified from [4] and [10])	2
Figure 1.4 – Concrete-to-concrete interface observed in this research (modified from [10])	3
Figure 1.5 – Research workflow with numbers in circles indicating the related supporting research question.....	4
Figure 2.1 –Shear mechanisms of concrete-to-concrete interface [16].....	8
Figure 2.2 – Bond transfer [14].....	10
Figure 2.3 – Concrete minimum cover [9].....	11
Figure 2.4 – Types of crack propagation after debonding process starts [14].....	12
Figure 2.5 – <i>fib</i> Model code for concrete structures 2010 bond stress-slip relationship [13].....	12
Figure 2.6 – Tensile lap splices load transfer [14].....	13
Figure 2.7 – Transverse reinforcement [9].....	14
Figure 2.8 – Compressive membrane action in slab [18]	14
Figure 2.9 – Load-displacement graph for clamp slab [17]	15
Figure 2.10 – Interaction diagram [17]	15
Figure 2.11 – Boundary stiffness effect in load-displacement graph [17].....	16
Figure 2.12 – Layouts of composite plank floor (a) row, (b) flat slab (modified from [19]).....	17
Figure 2.13 – Load distribution in flat slab [19].....	17
Figure 2.14 – Plank floor critical detail [19].....	17
Figure 2.15 – Bending moment due to lap splices eccentricity [1].....	18
Figure 2.16 – Interface shear and normal stress [19]	18
Figure 2.17 – Connecting reinforcement types [11].....	20
Figure 2.18 – Tensile force due to eccentricity taken by the connecting reinforcement [12].....	20
Figure 2.19 – Critical detail with bent reinforcement [20].....	21
Figure 2.20 – Failure mechanism 5 [21].....	22
Figure 2.21 – Numerical model of specimen B1 by Weglarzy [24].....	23
Figure 2.22 – Critical joint investigated by Lundgen [22].....	23
Figure 2.23 – Simulated crack pattern of Hedared model with roughened surface before failure [25] 23	23
Figure 2.24 – Simulated crack pattern of Hedared model without adhesion before failure [25].....	23
Figure 2.25 – Numerical model VL34a by abt [26]	24
Figure 2.26 – Simulated crack pattern of model 2 (above) and experiment (below) after failure	24
Figure 3.1 – Sample 1 geometrical properties [1]	29
Figure 3.2 – Sample 7 geometrical properties [1]	29
Figure 3.3 – Sample 1 (a) section A-A and (b) section B-B [1].....	29
Figure 3.4 – Sample 1 test setup [1].....	30
Figure 3.5 – Load-displacement, -interface opening, and -joint opening graphs of Sample 1 [1]	30
Figure 3.6 – DIC image of Sample 1 at load stage 1 (2.5 kN) [1].....	31
Figure 3.7 – DIC image of Sample 1 at load stage 2 (7.5 kN) [1].....	31
Figure 3.8 – DIC image of Sample 1 at load stage 3 (11 kN) [1].....	31

Figure 3.9 – DIC image of Sample 1 at load stage 4 (13 kN) [1].....	31
Figure 3.10 – DIC image of Sample 1 at failure [1].....	31
Figure 3.11 – Load-displacement, -interface opening, and -joint opening graphs of Sample 7 (black lines) [1].....	32
Figure 3.12 – DIC image of Sample 7 at load stage 1 (2.5 kN) [1].....	33
Figure 3.13 – DIC image of Sample 7 at load stage 2 (7.5 kN) [1].....	33
Figure 3.14 – DIC image of Sample 7 at load stage 3 (15 kN) [1].....	33
Figure 3.15 – DIC image of Sample 7 at load stage 4 (25 kN) [1].....	33
Figure 3.16 – DIC image of Sample 7 at failure [1].....	33
Figure 3.17 – Rotational restraint at the stirrup resulting in tensile cracks [1].....	33
Figure 3.18 – Typical 2D finite element model based on Sample 1 (model name started with 2D-SI)...	34
Figure 3.19 – Typical 2D finite element model based on Sample 7 (model name started with 2D-SI-SJ).....	34
Figure 3.20 – Typical 3D finite element model based on Sample 1 (model name started with 3D-SI)...	34
Figure 3.21 – Typical 3D finite element model based on Sample 7 (model name started with 3D-SI-SJ).....	35
Figure 3.22 – Element type of typical 2D model based on Sample 1 (model name started with 2D-SI).....	36
Figure 3.23 – Element type of 2D model based on Sample 7 (model name started with 2D-SI-SJ).....	36
Figure 3.24 – Element type of typical 3D model based on Sample 1 (model name started with 3D-SI).....	37
Figure 3.25 – Element type of typical 3D model based on Sample 7 (model name started with 3D-SI-SJ).....	37
Figure 3.26 – (a) Tensile and (b) compressive constitutive model of concrete [28].....	38
Figure 3.27 – (a) Tensile and (b) compressive constitutive model of SHCC [28].....	38
Figure 3.28 – (a) Axial [28] and (b) bond-slip constitutive model [29] of steel rebar.....	39
Figure 3.29 – Coulomb friction model with tension cut-off [29].....	40
Figure 3.30 – Load, boundary, and symmetry conditions of typical 2D model based on Sample 1 (model name started with 2D-SI).....	41
Figure 3.31 – Load, boundary, and symmetry conditions of 2D model based on Sample 7 (model name started with 2D-SI-SJ).....	41
Figure 3.32 – Load, boundary, and symmetry conditions of typical 3D model based on Sample 1 (model name started with 3D-SI).....	41
Figure 3.33 – Load, boundary, and symmetry conditions of typical 3D model based on Sample 7 (model name started with 3D-SI-SJ).....	41
Figure 3.34 – Mesh size of typical 2D model based on Sample 1 (model name started with 2D-SI).....	42
Figure 3.35 – Mesh size of typical 2D model based on Sample 7 (model name started with 2D-SI-SJ).....	42
Figure 3.36 – Mesh size of typical 3D model based on Sample 1 (model name started with 3D-SI).....	42
Figure 3.37 – Mesh size of typical 3D model based on Sample 7 (model name started with 3D-SI-SJ).....	42
Figure 3.38 – Load-displacement graph of Sample 1 experiment [1] and models with and without reinforcement bond-slip function.....	43
Figure 3.39 – Crack strain at failure of (a) 2D model (2D-SI-BS) and (b) 3D model (3D-SI-BS) with reinforcement bond-slip function.....	44
Figure 3.40 – Crack strain at failure of (a) 2D model (2D-SI) and (b) 3D model (3D-SI) without reinforcement bond-slip function.....	44
Figure 3.41 – Load-displacement graph of Sample 7 experiment [1] and models with and without reinforcement bond-slip function.....	45
Figure 3.42 – Crack strain at failure of (a) 2D model (2D-SI-SJ-BS) and (b) 3D model (3D-SI-SJ-BS) with reinforcement bond-slip function.....	46
Figure 3.43 – Crack strain at failure of (a) 2D model (2D-SI-SJ) and (b) 3D model (3D-SI-SJ) without reinforcement bond-slip function.....	46
Figure 3.44 – Crack strain at 15 kN load of (a) 2D model (2D-SI-SJ-BS) and (b) 3D model (3D-SI-SJ-BS) with reinforcement bond-slip function.....	46
Figure 3.45 – Crack strain at 15 kN load of (a) 2D model (2D-SI-SJ) and (b) 3D model (3D-SI-SJ) without reinforcement bond-slip function.....	46

Figure 4.1 – Load-displacement graph of model 2D-SI with various interface stiffness.....	50
Figure 4.2 – Maximum total load-interface stiffness relationship based on model 2D-SI.....	50
Figure 4.3 – Interface tensile stress of base model (2D-SI) with interface stiffness 10 N/mm ³ at vertical displacement 0.5 mm.....	50
Figure 4.4 – Load-displacement graph of model 2D-SI with various interface tensile strength with markers indicating the start of horizontal crack at the joint.....	51
Figure 4.5 – Maximum total load-interface tensile strength relationship based on model 2D-SI.....	51
Figure 4.6 – Load-displacement graph of model 2D-SI with various cohesion.....	52
Figure 4.7 – Maximum total load-cohesion relationship based on model 2D-SI.....	52
Figure 4.8 – Comparison of Mohr-Coulomb failure envelop of model 2D-SI with cohesion 0.1 MPa and 0.5 MPa (reference).....	53
Figure 4.9 – Load-displacement graph of model 2D-SI with various friction angle.....	53
Figure 4.10 – Maximum total load-friction angle relationship based on model 2D-SI.....	54
Figure 4.11 – Comparison of Mohr-Coulomb failure envelop of model 2D-SI with friction angle 1.0 rad and 0.54 rad (reference).....	54
Figure 4.12 – Load-displacement graph of various interface stiffness based on model 2D-SI-SJ.....	55
Figure 4.13 – Maximum total load-interface stiffness relationship based on model 2D-SI-SJ.....	55
Figure 4.14 – Load-displacement graph of various interface tensile strength based on model 2D-SI-SJ.....	56
Figure 4.15 – Maximum total load-interface tensile strength relationship based on model 2D-SI-SJ.....	56
Figure 4.16 – Load-displacement graph of various cohesion based on model 2D-SI-SJ.....	57
Figure 4.17 – Maximum total load-cohesion relationship based on model 2D-SI-SJ.....	57
Figure 4.18 – Load-displacement graph of various friction angle based on model 2D-SI-SJ.....	58
Figure 4.19 – Maximum total load-friction angle relationship based on model 2D-SI-SJ.....	58
Figure 4.20 – Maximum total load-interface parameters relationship of unreinforced interface beam based on model 2D-SI.....	59
Figure 4.21 – Maximum total load-interface parameters relationship of reinforced interface beam based on model 2D-SI-SJ.....	59
Figure 5.1 – Load-displacement graph of unreinforced interface model with smooth interface (2D-SI and 3D-SI).....	63
Figure 5.2 – Crack strain on the side of model 3D-SI at (a) load stage 1, (b) load stage 2, (c) load stage 3, (d) failure stage.....	63
Figure 5.3 – Location of node A, B, C, and D for the interface stresses development analysis.....	64
Figure 5.4 – Interface stresses development of model 3D-SI at four nodes location.....	64
Figure 5.5 – Interface normal stress STNz development of model 3D-SI at (a) load stage 1, (b) load stage 2, (c) load stage 3, (d) failure stage.....	64
Figure 5.6 – Interface shear stress STSx development of model 3D-SI at (a) load stage 1, (b) load stage 2, (c) load stage 3, (d) failure stage.....	65
Figure 5.7 – Stress concentration around the joint at the beginning of the analysis of model 3D-SI.....	65
Figure 5.8 – Tensile force transfer and the resulted moment around the joint.....	65
Figure 5.9 – Interface normal stress at the mid-section of model 3D-SI at different stages.....	66
Figure 5.10 – Interface shear stress at the mid-section of model 3D-SI at different stages.....	66
Figure 5.11 – Load-displacement graph of unreinforced interface model with perfect bonded interface (2D-PB and 3D-PB).....	68
Figure 5.12 – Crack strain on the side of model 3D-PB (a) at load stage 1, (b) a few load step after load stage 3, (c) at load stage 4, (d) at failure stage.....	68
Figure 5.13 – Elements of interest at the level of coupling reinforcement for the stress and strain analysis of model with perfect bonded interface.....	68
Figure 5.14 – Stress Szz of the elements at the level of the coupling reinforcement of model 3D-PB (a) at load stage 1, (b) right after load stage 2, (c) at load stage 4, (d) at failure stage.....	69
Figure 5.15 – Strain Ezz of the elements at the level of the coupling reinforcement of model 3D-PB (a) at load stage 1, (b) right after load stage 2, (c) at load stage 4, (d) at failure stage.....	69
Figure 5.16 – Reinforcement setup and concrete-to-concrete interface of model with a smooth interface (3D-SI-1L).....	71

Figure 5.17 – Reinforcement setup of model with a perfect bonded interface (3D-PB-1L).....	71
Figure 5.18 – Load-displacement graph of unreinforced interface model (smooth interface) with single lap splice setup (3D-SI-1L) and experimental setup (3D-SI)	71
Figure 5.19 – Crack strain on the side of model 3D-SI-1L (a) at load stage 1, (b) at load stage 3, (c) at load stage 4, (d) at failure stage.....	72
Figure 5.20 – Interface stresses development of model 3D-SI-1L at four nodes location.....	72
Figure 5.21 – Interface normal stress STN_z development of model 3D-SI-1L (a) at load stage 1, (b) right after load stage 2, (c) at load stage 4, (d) at failure stage	73
Figure 5.22 – Interface shear stress STS_x development of model 3D-SI-1L (a) at load stage 1, (b) right after load stage 2, (c) at load stage 4, (d) at failure stage	73
Figure 5.23 – In-plane principal stress at mid-section of model 3D-SI-1L (a) at load step 1, (b) right after load stage 2, (c) at load stage 4, (d) at failure stage	74
Figure 5.24 – In-plane principal stress at the top side of interface of model 3D-SI-1L (a) at load step 1, (b) right after load stage 2, (c) at load stage 4, (d) at failure stage.....	74
Figure 5.25 – In-plane principal stress at the location of stress concentration in transverse direction right after load stage 2 of model 3D-SI-1L	75
Figure 5.26 – Load-displacement graph of unreinforced interface model (perfect bonded interface) with single lap splice setup (3D-PB-1L) and experimental setup (3D-PB).....	76
Figure 5.27 – Crack strain on the side of model 3D-PB-1L (a) at load stage 1, (b) a few load steps after load stage 3, (c) at load stage 4, (d) at failure stage	76
Figure 5.28 – Stress S_{zz} of the elements at the level of coupling reinforcement of model 3D-PB-1L (a) at $P = 20$ kN, (b) at $P = 23.5$ kN, (c) at load stage 4, (d) at failure	77
Figure 5.29 – Stress E_{zz} of the elements at the level of coupling reinforcement of model 3D-PB-1L (a) at $P = 20$ kN, (b) at $P = 23.5$ kN, (c) at load stage 4, (d) at failure.....	77
Figure 5.30 – In-plane principal stress at mid-section of model 3D-PB-1L (a) at $P = 20$ kN, (b) at $P = 23.5$ kN, (c) at load stage 4, (d) at failure	78
Figure 5.31 – In-plane principal stress at level of coupling reinforcement of model 3D-PB-1L (a) at $P = 20$ kN, (b) at $P = 23.5$ kN, (c) at load stage 4, (d) at failure.....	78
Figure 5.32 – Reinforcement bond transfer stress patterns in transverse direction at a few load steps after load stage 2 (load step 12) in model 3D-PB-1L.....	78
Figure 5.33 – Load-displacement graph of unreinforced interface model (3D-PB and 3D-PB-1L) with perfect bonded interface and concrete in both layers.....	80
Figure 5.34 – Crack strain on the side of model 3D-PB-1L-RC (a) at load stage 1, (b) right after load stage 2, (c) at load stage 4, (d) at failure stage	80
Figure 5.35 – Stress S_{zz} of the elements at the level of coupling reinforcement of model 3D-PB-1L-RC (a) at load stage 3A, (b) at load stage 3B, (c) at load stage 4, (d) at failure stage.....	81
Figure 5.36 – Strain E_{zz} of the elements at the level of coupling reinforcement of model 3D-PB-1L-RC (a) at load stage 3A, (b) at load stage 3B, (c) at load stage 4, (d) at failure stage.....	81
Figure 5.37 – Load-displacement graph of reinforced interface model with smooth interface (2D-SI-SJ and 3D-SI-SJ)	82
Figure 5.38 – Crack strain on the side of model 3D-SI-SJ (a) right after load stage 2, (b) at load stage 3	83
Figure 5.39 – Interface stresses development of model 3D-SI-SJ at four nodes location	83
Figure 5.40 – Interface normal stress at the mid-section of model 3D-SI-SJ at different load stages....	83
Figure 5.41 – Interface shear stress at the mid-section of model 3D-SI-SJ at different load stages.....	84
Figure 5.42 – Interface normal stress STN_z development of model 3D-SI-SJ (a) at the beginning of analysis, (b) at load stage 1, (c) right after load stage 2, (d) at load stage 3.....	84
Figure 5.43 – Interface shear stress STS_x development of model 3D-SI-SJ (a) at the beginning of analysis, (b) at load stage 1, (c) right after load stage 2, (d) at load stage 3.....	85
Figure 5.44 – In-plane principal stress at mid-section of model 3D-SI-SJ (a) at the beginning of analysis, (b) at load stage 1, (c) right after load stage 2, (d) at load stage 3.....	85
Figure 5.45 – In-plane principal stress at the stirrup section of model 3D-SI-SJ (a) at the beginning of analysis, (b) at load stage 1, (c) right after load stage 2, (d) at load stage 3.....	86

Figure 5.46 – In-plane principal stress at the top side of interface of model 3D-SI-SJ (a) at the beginning of analysis, (b) at load stage 1, (c) right after load stage 2, (d) at load stage 3.....	86
Figure 5.47 – In-plane principal stress at the bottom side of interface of model 3D-SI-SJ (a) at the beginning of analysis, (b) at load stage 1, (c) right after load stage 2, (d) at load stage 3.....	86
Figure 5.48 – In-plane principal stress at the stirrup location of model 3D-SI-SJ (a) at the beginning of analysis, (b) at load stage 1, (c) right after load stage 2, (d) at load stage 3.....	87
Figure 5.49 – Crack-width E_{cwXX} of (a) model 2D-SI-SJ and (b) model 3D-SI-SJ at 3.0 mm displacement	88
Figure 5.50 – Load-displacement graph of reinforced interface model with perfect bonded interface (2D-PB-SJ and 3D-PB-SJ).....	88
Figure 5.51 – Crack strain on the side of model 3D-PB-SJ (a) at $P = 20$ kN, (b) at load stage 4.....	89
Figure 5.52 – Stress S_{zz} of the elements at the level of coupling reinforcement of model 3D-PB-SJ (a) at load stage 1, (b) right after load stage 2 (c) at $P = 20$ kN, (d) at load stage 4.....	89
Figure 5.53 – Strain E_{zz} of the elements at the level of coupling reinforcement of model 3D-PB-SJ (a) at load stage 1, (b) right after load stage 2 (c) at $P = 20$ kN, (d) at load stage 4.....	89
Figure 5.54 – In-plane principal stress at mid-section of model 3D-PB-SJ (a) at load stage 1, (b) right after load stage 3, (c) at $P = 20$ kN, (d) at load stage 4.....	90
Figure 5.55 – In-plane principal stress at the stirrup section of model 3D-PB-SJ (a) at load stage 1, (b) right after load stage 3, (c) at $P = 20$ kN, (d) at load stage 4	90
Figure 5.56 – In-plane principal stress at level of coupling reinforcement of model 3D-PB-SJ (a) at load stage 1, (b) right after load stage 3, (c) at $P = 20$ kN, (d) at load stage 4.....	90
Figure 5.57 – In-plane principal stress at the stirrup location of model 3D-PB-SJ (a) at load stage 1, (b) right after load stage 3, (c) at $P = 20$ kN, (d) at load stage 4	91
Figure 5.58 – Reinforcement setup and concrete-to-concrete interface of model with smooth interface (3D-SI-SJ-1L)	92
Figure 5.59 – Reinforcement setup of model with perfect bonded interface (3D-PB-SJ-1L).....	92
Figure 5.60 – Load-displacement graph of reinforced interface model with smooth interface and single leg stirrup (3D-SI-SJ-1L)	93
Figure 5.61 – Crack strain on the side of model 3D-SI-SJ-1L (a) right after load stage 2, (b) at load stage 3.....	93
Figure 5.62 – Interface stresses development of model 3D-SI-1L at four nodes location.....	93
Figure 5.63 – Interface normal stress STN_z development of model 3D-SI-SJ-1L (a) at the beginning of analysis, (b) at load stage 1, (c) right after load stage 2, (d) at load stage 3.....	94
Figure 5.64 – Interface shear stress STS_x development of model 3D-SI-SJ-1L (a) at the beginning of analysis, (b) at load stage 1, (c) right after load stage 2, (d) at load stage 3.....	94
Figure 5.65 – In-plane principal stress at mid-section of model 3D-SI-SJ-1L (a) at the beginning of analysis, (b) at load stage 1, (c) right after load stage 2, (d) at load stage 3.....	95
Figure 5.66 – In-plane principal stress at the top side of interface of model 3D-SI-SJ-1L (a) at the beginning of analysis, (b) at load stage 1, (c) right after load stage 2, (d) at load stage 3.....	95
Figure 5.67 – In-plane principal stress at the bottom side of interface of model 3D-SI-SJ-1L (a) at the beginning of analysis, (b) at load stage 1, (c) right after load stage 2, (d) at load stage 3.....	95
Figure 5.68 – In-plane principal stress at the stirrup location of model 3D-SI-SJ-1L (a) at the beginning of analysis, (b) at load stage 1, (c) right after load stage 2, (d) at load stage 3.....	96
Figure 5.69 – S_{xx} of connecting reinforcement of (a) model 3D-SI-SJ (b) model 3D-SI-SJ-1L at 4 mm vertical displacement.....	96
Figure 5.70 – Load-displacement graph of reinforced interface model with perfect bonded interface and single leg stirrup (3D-PB-SJ-1L).....	97
Figure 5.71 – Crack strain on the side of model 3D-PB-SJ-1L (a) at $P = 20$ kN, (b) at load stage 4	97
Figure 5.72 – Stress S_{zz} of the elements at the level of coupling reinforcement of model 3D-PB-SJ-1L (a) at load stage 1, (b) right after load stage 3 (b) at $P = 20$ kN, (b) at load stage 4.....	98
Figure 5.73 – Strain E_{zz} of the elements at the level of coupling reinforcement of model 3D-PB-SJ-1L (a) at load stage 1, (b) right after load stage 3 (b) at $P = 20$ kN, (b) at load stage 4.....	98

Figure 5.74 – In-plane principal stress at mid-section of model 3D-PB-SJ-1L (a) at load stage 1, (b) right after load stage 3, (c) at P = 20 kN, (d) at load stage 4.....	98
Figure 5.75 – In-plane principal stress at level of coupling reinforcement of model 3D-PB-SJ-1L (a) at load stage 1, (b) right after load stage 3, (c) at P = 20 kN, (d) at load stage 4.....	99
Figure 5.76 – In-plane principal stress at the stirrup location of model 3D-PB-SJ-1L (a) at load stage 1, (b) right after load stage 3, (c) at P = 20 kN, (d) at load stage 4.....	99
Figure 5.77 – Finite element model of laterally restraint unreinforced beam with a perfect bonded interface (2D-PB-RC-FR)	100
Figure 5.78 – Finite element model of laterally restraint unreinforced beam with a smooth interface (2D-SI-RC-FR)	100
Figure 5.79 – Load-displacement graph of laterally restrained unreinforced interface model with perfect bonded interface (2D-PB-RC-FR).....	101
Figure 5.80 – Total load-total lateral force graph of laterally restrained unreinforced interface model with perfect bonded interface (2D-PB-RC-FR)	101
Figure 5.81 – Crack strain of model 2D-PB-RC-FR at load stage (a) 1, (b) 3, (c) 3, (d) 4, (e) 5, (f) 6	102
Figure 5.82 – In-plane principal stress of model 2D-PB-RC-FR at load stage (a) 1, (b) 2, (c) 3.....	102
Figure 5.83 – Load-displacement graph of laterally restrained unreinforced interface model with smooth interface (2D-SI-RC-FR).....	104
Figure 5.84 – Total load-total lateral force of laterally restrained unreinforced interface model with smooth interface (2D-SI-RC-FR).....	105
Figure 5.85 – Crack strain of model 2D-SI-RC-FR at load stage (a) 1, (b) 3, (c) 3, (d) 4, (e) 5, (f) 6	105
Figure 5.86 – In-plane principal stress of model 2D-SI-RC-FR at load stage (a) 1, (b) 2, (c) 3, (d) 4, (e) 5, (f) 6.....	106
Figure A2.1 – Convergence behaviour of model 2D-SI.....	122
Figure A2.2 – Convergence behaviour of model 3D-SI.....	122
Figure A2.3 – Convergence behaviour of model 2D-SI-SJ.....	123
Figure A2.4 – Convergence behaviour of model 3D-SI-SJ.....	123

LIST OF TABLES

Table 2.1 – Coefficients for different surface roughness according to fib Model Code [13]	8
Table 2.2 – Coefficients for different surface roughness according to Eurocode [8]	9
Table 2.3 – Coefficients for different surface roughness [19].....	19
Table 2.4 – Concrete properties of several research with DIANA.....	25
Table 2.5 – Reinforcement properties of several research with DIANA.....	25
Table 2.6 – Concrete-to-concrete interface properties of several research with DIANA	26
Table 3.1 – Various values of Sample 1 at failure [1].....	30
Table 3.2 – Various values of Sample 7 at failure [1].....	32
Table 3.3 – Parameter variations in each numerical study.....	35
Table 3.4 – Model name abbreviations	35
Table 3.5– Finite element types for 2D models.....	36
Table 3.6 – Finite element types for 3D models	36
Table 3.7 – Material properties of concrete.....	37
Table 3.8 – Material properties of SHCC	38
Table 3.9 – Material properties of steel reinforcement.....	39
Table 3.10 – Material properties of steel load and bearing pads	39
Table 3.11 – Material properties of concrete-to-concrete interface (smooth interface).....	40
Table 3.12 – Iterative scheme.....	43
Table 3.13 – Load capacity of Sample 1 [1] and its simulated numerical models	44
Table 3.14 – Load capacity of Sample 7 [1] and its simulated numerical models	45
Table 3.15 – Comparison of interface parameters according to several codes and research.....	47
Table 4.1 – Interface tensile stress at the joint at 0.5 mm vertical displacement	51
Table A1.1 – List of models used in this research along with their variations.....	117

| 1 | INTRODUCTION

1.1. Background

In 2017, a new parking garage of Eindhoven airport was partially collapsed due to the failure along the longitudinal joint (long-side) of the composite plank floor on the roof level [3]. Both experimental and numerical results [4] showed that the joint became a critical detail which suffered high positive bending moment in its transverse direction. At the day of failure, in addition to the self-weight, additional bending moment was imposed by high temperature loading due to the sunny day. The resulted tensile force from the permanent and temperature loads has to be taken by reinforcement at the bottom part of the slab. However, since the bottom part of the composite plank floor were precast segments, the joints between segments interrupted the tensile reinforcement. The typical solution for this system used in this project was using coupling reinforcement over the joint on top of the precast elements as lap splices. Transfer of tensile force between those reinforcements will occur in concrete as tension ties and compressive struts. Since there is also an interface between precast and cast-in-situ concrete layers in through-thickness direction, the tensile force should also be transferred through shear at the interface in addition to the couple of tension near the joint and compression near the coupling end in perpendicular direction of the interface. From the investigation, there is not enough resistance at the interface to transfer the force which leads to failure between two layers of concrete.

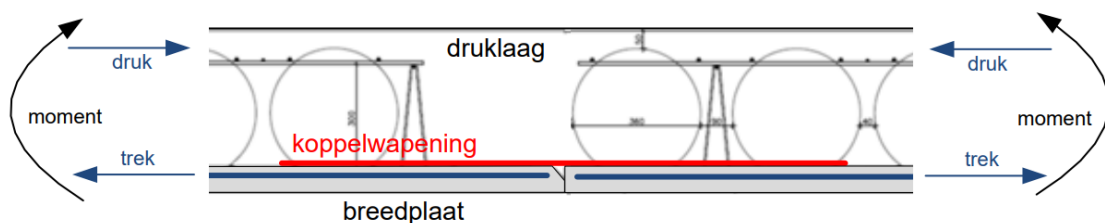


Figure 1.1 – Critical detail at composite plank floor joint [3]

1.2. Problem description and statement

Composite plank floor (*breedplaatvloer* in Dutch) is not a new thing in the Netherlands [5]. It has been used for decades and hundreds of thousands of square meters of structures are using this system. However, once it was discovered that the concrete-to-concrete interface around the joint is the weakest link of the structure in the case of Eindhoven airport parking garage, the safety of existing structures became a concern. There was also a concern about the new structures design based on the design codes and guideline back then, the very same which were used for the collapsed structure. Consequently, it was needed to evaluate the design rules and details around the joint and the interface. In order to do so, numerous research have been and are to be conducted. Recently, more research have been conducted by Adviesbureau Hageman [4], BAM-Cobax [6], and Betonhuis [7]. In 2019, “step-by-step plan for existing building assessment” [8] has been released, but new research is still needed until the release of the new design rules.

One of the details is tensile lap splices (coupling reinforcement in cast-in-situ layer and bottom reinforcement in precast layer). The spacing between coupling reinforcements usually depends on the presence of weight-saving elements. Due to their presence, the spacings between coupling reinforcements are determined by their size. Sometimes, it could be more than 250 mm, the maximum spacing required by the code [9]. When the flexural crack appears, effectively only the coupling reinforcements take the tensile forces at the joint. In this situation, near the crack, stress transfer will be concentrated to the coupling reinforcement. However, if the spacing between coupling reinforcement becomes too far, there could be parts of concrete which are too far to distribute the stress to the reinforcement. Since the coupling reinforcement is part of the lap splices and it has to transfer the tensile force through the interface, there could be parts of the interface which have higher stress and parts which are not effective to transfer the force.

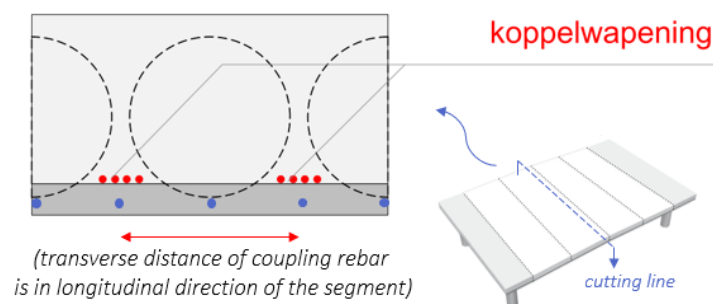


Figure 1.2 – Spacing between coupling reinforcements (modified from [4] and [10])

The other detail is transverse distance between connecting reinforcement (reinforcement crossing the interface between precast and cast-in-situ layer). Lattice girder is one of connecting reinforcement types which is common to be used in the Netherlands. The lattice girder is applied in the longitudinal direction of the precast segment and could be put as far as 418 mm from the joint (edge) as it is required in the Dutch code [11]. In the specimen taken from Eindhoven airport parking garage, the lattice girder was applied approximately 400 mm from the joint, close to the maximum distance required [4]. It turns out that the plank floor was failed due to the delamination of the interface which was caused by stress concentration at the joint and followed by pull-out of the lattice girder. One of the solutions to prevent that failure mechanism at existing structures is the application of vertical anchor near the joint. The similar use of connecting reinforcement near the joint in the form of bent reinforcement is one of the solutions in the background for the new construction rules [12] which is based on the research of BAM-Cobiax [6]. However, in the current design code, there is no specific requirement for the spacing between the connecting reinforcement in the longitudinal direction of the segment. If the spacing between connecting reinforcements is too far away, there could be parts of concrete which are too far to distribute the stress from the lap splices to the connecting reinforcements.

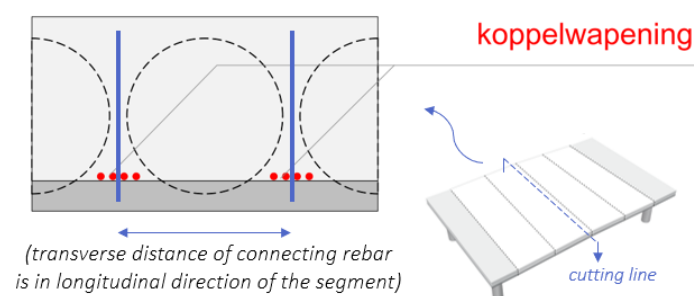


Figure 1.3 – Spacing between connecting reinforcement (modified from [4] and [10])

One thing rarely discussed in the research of composite plank floors is the fact that most of the existing structures are not collapsed until this day. In [5], it is discussed that there is a possibility of additional strength, such as compressive membrane action (arching/arch of compressive stress) from the structure which is laterally restrained in certain degree of stiffness. Actually, membrane action in slab is not a new

thing. It has been long known to be another load transfer mechanism in slabs [2]. However, there is no specific research about it in the composite plank floor.

In summary, after the partial collapse of Eindhoven airport parking garage, there is a need to have new revised design rules for composite plank floor. However, there is still a lack of knowledge in the interface behaviour and its influence on the capacity of the structure. Moreover, there is also a lack of research in the membrane action influence on the failure of composite plank floor.

1.3. Research objectives and questions

In relation to the problems described in the chapter 1.2, there are several objectives which will be achieved in this thesis. First, this thesis aims to understand the influence of lap splices spacing and connecting reinforcements (reinforcement crossing the interface) spacing to the interface behaviour. Since the direction of the spacings which will be researched is in the longitudinal direction of the segments while the direction of the critical detail with high bending moment is in transverse direction of the segment, stress distribution will be studied on 2D plane interface as can be seen in Figure 1.4. Moreover, this thesis aims to understand the influence of the interface behaviour on the capacity of the composite structure. This knowledge will be beneficial to understand the effectiveness of connecting reinforcement distance for the repairment of existing structures, such as vertical anchoring. It could also be beneficial to understand the effectiveness of spacing between connecting reinforcement and lap splices for the design of new structures. Another aim of this thesis is to investigate the presence and the influence of compressive membrane action in composite structure on its capacity. Understanding the membrane action in the composite plank floor will be beneficial for the assessment of existing structures as a possible additional strength present in the structure.

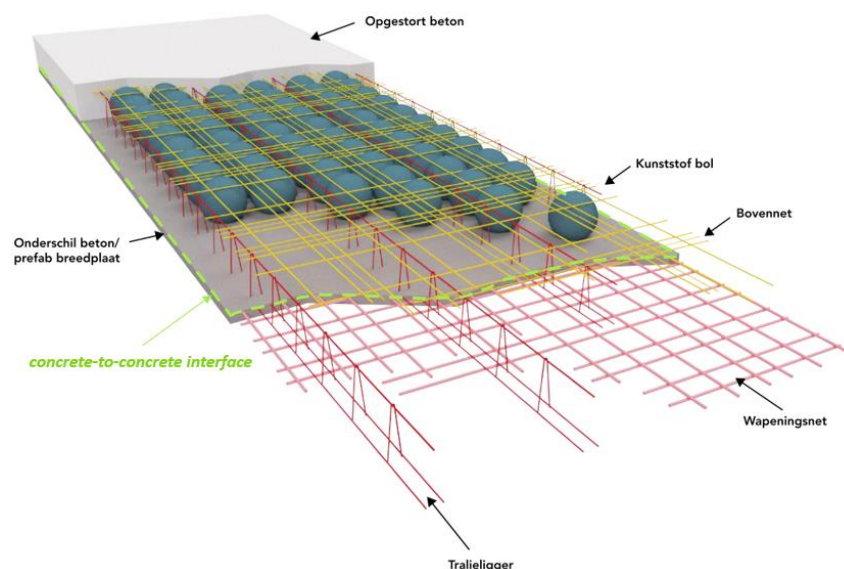


Figure 1.4 – Concrete-to-concrete interface observed in this research (modified from [10])

Main research question:

How does the interface behaviour influence the capacity of the joint in composite structure?

Supporting research questions:

1. How does the spacing between lap splices influence the interface behaviour?
2. How does the spacing between stirrup crossing the interface near the joint influence the interface behaviour?
3. What is a suitable approach to numerically model the critical detail?
4. What is the influence of interface parameters to the interface behaviour?

Additional research question:

What is the influence of lateral restraint to the capacity of composite structure?

1.4. Research methodology

In order to achieve the research objectives, there are several stages which need to be done. First, the review of literatures which are related to this research, including the composite plank floor and its components, numerical research, and experimental research of composite plank floor. This literature will provide fundamental knowledge about composite structure, guidance for the numerical analysis, and experimental result for the verification of numerical models. Second, the verification of the numerical results with the chosen experimental specimens. In a numerical study, verification with experimental research is important to support the result of the study. It also helps to find the suitable approach to model the critical detail of the composite structure (3rd supporting research question). Third, the sensitivity study of interface parameters. After the model has been verified, sensitivity study could be a help for the numerical analysis by providing the knowledge about the effect of each interface parameters on the capacity of the composite structure in numerical model (4th supporting research question). Fourth, the numerical modelling and analysis. With the knowledge from literature review and sensitivity study, and with the support from the verification result, the numerical analysis could be started to answer the main research question, its supporting questions, and the additional research question. After the 4 stages have been done, at the last stage, the conclusions of this research will be made with some recommendations about the future study. All of these stages are summarized in the following figure with a blue circle at the top-left corner as an indication of the related supporting question.

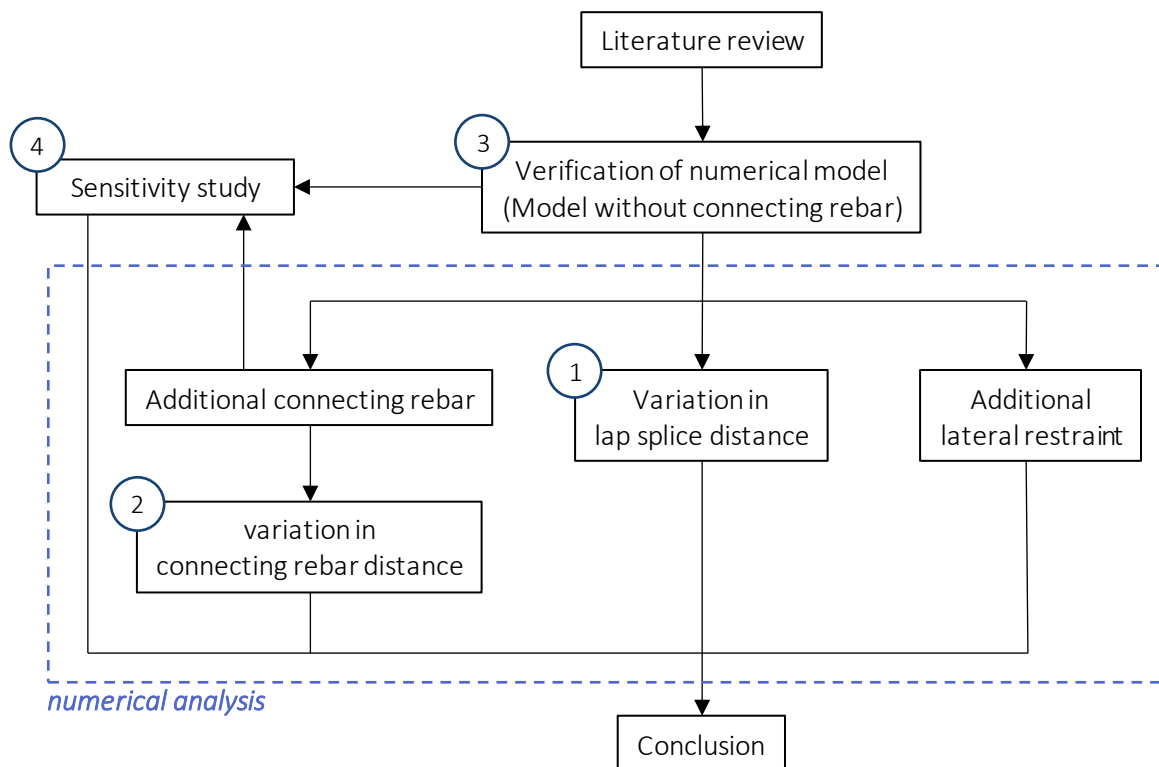


Figure 1.5 – Research workflow with numbers in circles indicating the related supporting research question

1.5. Thesis outline

This thesis consists of 6 chapters. The research background, problem description and statement, research objectives and questions, research methodology, and this thesis outline are presented in the first chapter. Several literatures which are related to the research are presented in the chapter 2. It contains the description of concrete-to-concrete interface, reinforcement bond transfer, lap splices and membrane action. Their relation specifically to the composite plank floor are presented in addition to the various known failure mechanisms and recent numerical modelling references. In chapter 3, the numerical setup used in the numerical models is presented and verified with the experimental specimens. This chapter includes the chosen experimental specimens, the numerical setup, and the reference numerical models and their results, which are discussed and verified with the experimental result at the end of the chapter. In chapter 4, sensitivity study of interface parameters is presented, both for unreinforced and reinforced interface model. The effect of each parameter to the capacity of the structures is discussed in this chapter. The results of various numerical models which are used to answer the remaining supporting research questions are presented and discussed in chapter 5. It is divided into three parts for three numerical studies. The first part is the study of lap splices spacing in unreinforced interface models, the second part is the study of connecting reinforcements spacing in reinforced interface models, and the third part is the study of lateral restraint influence. In the last chapter, conclusions of the research are presented. The recommendations for the future research are also included.

| 2 | LITERATURE REVIEW

In this chapter, several literatures related to this research are summarized into five parts. In the first four parts, four main topics are described in general which include the concrete-to-concrete interface, reinforcement bond transfer, lap splice, and membrane action. In the fifth part, the composite plank floor system is described including its relation to the four main topics. Moreover, failure mechanisms of the floor and several things related to numerical modelling of these types of structures are also described. The relevant experimental and numerical research, codes, and guidelines related to each topic and the problem descriptions are referenced and described in this part to provide the knowledge base for the numerical study. In the last part, the conclusion of the literature review is presented.

2.1. Concrete-to-concrete interface

Casting concrete sections at different times is a common construction technique. Its purpose can vary from continuing different casting phases, optimizing different concrete type, to creating composite section which consist of precast and cast-in-situ sections. When load transfer at the interface is expected, it should be designed carefully. The load transfer mechanism depends on the load type and direction. Compressive and tensile forces perpendicular to the interface are transferred through the concrete interface while the latter is also transferred through stirrup crossing the interface [13]. In case those members slip relative to one another, shear must be transferred across the interface through several mechanisms [14] as described in this chapter.

Several research and design codes describe the mechanism of shear transfer at the interface. Each mechanism is expressed by several influencing factors which will determine the resistance. Below, interface shear resistance expressions from *fib* Model Code for concrete structures 2010 [13] and Eurocode NEN-EN 1992-1-1+C2:2011 [9] are presented. A recent research by Croes [15] is also described in regard to the interface behaviour of unreinforced interface.

2.1.1. *fib* model code for concrete structures 2010

In *fib* model code [13], chapter 7.3.3.6 describes the shear at the interface between concrete cast at different times. There are 2 formulas for the design shear resistance at the interface. Equation (2.1) is for the case of interface without reinforcement while equation (2.2) is for the case of interface intersected by dowels or reinforcement.

$$\tau_{Rdi} = c_d f_{ctd} + \mu \sigma_n \leq 0.5 \nu f_{cd} \quad (2.1)$$

$$\tau_{Rd} = c_r f_{ck}^{1/3} + \mu \sigma_n + \kappa_1 \rho f_{yd} (\mu \sin \alpha + \cos \alpha) + \kappa_2 \rho \sqrt{f_{yd} f_{cd}} \leq \beta_c \nu f_{cd} \quad (2.2)$$

τ_R shear resistance

f_c	concrete compressive strength
c_a	coefficient for adhesive bond
c_r	coefficient for aggregate interlock effects at rough interfaces
μ	coefficient of friction
κ_1	coefficient of interaction of efficiency for tensile force in reinforcement
κ_2	coefficient of interaction for flexural resistance
β_c	coefficient for strength of compression strut
σ_n	minimum external compressive stress perpendicular to interface
ρ	ratio of reinforcement crossing the interface
ν	reduction factor for strength of diagonal concrete strut
α	angle of reinforcement crossing the interface

Table 2.1 – Coefficients for different surface roughness according to fib Model Code [13]

Surface roughness	c_a	c_r	κ_1	κ_2	β_c	$\mu (f_{ck} \geq 35)$
Very smooth	0.025	0	0	1.5	0.3	0.5
Smooth	0.2	0	0.5	1.1	0.4	0.6
Rough	0.4	0.1	0.5	0.9	0.5	0.7
Very rough	0.5	0.2	0.5	0.9	0.5	1.0

As explained by Randl [16], in case of interface without reinforcement, it is classified as rigid bond-slip behaviour since it has brittle failure at low slip <0.05 mm. The shear force is transferred through adhesion (first right hand term) and friction (second right hand term) mechanisms. In case of interface intersected by reinforcement, it is classified as non-rigid bond-slip behaviour due to its ductile failure at slip 0.5 to 1.5 mm. The shear force is transferred through aggregate interlock, friction (normal stress and reinforcement), and dowel action mechanisms.

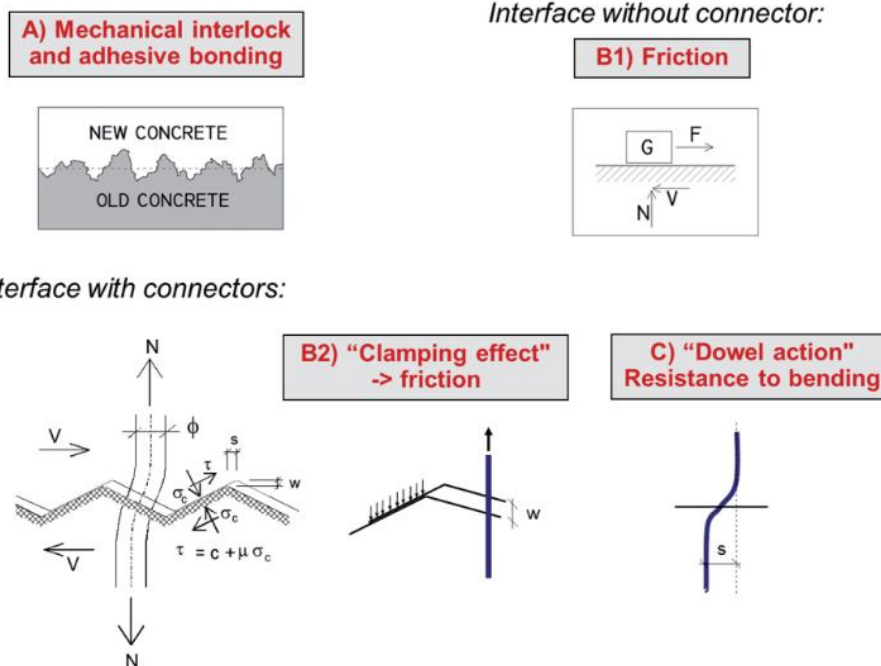


Figure 2.1 –Shear mechanisms of concrete-to-concrete interface [16]

From the table above, surface roughness plays its role in every shear transfer mechanism. With a rougher interface, higher adhesive bond, aggregate interlock, friction, and even dowel action can be expected, thus higher interface shear resistance can also be expected.

2.1.2. Eurocode NEN-EN 1992-1-1+C2:2011

In Eurocode [9], chapter 6.2.5 describes the shear at the interface between concrete cast at different times. Formula of the design shear resistance at the interface is presented below.

$$v_{Rdi} = cf_{ctd} + \mu\sigma_n + \rho f_{yd} (\mu \sin \alpha + \cos \alpha) \leq 0.5v f_{cd} \quad (2.3)$$

- c coefficient of cohesion
- μ coefficient of friction
- σ_n minimum external stress perpendicular to interface
- ρ ratio of any reinforcement crossing the interface to interface area
- α angle of reinforcement crossing the interface

Table 2.2 – Coefficients for different surface roughness according to Eurocode [8]

Surface roughness	c	μ
Very smooth	0.25	0.5
Smooth	0.35	0.6
Rough	0.45	0.7
Intended	0.5	0.9

According to the equation above, the shear force is transferred through cohesion and friction mechanisms. Its friction mechanism is consisting of friction due to external normal stress and reinforcement crossing the interface. It does not take into account the dowel action as compared to the fib Model Code. When the reinforcement crossing the interface is zero, the equation becomes similar to equation (2.1).

From the table above, the value of friction coefficient in Eurocode is similar to the ones in fib Model Code, while the coefficient of cohesion in Eurocode and coefficient of adhesive bond in fib Model Code is more similar in rougher surface.

2.1.3. Research by Croes

In 2019, Croes [15] conducted an experimental research to re-evaluate material influence on adhesion shear transfer in unreinforced interface. There were 48 specimens tested by direct shear test with variations in concrete types (regular and self-compacting concrete) and interface roughness.

It was found that in the absence of normal load, the shear strength was ranged from 0.57 to 1.87 MPa while the slope coefficient of the linear part in Mohr-Coulomb interface failure envelop was ranged from 0.50 to 2.94. From that result, it was concluded that there is no relation found between interface roughness and interface shear strength. There is also no relation found between the concrete strength and interface shear strength as assumed in Eurocode and fib Model Code. However, it was found that the use of different concrete type with different modulus of elasticity resulted in lower interface tensile strength. At the end of the study, the formulas of shear strength from codes were compared to the characteristic value from the experiment. From the comparison, the results from the codes are more conservative in compared to the experiment, thus concluded as sufficiently safe to be used.

2.2. Reinforcement bond transfer

In reinforced concrete structures, reinforcement, and concrete work together to bear the load. Concrete is good in resisting compression while steel reinforcement is good in resisting tension. However, since external loads act on the surface of the concrete and reinforcements are located inside, tensile stress should be transferred through bond transfer mechanism from the concrete matrix to the reinforcements. The bond transfer is developed through adhesion, friction, and bearing mechanisms. However, the first two mechanisms will disappear when the reinforcement elongates and its diameter decreases in tension due to its Poisson's ratio. Moreover, bearing mechanism is only present when a ribbed bar is used for reinforcement. [14]

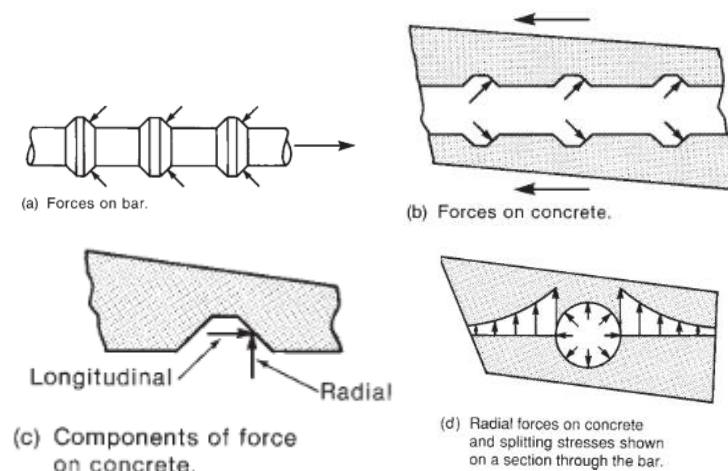


Figure 2.2 – Bond transfer [14]

There are two components of the bearing force, longitudinal and radial. As a reaction of the radial bearing force, the concrete is compressed radially in outward direction thus creating circumferential tensile stress around the reinforcement. The stress could lead to debonding (splitting) of the reinforcement from the concrete section and then followed by propagation of the crack to the surface or pull-out of the reinforcement, which depends on the distance between reinforcements and the surfaces [14]. The maximum bond transfer is influenced by several parameters in the code. These are explained in the following subchapter.

2.2.1. Ultimate bond stress

NEN-EN 1992-1-1 8.4.2 [9] describes the ultimate bond stress in relation to the anchorage of longitudinal reinforcement. The formula of the ultimate bond stress for ribbed bars is presented below.

$$f_{bd} = 2.25\eta_1\eta_2f_{ctd} \quad (2.4)$$

f_b	ultimate bond stress of ribbed bars
f_{ct}	concrete axial tensile strength
η_1	coefficient related to quality of bond condition and position of bar during casting
η_2	coefficient related to bar diameter

From the formula of Eurocode, for reinforcement with diameter larger than 32 mm, the bigger the diameter, the smaller the η_2 thus the smaller the ultimate bond stress. The ultimate stress then can be used for the calculation of anchorage and lap length.

2.2.2. Anchorage length

NEN-EN 1992-1-1 8.4.3 and 8.4.4 [9] describe the basic and design anchorage length of reinforcement. The anchorage length is needed to be satisfied in order to reach the design stress at a particular location of reinforcement.

$$l_{b,rqd} = \frac{\phi \sigma_{sd}}{4 f_{bd}} \quad (2.5)$$

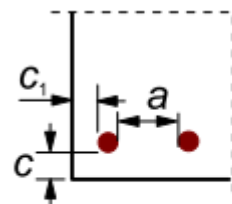
$$l_{bd} = \alpha_1 \alpha_2 \alpha_3 \alpha_4 \alpha_5 l_{b,rqd} \geq l_{b,min} \quad (2.6)$$

l_b	anchorage length
$l_{b,rqd}$	basic required anchorage length in straight bar assuming constant bond stress
ϕ	diameter of reinforcement
σ_{sd}	design stress of reinforcement
α_1	coefficient due to effect of reinforcement form
α_2	coefficient due to effect of concrete minimum cover
α_3	coefficient due to effect of confinement by transverse reinforcement
α_4	coefficient due to influence of welded transverse reinforcement
α_5	coefficient due to effect of pressure transverse to splitting plane

The diameter of reinforcement is also affecting the anchorage length needed (in addition to reduced ultimate bond stress). There are multiple parameters which affect the anchorage length which can be found in detail in the Eurocode.

2.2.3. Bar spacing

In the chapter 2.2.2, one of the parameters of anchorage length is concrete minimum cover. The minimum of spacing between reinforcements (a) and spacing between reinforcement and surface in each direction (c or c_1) then will be used to calculate the parameter, which affects the design value of anchorage and lap length. The less the minimum concrete cover, the more anchorage length is needed. It means, more length is needed to transfer the same design stress to the reinforcement.



a) Straight bars

$$c_d = \min(a/2, c_1, c)$$

Figure 2.3 – Concrete minimum cover [9]

As mentioned before, the crack propagation after the debonding process starts is determined by the distance between reinforcement and the surfaces. It means that the shortest cover will determine the crack propagation direction. [14]

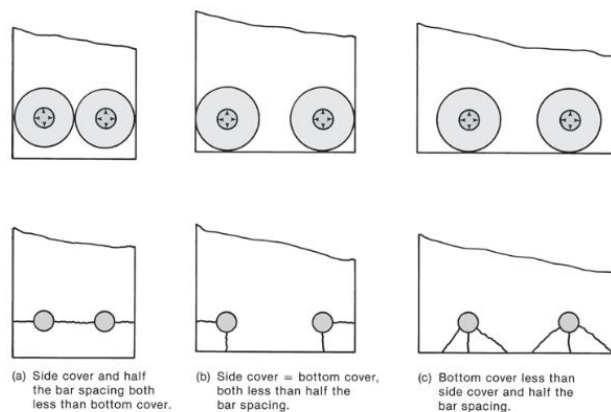


Figure 2.4 – Types of crack propagation after debonding process starts [14]

The required spacing of c and a are described in Eurocode [9] in chapter 4.4.1.2 and 9.3.1.1 respectively.

2.2.4. Bond-slip

As the bond mechanism transfer the force from the concrete section to the reinforcement, multiple cracks will appear around the reinforcement and eventually the bond will drop due to the crack propagation to the concrete surface or pull-out of the reinforcement. The development of this process can be described through a bond stress-slip relation. Slip between reinforcement and concrete is developing as the cracks grow.

There are several models to describe the bond stress-slip relation. One of the models is presented in the figure below. According to *fib* model code 2010 [13], the model includes the descending part after the plateau which simulates the drop of the bond stress. The detail of the bond-slip interface parameters and the equation of the bond stress-slip curves below are available in chapter 6.1.1.1.

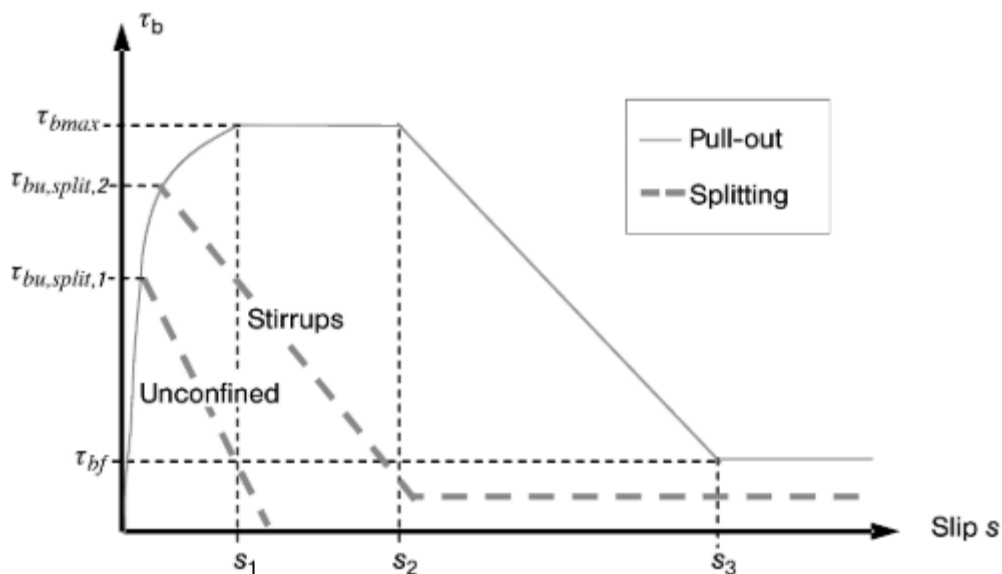


Figure 2.5 – *fib* Model code for concrete structures 2010 bond stress-slip relationship [13]

2.3. Lap splice

To ensure the continuity of tensile force in the reinforcement at points where there is a discontinuity of reinforcement, lap splices are often used. The discontinuity usually occurs due to the limited length of

the reinforcement, but in the particular case of composite plank floors, it occurs due to discontinuity of the precast concrete section. In this chapter, lap splice mechanism in the same concrete matrix is described while the one in which can be found in composite plank floor is discussed in chapter 2.5.2.

To transfer the force from one reinforcement to another in the same concrete matrix, the force is transferred from reinforcement to concrete through bond transfer mechanism which has been explained in chapter 2.2, using diagonal compressive struts and perpendicular tensile ties. The force is transferred again from concrete to the reinforcement through the same mechanism. [14]

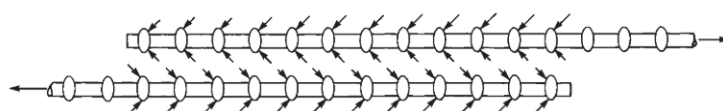


Figure 2.6 – Tensile lap splices load transfer [14]

In addition to splitting crack along reinforcement from the concrete section due to the bond transfer mechanism, large transverse cracks at the end of the splices may occur. Transverse reinforcements are usually used at the end of the lap splices since the splitting cracks are started there due to larger splitting stress. [14]

There are a lot of details for lap splices according to NEN-EN 1992-1-1 [9]. Laps are normally arranged to be staggered symmetrically and not placed in the high bending moment area in order to avoid the accumulation of splitting stress at the end of the lap splices. The requirements about distances between lap splices are described in chapter 8.7.2. If the requirements are complied, ratio of lapped splices in particular section are permitted to be 100% in 1 layer and 50% in several layers.

2.3.1. Lap length

NEN-EN 1992-1-1 8.7 [9] describes the laps and mechanical couplers. The formula of the design lap length is presented below.

$$l_0 = \alpha_1 \alpha_2 \alpha_3 \alpha_5 \alpha_6 l_{b,rqd} \geq l_{0,\min} \quad (2.7)$$

l_0 lap length

α_6 coefficient due to effect of percentage of lapped bars relative to total cross-section area

The formula above is similar to anchorage length formula. The only difference is the presence of influence of lapped bars ratio instead of transverse pressure in the anchorage length formula (2.6). It shows that the higher the ratio of the lapped bars, the longer the lap length needed.

2.3.2. Transverse reinforcement

NEN-EN 1992-1-1 8.7.4.1 [9] describes the details of transverse reinforcement for tensile lap splices. For the lap splices with diameter less than 20 mm, or less than a quarter of lap splices in one lapped section, no additional transverse reinforcement is needed. All reinforcements in the transverse direction which cross the lap splices can be assumed to be sufficient enough to resist the transverse tensile force at the end of the lap splices. If those conditions are not satisfied, transverse reinforcement is needed and should follow the details in NEN-EN 1992-1-1 8.7.4.1 (3).

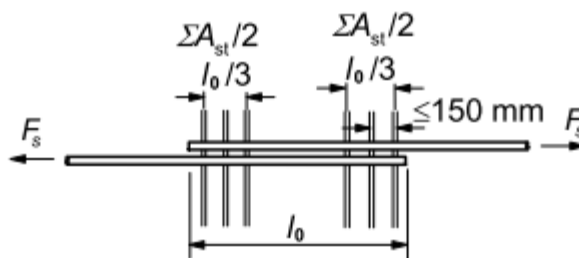


Figure 2.7 – Transverse reinforcement [9]

2.4. Membrane action

In [2], lightly reinforced two-way slabs with edges bounded to beams as part of a beam-slab floor system were tested twice. First, uniformly distributed load was applied on top of the single panel while the second, it was applied on the adjacent panels. As a result, both tests had higher ultimate load, more than twice the ultimate load compared to the calculation based on yield-line theory.

The increase of flexural strength occurred due to a load transfer mechanism which is called as membrane action [17]. A slab can develop this mechanism when all of the edges are restrained in its lateral direction. This situation is common especially in building constructions since a panel of slab is connected to the adjacent panels as part of the whole floor system. The connections between the panels give a certain degree of restraint in the lateral direction. However, this membrane action will not be activated until the slab starts to deform and crack. There are 2 stages of membrane action, the compressive and tensile ones. Both of them are described below.

2.4.1. Compressive membrane action

The first membrane action which will occur is the compressive membrane action (CMA). When a slab which is clamped at all of its edges starts to deform in its elastic region, at its bottom part, there is a tensile strain in the middle and compressive strain at the boundaries. The total of these strains does not result in an increase of length. However, when the flexural crack appears, this crack increases the length of the bottom part of the slab. As a result of this expansion, the bottom part at the boundaries is compressed. In this situation, the slab has another load transfer mechanism through the arch of compression along the slab [17]. This is why in several publications [18], CMA is also known as arching.

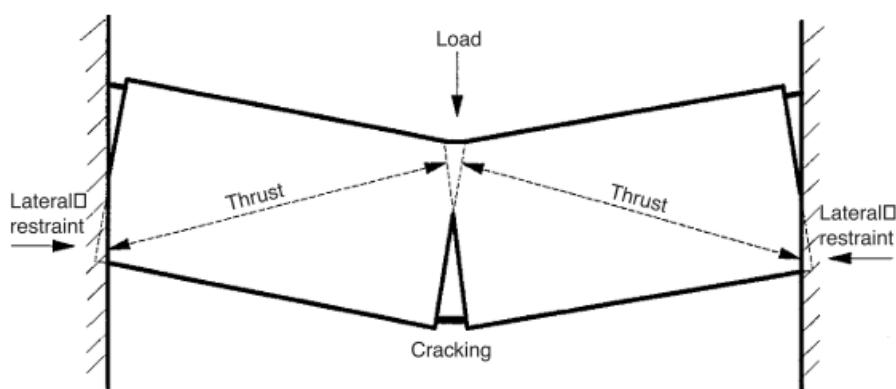


Figure 2.8 – Compressive membrane action in slab [18]

In addition to the flexural strength, the CMA increases the strength of the slab until reaching point B in Figure 2.9. The following increase of deformation is part of the development of plastic hinge mechanism. Due to the plastic rotation, the slab curvature is increased and the slab is moving inward towards the centre line of the load. As a result, there will be less area in compression at the bottom part of the

boundary. The reduction of the compressive area leads to reduction of the CMA. When the deformation continues to increase and all the compressive area at the boundary become tensile, the CMA is no longer working and point C is reached [17].

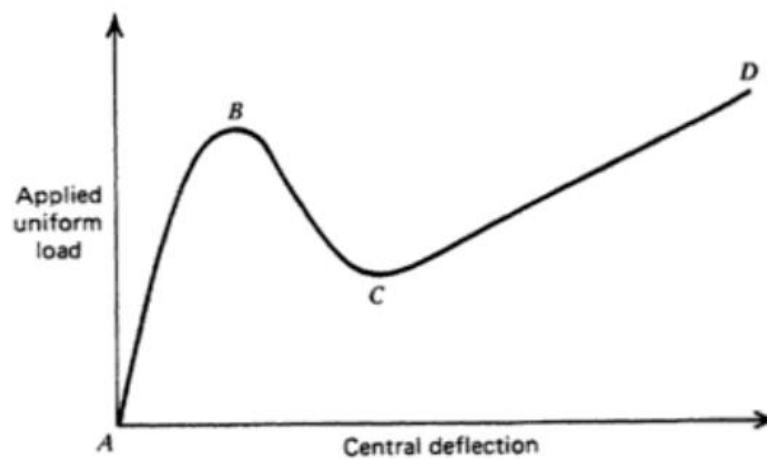


Figure 2.9 – Load-displacement graph for clamp slab [17]

In the interaction diagram in Figure 2.10, CMA always occurs below the horizontal dashed line since the magnitude of the compressive force is not large enough to prevent the yielding of tensile reinforcement in the slab. In this situation, the additional compressive force from CMA always increases the ultimate moment resistance. From the same figure, it can be seen that section with less reinforcement has a smaller curve. As a result, with the same increase of compression, the increase of strength is larger in lightly reinforced slab.

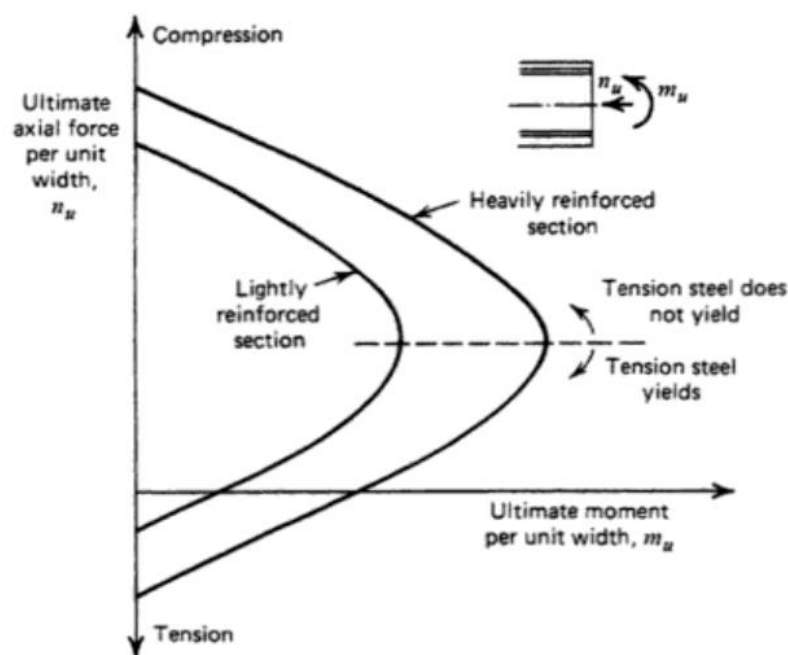


Figure 2.10 – Interaction diagram [17]

There are several other things which influence the CMA. From Figure 2.11, the slab with lower slenderness ratio has higher increase of strength for the same boundary stiffness. Therefore, for thicker slab, the lateral restraint at the boundary can be less stiff to achieve the same CMA influence. The figure also shows that the lower the boundary stiffness, the smaller the increment of the stiffness needed to get higher strength increase. The stiffness need not to be infinitely stiff since the increase of strength is lower for higher stiffness.

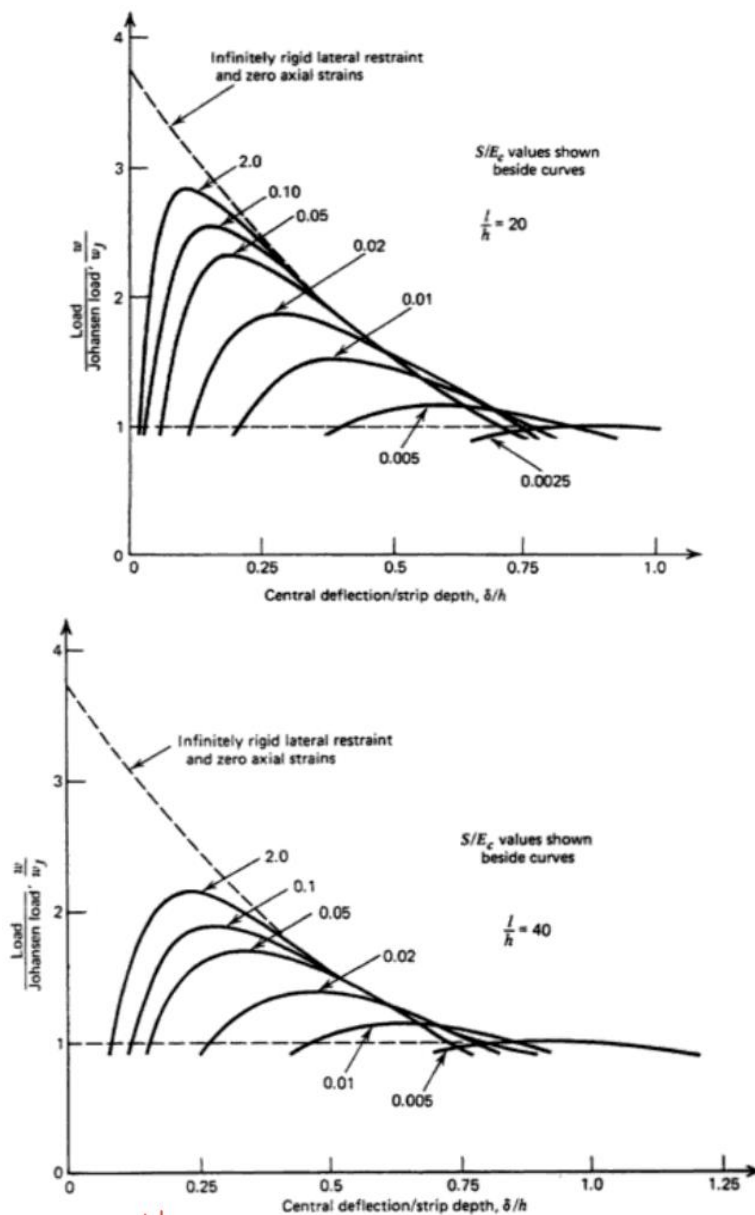


Figure 2.11 – Boundary stiffness effect in load-displacement graph [17]

2.4.2. Tensile membrane action

After reaching point C in Figure 2.9, if the slab keeps deforming, the catenary action of the reinforcement is developed and the tensile membrane action (TMA) is induced [17]. Since TMA development depends on the catenary action of reinforcement, higher reinforcement ratio can increase the strength further, even greater than the enhancement due to CMA. In this case, point D will be the ultimate resistance of the slab. To ensure this mechanism, the reinforcements should have sufficient anchorage. TMA can also be developed in a thin plate at large deformation unlike CMA.

2.5. Composite plank floor

Composite plank floor generally consists of prefabricated reinforced or prestressed concrete sections as bottom layer and cast-in-situ reinforced concrete as the top layer. Due to the limited dimension of prefabricated section, the bottom layer is arranged as an array of multiple sections in various layouts, from the more traditional row of sections to the more complex system of flat slab.

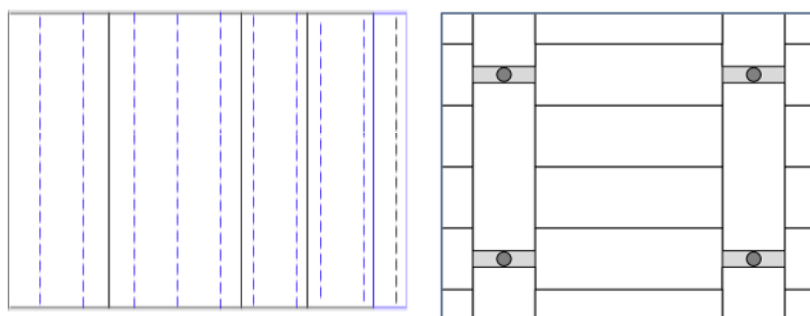


Figure 2.12 – Layouts of composite plank floor (a) row, (b) flat slab (modified from [19])

In layout such as in Figure 2.13 (b), according to linear elastic approach, the load will be distributed in both longitudinal and transverse directions for the middle part of the slab [19] as shown in Figure 2.13. When the load is distributed in transverse direction of the precast section, the positive bending moment will cross the longitudinal (long-side) joints of the sections which is proven to be critical in the case of the collapse of Eindhoven airport parking garage [4]. However, the load distribution in longitudinal direction can also be critical in the situation where high bending moment and high shear force at the end of the precast section need to be transferred through the transverse (short-end) joint of the section to the long-side joint of other section. This case will not be discussed in this research, only the critical joint in transverse direction (long-side) will be discussed.

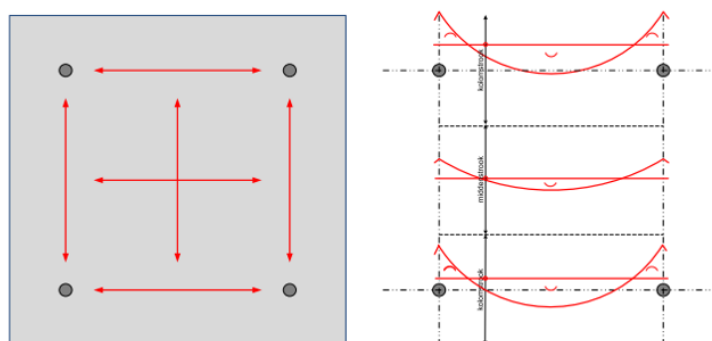


Figure 2.13 – Load distribution in flat slab [19]

The presence of a gap at the joint between the precast sections creates a discontinuity in the tensile reinforcements of the bottom layer. Therefore, to transfer the tensile force in the positive bending moment region between sections, non-contact tensile lap splices are introduced with the presence of coupling reinforcement (*koppelwapening* in Figure 2.14) at the bottom of cast-in-situ layer across the joint.

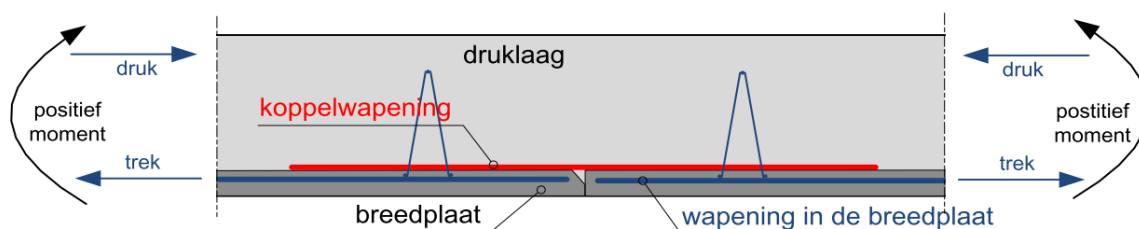


Figure 2.14 – Plank floor critical detail [19]

As described in the chapter 2.3, the tensile lap splices work through the diagonal compressive struts and perpendicular tensile ties in the concrete in between the lapped reinforcements. However, since there is a concrete-to-concrete interface which separate the concrete layers, those struts and ties need

to be transferred through the interface as interface shear and normal stresses around the joint. Moreover, the presence of interface creates a distance between the lap splices, thus introducing additional bending moment as a result of the eccentricity which also increases the stresses at the interface. It is the lack of interface strength to accommodate those load transfer mechanisms which was concluded in the case of partial collapse of Eindhoven airport parking garage [3].

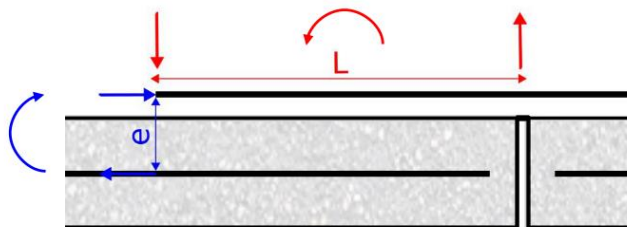


Figure 2.15 – Bending moment due to lap splices eccentricity [1]

Currently, composite plank floor is specifically addressed in NEN-EN 13747+A2:2010 [11]. In there, some details for the design purpose are described in conjunction with NEN-EN 1992-1-1:2004, the late version of Eurocode 2. However, the content is suitable for more traditional design of unidirectional composite plank floor, compared to the recent development of 2-way load distribution. The situation of critical joint in Figure 2.14 is only discussed in Annex F.5 specifically for the transverse lap splices, but other details regarding the situation such as the interface strength and other details are not discussed. In recent years, especially after the partial collapse of Eindhoven airport parking garage, a lot of new research have been done in order to study more about the details around the joint. Some topics related to the components around the joint, failure, and analysis are described below.

2.5.1. Interface of composite plank floor

In the situation which is shown in Figure 2.14, due to the presence of the joint, the tensile stress from the precast layer should be redirected to the cast-in-situ layer by the lap splices. Therefore, the interface of the plank floor around the critical joint does not only carry the interface shear stress, but also tensile and compression due to the eccentricity of the lap splices.

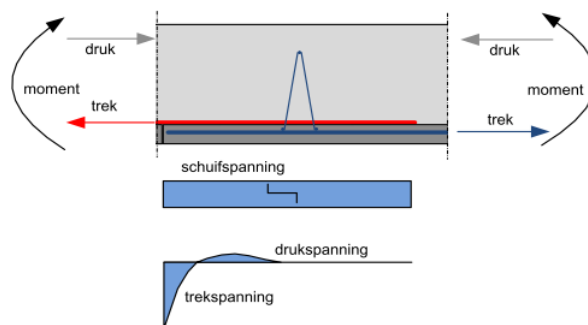


Figure 2.16 – Interface shear and normal stress [19]

With various load transfer mechanisms around the critical joint, the resistance of the joint should be ensured, especially if the yielding of coupling reinforcement is to be expected. According to “Step-by-step plan for existing building assessment 2019” [8], the resistance could be assessed by 3 failure criteria: yielding of coupling reinforcement, pull-out of the lattice girder, and shear failure of the interface. The last criterion which is related to the interface resistance is formulated with the equation derived from the proposed revision of Eurocode 2 which is discussed in [19].

$$\tau_{Rdi} = c_{v1} \frac{\sqrt{f_{ck}}}{\gamma_c} + \rho f_{yd} \mu_v \leq v f_{cd} \quad (2.8)$$

c_{v1} coefficient of cohesion
 μ_v coefficient of friction

Table 2.3 – Coefficients for different surface roughness [19]

Surface roughness	c_{v1}	μ_v
Very smooth	0.0095	0.5
Smooth	0.075	0.6
Rough	0.15	0.7
Very rough	0.19	0.9

According to Report 9780-1-0 by Adviesbureau Hageman [19], the equation was chosen instead of the formula from current NEN-EN 1992-1-1+C2:2011 because of the clear differentiation between the shear interface resistance formula for brittle and ductile behaviour which is similar to fib model code 2010. While in the present Eurocode 2, there is only 1 formula for both behaviours. The equation above is derived from the formula for interface with sufficient anchorage of stirrup crossing the interface and only applicable with zero external stress perpendicular to the interface and if there is symmetrical stirrups at least 100 mm from the joint with at least 15 mm anchorage depth to the precast layer from the interface.

Similar to the formula of the present Eurocode 2 and *fib* Model Code 2010, surface roughness also influences the interface strength according to the equation above. A series of experiments conducted on behalf of Betonhuis [7] varied the interface roughness in specimen R1, R2, and R3. As a result, these specimens have higher capacity compared to the controls specimen T4, T5, and T6 which were not roughened. The roughened specimens even reach yielding of coupling reinforcement in the experiment.

2.5.2. Non-contact lap splice

Since the lap splices in the composite plank floor are located in two separate layers divided by the interface, there are some details which are not present in contact lap splices or should be adjusted due to its distance in between.

Distance between coupling reinforcement and the top of precast section should be designed according to NEN-EN 1992-1-1 4.4.1 [9]. The concrete cover can be reduced into minimum one with regard to bond ($c_{min,b}$) when the requirements of 4.4.1.2 (9) are satisfied. In most situations, the requirements of concrete strength class and exposure time are satisfied, however the requirement to roughen the surface is often not satisfied in practice. Even more, in practice, the coupling reinforcement are often placed directly on top of the precast layer [19].

According to NEN-EN 13747 Annex F.5 [11], in the situation where transverse moment should be considered, the transverse lap should be designed according to EN 1992-1-1 8.7 [9], the same requirement for lap splice in the same concrete matrix. In 8.7.2 (2), lap splices should normally be staggered and not located in high bending moments while in 8.7.2 (4), lap splices in several layers should be maximum 50% (instead of 100% for lap splices in the same layer) in one lapped section. In the case which is shown in Figure 2.14, both requirements are not possible to be satisfied since the position of the longitudinal joint requires 100% non-contact lap splices in one lapped section. For the design purpose of new structures, TGB Betonconstructies released the background rules for the new guideline in [12] and [20] prior to the expected new guideline. In there, a solution based on BAM-Cobiax research specimens [6] is presented. The solution is including the additional bent tensile reinforcement from the

precast layer which cross the interface into the cast-in-situ layer in order to take into account the eccentricity in between the lap splices and to increase the interface shear strength. From the research, although 8.7.2 (4) is not satisfied, the specimen is analytically and experimentally proven to achieve the ultimate load with yielding of coupling reinforcement as the desired failure mechanism. It will be described further in chapter 2.5.3.

The other detail about the lap splices is the transverse (width direction) distance between the lap splices. Since the coupling reinforcements above the joint work as flexural reinforcement, NEN-EN 1992-1-1 9.3.1.1 (3) should be satisfied. The maximum transverse distance is $2h \leq 250$ mm. In some case, especially when weight-saving elements are used, this requirement cannot be satisfied. Until now, there is no particular laboratory research which study the effect of the transverse spacing of lap splices to the critical joint in Figure 2.14. In this case, *Werkgroep onderhoud EC2* of TGB Betonconstructies gave an answer in VARCE 13 [20] prior to the expected new guideline for design purpose of new structures with this type of joint. In case the limitation of 9.3.1.1 (3) is exceeded, additional connecting reinforcement, transverse reinforcement, and extension of coupling reinforcement should be provided in order to achieve the desired resistance.

2.5.3. Connecting reinforcement

According to NEN-EN 13747+A2:2010 3.5.1 [11], connecting reinforcements are reinforcements which cross the interface and are anchored in both precast and cast-in-situ layers. There are various types of connecting reinforcements, such as lattice girder, individual or continuous loops, and prestressing wires and strands. In the Netherlands, lattice girder is common to be used in composite plank floor systems. In NEN-EN13747 4.2.4.2, details about lattice girder such as distance in between, distance to the nearest edge or joint, minimum embedment in precast layer, and longitudinal position of lattice girder are described.



Figure 2.17 – Connecting reinforcement types [11]

In the situation which is shown in Figure 2.14, the presence of connecting reinforcement is related to the presence of the joint between precast section which requires the tensile force to be transferred from precast layer to the cast-in-situ layer. Since concrete has low resistance to tensile, lap splices are introduced to take the tensile force. However, the eccentricity of lap splice creates moment which induces the interface tensile stress near joint. This tensile stress is the reason why the connecting reinforcement is important to be there.

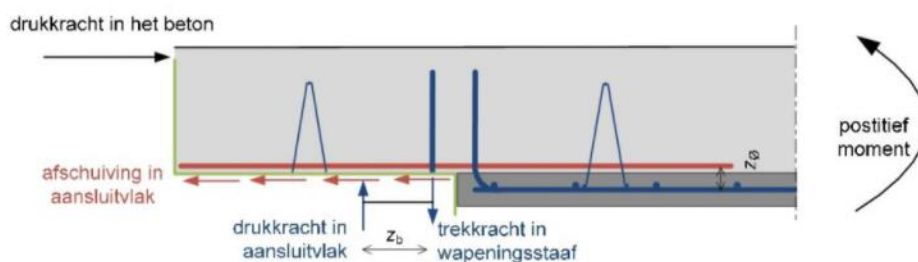


Figure 2.18 – Tensile force due to eccentricity taken by the connecting reinforcement [12]

Due to the importance of connecting reinforcement, the case of Eindhoven parking garage raised a question whether lattice girder is suitable as connecting reinforcement. It is also related to the fact that lattice girder only lies on top of the tensile reinforcement in precast section.

In an experiment conducted on behalf of Betonhuis [7], specimen T22, T23, and T24 have lattice girders 100 mm from the critical joint, closer than the control specimen T04, T05, and T06 which have lattice girders 400 mm from the joint. According to the report, the specimens with lattice girders closer to the joint have an increased ultimate load though still have the same failure mechanism of delamination and pull-out of lattice girders.

In relation to the aforementioned and many other research, as described in chapter 2.5.1, "Step-by-step plan for existing building assessment 2019" [8] includes the pull-out of lattice girder as one of the failure criteria to determine the resistance of the structure. The maximum tensile force in the coupling reinforcement based on this failure mechanism is presented below.

$$F_{R,kop,b,d} = 2f_{ctd,breedplaat}diepte^{1.5}k_2k_3 \quad (2.9)$$

$$k_2 = \frac{l_{eff}}{600} \leq 1.0 \quad (2.10)$$

$$k_3 = \frac{56 - \phi_{koppel}}{40} \begin{cases} \leq 0.9 \\ \geq 1.1 \end{cases} \quad (2.11)$$

$F_{R,kop,b,d}$	maximum tensile force in coupling reinforcement
$f_{ctd,breedplaat}$	design value of concrete tensile strength
$diepte$	depth of the bottom of lattice girder in the precast layer
l_{eff}	length from centre line of the first lattice girder from joint to the end of coupling reinforcement
ϕ_{koppel}	coupling reinforcement diameter

For new structures, since the new guideline has not been released yet, *Werkgroep onderhoud EC2* of TGB Betonconstructies gave an answer in VARCE 13 [20] as part of the questions and answers related to the composite plank floor details. An experiment is conducted on behalf of the BAM-Cobix [6] and became one of the solutions which is presented in the background rules for the new guideline [12] by TGB Betonconstructies prior to the expected new guideline. In one of the specimens, 50% of the tensile reinforcements in the precast layer are bent and anchored to the cast-in-situ layer. As a result, the specimen can reach the yielding of the coupling reinforcement. The bent reinforcements are not only contributing to withstand the vertical tensile force due to the eccentricity of the lap splices, but also for the interface shear strength. Nevertheless, more research is still needed prior to the release of the new guideline.

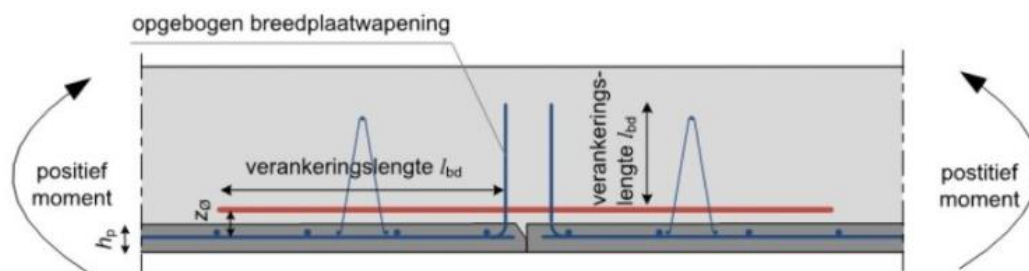


Figure 2.19 – Critical detail with bent reinforcement [20]

The other detail is the distance between the connecting reinforcement along the length of the joint. As a result of the previous mentioned research of BAM-Cobiax [6], TGB Betonconstructies in the background rules for the new guideline [12] limits the distance between the bent bars to at least $2c_{min,b}$ and less than 200 mm. These values are taken only from this research and could be changed after more research are conducted.

At the time of writing this thesis, there is an ongoing research conducted at TU Eindhoven by S.N. Wijte which studies the influence of the non-uniform distributed shear strength. In this research, the end joint (short-side) between precast sections is tested. To check the influence of the shear strength distribution, total area of diagonal bar of lattice girders are varied while the distance between the lattice girders is kept the same.

2.5.4. Failure mechanisms

There are several failure mechanisms that could be expected from the composite plank floor, particularly in the situation of Figure 2.14. The most desirable failure mechanism is the yielding of the coupling reinforcement or tensile reinforcement since its ductile behaviour can give enough warning before the exceedance of the structures' ultimate capacity.

According to [21], there are 6 failure mechanisms which should be considered.

1. Yielding of the coupling reinforcement
2. Yielding of tensile reinforcement in precast section
3. Pull-out of coupling reinforcement
 - a. Due to splitting
 - b. Due to splitting in combination with V-notch failure
 - c. Due to splitting in combination with bending failure
4. Pull-out of tensile reinforcement in precast section
5. Delamination of the interface
6. Pull-out of coupling reinforcement in combination with partial delamination of the interface

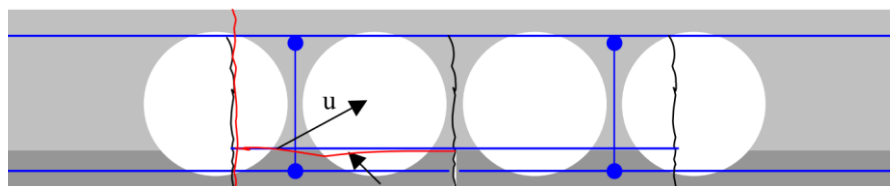


Figure 2.20 – Failure mechanism 5 [21]

From several experimental researches such as [6], [7], [21], [22], [23], and [24], failure mechanism 1 and 5 are the most common failure mechanisms which occurred. The delamination of the interface is usually followed by the pull-out of lattice girder from the precast layer.

2.5.5. Numerical models

Beside the experimental research, there are several numerical research which have been done. In [24], Weglarzy did both experimental and numerical research in solid composite plank floor (without weight-saving elements). Abaqus was used to numerically model the experimental specimen which are used as verification. To model the concrete-to-concrete interface, a friction model was not used thus the interface was assumed as rigid. However, a pre-damage model was used by disconnecting the first row of elements adjacent to the joint to model the behaviour of the structure without using a friction model.

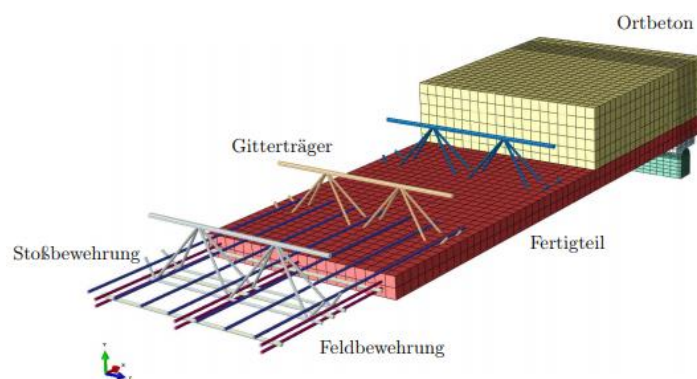


Figure 2.21 – Numerical model of specimen B1 by Weglarzy [24]

In 2003, Lundgren [22] did a numerical study for solid composite plank floor (without weight-saving element) to investigate the bending capacity at the critical detail. DIANA 8.1 was used as the finite element software. Symmetry at the precast joint was defined to reduce the model size and the load was applied as bending moment away from the joint. Both concrete-to-concrete interface and reinforcement bond-slip model were used. Details of the concrete, reinforcement, and concrete-to-concrete interface properties of the normal case are available in Table 2.4 until Table 2.6. Several interface parameters, reinforcement properties, and bent reinforcement are used as variants of the normal case. From the research, the model without bent reinforcement could almost reach yielding. However, he highlighted the need of bent reinforcement to increase the ductility of the structure.

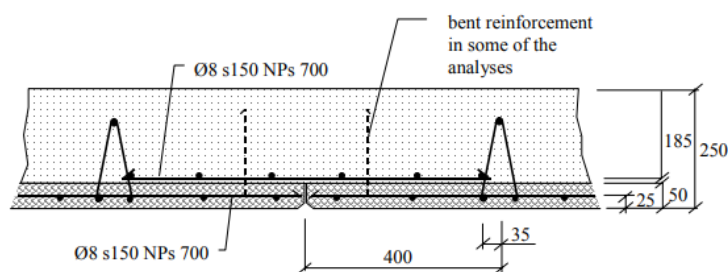


Figure 2.22 – Critical joint investigated by Lundgren [22]

In another research done in 2005 [25], Lundgren did both experimental and numerical research for solid composite plank floor without any connecting rebar. Shear test and wedge split test were done with roughened and single grooves surface specimens which resulted in high shear and adhesive strength. Full-scale tests were conducted experimentally and then modelled with DIANA using the test results. The model with roughened surface can reach yielding and only showed one flexural crack as shown in Figure 2.23. For the model without adhesion, delamination occurred and followed by flexural crack at the lattice girder position which reduced the load capacity as shown in Figure 2.24. It was concluded that composite plank floor without connecting rebar is sensitive to roughness of the interface surface.

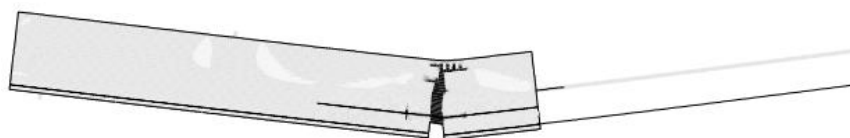


Figure 2.23 – Simulated crack pattern of Hedared model with roughened surface before failure [25]

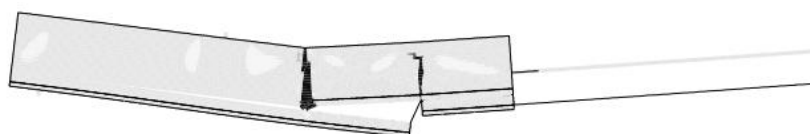


Figure 2.24 – Simulated crack pattern of Hedared model without adhesion before failure [25]

In their report in 2018, abt [26] did a numerical study to provide the calculation of a strengthening concept of composite plank floor based on the test specimen from Eindhoven airport parking garage (with weight-saving element). In order to do that, 3D base model (VL34a) and 5 other models are created using DIANA 10.2. The model was created in full span with 150 mm width. The concrete-to-concrete interface was modelled with Coulomb friction and the reinforcement bond-slip was also used. Details of the concrete, reinforcement, and concrete-to-concrete interface properties of model VL34a are available in Table 2.4 until Table 2.6. From the load-displacement graph, the model could give similar equilibrium path until 80 kN, but less good convergence until the failure. The maximum load is lower from the experimental result, but it has the same global behaviour.

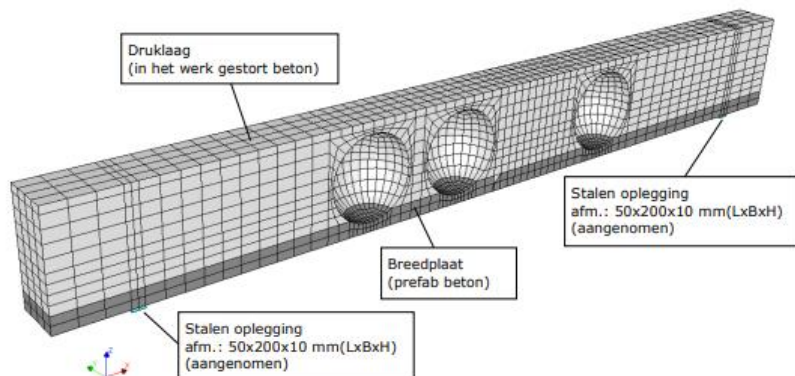


Figure 2.25 – Numerical model VL34a by abt [26]

Another numerical study which used DIANA was done by Harrass in 2020 [1]. He did both experimental and numerical research of composite plank floor without weight-saving element. In the research, different concrete layers were used, SHCC for the precast layer and regular concrete for the cast-in-situ layer. The research studied multiple parameters (concrete-to-concrete interface surface, curing method, coupling rebar cover, and additional connecting rebar) and their influence on the global behaviour. For the numerical study, 5 models were made and 4 of them were verified with the experimental results. The models included the Coulomb friction model for the concrete-to-concrete interface, but without the reinforcement bond-slip model. Details of the concrete, reinforcement, and concrete-to-concrete interface properties of Model 2 (smooth interface) are available in Table 2.4 until Table 2.6. The load-displacement graph shows similar load and displacement capacity, while the similar failure mechanism (delamination and flexural crack) can be seen from the crack pattern.

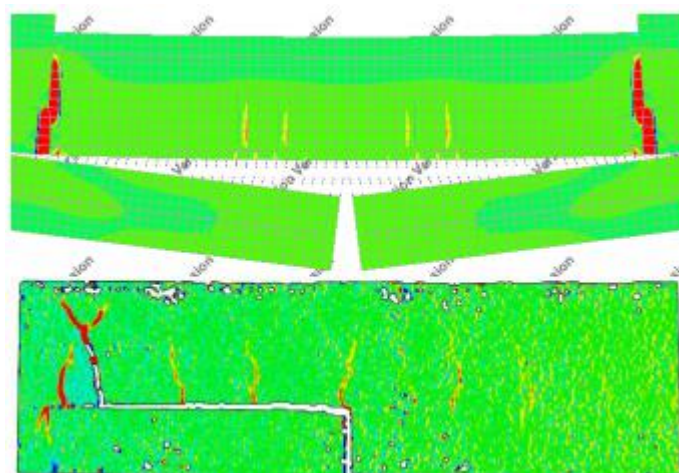


Figure 2.26 – Simulated crack pattern of model 2 (above) and experiment (below) after failure

In 2021, Bouwsema [27] did a numerical research in solid composite plank floor with connecting reinforcement. The reference for this research was based on Betonhuis experiment [7]. The study aimed

to understand the numerical modelling knowhow of composite plank floor with pull-out of lattice girder as its failure. DIANA 10.4 was used as the finite element software to model the specimen in both 2D and 3D. The 2D model T13 V10 could show the expected failure mechanism with similar load-displacement behaviour. The details of the concrete, reinforcement, and concrete-to-concrete interface properties of this model are available in Table 2.4 until Table 2.6. However, the 3D model T13 3D could not give similar load and displacement capacity since the model failed prematurely although with similar failure mechanism. In the conclusion, further research is still needed to accurately model the specimen with pull-out of lattice girder failure.

Three tables below show the comparison of concrete, reinforcement, and concrete-to-concrete interface properties of the normal case of Lundgren [22], model VL34a of abt [26], model 2 – smooth interface of Harrass [1], and model T13 V10 of Bouwsema [27]. It should be noted that for Harrass' model, the precast layer used SHCC which is not included in Table 2.4.

Table 2.4 – Concrete properties of several research with DIANA

Reference	Lundgren [22]	abt [26]	Harrass [1]	Bouwsema [27]
Element type	Linear regular plane stress	Quadratic structural solid	Quadratic regular plane stress	Quadratic regular plane stress
Material model	Total strain based crack model	Total strain based crack model	Total strain based crack model	Total strain based crack model
Young's modulus (GPa)	32.1 (cast-in-situ) 33.2 (precast)	31.5 (cast-in-situ) 37.5 (precast)	35.5 (cast-in-situ) (Precast: SHCC)	26.0 (cast-in-situ) 33.4 (precast)
Crack orientation	Rotating	Rotating	Rotating	Rotating
Tensile curve	Hordijk	Hordijk	Hordijk	Hordijk
Compressive curve	Thorenfeldt	Parabolic	Parabolic	Ideal
Compressive strength (MPa)	33 (cast-in-situ) 36.5 (precast)	31.6 (cast-in-situ) 53.0 (precast)	40.0 (cast-in-situ) (Precast: SHCC)	17.6 (cast-in-situ) 40.1 (precast)

In model VL34a of abt, only the lattice girder and coupling reinforcement which used reinforcement bond-slip model, while top, bottom, and transverse reinforcement used the embedded reinforcement. In model T13 V10 of Bouwsema, he also included additional anchorage force to prevent early pull-out of the lattice girder in the model.

Table 2.5 – Reinforcement properties of several research with DIANA

Reference	Lundgren [22]	abt [26]	Harrass [1]	Bouwsema [27]
Material model	Bond-slip reinforcement	Bond-slip reinforcement	Embedded reinforcement	Bond-slip reinforcement
Young's modulus (GPa)	200	200	210	200
Non-linear model	Von Mises plasticity	Von Mises plasticity	Von Mises plasticity	Von Mises plasticity
Hardening hypothesis	Strain hardening	Strain hardening	Strain hardening	Strain hardening
Hardening type	Isotropic hardening	Isotropic hardening	Isotropic hardening	Isotropic hardening
Yield strength (MPa)	700	550	550	550
Ultimate strength (MPa)	<i>Not available</i>	594	650	594
Bond-slip model	CEB 1993	Shima	<i>Not used</i>	CEB-FIB 2010

Table 2.6 – Concrete-to-concrete interface properties of several research with DIANA

Reference	Lundgren [22]	abt [26]	Harrass [1]	Bouwsema [27]
Material model	Coulomb friction	Coulomb friction	Coulomb friction	Non-linear elastic friction
Normal stiffness modulus	1000	60000	1200	10
Shear stiffness modulus	100	6000	1200	10
Cohesion (MPa)	0.58	0.5	1.0	0.2
Friction angle (rad)	0.73	0.54	0.85	0.38
Dilatancy angle (rad)	0.1	0	1.0	<i>Not applicable</i>
Tensile strength (MPa)	<i>Not available</i>	0.5	0.5	<i>Not applicable</i>

2.6. Summary

In summary, there are three main research components discussed in this chapter:

1. **Tensile lap splice** which is needed to transfer the tensile force from the precast layer to the cast-in-situ layer due joint between precast sections. This force is transferred through concrete-to-concrete interface as interface shear and normal stresses. In the codes, these stresses could be assumed evenly distributed due to the limit of the lap splice transverse distance. However, the presence of weight-saving element in practice usually enlarges this distance and the stress distribution across the interface become questionable. In this situation, *Werkgroep onderhoud EC2* [20] suggests the use of additional connecting reinforcement, transverse reinforcement, and extension of coupling reinforcement.
2. **Connecting reinforcement** (vertical stirrup crossing the interface) which is used to carry the perpendicular tensile stress due to the eccentricity between the lap splice components. Bent tensile reinforcement is currently suggested to be used in the composite plank floor by background article for the proposed new guideline. In the situation similar to lap splice transverse distance, TGB Betonconstructies [12] limits the distance between bent bars according to the conducted research.
3. **Compressive membrane action** is a load transfer mechanism which occurs after concrete cracking when a structure is laterally restrained. This type of boundary is common in building structures, including the continuous composite plank floor with multiple spans connected to each other. The boundary stiffness need not to be infinite since the increase of strength is higher in lower stiffness [17].

To do the numerical study, two main modelling components are discussed in this chapter:

1. **Concrete-to-concrete interface** between precast and cast-in-situ concrete layers is an important factor which considerably affect the failure mechanism of composite plank floor without connecting rebar according to several research [7] [25]. For the design purpose, some interface parameters are given in the codes. However, from several numerical research, various values were used for the interface parameters to fit the experimental results.
2. **Reinforcement bond-slip** occurs when cracks around the reinforcement reduce the bond between concrete and reinforcement. Several bond-slip models are used in several numerical research (though some research did not use it), especially to model the failure mechanism pull-out of lattice girder or connecting rebar. However, there is a difficulty to accurately simulate the pull-out failure using reinforcement bond-slip [26] [27].

| 3 | NUMERICAL MODEL SETUP

Finite element analysis is a numerical approach which is based on a discretization of a mechanical model. In order to build the finite element model, several assumptions have to be chosen. However, since the result depends on these assumptions, they need to be checked by verifying the result with other means, such as an experimental result. Therefore, in the beginning of this numerical research, the numerical setup is determined and the numerical results based on the setup are verified with experimental results.

To verify the numerical models in this research, the experimental result from Harrass [1] is used. This experiment is chosen since it has unreinforced interface (Sample 1) and reinforced interface (Sample 7) specimens. The availability of unreinforced interface specimen in particular is important since the influence of lap splice spacing (first supporting research question) can be specifically studied without any influence from the connecting reinforcement on the concrete-to-concrete interface. It also provides the possibility to understand the influence of each interface parameter through a sensitivity study without any influence coming from the connecting reinforcement.

The experimental results which will be used for the verification of the numerical models are shown in chapter 3.1. Afterwards, the numerical setup of the reference models which represent the experimental specimens are shown in chapter 3.2. Finally, the result of the numerical models is presented and verified with the experimental result in the last part of this chapter.

3.1. Experimental reference

This chapter describes the specimens which are used for the verification. The configuration of the specimens is described in chapter 3.1.1, while the load-displacement graph, maximum values of load, displacement at multiple location, reinforcement stress, and DIC (Digital Image Correlation) images at several load stages are presented in chapter 3.1.2 for Sample 1 and in chapter 3.1.3 for Sample 7.

3.1.1. Test specimens

Sample 1 and Sample 7 are simply supported composite beams with SHCC (Strain Hardening Cementitious Composite) for the precast (bottom) layer and regular concrete for the cast-in-situ (top) layer. The interface between both layers is untreated (smooth). To resemble the joint between precast layers of composite plank floor slabs, at the mid span a 4 mm gap is created in the precast layer. The average cube compressive strength of both SHCC and concrete are 50 MPa.

The total length of the specimen is 1900 mm while the total span is 1700 mm. The width is 150 mm and the total height is 200 mm (70 mm SHCC layer and 130 mm concrete layer). There are 3 bottom (tensile) rebars in the precast layer on both sides of the gap, 3 coupling rebars with 600 mm length at the mid span which has 10 mm cover from the top of precast layers, 2 top rebars along the specimen, and 3 2-legs stirrups to prevent shear failure between the load and the supports. All of the rebars are B500 and

8 mm in diameter. The only difference between Sample 1 and Sample 7 is that the latter has additional 6 mm diameter rectangular stirrup 50 mm from the joint.

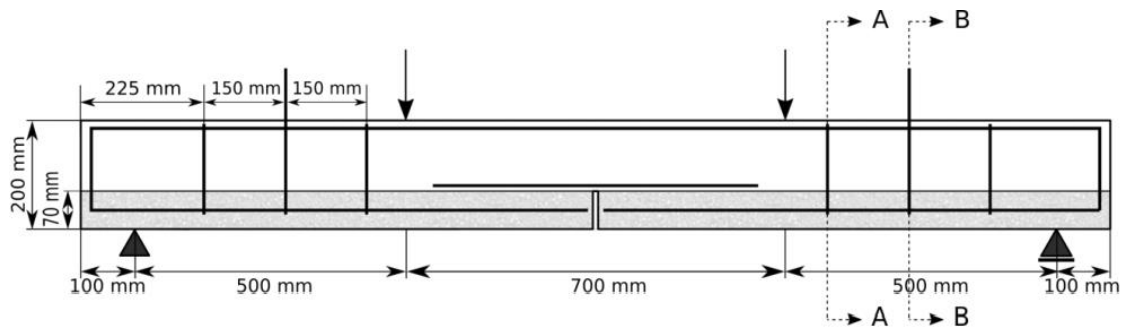


Figure 3.1 – Sample 1 geometrical properties [1]

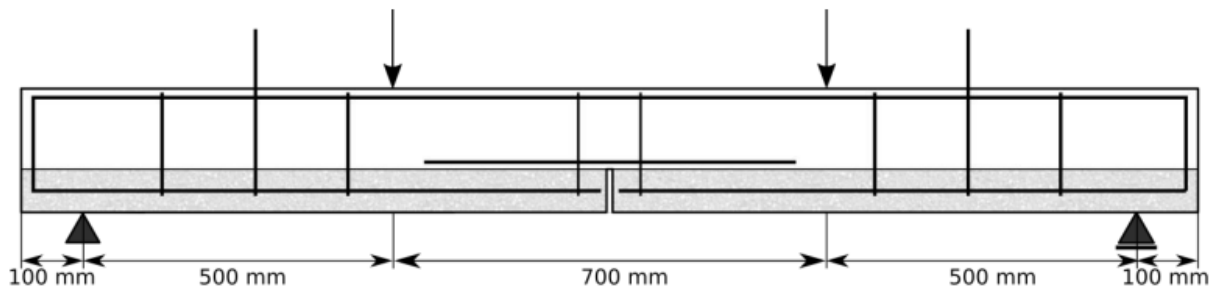


Figure 3.2 – Sample 7 geometrical properties [1]

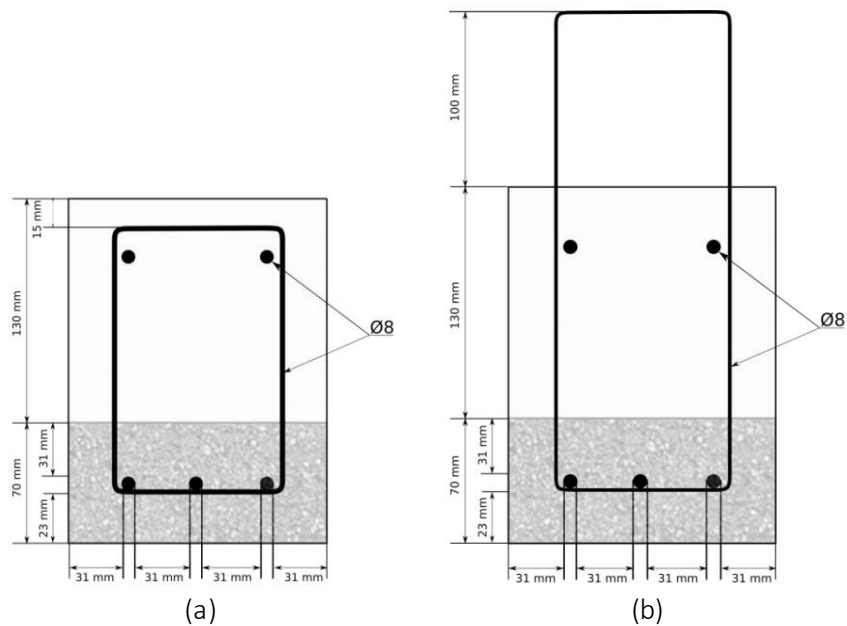


Figure 3.3 – Sample 1 (a) section A-A and (b) section B-B [1]

The specimen was tested with 4-point bending test. Displacement controlled loading was applied to the specimen with a rate 0.002 mm/s. LVDTs (Linear Variable Differential Transformers) were installed to measure the vertical displacement at the mid-span and the joint and interface opening. DIC was used to capture the side displacement of the specimen.



Figure 3.4 – Sample 1 test setup [1]

3.1.2. Experimental result of Sample 1

In Figure 3.5, the vertical displacement at the mid-span, interface opening at the joint and the joint opening in horizontal direction of Sample 1 are shown with their relation to the total vertical load at both loads location. From Figure 3.5, the specimen failed at the maximum load of 13.9 kN and maximum vertical displacement at mid-span 1.24 mm. Several other values such as the maximum opening, and maximum rebar stress values at failure are shown in Table 3.1.

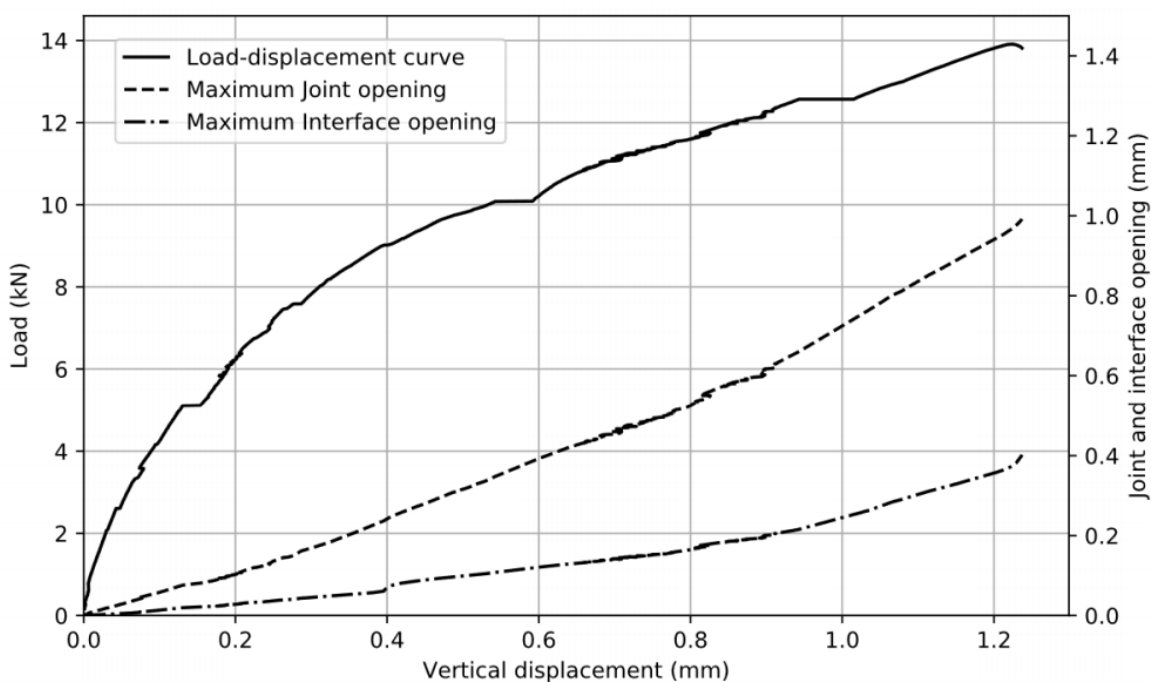


Figure 3.5 – Load-displacement, -interface opening, and -joint opening graphs of Sample 1 [1]

Table 3.1 – Various values of Sample 1 at failure [1]

Property	Value	Unit
Load capacity	13.9	kN
Maximum displacement	1.24	mm
Maximum interface opening	0.4	mm
Maximum joint opening	0.99	mm
Maximum steel stress	241	MPa

In the following figures, the DIC images at several load stages are shown. At load stage 1, the joint opened and followed by horizontal cracking through the interface as shown in Figure 3.6. Several flexural cracks beginning at the level of delamination started to appear at load stage 3 as shown in Figure 3.8. When the delamination reached the end of coupling rebar, a large flexural crack appeared and the specimen failed at that moment as shown in Figure 3.10.

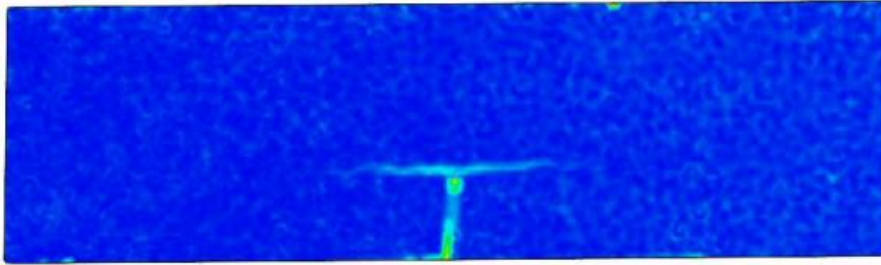


Figure 3.6 – DIC image of Sample 1 at load stage 1 (2.5 kN) [1]

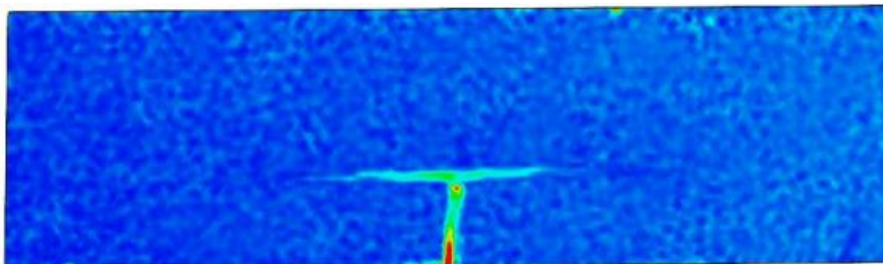


Figure 3.7 – DIC image of Sample 1 at load stage 2 (7.5 kN) [1]

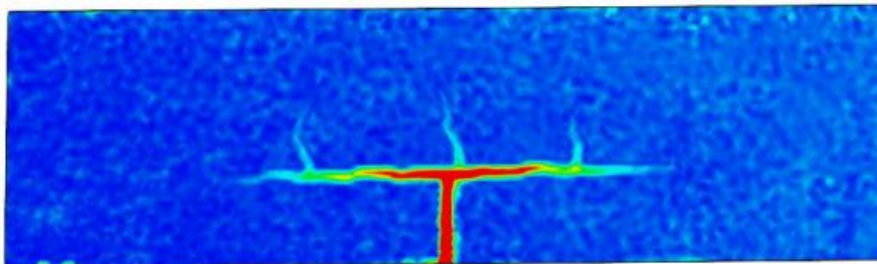


Figure 3.8 – DIC image of Sample 1 at load stage 3 (11 kN) [1]

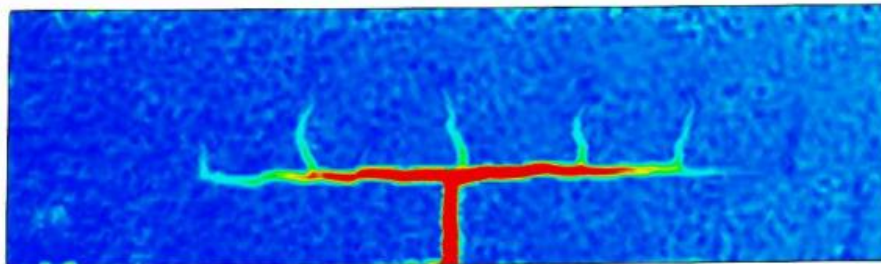


Figure 3.9 – DIC image of Sample 1 at load stage 4 (13 kN) [1]

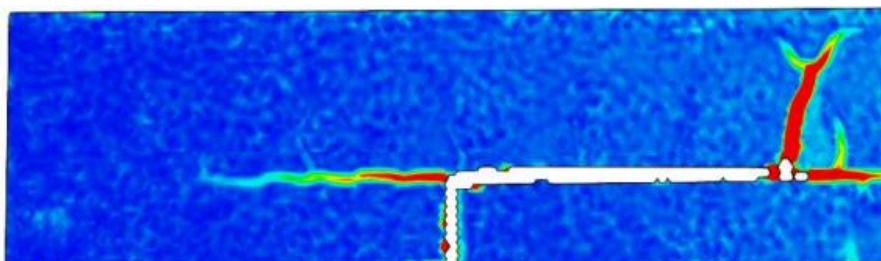


Figure 3.10 – DIC image of Sample 1 at failure [1]

3.1.3. Experimental result of Sample 7

In Figure 3.11, the vertical displacement at the mid-span, interface opening at the joint and the joint opening in horizontal direction of Sample 7 are shown with their relation to the total vertical load at both loads location in black lines. From Figure 3.11, the specimen failed at the maximum load of 28.17 kN and maximum vertical displacement at mid-span 1.68 mm. Several other values such as the maximum opening, and maximum rebar stress values at failure are shown in Table 3.1.

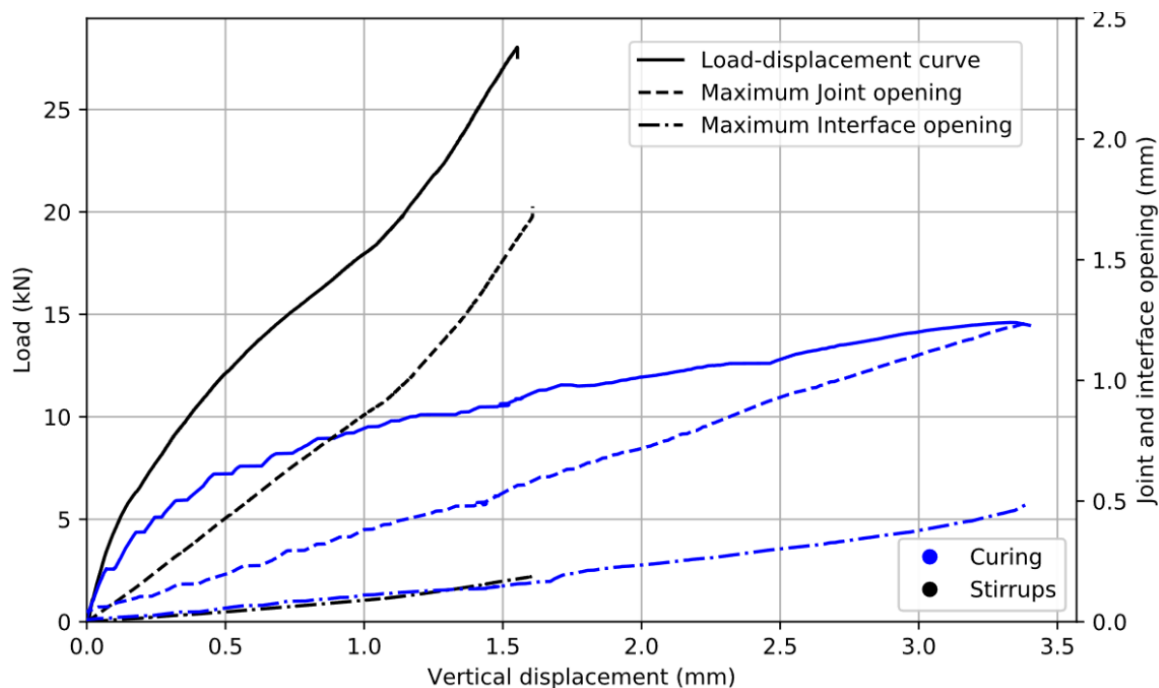


Figure 3.11 – Load-displacement, -interface opening, and -joint opening graphs of Sample 7 (black lines) [1]

Table 3.2 – Various values of Sample 7 at failure [1]

Property	Value	Unit
Load capacity	28.17	kN
Maximum displacement	1.68	mm
Maximum interface opening	0.19	mm
Maximum joint opening	1.72	mm
Maximum steel stress	488	MPa

In the following figures, the DIC images at several load stages are shown. Similar to Sample 1, Sample 7 also developed a horizontal crack along the interface until the end of coupling reinforcement as shown in Figure 3.16. However, the presence of stirrup limited the interface opening which was only 0.19 mm when the specimen failed. As shown in Figure 3.16, at the failure, beside the propagation of flexural crack at the end of coupling reinforcement, there was a tensile crack at the stirrup location in the precast layer. This tensile crack was resulted by the tensile stress at the upper part of precast layer at the stirrup due to the rotational restraint from the stirrup as shown in Figure 3.17. The failure is determined when the load capacity dropped to around 20 kN. The pull-out failure of the stirrup was most likely happened if the test was continued.

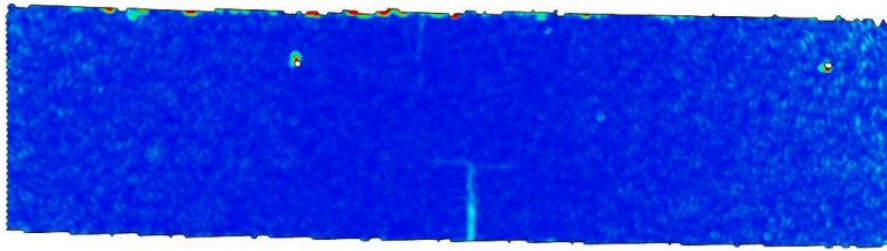


Figure 3.12 – DIC image of Sample 7 at load stage 1 (2.5 kN) [1]

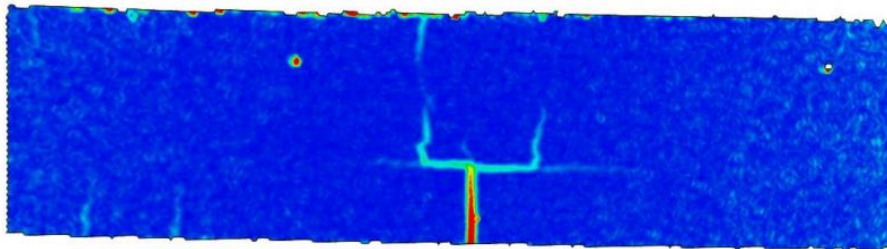


Figure 3.13 – DIC image of Sample 7 at load stage 2 (7.5 kN) [1]

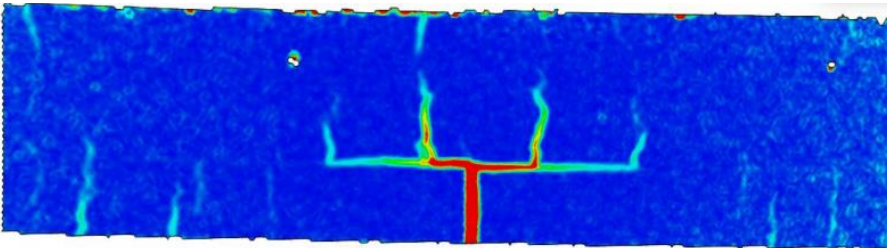


Figure 3.14 – DIC image of Sample 7 at load stage 3 (15 kN) [1]

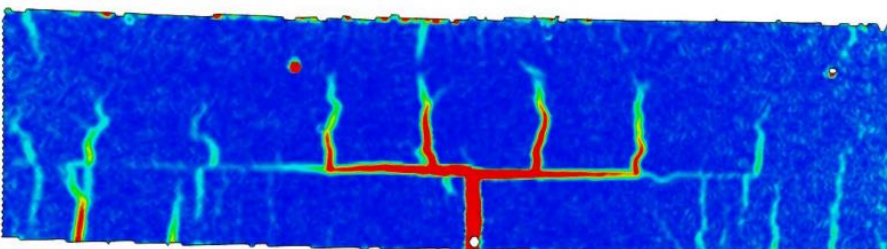


Figure 3.15 – DIC image of Sample 7 at load stage 4 (25 kN) [1]

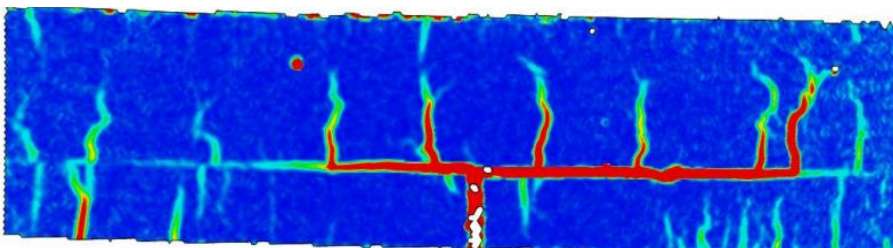


Figure 3.16 – DIC image of Sample 7 at failure [1]

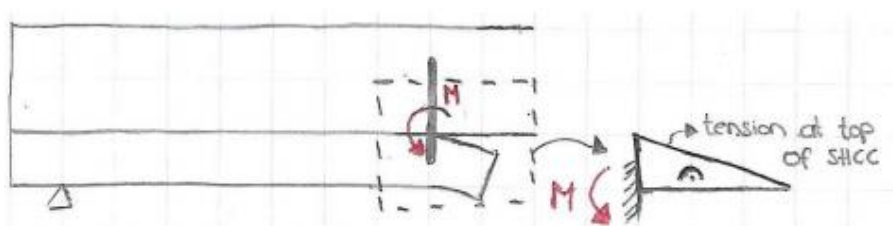


Figure 3.17 – Rotational restraint at the stirrup resulting in tensile cracks [1]

3.2. Numerical setup

In this research, DIANA FEA 10.4 is used as the finite element software for the calculation. This software is chosen because of several reasons, such as, it was widely used in several recent numerical research related to composite structures [1], [22], [26], [27], its features include the concrete-to-concrete interface and reinforcement bond-slip model, and it is available.

In order to answer the main, supporting, and additional research questions, there are numerous numerical models which are made in this numerical research. In general, there are four reference models which parameters are varied for five different studies. Those five studies are the verification study in chapter 3.3, the sensitivity study of interface parameters in chapter 4.1 and 4.2, the study of lap splice spacing influence in chapter 5.1, the study of connecting reinforcement spacing influence in chapter 5.2, and the study of lateral restraint influence in chapter 5.3. The four reference models are:

1. model 2D-SI which is a 2D model based on Sample 1 (Figure 3.18),
2. model 2D-SI-SJ which is a 2D model based on Sample 7 (Figure 3.19),
3. model 3D-SI which is a 3D model based on Sample 1 (Figure 3.20), and
4. model 3D-SI-SJ which is a 3D model based on Sample 7 (Figure 3.21).

The reference models which are based on Sample 1 are necessary for the study of interface behaviour without any influence from connecting reinforcement while the reference models based on Sample 7 are necessary for the study of interface behaviour of reinforced interface beams. 3D models are needed since the objective of this research, especially for the 1st and the 2nd supporting research questions, is to study the interface stress distribution in longitudinal and transverse directions. However, for the additional research question, it is not necessary to use the 3D model since the membrane action could also be seen in a 2D model, thus 2D models are also needed.

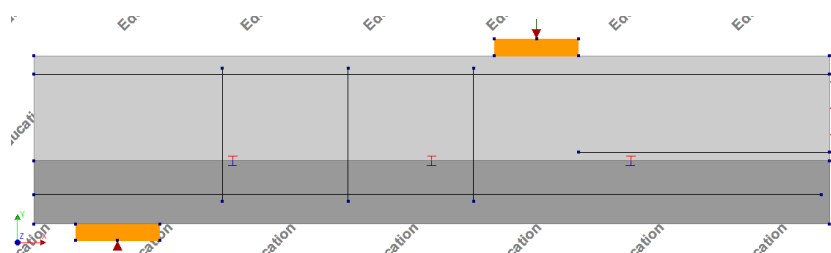


Figure 3.18 – Typical 2D finite element model based on Sample 1 (model name started with 2D-SI)

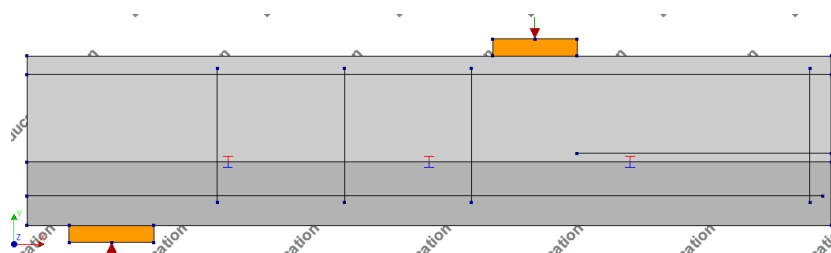


Figure 3.19 – Typical 2D finite element model based on Sample 7 (model name started with 2D-SI-SJ)

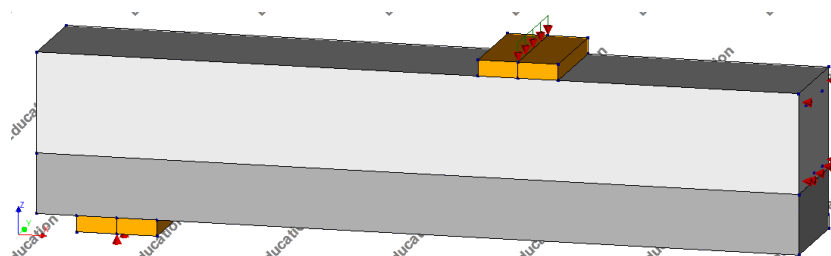


Figure 3.20 – Typical 3D finite element model based on Sample 1 (model name started with 3D-SI)



Figure 3.21 – Typical 3D finite element model based on Sample 7 (model name started with 3D-SI-SJ)

In order to do the five numerical studies, several parameters of the reference models are varied. Table 3.3 describes the parameter variations made in each reference model for each numerical study. The complete list of all the models used in the five studies and their respective parameter variations are available in appendix.

Table 3.3 – Parameter variations in each numerical study

Numerical study	Reference models	Parameter variations
Verification of numerical models	2D-SI, 3D-SI, 2D-SI-SJ, 3D-SI-SJ	<ul style="list-style-type: none"> Concrete-to-reinforcement interface (circular bond-slip bar with CEB-FIB 2010 bond-slip function or embedded bar)
Sensitivity study of interface parameters	2D-SI, 2D-SI-SJ	<ul style="list-style-type: none"> Interface stiffness (5 – 1000 N/mm³) Interface tensile strength (0.1 – 1.0 MPa) Cohesion (0.1 – 1.0 MPa) Friction angle (0.1 – 1.0 rad)
Lap splices spacing	3D-SI	<ul style="list-style-type: none"> Interface type (smooth interface or perfect bonded interface) number and equivalent diameter of lap splice(s) (1 D14 or 3 D8)
Connecting reinforcements spacing	3D-SI-SJ	<ul style="list-style-type: none"> Interface type (smooth interface or perfect bonded interface) Number and equivalent diameter of stirrup legs near the joint (1 D9 or 3 D8.5)
Lateral restraint	2D-SI	<ul style="list-style-type: none"> Interface type (smooth interface or perfect bonded interface) Boundary condition (clamped or simply supported)

The dimension of all numerical models in this research are based on Sample 1 and Sample 7, which can be seen in chapter 3.1. Due to the large number of the numerical models made in this research, these models are named with abbreviations which are described in Table 3.4.

Table 3.4 – Model name abbreviations

Abbr.	Model type or variation
2D	Two-dimensional model
3D	Three-dimensional model
SI	<u>S</u> mooth <u>I</u> nterface (untreated/parameter fit to Sample 1 [7])
PB	<u>P</u> erfect <u>B</u> onded interface
SJ	Presence of connecting reinforcement (<u>S</u> tirrup near the <u>J</u> oint)
1L	Variation of lap splice spacing using <u>1</u> <u>L</u> ap splice or variation of connecting reinforcement spacing using <u>1</u> <u>L</u> eg stirrup
RC	Substitution of precast concrete type from SHCC to <u>R</u> egular <u>C</u> oncrete
FR	<u>F</u> ull height lateral <u>R</u> estraint

3.2.1. Finite element types

There are 4 structural members which finite element type need to be defined, the concrete layers, load and bearing pads, concrete-to-concrete interface, and the reinforcements. According to the Guideline for non-linear finite element analysis of concrete structures [28], quadratic interpolation should be used. Moreover, the guideline also suggests the use of a bond-slip reinforcement to model the slip explicitly in addition to the circular beam type of bond-slip bar to also capture dowel action of the rebar. However, to reduce the running duration of the analysis, only for reinforcements around the critical joint such as coupling reinforcements and stirrup near the joint the bond-slip model is used. The full list of the element types is provided in Table 3.5 for the 2D models and in Table 3.6 for the 3D models.

Table 3.5– Finite element types for 2D models

Structural Member	Element type	
Concrete layers	Quadratic regular plane stress (CQ16M)	
Loading and bearing pads	Quadratic regular plane stress (CQ16M)	
Concrete-to-concrete interface	2D line interface (CL12I)	
Reinforcements	Top, bottom rebar, stirrup	Embedded bar
	Coupling rebar, stirrup at joint	Circular bond-slip bar

Table 3.6 – Finite element types for 3D models

Structural Member	Element type	
Concrete layers	Quadratic structural solids (CHX60, CPY39, CTE30)	
Loading and bearing pads	Quadratic structural solids (CHX60, CPY39, CTE30)	
Concrete-to-concrete interface	Structural surface interface (CQ48II)	
Reinforcements	Top, bottom rebar, stirrup	Embedded bar
	Coupling rebar, stirrup at joint	Circular bond-slip bar

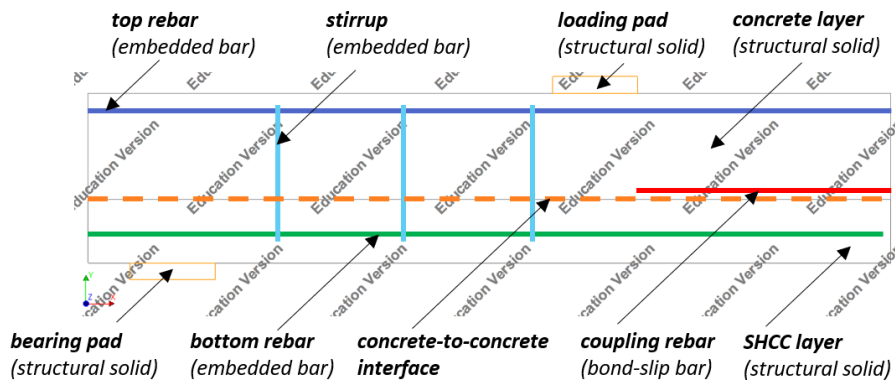


Figure 3.22 – Element type of typical 2D model based on Sample 1 (model name started with 2D-SI)

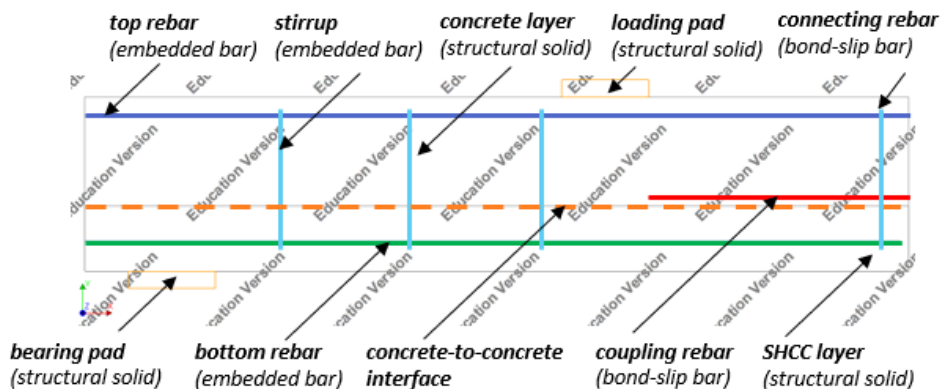


Figure 3.23 – Element type of 2D model based on Sample 7 (model name started with 2D-SI-SJ)

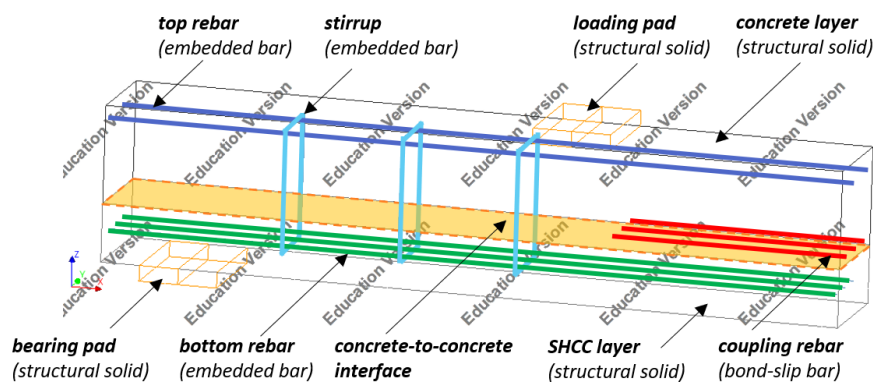


Figure 3.24 – Element type of typical 3D model based on Sample 1 (model name started with 3D-SI)

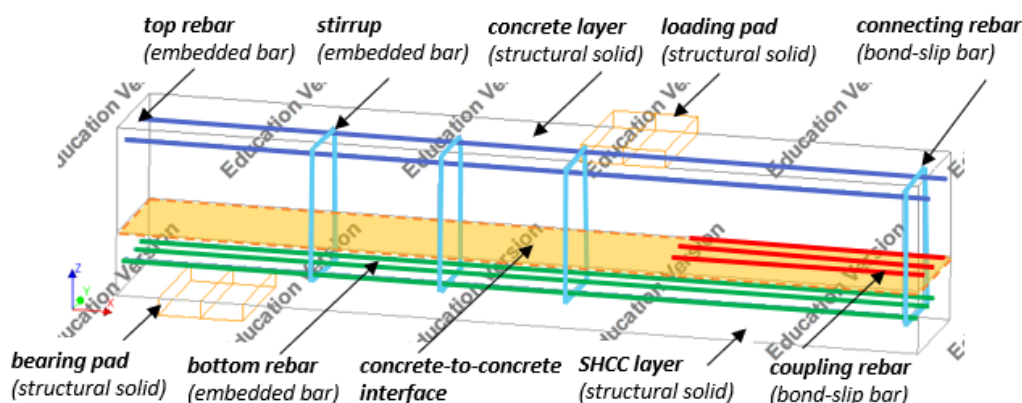


Figure 3.25 – Element type of typical 3D model based on Sample 7 (model name started with 3D-SI-SJ)

3.2.2. Material properties and constitutive models

There are 5 different material properties which are used in the numerical models, which are the regular concrete (cast-in-situ layer), SHCC (precast layer), steel (rebar), steel (loading and bearing pads), and concrete-to-concrete interface. For the regular concrete, the average compressive strength and the Young’s modulus are obtained from the cube compressive test [1], while the constitutive model, fracture energy, and the reduction due to lateral cracking are according to [28].

Table 3.7 – Material properties of concrete

Material properties	Symbol	Input	Unit
Class		Concrete and masonry	
Material model		Total strain based crack model	
Young’s modulus	E_{cm}	35500	MPa
Poisson’s ratio	ν	0.2	
Crack orientation		Rotating	
Tensile curve		Hordijk	
Tensile strength	f_{ctm}	2.9	MPa
Mode-I tensile fracture energy	G_{fm}	0.141	N/mm
Crack bandwidth specification		Rots	
Poisson’s ratio reduction model		Damage based	
Compressive curve		Parabolic	
Compressive strength	f_{cm}	40	MPa
Compressive fracture energy	G_{cm}	35.4	N/mm
Reduction due to lateral cracking		Vecchio and Collins 1993	
Lower bound reduction curve	β_{σ}^{\min}	0.4	

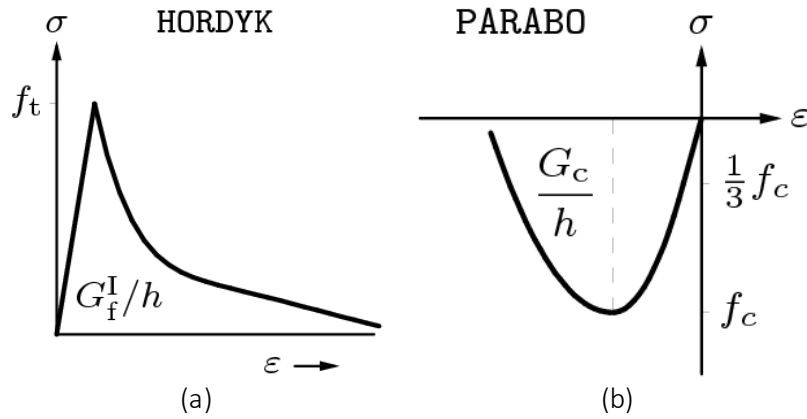


Figure 3.26 – (a) Tensile and (b) compressive constitutive model of concrete [28]

For the SHCC, the average compressive strength and the Young’s modulus are also obtained from the cube compressive test [1], while the reduction due to lateral cracking is also according to [28]. The constitutive model with strain hardening is chosen to suit the SHCC behaviour in tensile stress.

Table 3.8 – Material properties of SHCC

Material properties	Symbol	Input	Unit
Class		Concrete and masonry	
Material model		Total strain based crack model	
Young’s modulus	E_{cm}	23000	MPa
Poisson’s ratio	ν	0.2	
Crack orientation		Rotating	
Tensile curve		<i>fib</i> fibre reinforced concrete	
Strain curve		Total strain	
Uniaxial tensile strength	f_L	3.0	MPa
Uniaxial residual strength i	f_{Ri}	3.1	MPa
Uniaxial total strain i	ϵ_{Ri}	0.006	
Uniaxial residual strength j	f_{Rj}	3.2	MPa
Uniaxial total strain j	ϵ_{Rj}	0.012	
Uniaxial residual strength k	f_{Rk}	3.5	MPa
Uniaxial total strain k	ϵ_{Rk}	0.03	
Uniaxial ultimate total strain	ϵ_u	0.03	
Compressive curve		Ideal	
Compressive strength	f_{cm}	40	MPa
Reduction due to lateral cracking		Vecchio and Collins 1993	
Lower bound reduction curve	β_σ^{\min}	0.4	

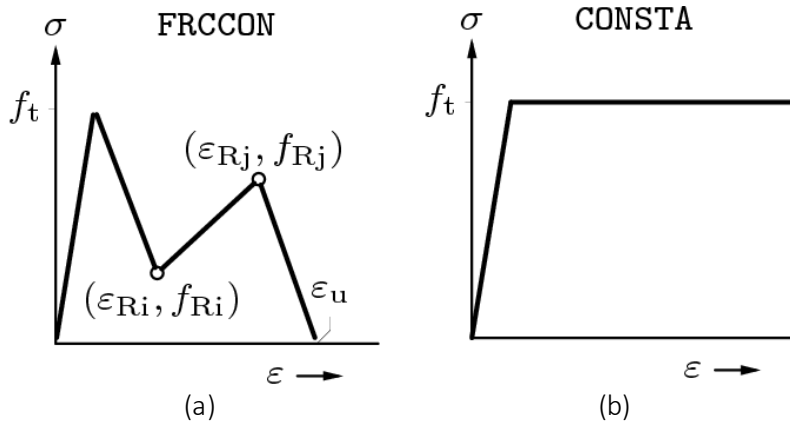


Figure 3.27 – (a) Tensile and (b) compressive constitutive model of SHCC [28]

For the steel reinforcement, grade B500 is used. The constitutive model of the reinforcement is according to [28]. The bond-slip interface parameters which are marked with asterisks in Table 3.10, are according to the *fib* model code for concrete structures 2010 [13]. For steel reinforcement with “embedded bar” as its element type, the parameters with asterisks are not used.

Table 3.9 – Material properties of steel reinforcement

Material properties	Symbol	Input	Unit
Class		Reinforcement	
Material model		Bond-slip reinforcement	
Young's modulus	E_s	210000	MPa
Poisson's ratio	ν	0.3	
Non-linear model		Von Mises plasticity	
Hardening function		Plastic strain-yield stress	
Hardening hypothesis		Strain hardening	
Hardening type		Isotropic hardening	
Yield strength	f_y	550	MPa
Ultimate strength	f_u	650	MPa
Yield strain	ϵ_y	0.00262	
Ultimate strain	ϵ_u	0.04738	
Normal stiffness modulus*	k_n	1000000	N/mm ³
Shear stiffness modulus*	k_v	250.594	N/mm ³
Bond-slip interface failure model*		CEB-FIB 2010 bond-slip function	
Maximum shear stress*	τ_{max}	15.811	MPa
Ultimate shear stress*	τ_f	6.325	MPa
Linearized initial slip section*	s_0	0.01	mm
Relative slip section 1*	s_1	1	mm
Relative slip section 2*	s_2	2	mm
Relative slip section 3*	s_3	10	mm
Exponent alpha*	α	0.4	

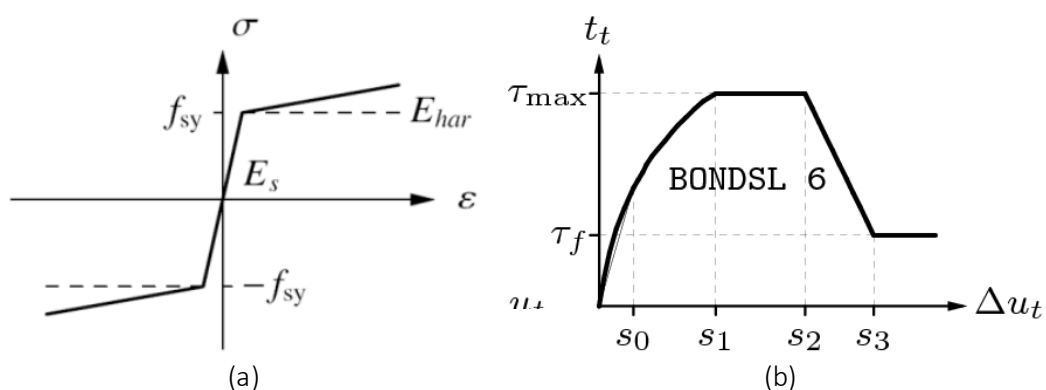


Figure 3.28 – (a) Axial [28] and (b) bond-slip constitutive model [29] of steel rebar

For the steel load and bearing pads, the linear elastic constitutive model is used to prevent failure at the pads. It is also not of interest in this study to see the failure of the steel pads.

Table 3.10 – Material properties of steel load and bearing pads

Material properties	Symbol	Input	Unit
Class		Steel	
Material model		Linear elastic isotropic	
Young's modulus	E_s	210000	MPa
Poisson's ratio	ν	0.3	

To model the concrete-to-concrete interface between SHCC (precast) layer and regular concrete (cast-in-situ) layer in Sample 1 and Sample 7, the guideline for non-linear finite element analysis of concrete structures [28] suggest the use of the Coulomb friction model with tension cut-off as shown in Figure 3.29. All of the interface parameters (normal and shear stiffness modulus, cohesion, friction angle, and tensile strength) which are shown in Table 3.11 are adjusted after several trials to best fit the experimental result of Sample 1 and Sample 7.

Table 3.11 – Material properties of concrete-to-concrete interface (smooth interface)

Material properties	Symbol	Input	Unit
Class		Interface	
Material model		Coulomb friction	
Linear material type		2D line interface / 3D surface interface	
Normal stiffness modulus	k_n	10	N/mm ³
Shear stiffness modulus	k_v	10	N/mm ³
Cohesion	c	0.5	MPa
Friction angle	ϕ	0.54	rad
Interface opening model		Gapping model	
Tensile strength	f_t	0.5	MPa
Model for gap appearance		Brittle	

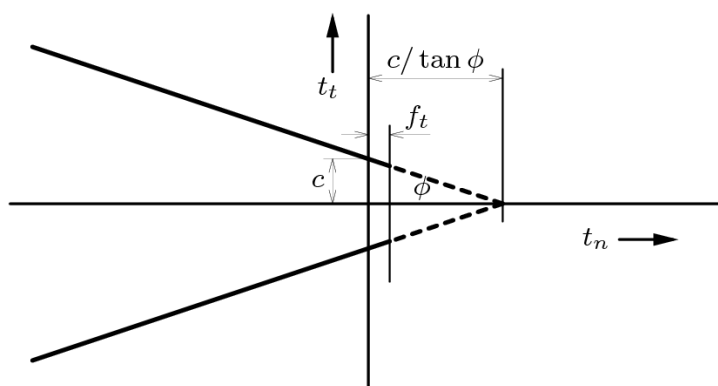


Figure 3.29 – Coulomb friction model with tension cut-off [29]

3.2.3. Load, boundary, and symmetry conditions

To represent the experimental 4-point bending test, the numerical models are loaded in the same configuration. A deformation controlled prescribed deformation is applied in y-direction as a point load on the loading pad for the 2D models. For the 3D models, the prescribed deformation is applied as a strip pointing in z-direction on the loading pad.

At the bottom of the bearing pad and on top of the loading pad (necessary to introduce prescribed deformation), the translational restraint in y-direction is applied for the 2D models (z-direction for the 3D models) as boundary conditions. At the end of the coupling reinforcement and along the side edge of the cast-in-situ layer in 2D models (side surface in 3D models), the translational restraint in x-direction is applied as symmetry conditions. This symmetry conditions are applied in order to reduce the the length of the specimen into half so the size of the file could be reduced. The joint between precast sections is modelled with no restraint applied on the side edge of precast layer in 2D models (side surface of precast layer in 3D models).

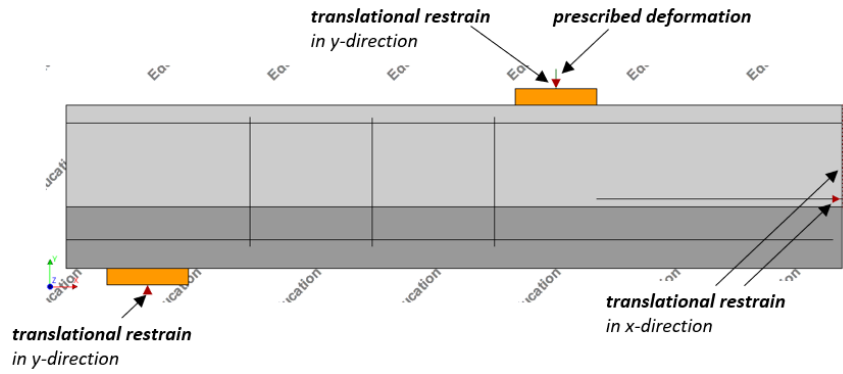


Figure 3.30 – Load, boundary, and symmetry conditions of typical 2D model based on Sample 1 (model name started with 2D-SI)

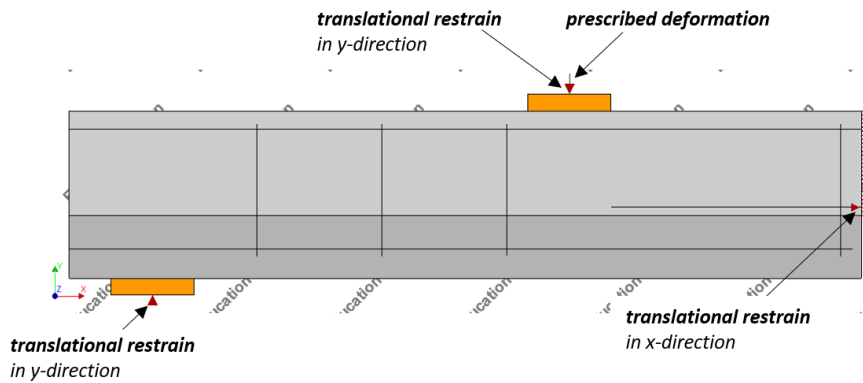


Figure 3.31 – Load, boundary, and symmetry conditions of 2D model based on Sample 7 (model name started with 2D-SI-SJ)

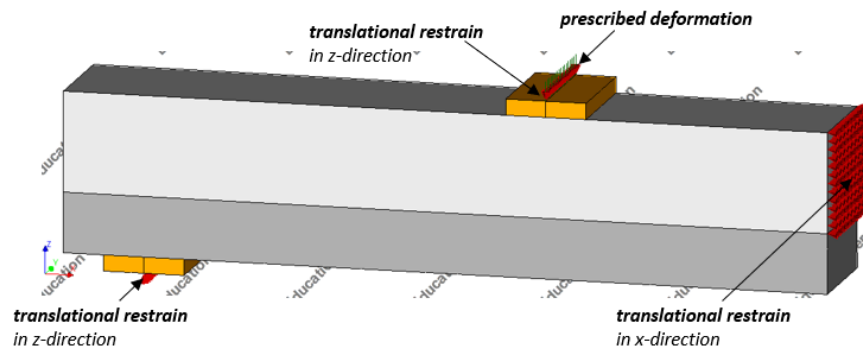


Figure 3.32 – Load, boundary, and symmetry conditions of typical 3D model based on Sample 1 (model name started with 3D-SI)

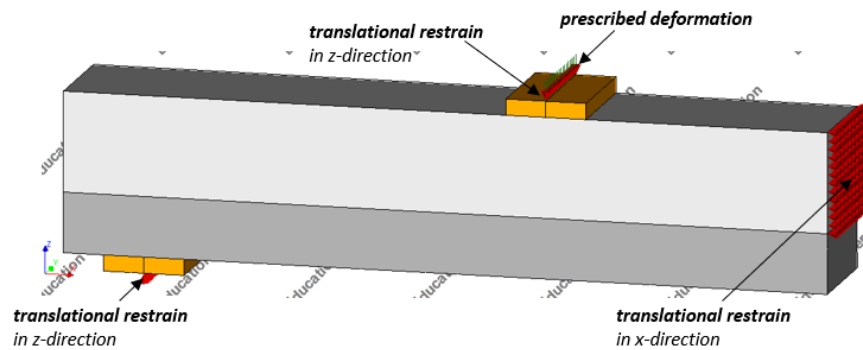


Figure 3.33 – Load, boundary, and symmetry conditions of typical 3D model based on Sample 7 (model name started with 3D-SI-SJ)

3.2.4. Mesh size

The mesh size of the 2D models is 10 mm while the 3D model is in average 20 mm. The larger mesh size in the 3D models is intended to reduce the running duration of the finite element analysis. Nevertheless, both models are compliant to [28]. According to the guideline, the minimum number of element in the through-thickness and through-width direction is 6 elements, while in the longitudinal direction the minimum is 50 elements.

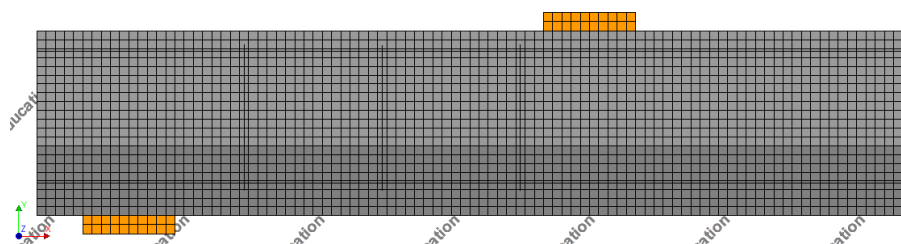


Figure 3.34 – Mesh size of typical 2D model based on Sample 1 (model name started with 2D-SI)

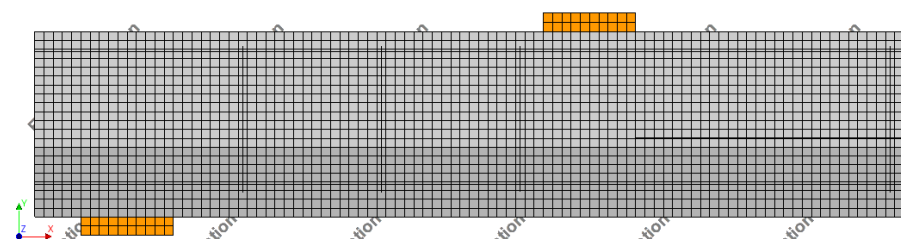


Figure 3.35 – Mesh size of typical 2D model based on Sample 7 (model name started with 2D-SI-SJ)

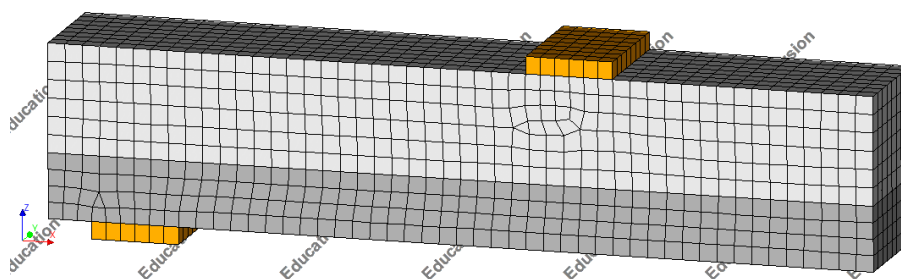


Figure 3.36 – Mesh size of typical 3D model based on Sample 1 (model name started with 3D-SI)

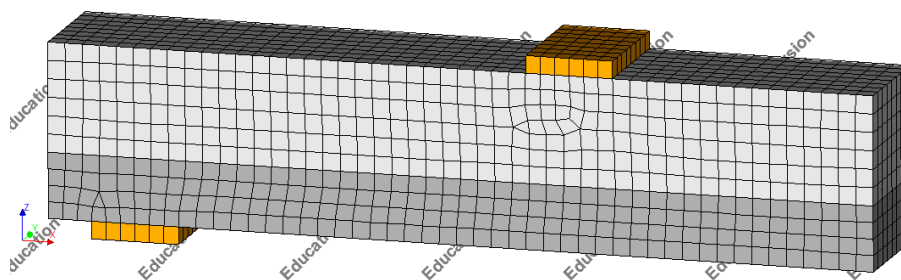


Figure 3.37 – Mesh size of typical 3D model based on Sample 7 (model name started with 3D-SI-SJ)

3.2.5. Iterative scheme

The iterative scheme for the numerical models in this research is in accordance with [28]. According to the guideline, at least one of two norms should be satisfied to be considered as convergence, thus less strict convergence requirement applies. The non-convergence load increments could still be accepted as long as they are followed by the convergence results.

Table 3.12 – Iterative scheme

Non-linear effect	Physically non-linear
Iteration method	Regular (Full) Newton-Raphson
Convergence norm	Energy, Force
Convergence tolerance	0.001, 0.01
Satisfy all norms	No
Step size	0.01(100)
Maximum number of iterations	100

3.3. Verification of numerical models

After completing the numerical setup into DIANA FEA for the models used in the verification study as listed in Table A1.1, the results are presented below and will be verified with the experimental result. The verification of the unreinforced interface beams with Sample 1 is presented in the first part while the verification of the reinforced interface beams with Sample 7 is presented in the second part.

3.3.1. Unreinforced interface beams

Figure 3.38 shows the load-displacement graph of experimental result of Sample 1 and unreinforced interface beam models represented Sample 1 which numerical setup is provided in chapter 3.2 (with bond-slip function). The figure also shows the load-displacement graph of models which instead of using CEB-FIB 2010 bond-slip function, they use embedded bar for the coupling reinforcement (without bond-slip function). From that figure, all numerical models have similar load capacity compared to the experiment. In terms of the stiffness, the stiffness of all models differs from the experimental result at the beginning of the load increments. However, from around 0.6 mm of displacement, there is a considerable change of stiffness for models with bond-slip and they follow the similar equilibrium path of the experiment until failure.

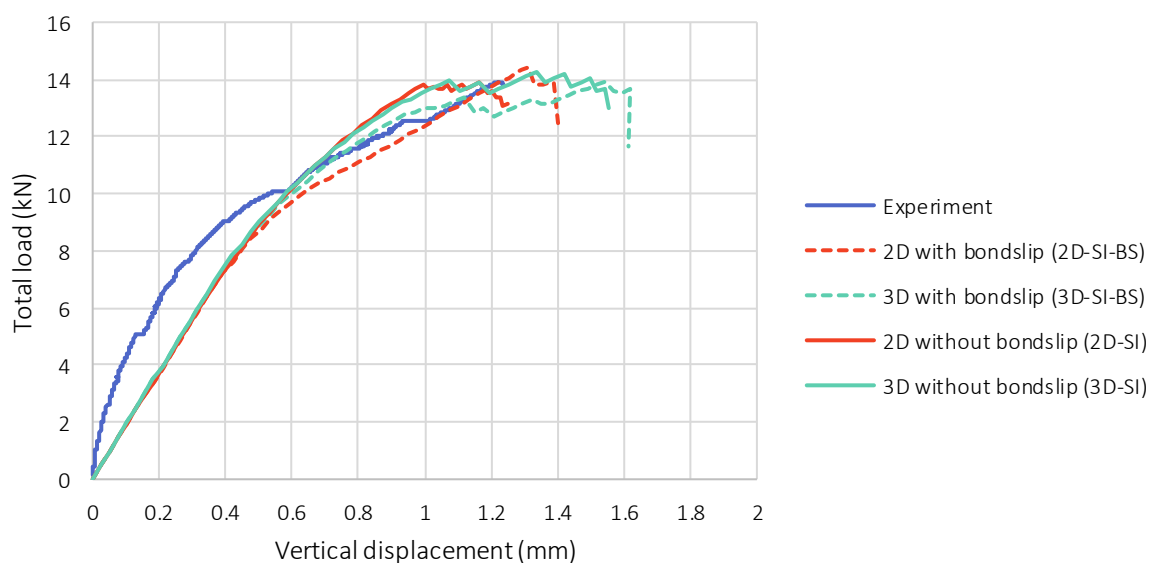


Figure 3.38 – Load-displacement graph of Sample 1 experiment [1] and models with and without reinforcement bond-slip function

Table 3.13 – Load capacity of Sample 1 [1] and its simulated numerical models

Results	Maximum total load (kN)
Experiment (Sample 1)	13.91
2D model with bond-slip function (2D-SI-BS)	14.41
3D model with bond-slip function (3D-SI-BS)	13.92
2D model without bond-slip function (2D-SI)	13.90
3D model without bond-slip function (3D-SI)	14.26

In Figure 3.39, the crack strain at the failure load of models with bond-slip function is presented, while the ones of models without bond-slip is presented in Figure 3.40. All models could represent the same failure mechanism as the experiment which can be seen in Figure 3.10. The failure development is started with the horizontal crack at the gap between precast sections and continues to grow along the interface between the concrete layers (delamination) until it reaches the end of the coupling reinforcement and a large flexural crack reaches the top part of the cast-in-situ layer.

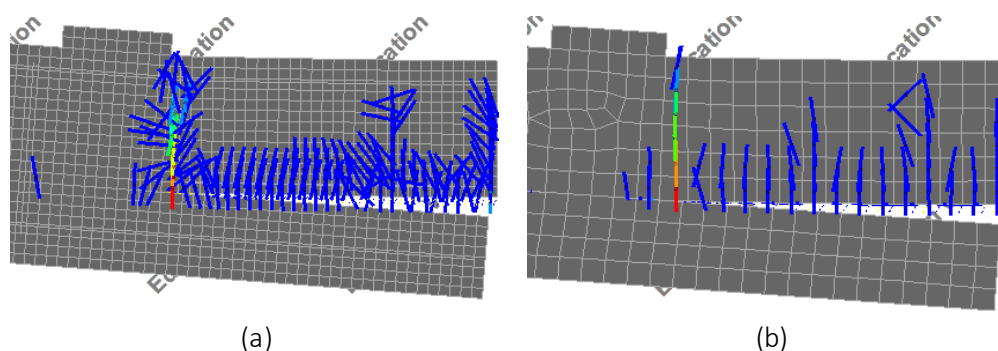


Figure 3.39 – Crack strain at failure of (a) 2D model (2D-SI-BS) and (b) 3D model (3D-SI-BS) with reinforcement bond-slip function

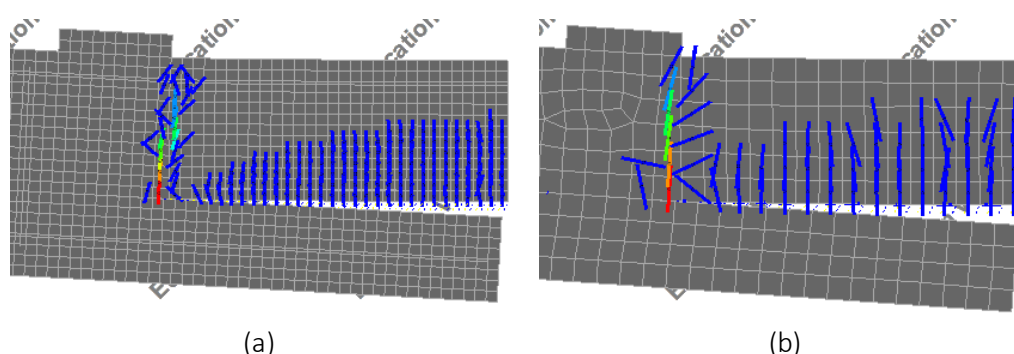


Figure 3.40 – Crack strain at failure of (a) 2D model (2D-SI) and (b) 3D model (3D-SI) without reinforcement bond-slip function

3.3.2. Reinforced interface beams

Figure 3.41 shows the load-displacement graph of experimental result of Sample 7 and reinforced interface beam models represented Sample 7 which numerical setup is provided in chapter 3.2 (with bond-slip function). The figure also shows the load-displacement graph of models which instead of using CEB-FIB 2010 bond-slip function, they use embedded bar for the coupling reinforcement and stirrup near the joint (without bond-slip function). From that figure, all 2D numerical models have a similar load capacity compared to the experiment. However, all of the 3D models' equilibrium path continue to increase until the end of analysis, although the structural stiffness of both 3D models decreases at the failure displacement of the 2D models. All models have different structural stiffness and displacement capacity compared to the experiment, especially after 1.1 mm of vertical displacement. These differences are analysed in the following paragraph since they are related to the crack development of the models.

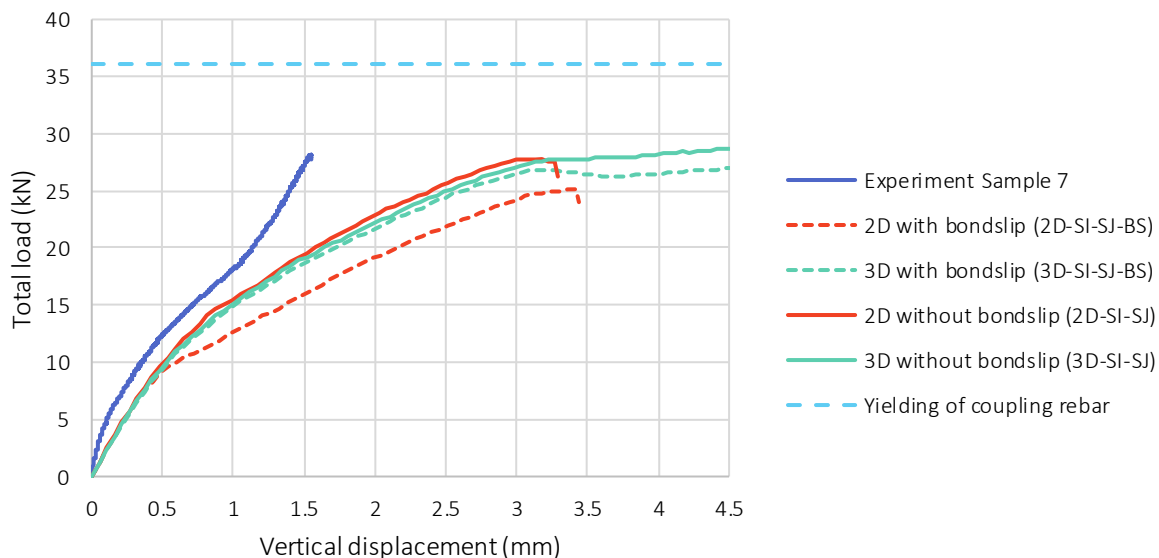


Figure 3.41 – Load-displacement graph of Sample 7 experiment [1] and models with and without reinforcement bond-slip function

Table 3.14 – Load capacity of Sample 7 [1] and its simulated numerical models

Experiment	Maximum total load (kN)
Experiment (Sample 7)	28.17
2D model with bond-slip function (2D-SI-SJ-BS)	25.16
3D model with bond-slip function (3D-SI-SJ-BS)	27.31*
2D model without bond-slip function (2D-SI-SJ)	27.78
3D model without bond-slip function (3D-SI-SJ)	28.96*

* The total load of 3D models is taken at the maximum vertical displacement of the 2D models.

In Figure 3.42, the crack strain at the failure load of models with bond-slip function is presented, while the ones of models without bond-slip is presented in Figure 3.43. All 2D models could represent the similar failure mechanism as the experiment which can be seen in Figure 3.16. The failure development is started with the horizontal crack at the gap between precast sections and continues to grow along the interface between the concrete layers (delamination). At the same time, tensile crack at the stirrup in precast layer grows larger and followed by the growth of flexural crack at the end of coupling reinforcement. The failure occurs when both the crack at the stirrup and at the end of coupling reinforcement become large enough and the equilibrium path drops.

This failure mechanism has a slight difference compared to the experiment. First, although all of the crack patterns of both 2D models at failure are the same as the experiment, both models develop a shorter horizontal crack at interface level, not until the end of coupling reinforcement as happened in Sample 7. The second difference is the development of the tensile crack at the stirrup in precast layer. In the experiment, as shown in Figure 3.14, this crack was developed at the failure. However, in all models as shown in Figure 3.44 and Figure 3.45, the crack has already been developed earlier. At the failure, especially for the 2D models, as shown in Figure 3.42(a) and Figure 3.43(a), it even become the major crack which has larger crack strain in compared to the flexural crack at the end of coupling reinforcement. The difference in this crack development might be caused by the material model of SHCC in DIANA FEA. Furthermore, this difference could be the cause of the differences in the structural stiffness and the displacement capacity of the models in compared to Sample 7.

All 3D models have a similar damage development compared to the 2D models until around 3.2 mm of vertical displacement or around the displacement capacity of the 2D models. Beyond that point, the concentrated crack development at the stirrup in precast layer results in the increase of the equilibrium

path, although the structural stiffness decreases. This interface behaviour of 3D models is discussed further in chapter 5.2.1

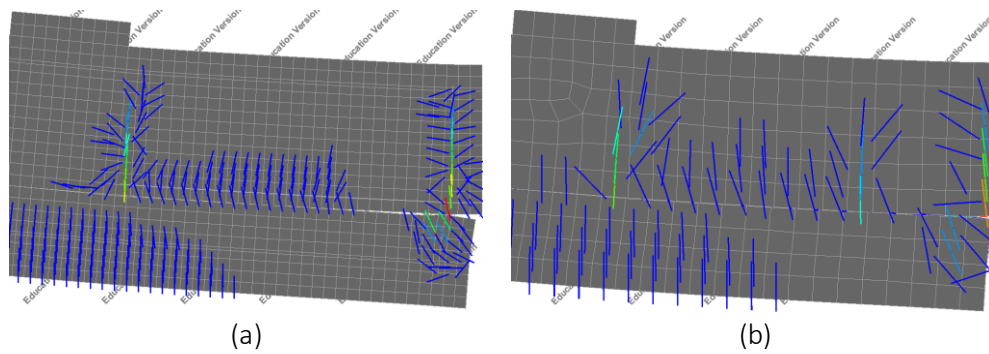


Figure 3.42 – Crack strain at failure of (a) 2D model (2D-SI-SJ-BS) and (b) 3D model (3D-SI-SJ-BS) with reinforcement bond-slip function

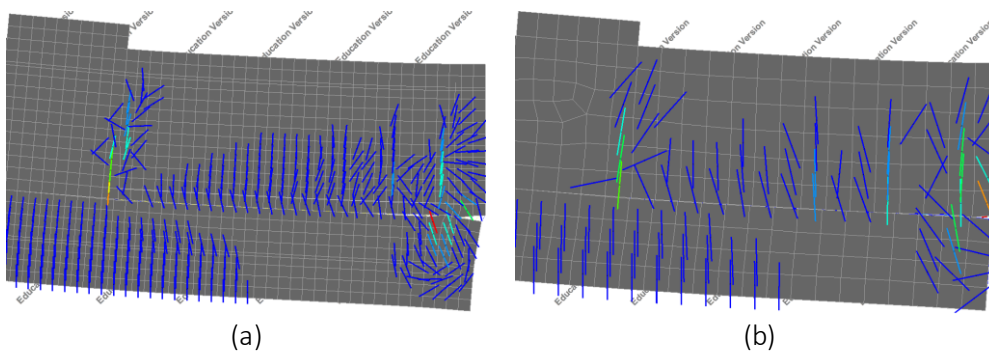


Figure 3.43 – Crack strain at failure of (a) 2D model (2D-SI-SJ) and (b) 3D model (3D-SI-SJ) without reinforcement bond-slip function

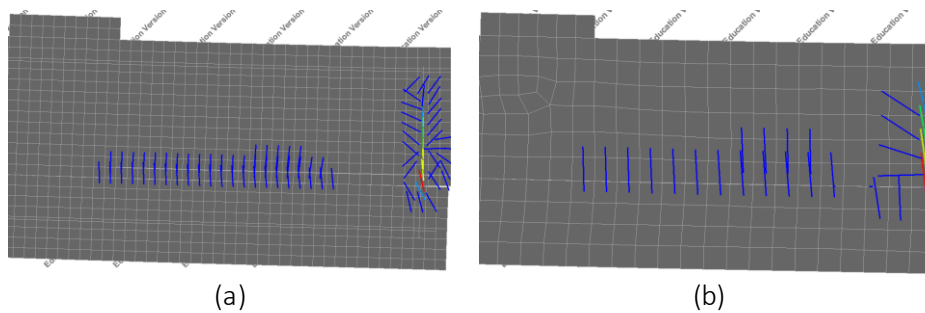


Figure 3.44 – Crack strain at 15 kN load of (a) 2D model (2D-SI-SJ-BS) and (b) 3D model (3D-SI-SJ-BS) with reinforcement bond-slip function

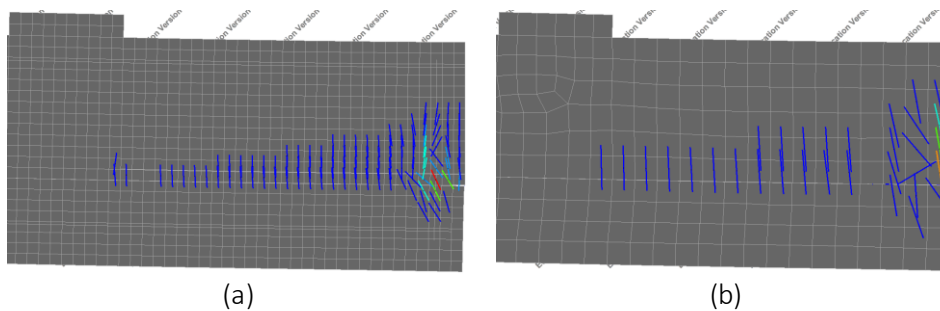


Figure 3.45 – Crack strain at 15 kN load of (a) 2D model (2D-SI-SJ) and (b) 3D model (3D-SI-SJ) without reinforcement bond-slip function

3.4. Interface parameters in codes and other research

Table 3.15 shows the comparison of the interface parameters of this research and the current codes for the smooth category as described in chapter 2.1. The chosen cohesion value is similar to the value from *fib* model code for concrete structures 2010 [13] for the smooth category, while the friction angle has the same value as both *fib* and Eurocode 2 [9]. The ratio between cohesion and interface tensile strength chosen is also in accordance with a research from Zanotti and Randl [30] which is supposed to be in a range between 0.6 and 2.8.

The table also presents the interface parameters from several other recent research which use the same finite element software DIANA FEA. As shown in the table, a wide range of the value of interface parameters was used in different numerical research. There is a really high value used for interface stiffness by abt [26], but there is also a really low cohesion value used by Bouwsema [27]. There is no consistency in the values of these interface parameters. Therefore, it is necessary to perform a sensitivity study of interface parameters in order to understand the influence of each parameter to the numerical results of composite structures.

Table 3.15 – Comparison of interface parameters according to several codes and research

Reference	k_n (N/mm ³)	k_v (N/mm ³)	c (MPa)	ϕ (rad)	f_t (MPa)
This research	10	10	0.5	0.54	0.5
<i>fib</i> model code 2010 [13]			0.58	0.54	
Eurocode NEN-EN 1992-1-1 [9]			1.02	0.54	
Harrass [1]	1200	1200	1.0	0.85	0.5
abt [26]	60000	6000	0.5	0.5	0.5
Bouwsema [27]	10	10	0.2	0.38	

3.5. Summary

Both 2D and 3D numerical models of unreinforced interface beams can simulate the similar experimental result of Sample 1 [1]. They have a similar load and displacement capacity and can simulate the same failure development as the experiment. 2D models of reinforced interface beams can simulate the similar experimental result of Sample 7 [1] since the model has a similar load capacity and failure mechanism as the experiment. 3D models of reinforced interface beams can also develop the similar damage development, although there is a different crack distribution across the width of the specimen so the equilibrium path can continue to increase although with a lower structural stiffness.

Due to insignificant effect of CEB-FIB 2010 bond-slip function which is found in unreinforced and reinforced interface models, the reinforcement bond transfer for the rest of this research will be modelled as perfect bond (embedded bar reinforcement type). Consequently, pull-out failure of stirrup is excluded for the rest of this study.

The interface parameters used in the models are in accordance with the current code (*fib* and Eurocode) and a research regarding to the ratio of cohesion to tensile strength. However, there is a wide range of the value of interface parameters used in different research (no consistency). Therefore, it is necessary to do a sensitivity study of interface parameters to understand the influence of each parameter to the numerical results of composite structures.

|4| SENSITIVITY STUDY OF INTERFACE PARAMETERS

In numerical study, the interface properties of specimen are modelled with several interface parameters of a certain model, such as the Coulomb friction model which is used in this research. As explained in chapter 3.2.2, the numerical parameters which are shown in Table 3.11 have been adjusted several times to best fit the experimental result of Sample 1 [1] which is used for verification. The repeated adjustments are necessary since with a slight change of one parameter, the load and displacement capacity and/or stiffness of the structure was considerably different. In the other hand, chapter 3.4 shows that there is a wide range of the values of interface parameters used in different research (no consistency). Therefore, it is necessary to understand the influence of each interface parameters so it could provide the basis for the understanding of the interface behaviour in numerical analysis for the next chapter.

This chapter includes two sensitivity studies. The first analysis is based on model 2D-SI (smooth unreinforced interface) while the second analysis is based on model 2D-SI-SJ (smooth reinforced interface) which numerical setup and results are available in the previous chapter. There are four parameters which are studied in each analyses, the interface stiffness, interface tensile strength, cohesion, and friction angle. The range of each parameter used in these studies is in accordance with the values which are suggested by the codes [8] [13] and/or commonly used in the recent numerical research [1] [26] [27].

4.1. Unreinforced interface beams

The first sensitivity study of interface parameters is based on model 2D-SI, the model without connecting reinforcement (vertical stirrup near the joint), which reproduces the experimental result of Sample 1 [1]. The finite element model and its numerical setup have been explained in chapter 3.2, while its result is described in chapter 3.3.1. Each interface parameter is varied independently from other parameters and its results are discussed in the following chapters.

4.1.1. Interface stiffness

By varying the interface stiffness (both normal and shear), the load and displacement capacity and the stiffness of the overall structure are changed. The higher the interface stiffness, the lower the capacity but the higher the structural stiffness which can be seen in Figure 4.1. Figure 4.2 shows that the maximum total load and interface stiffness have a logarithmic relation until it reaches a plateau at around 100 N/mm³. All of the results have the same failure mechanism compliant with the base model 2D-SI, which is the delamination of concrete-to-concrete interface starting from the joint until the end of coupling reinforcement and a flexural crack at the end of the coupling reinforcement reaching the top of the cast-in-situ layer.

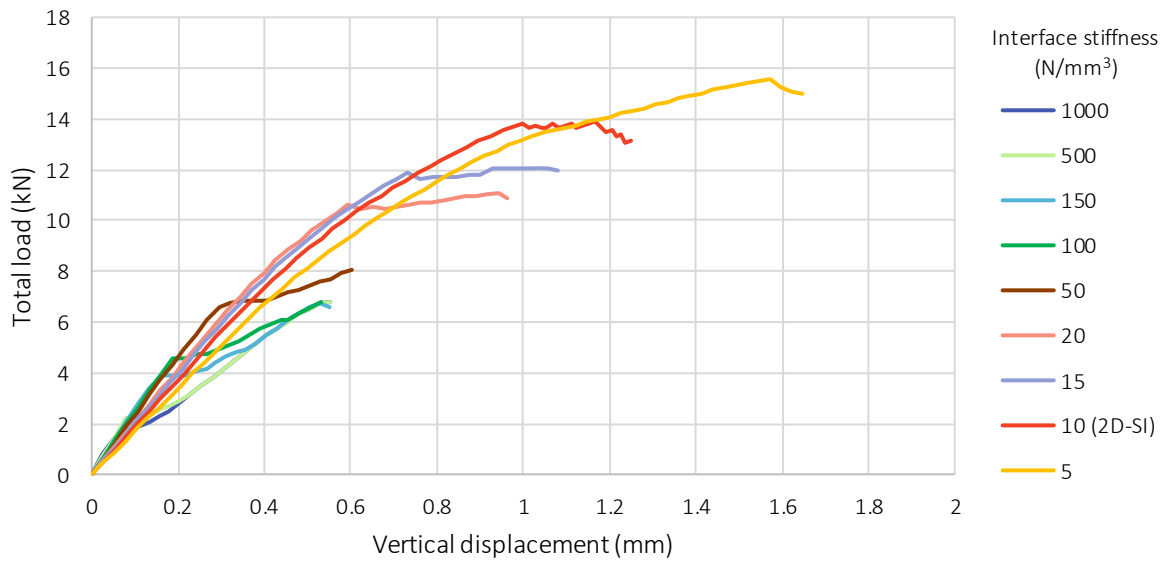


Figure 4.1 – Load-displacement graph of model 2D-SI with various interface stiffness

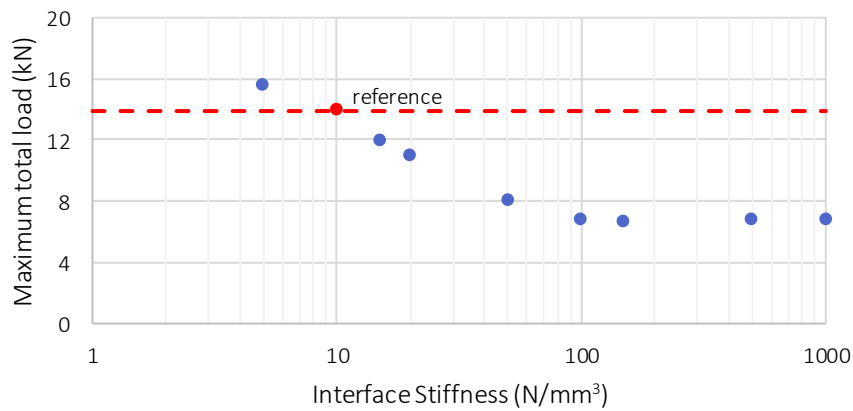


Figure 4.2 – Maximum total load-interface stiffness relationship based on model 2D-SI

The higher capacity in the model with lower interface stiffness is related to the resulted lower interface tensile stress (see Table 4.1) at the joint which location is shown in Figure 4.3. With lower interface tensile stress, the delamination crack occurs later compared to the model with higher interface stiffness and accordingly higher tensile stress, thus delaying the failure of the structure and resulting in higher load and displacement capacity. The relation between the interface tensile stress and the failure of model 2D-SI is discussed further in chapter 5.1.1.



Figure 4.3 – Interface tensile stress of base model (2D-SI) with interface stiffness 10 N/mm³ at vertical displacement 0.5 mm

In Table 4.1, the interface tensile stress at the joint of models with different interface stiffness are compared at 0.5 mm vertical displacement. Zero tensile stress at the models means the delamination crack has been started before 0.5 mm displacement.

Table 4.1 – Interface tensile stress at the joint at 0.5 mm vertical displacement

Interface stiffness (N/mm ³)	5	10	15	20	50	100	150	500	1000
Interface tensile stress (MPa)	0.19	0.32	0.42	0.49	0	0	0	0	0

4.1.2. Interface tensile strength

With the variation of interface tensile strength (tension cut-off value), the load and displacement capacity are changed but the stiffness of the structure remains the same. In general, the higher the interface tensile strength, the higher the load and displacement capacity as can be seen in Figure 4.4, though this relation becomes less prominent in lower and higher values of interface tensile strength as shown in Figure 4.5. All of the results also have the same failure mechanism as the base model 2D-SI.

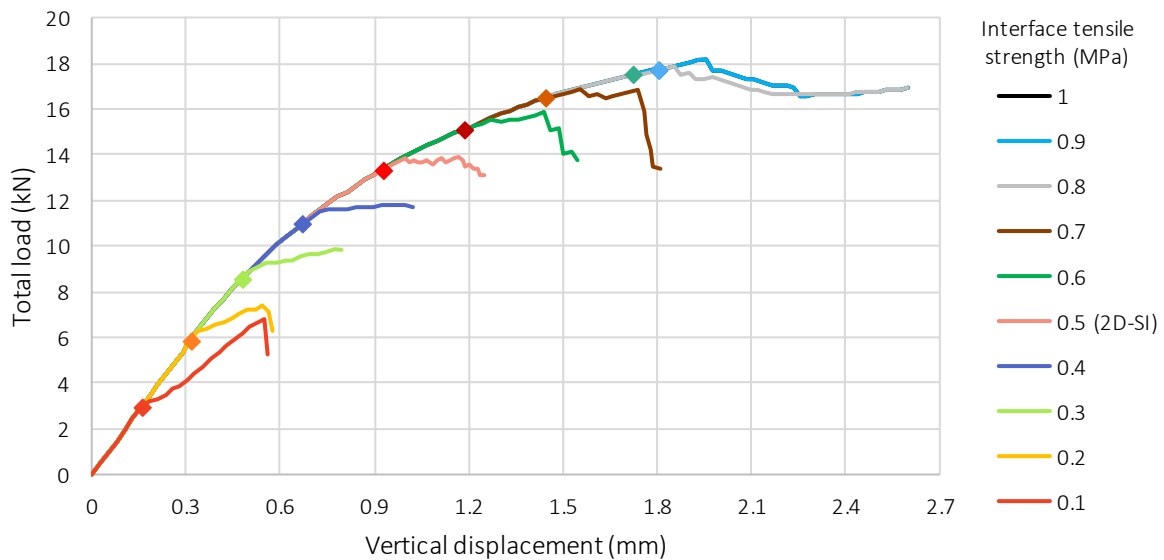


Figure 4.4 – Load-displacement graph of model 2D-SI with various interface tensile strength with markers indicating the start of horizontal crack at the joint

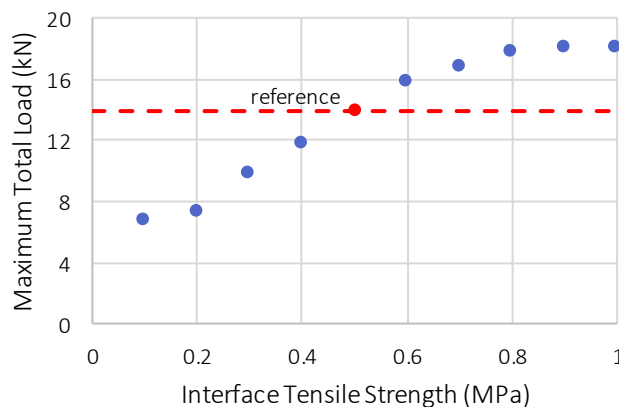


Figure 4.5 – Maximum total load-interface tensile strength relationship based on model 2D-SI

With higher interface tensile strength, the interface capacity to bear the peeling force is higher, thus resulted in higher load and displacement capacity, although this relation is less prominent in very low

and very high interface tensile strength. The more in-depth analysis about the relation between the interface tensile stress and the failure of model 2D-SI is discussed further in chapter 5.1.1.

4.1.3. Cohesion

In contrast to the previous 2 interface parameters, with the variation of the cohesion parameter, the load and displacement capacity remains the same with some exception for the lower cohesion values as shown in Figure 4.6 and Figure 4.7. All of the results also have the same failure mechanism as the base model 2D-SI.

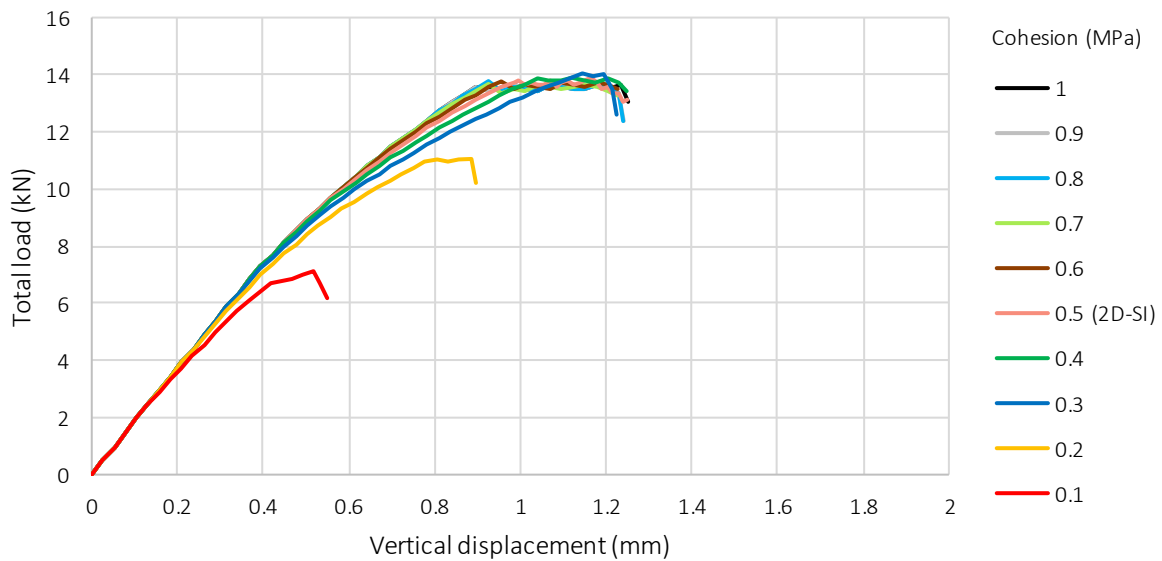


Figure 4.6 – Load-displacement graph of model 2D-SI with various cohesion

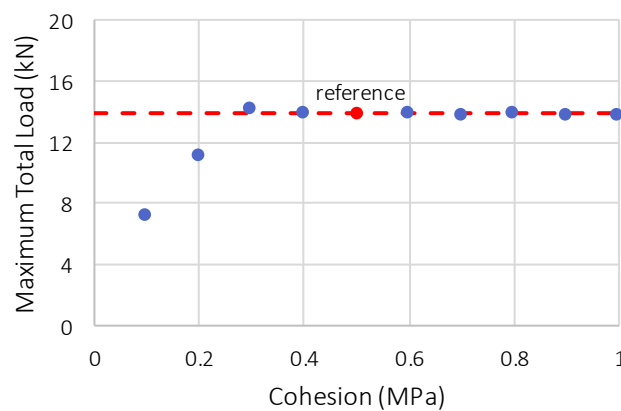


Figure 4.7 – Maximum total load-cohesion relationship based on model 2D-SI

From Figure 4.7, it can be seen that there is barely any influence of the cohesion to the failure. The investigation about this relationship is discussed more in chapter 5.1.1. However, there is an exception of result for cohesion below the 0.3 MPa which has lower capacity for the lower cohesion value. This behaviour at low cohesion value can be explained by the relation between the cohesion and the Coulomb friction failure criteria. In the description about the interface model which is used in model 2D-SI in chapter 3.2.2, the model uses the Coulomb friction model with tension cut-off. It means that the interface tensile strength used in the model limits the maximum tensile stress of the interface. However, as shown in Figure 4.8, at a low cohesion value, the failure line will be shifted closer to the x-

axis, which results in the lower maximum tensile stress, even lower than the prescribed interface tensile strength. As shown in Figure 4.5, lower interface tensile strength limit results in lower capacity, which explains the behaviour for the lower cohesion values. The relation between the cohesion and failure is discussed more in chapter 5.1.1.

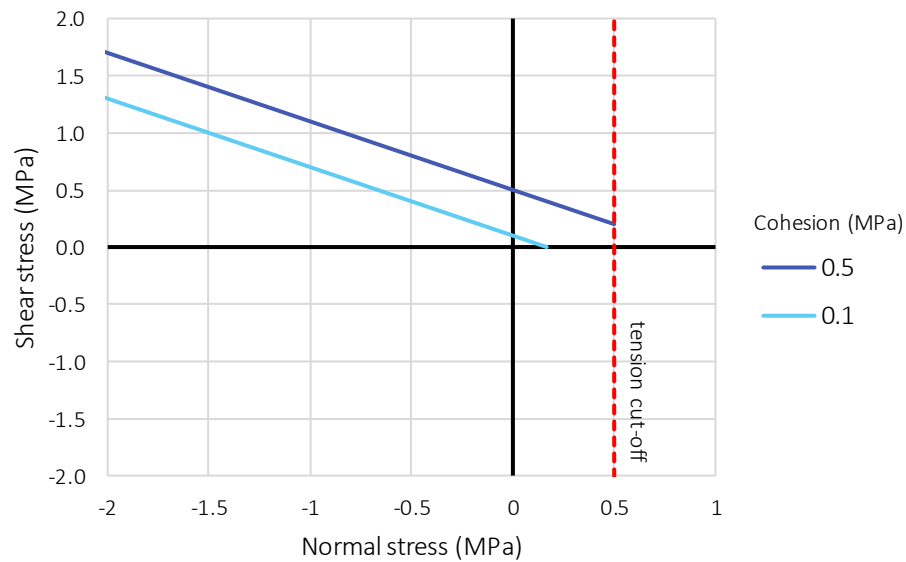


Figure 4.8 – Comparison of Mohr-Coulomb failure envelope of model 2D-SI with cohesion 0.1 MPa and 0.5 MPa (reference)

4.1.4. Friction angle

Similar to the cohesion, with the variation of the friction angle, the load and displacement capacity remain the same with some exception in the higher values as shown in Figure 4.9. All of the results also have the same failure mechanism as the base model 2D-SI.

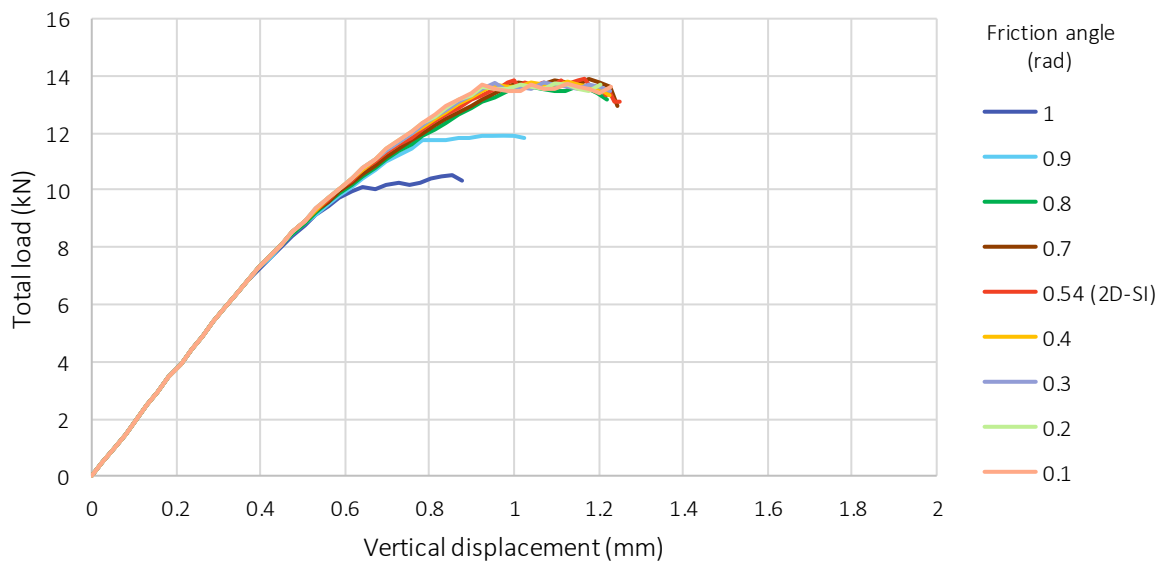


Figure 4.9 – Load-displacement graph of model 2D-SI with various friction angle

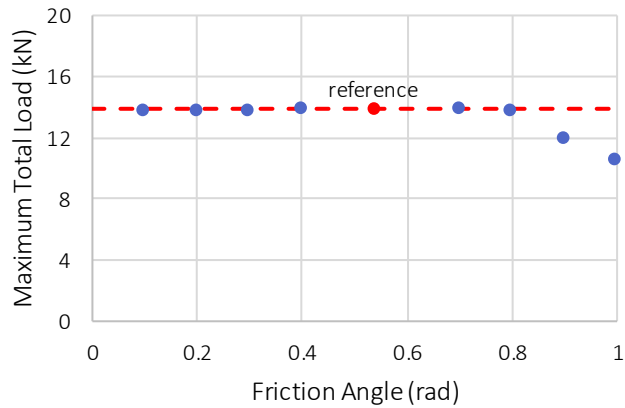


Figure 4.10 – Maximum total load-friction angle relationship based on model 2D-SI

From Figure 4.10, it can be seen that the friction angle has not much influence on the capacity of the models based on 2D-SI. However, there is an exception for friction angles above 0.8 rad which have lower capacity with the higher friction angle value. The behaviour at higher friction angles can be explained by the relation between the friction angle and the Coulomb friction failure criteria, which is similar to the explanation in chapter 4.1.3. As shown in Figure 4.11, with higher friction angle, the failure line has a higher gradient and intersect the x-axis at a lower value, which results in the lower maximum tensile stress, even lower than the prescribed interface tensile strength. As shown in Figure 4.5, a lower interface tensile limit results in lower capacity, which explains the behaviour for the higher friction angle values.

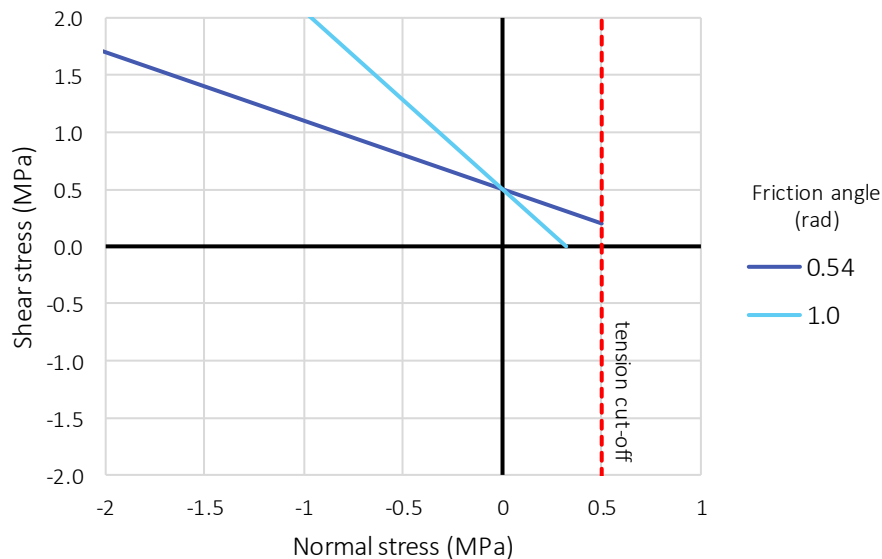


Figure 4.11 – Comparison of Mohr-Coulomb failure envelop of model 2D-SI with friction angle 1.0 rad and 0.54 rad (reference)

4.2. Reinforced interface beams

The second sensitivity study of interface parameters are based on model 2D-SI-SJ, the model with rectangular stirrup near the joint, which reproduces the experimental result of Sample 7 [1]. The finite element model and its numerical setup have been explained in chapter 3.2, while its result is described in chapter 3.3.2. Similar to the first sensitivity study, each interface parameter is varied independently from other parameters and its results are discussed in the following chapters.

4.2.1. Interface stiffness

With the variation of interface stiffness (both normal and shear), the load capacity and the stiffness of the structure do not change much as shown in Figure 4.12, although Figure 4.13 shows a slight decrease of load capacity with higher interface stiffness value. All of the results have the same failure mechanism as the base model 2D-SI-SJ although with a different length of interface delamination.

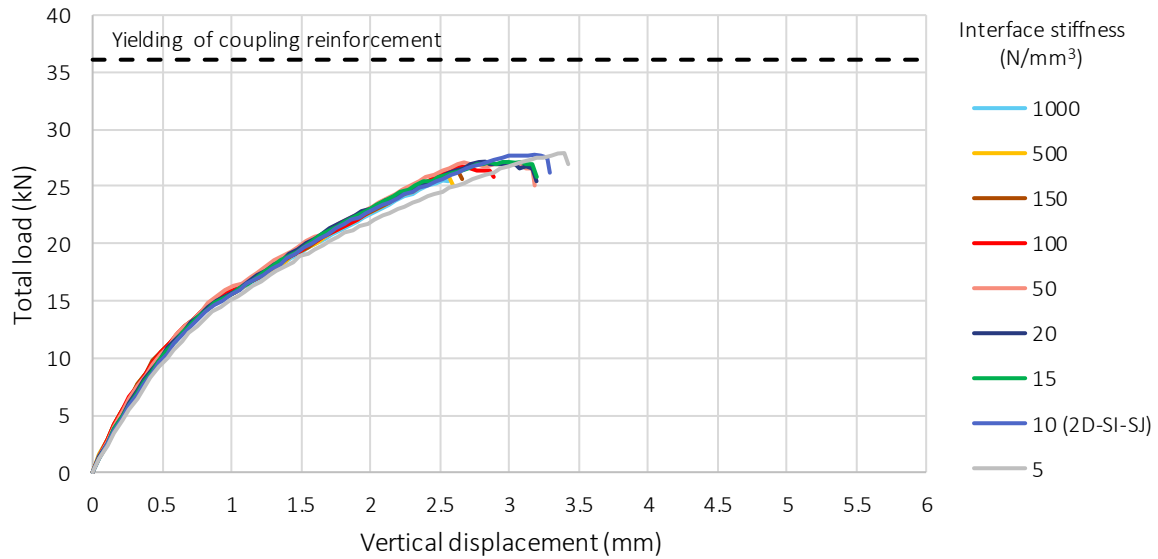


Figure 4.12 – Load-displacement graph of various interface stiffness based on model 2D-SI-SJ

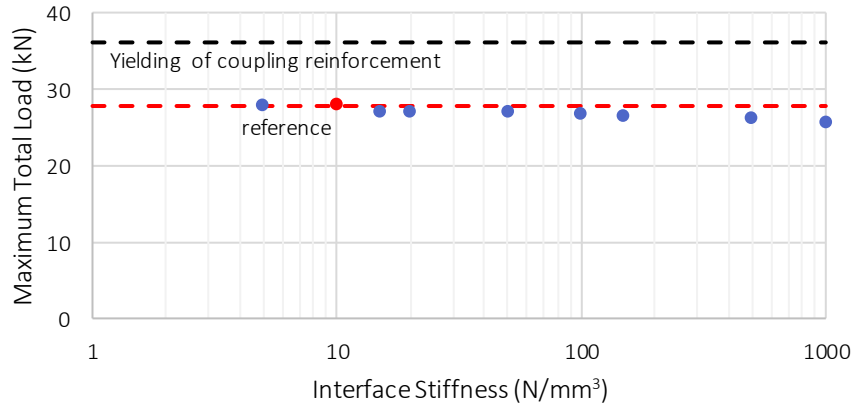


Figure 4.13 – Maximum total load-interface stiffness relationship based on model 2D-SI-SJ

4.2.2. Interface tensile strength

Similar to the interface stiffness parameter, with the variation of the interface tensile strength, the load capacity changes not much as shown in Figure 4.14. All of the results also have the same failure mechanism as the base model 2D-SI-SJ.

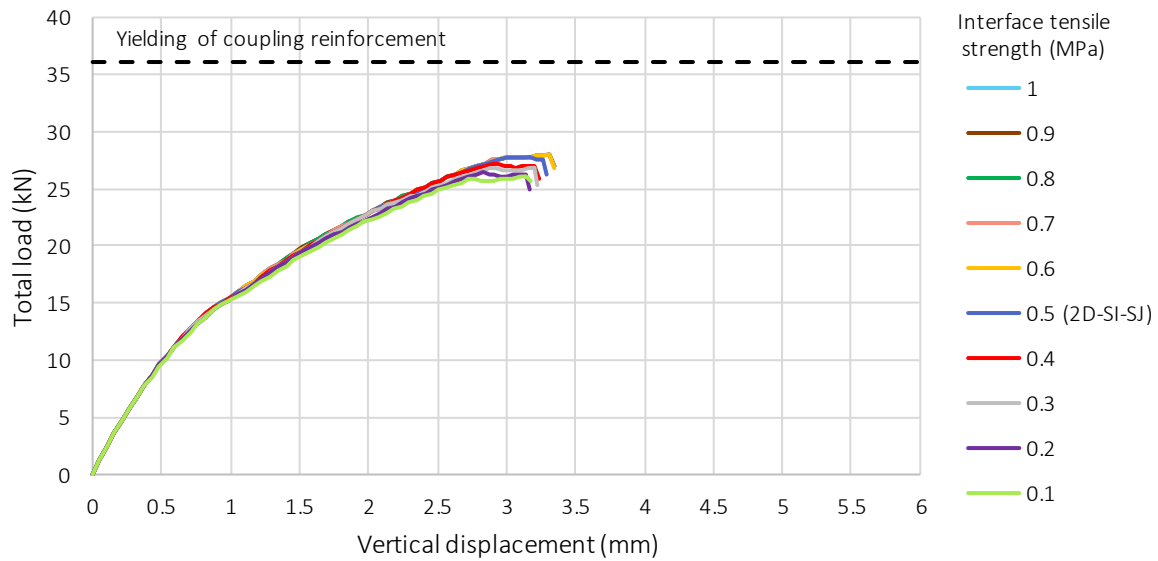


Figure 4.14 – Load-displacement graph of various interface tensile strength based on model 2D-SI-SJ

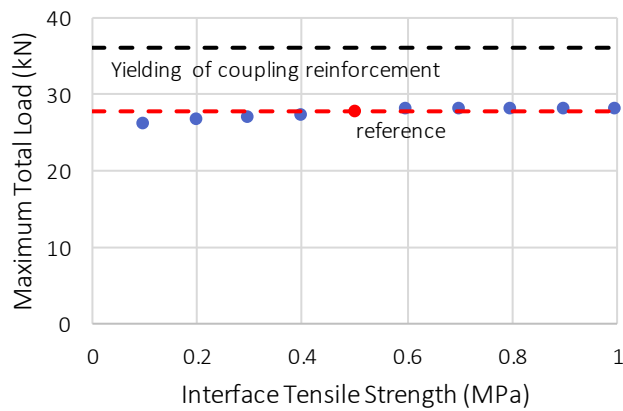


Figure 4.15 – Maximum total load-interface tensile strength relationship based on model 2D-SI-SJ

In contrast to the model without connecting rebar which is based on model 2D-SI, here there is barely any influence of interface tensile strength. There is only a slight increase of capacity with higher interface tensile strength values as shown in Figure 4.15. It is related to the presence of connecting rebar which restrict the delamination progress. The relation between the interface tensile strength and the capacity of the model is discussed further in chapter 5.2.1.

4.2.3. Cohesion

By varying the cohesion parameter, the load and displacement capacity change. The higher the cohesion value, the higher the load capacity as can be seen in Figure 4.16 and Figure 4.17. With 0.9 MPa of cohesion or higher, the failure of the beam reaches the yielding of coupling reinforcement. All of the results again have the same failure mechanism as the base model 2D-SI-SJ.

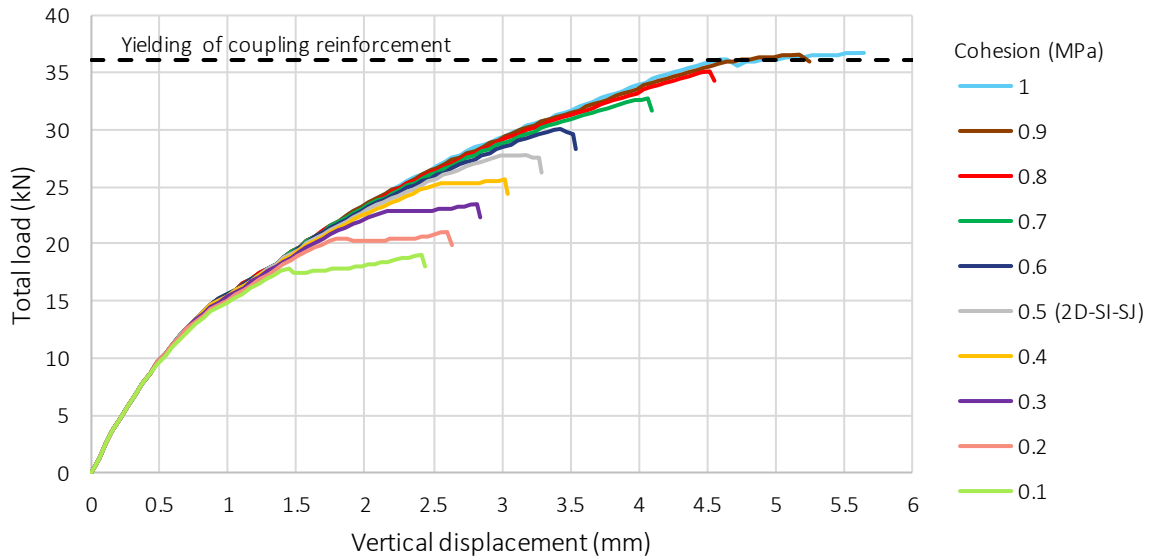


Figure 4.16 – Load-displacement graph of various cohesion based on model 2D-SI-SJ

With higher cohesion, the interface shear strength increases thus delaying the delamination progress. With a longer part of the interface still intact, the load transfer between the concrete layers keeps increasing. The more in-depth analysis about the relation between the cohesion and the load capacity of model 2D-SI-SJ is discussed further in chapter 5.2.1.

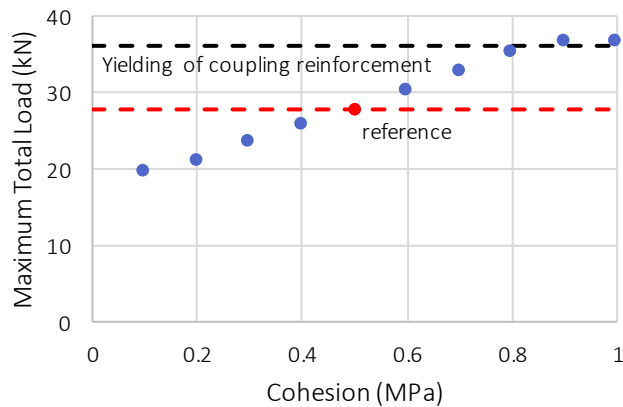


Figure 4.17 – Maximum total load-cohesion relationship based on model 2D-SI-SJ

4.2.4. Friction angle

With the variation of the friction angle, the load capacity is changes not much. There is only a slight increase of load capacity with higher friction angle values as shown in Figure 4.18 and Figure 4.19. All of the results have the same failure mechanism as the base model 2D-SI-SJ.

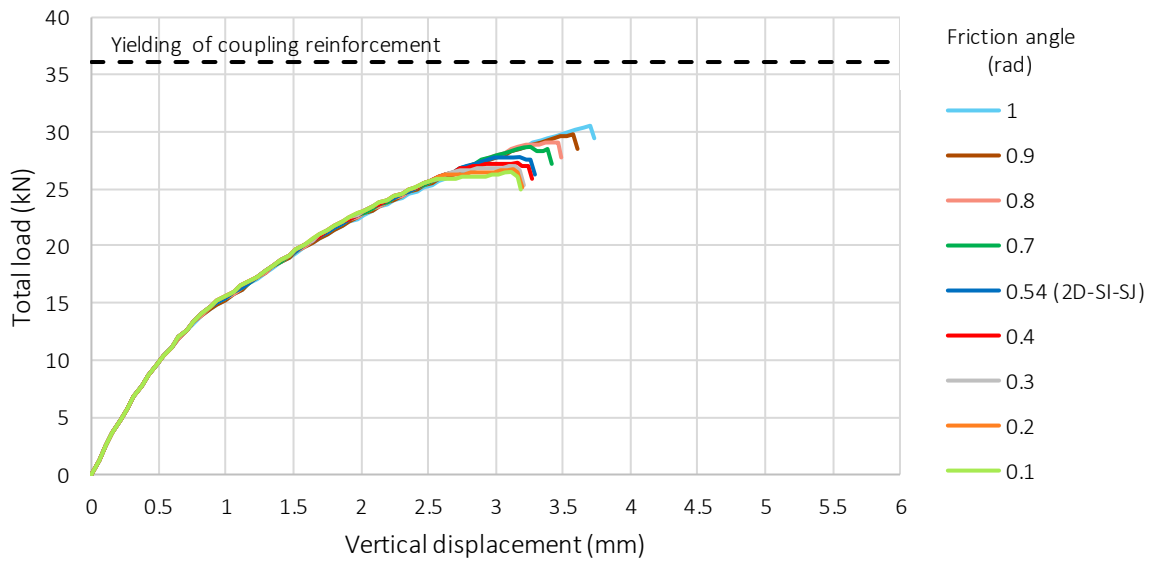


Figure 4.18 – Load-displacement graph of various friction angle based on model 2D-SI-SJ

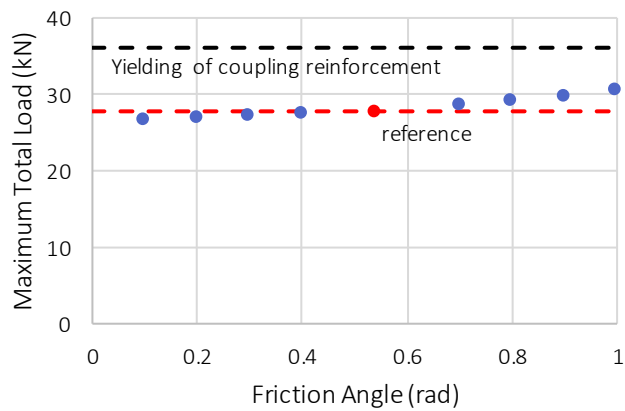


Figure 4.19 – Maximum total load-friction angle relationship based on model 2D-SI-SJ

4.3. Summary

From the sensitivity analyses, two different results are obtained. In the first analysis based on unreinforced interface beam (model 2D-SI), the interface stiffness and interface tensile strength are the two governing parameters. The higher the interface stiffness, the lower the capacity in logarithmic scale until it reaches a plateau at 100 N/mm^3 , while the higher the interface tensile strength, the higher the capacity in relatively linear relationship, though this relation becomes less prominent in lower and higher values. Within the range of those parameters, the load capacity is increased and decreased by more than 50% in compared to the parameters used in the reference model 2D-SI. The more in-depth analysis about the relation between the tensile stress and the failure is discussed in chapter 5.1.1.

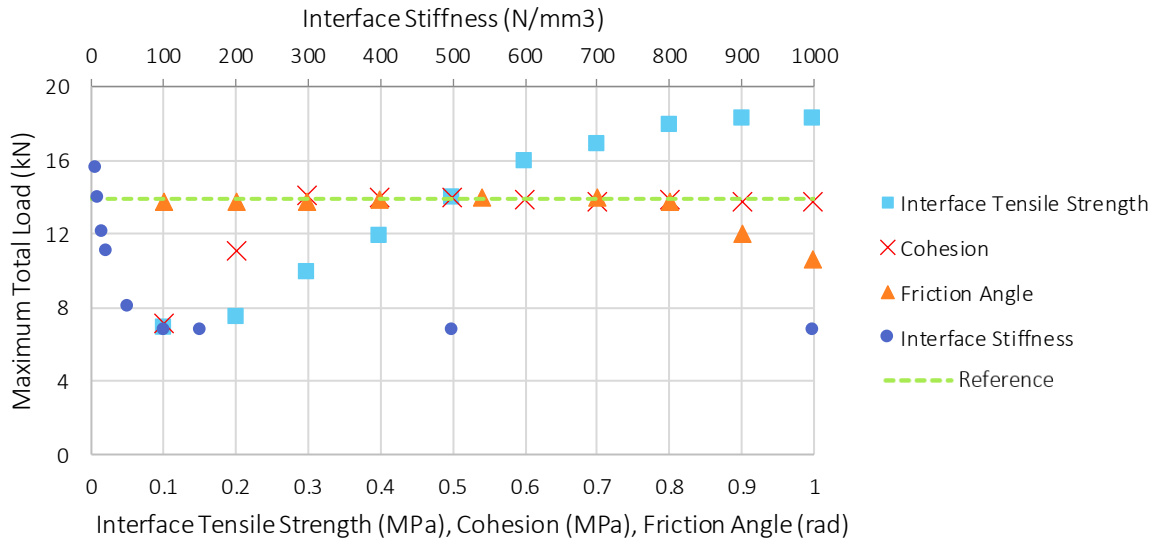


Figure 4.20 – Maximum total load-interface parameters relationship of unreinforced interface beam based on model 2D-SI

The second analysis is based on reinforced interface beam (model 2D-SI-SJ), which in general is the same specimen as the unreinforced interface beam of model 2D-SI with additional rectangular stirrup near the joint. By adding the stirrup, the cohesion becomes the governing parameter and the variability of the results decrease. In general, the higher the cohesion, the higher the capacity, until it reaches the failure of yielding reinforcement at 0.9 MPa of cohesion. Within the range of the cohesion, the load capacity was increased and decreased up to 30% in compared to the parameters used reference model. The more in-depth analysis about the relation between the cohesion and the failure is discussed in chapter 5.2.1.

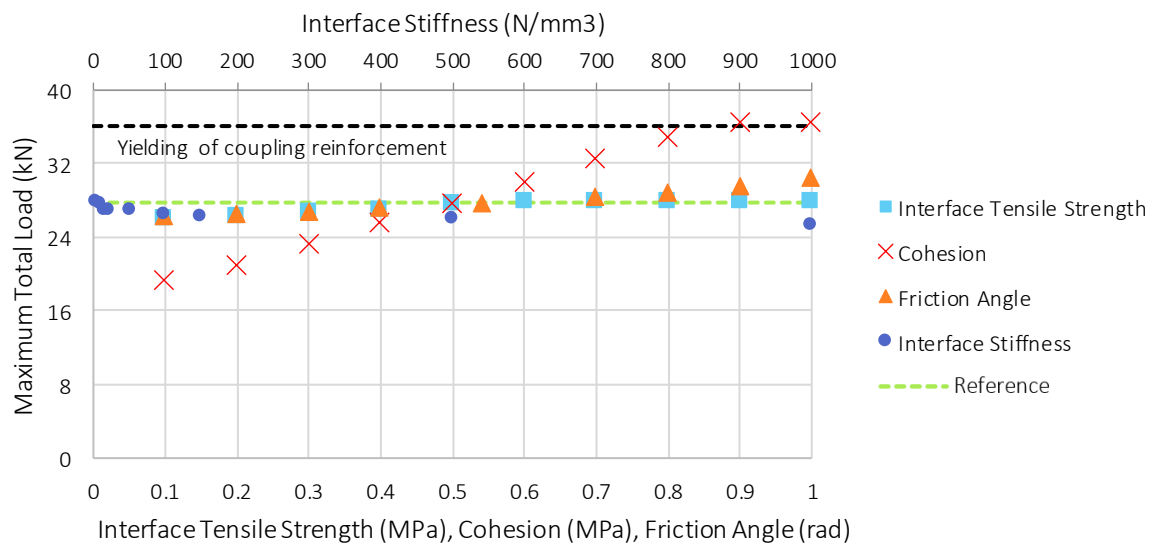


Figure 4.21 – Maximum total load-interface parameters relationship of reinforced interface beam based on model 2D-SI-SJ

However, there are several things that should be noted for these analyses:

- The sensitivity analysis of interface parameters in unreinforced interface beam is based on model 2D-SI which is verified with Sample 1 [1] in chapter 3.3.1, while the analysis in reinforced

interface beam is based on model 2D-SI-SJ which is verified with Sample 7 [1] in chapter 3.3.2. Therefore, the results of these sensitivity studies are related to these base models.

- Each parameter is varied independently or assumed not to be related to one another
- Models with connecting reinforcement do not include the reinforcement bond-slip model for the rebars, thus the possible pull-out failure of connecting reinforcement is not considered in the analyses
- The results of the sensitivity analyses which have been done with numerical simulation must be verified with the experimental results

From the sensitivity analyses, several governing parameters were found influencing the interface behaviour of unreinforced and reinforced interface beams. Since these parameters are related to the actual interface type or surface roughness, then a different interface type can lead to a different interface behaviour. Therefore, it is important to include different interface types to study the interface behaviour in the next chapter. However, due to the limited time and resources, only two different interface types are chosen to be used for the following studies. These interface types are “smooth interface” which parameters are used in the reference beams model 2D-SI and 2D-SI-SJ (Table 3.11) and “perfect bonded interface” which uses a rigid connection between two concrete layers elements. These interface types are chosen to simulate a weak and ideal bond of concrete-to-concrete interface.

| 5 | NUMERICAL RESULTS AND DISCUSSIONS

This chapter aims to bring together the topics studied in chapter 3 and 4 by answering the remaining supporting questions and the main research questions. In order to do this, the results of the numerical models are analysed. There are three main topics which are discussed in three subchapters. First, models of unreinforced interface beams which include the variation in lap splice spacing to discuss the first supporting research question. Second, models of reinforced interface beams which include the variation in connecting reinforcement spacing to discuss the second supporting research question. Third, models of unreinforced interface beams with additional lateral restraint to discuss the additional supporting research question.

As a result of the sensitivity study of interface parameters in chapter 4.1 and chapter 4.2, two types of concrete-to-concrete interface are included in each analyses, the smooth interface which Coulomb friction parameters are presented in Table 3.11 and the perfect bonded interface which is modelled by connecting the nodes of both concrete layers directly to each other. These two types of interfaces are studied to understand the interface behaviour in two different extremes, thus a more elaborate result can be captured.

5.1. Unreinforced interface beams

In the first part of this section, the results and analysis of the models which represent the experimental setup of Sample 1 [1] are discussed. In the second part, to understand the influence of lap splices spacing (in longitudinal direction of precast segments) on the interface behaviour, the number of lap splices (coupling reinforcement and bottom reinforcement) are reduced from three into a single one while maintaining the total area of the reinforcements. By reducing the number of the connecting reinforcement and the bottom reinforcement across the width of the model, effectively the transverse distance between lap splices is increased. By maintaining the total reinforcements area, the yield strength of the models is also maintained.

5.1.1. Experimental lap splices setup

As explained in the opening of this chapter, there are two types of concrete-to-concrete interface which are used in each analyses, the untreated (smooth) interface and perfect bonded interface. The model with the first type of interface is model 3D-SI which finite element model, reinforcement setup, and the numerical setup are presented in chapter 3.2. The model with the second type of interface, model 3D-PB which has the same numerical setup as model 3D-SI. However, instead of using Coulomb friction interface, this model uses a rigid connection to connect the precast and cast-in-situ layer.

5.1.1.1. Smooth interface

In Figure 5.1, the load-displacement graph of model 3D-SI is shown. The maximum vertical load of the model is 14.36 kN. In that figure, the damage development of this model is marked at three load stages prior to the failure, so the interface behaviour can be analysed step-by-step. The damage development at each load stage can be observed in Figure 5.2. Load stage 1 is at the onset of a flexural crack at the joint, load stage 2 is right before the start of interface delamination at the joint, and load stage 3 is right before the failure when the interface delamination reaches the end of coupling reinforcement and the flexural crack at the end of coupling reinforcement reaches the top part of the cast-in-situ layer. The term “load stage” should not be confused with “load step” which is the load increment in the finite element model as described in Table 3.12.

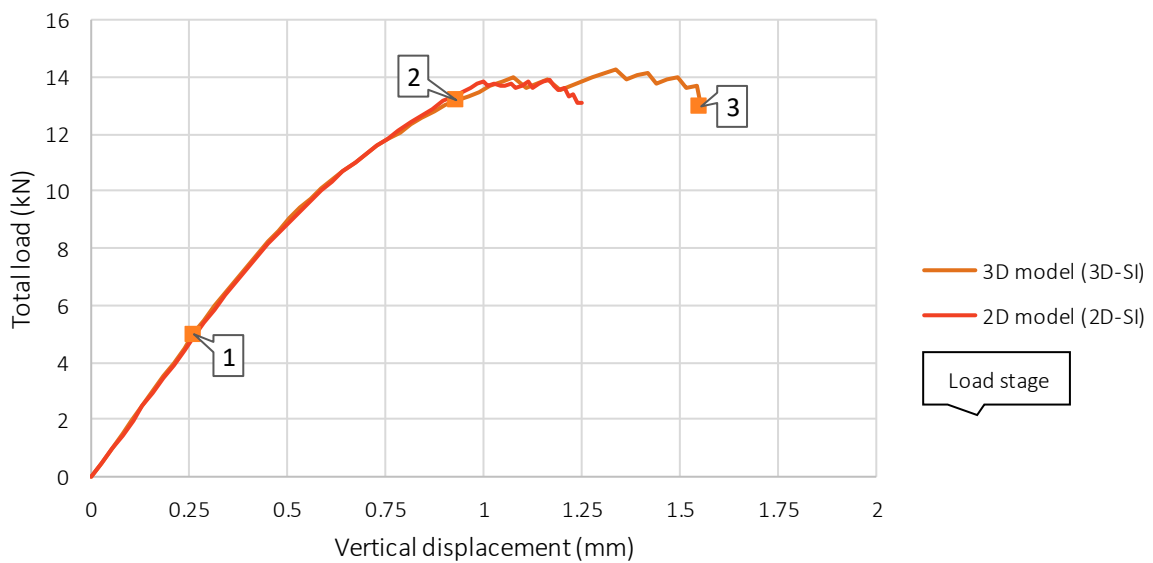


Figure 5.1 – Load-displacement graph of unreinforced interface model with smooth interface (2D-SI and 3D-SI)

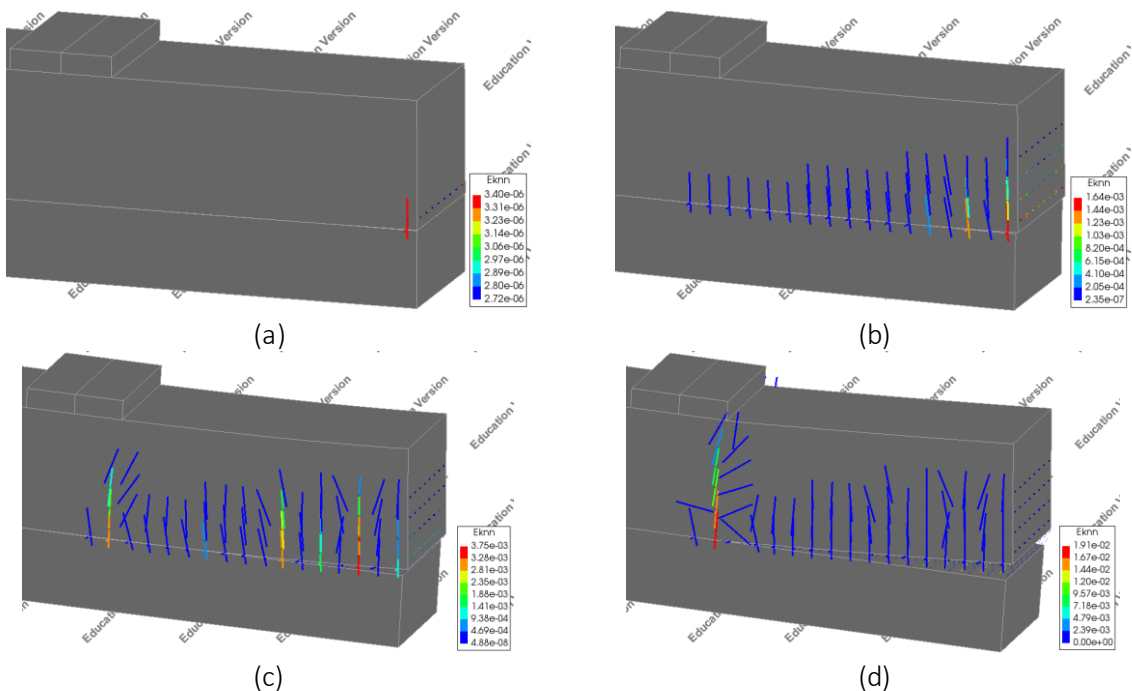


Figure 5.2 – Crack strain on the side of model 3D-SI at (a) load stage 1, (b) load stage 2, (c) load stage 3, (d) failure stage

Figure 5.3 indicates the location of the four nodes which interface stresses development are shown in Figure 5.4. The figure of interface stresses development is also marked with the three load stages which have been described before.

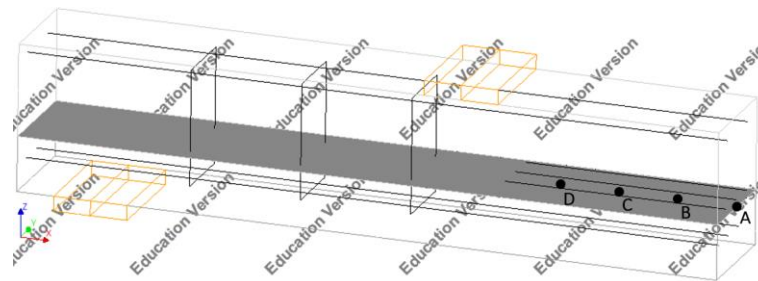


Figure 5.3 – Location of node A, B, C, and D for the interface stresses development analysis

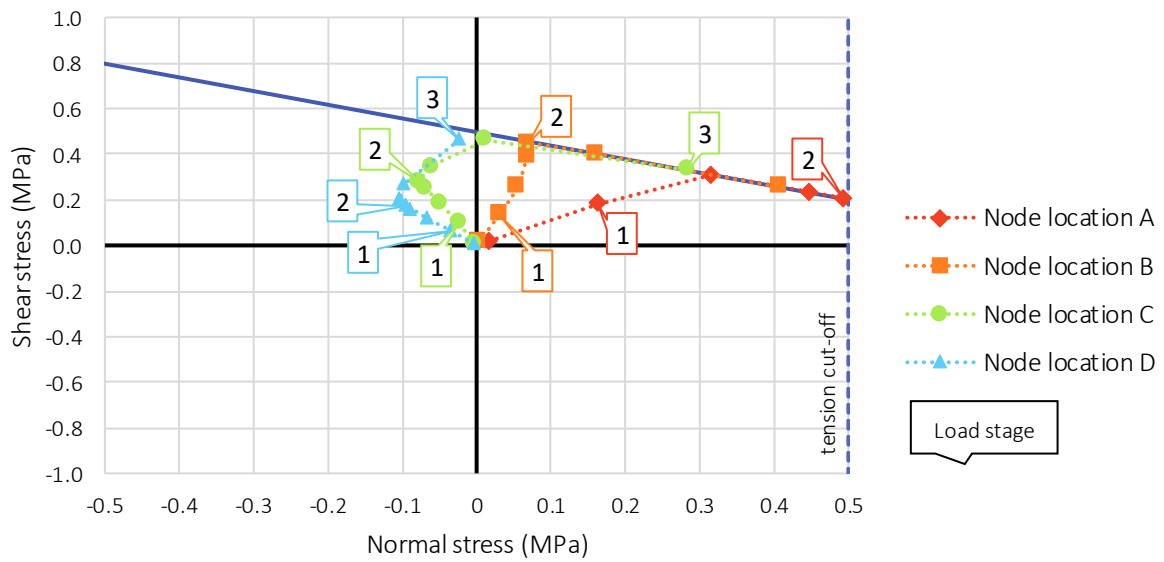


Figure 5.4 – Interface stresses development of model 3D-SI at four nodes location

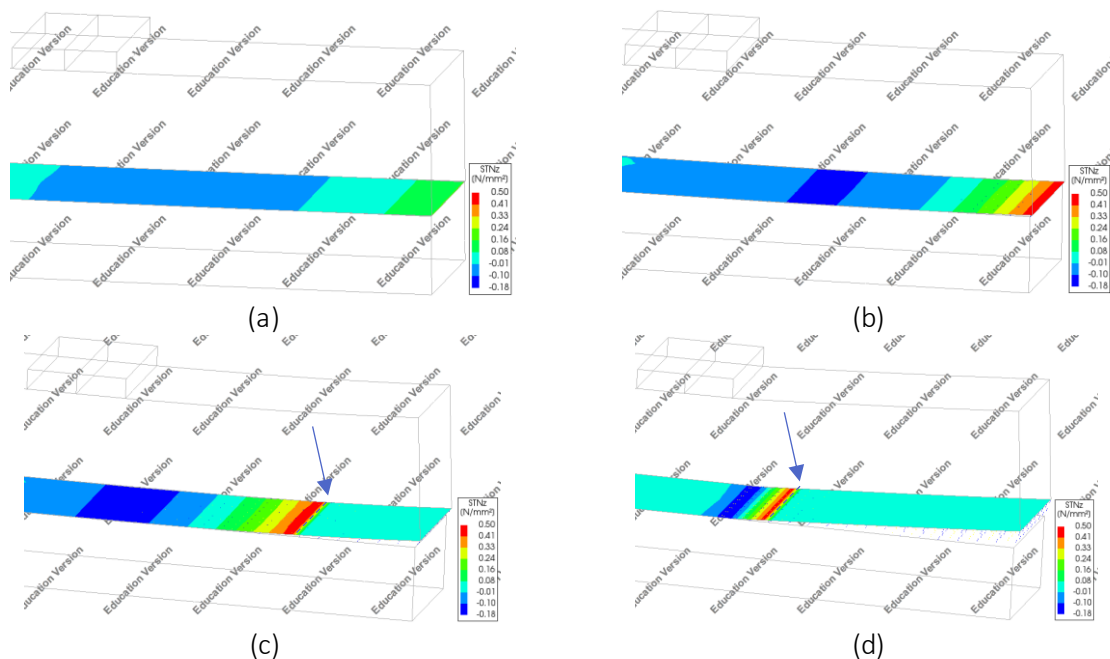


Figure 5.5 – Interface normal stress STN_z development of model 3D-SI at (a) load stage 1, (b) load stage 2, (c) load stage 3, (d) failure stage

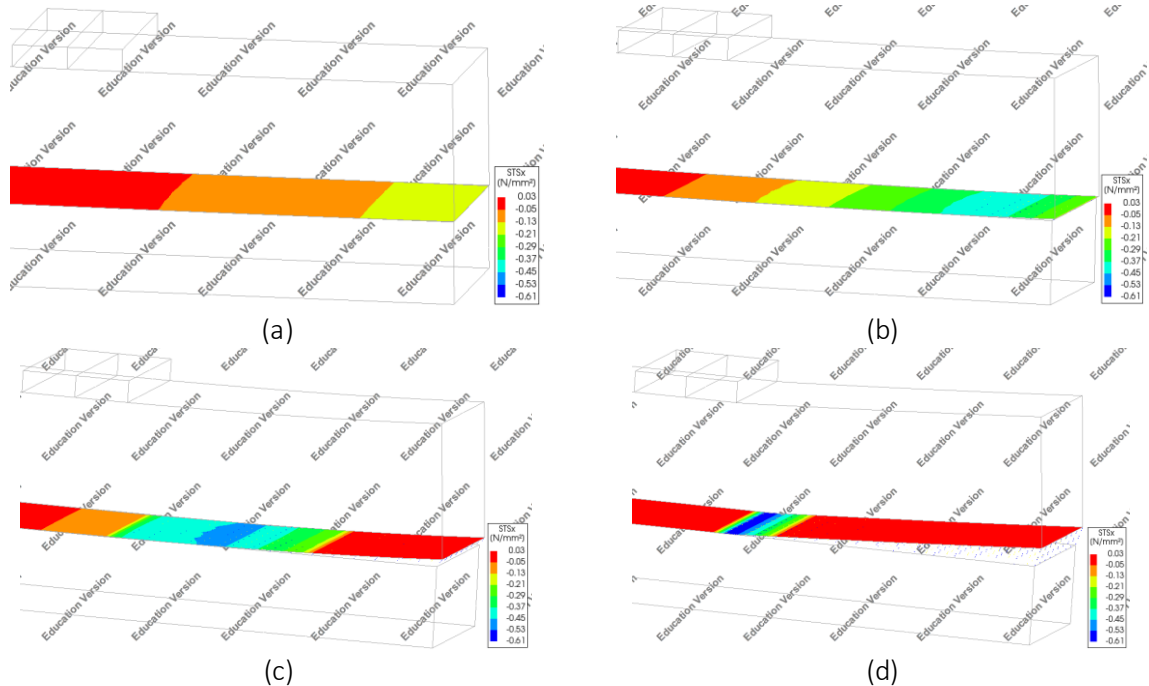


Figure 5.6 – Interface shear stress STS_x development of model 3D-SI at (a) load stage 1, (b) load stage 2, (c) load stage 3, (d) failure stage

At the beginning of the analysis, a stress concentration in longitudinal direction develops at that area indicated with a black dotted circle in Figure 5.7. This stress concentration is created by the transfer of the tensile force from the precast layer to cast-in-situ layer as shown in Figure 5.8. The eccentricity between the tensile force in the precast layer and the tensile force at the bottom part of the cast-in-situ layer induces the moment close to the joint. This moment causes a peak tensile stress at the joint and a compressive stress at a certain distance from the joint. This tensile and compressive stress at the beginning of analysis can be seen in Figure 5.9. The stress concentration at the joint is also reflected in the shear stress peak at the joint as shown in Figure 5.10. When the load reaches load stage 1, theoretically, the coupling reinforcement starts to take the tensile stress from the surrounding cracked concrete matrix. However, this situation is not observed in this model as can be seen in Figure 5.5 and Figure 5.6. Since this situation can be observed in the following chapter, this situation is discussed further in the following chapter.

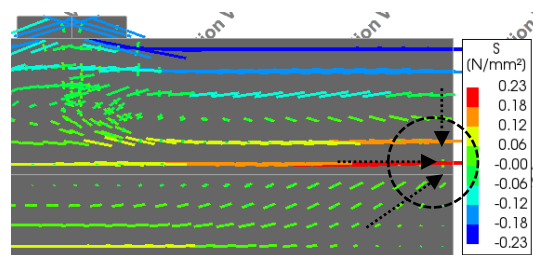


Figure 5.7 – Stress concentration around the joint at the beginning of the analysis of model 3D-SI

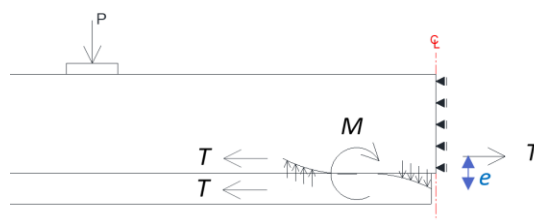


Figure 5.8 – Tensile force transfer and the resulted moment around the joint

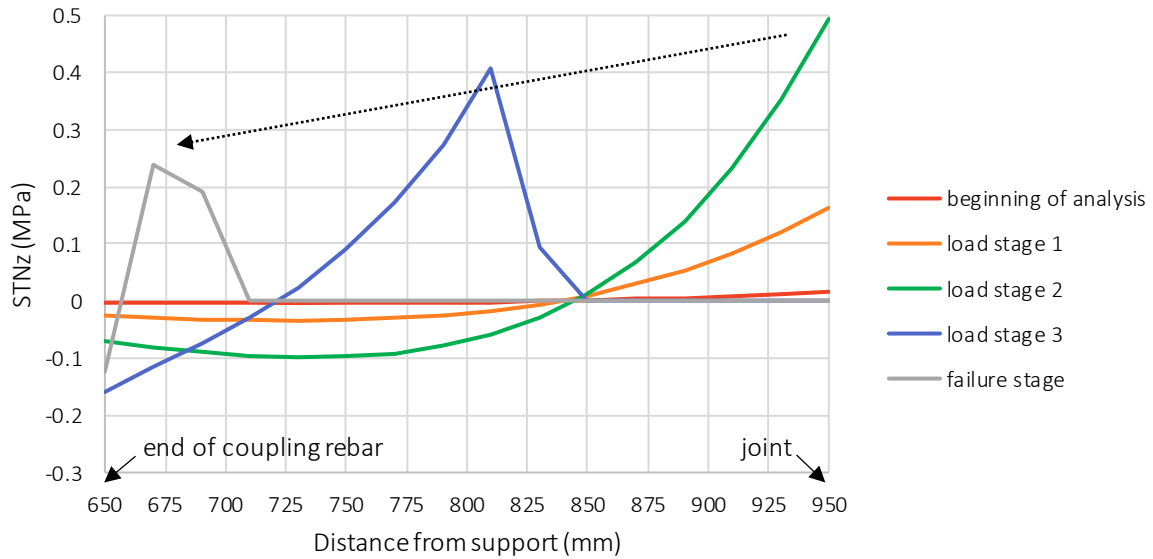


Figure 5.9 – Interface normal stress at the mid-section of model 3D-SI at different stages

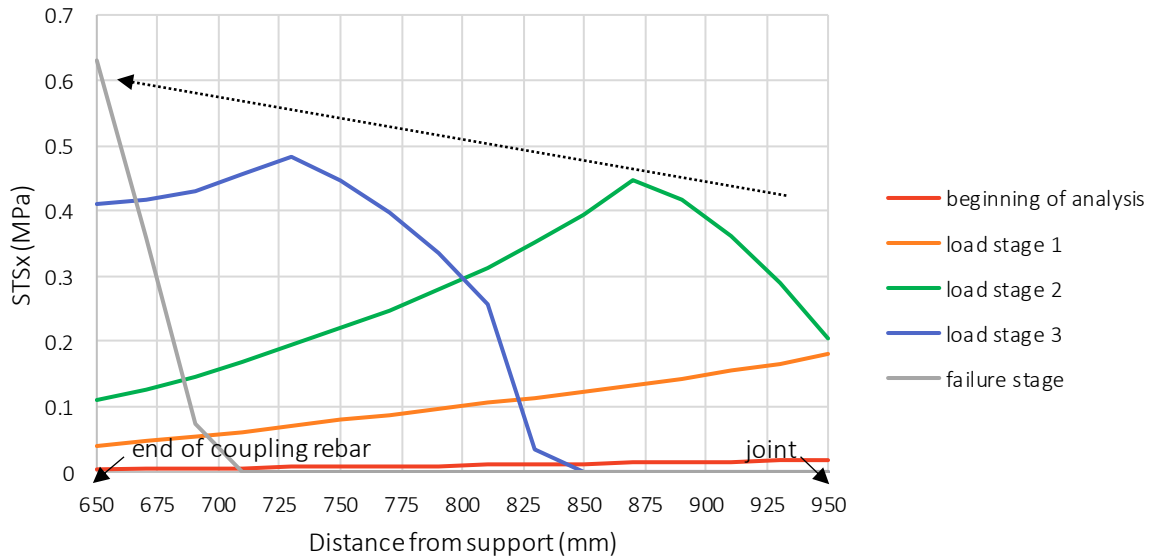


Figure 5.10 – Interface shear stress at the mid-section of model 3D-SI at different stages

Figure 5.4 shows that the tensile stress at node A and node B increases from load stage 1 to load stage 2, while the compressive stress at node C and node D also increases at the same time. As the load reaches load stage 2, the tensile stress at node A (the joint) reaches the interface tensile strength (cut-off limit), so that the delamination of the interface starts to occur at the joint (see Figure 5.2(b)). As shown in Figure 5.1, the maximum load is reached in a few load steps after load stage 2, when the delamination starts. This phenomenon can also be observed in sensitivity analysis of interface tensile strength which is indicated by the marks in Figure 4.4. Therefore, it explains why the interface tensile strength influence the load capacity of unreinforced interface beams as concluded in chapter sensitivity study.

With the increasing load, the horizontal crack grows along the interface as shown in Figure 5.2(c), not along the coupling reinforcement though the tensile stress is concentrated around the coupling reinforcement. This situation occurs due to the use of a weak Coulomb friction interface. Since the concrete-to-concrete interface has weaker strength in compared to the concrete elements around the coupling reinforcement, the interface is governing the horizontal crack development.

As the load increases, the peak of the tensile stress shifts towards end of coupling reinforcement as can be seen in Figure 5.9 and Figure 5.5. This shift can also be observed in Figure 5.4 as the stress development of point C changes its direction towards the x-axis positive direction after load stage 2. This is following the shift of shear stress peak in the same direction as can be seen in Figure 5.10 and Figure 5.6. However, the changes in the values of the peaks of tensile and shear stresses are not the same as they shift. This is indicated with the dotted arrows in Figure 5.9 and Figure 5.10. The trend of the interface tensile stress peak is decreasing while the trend of the interface shear stress is increasing. This can also be observed in Figure 5.4 as the further the node is located from the joint, the bigger the shear influence on the failure of the interface at the corresponding node. As can be seen in the load-displacement graph in Figure 5.1, these nodes with bigger shear influence do not hinder the delamination process much. Because, after load stage 2, the start of the delamination, the increase of load capacity of the model is really small. Therefore, it is in accordance with the result of sensitivity analysis in chapter 4.1 where cohesion and friction angle do not affect the load capacity of the structure.

When the load reaches load stage 3, the peaks of tensile and shear stresses have shifted closer to the end of coupling reinforcement following the delamination progress. When failure occurs, the delamination (horizontal crack at interface level) reaches the end of coupling reinforcement and the large flexural crack reaches the top of the cast-in-situ layer.

From Figure 5.5 and Figure 5.6, there is almost no stress concentrations in transverse direction observed at any load stages, both for normal stress and for shear stress. Figure 5.5 also shows that the horizontal crack propagation along the interface is uniform as indicated by the blue arrows pointing to the blue dashed line. In other words, the stress distribution and the horizontal crack propagation of this model across the width are uniform. In compared to the 2D model (2D-SI), by using a plane stress element in the specimen, the stress distribution and the horizontal crack propagation across the width are assumed to be uniform. Thus, both 2D and 3D model (experimental lap splice setup) of unreinforced interface beams with smooth interface have similar interface behaviour across the width. In Figure 5.1, it is also observed that there is no significant difference between these models in terms of load capacity and load-displacement behaviour. Therefore, the similar interface behaviour could be the cause of the similar capacity of these models. The influence of the interface behaviour of the specimen on the capacity is discussed further in the following chapter.

5.1.1.2. Perfect bonded interface

In Figure 5.11, the load-displacement graph of unreinforced interface model with perfect bonded interface (3D-PB) is shown. The maximum vertical load of this model is 22.33 kN, which is 57% higher than the model with smooth interface (3D-SI). In that figure, the damage development of this model is marked at four load stages prior to the failure. The damage development of this model can be observed in Figure 5.12. Load stage 1 is at the onset of a flexural crack at the joint, load stage 2 is at the start of an observed uneven stress distribution in transverse direction, load stage 3 is right before the start of horizontal crack at the joint, and load stage 4 is right before the failure. This model fails in a similar way as the model with the smooth interface. However, instead of a horizontal crack along the interface (delamination), this model develops a horizontal crack along the coupling reinforcement. It means that this model fails when the horizontal crack along the coupling reinforcement reaches the end of that reinforcement and the flexural crack at the end of that reinforcement reaches the top of the cast-in-situ layer.

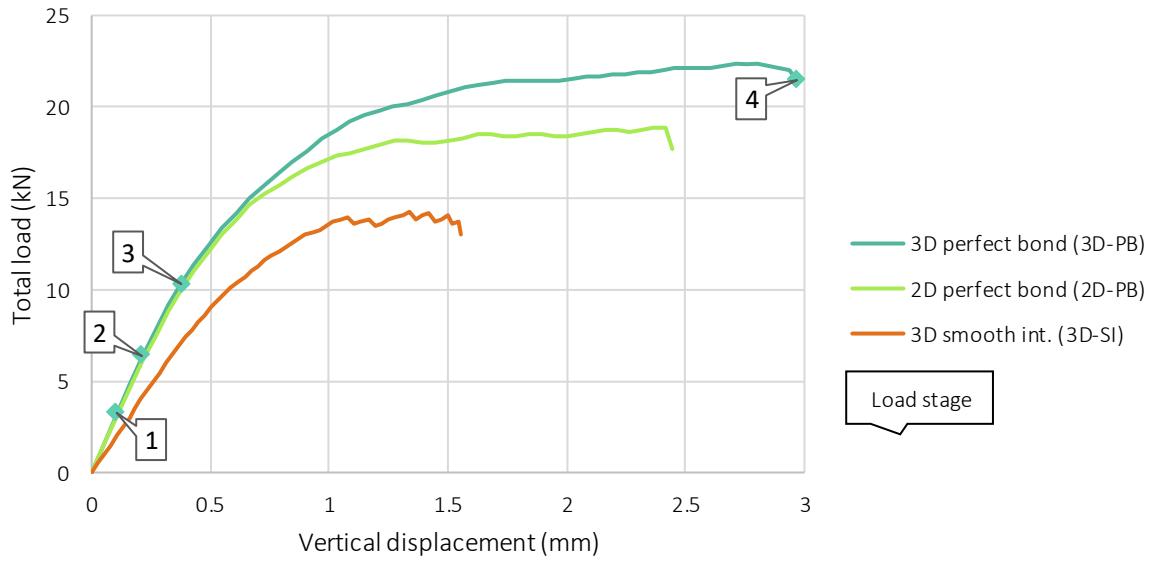


Figure 5.11 – Load-displacement graph of unreinforced interface model with perfect bonded interface (2D-PB and 3D-PB)

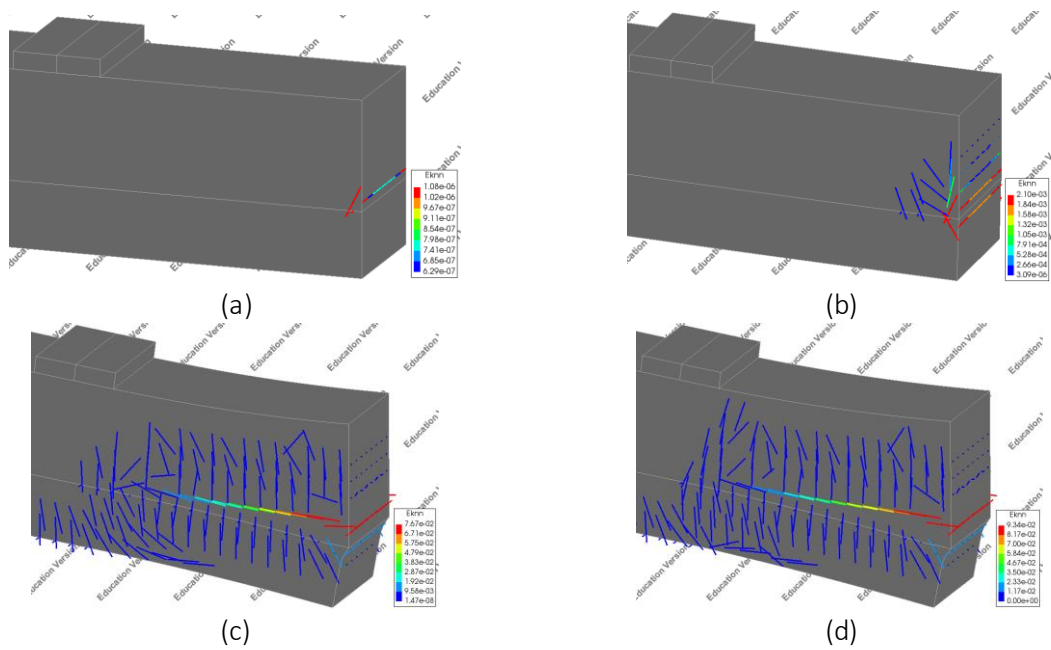


Figure 5.12 – Crack strain on the side of model 3D-PB
 (a) at load stage 1, (b) a few load step after load stage 3, (c) at load stage 4, (d) at failure stage

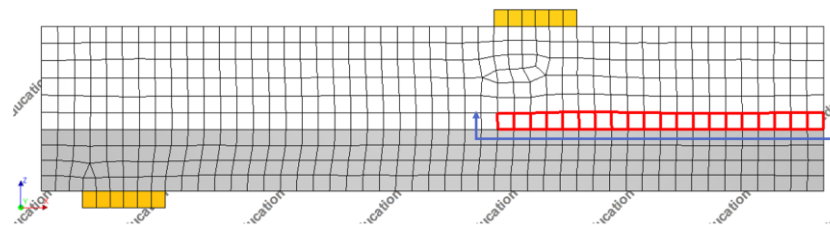


Figure 5.13 – Elements of interest at the level of coupling reinforcement for the stress and strain analysis of model with perfect bonded interface

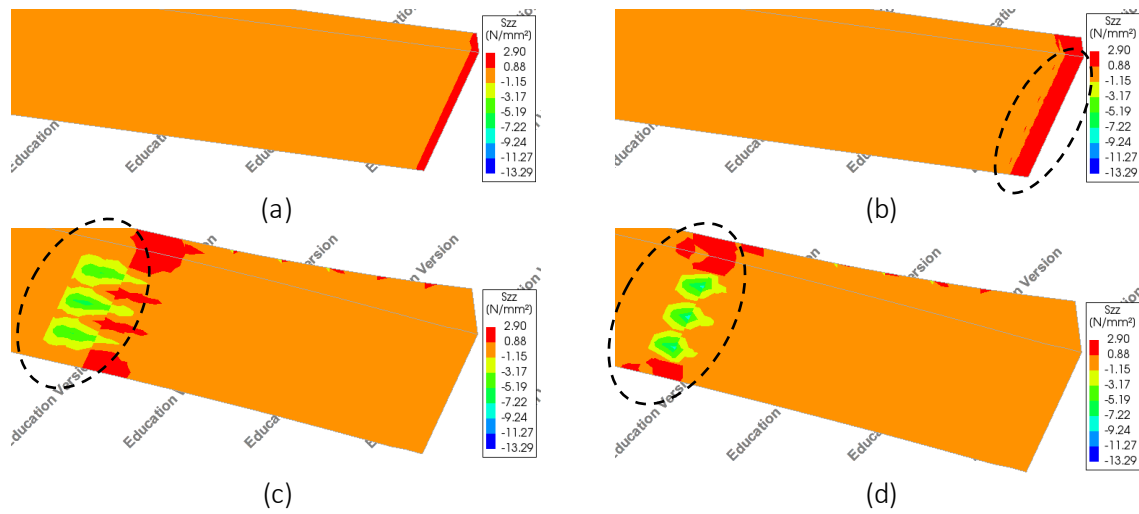


Figure 5.14 – Stress S_{zz} of the elements at the level of the coupling reinforcement of model 3D-PB (a) at load stage 1, (b) right after load stage 2, (c) at load stage 4, (d) at failure stage

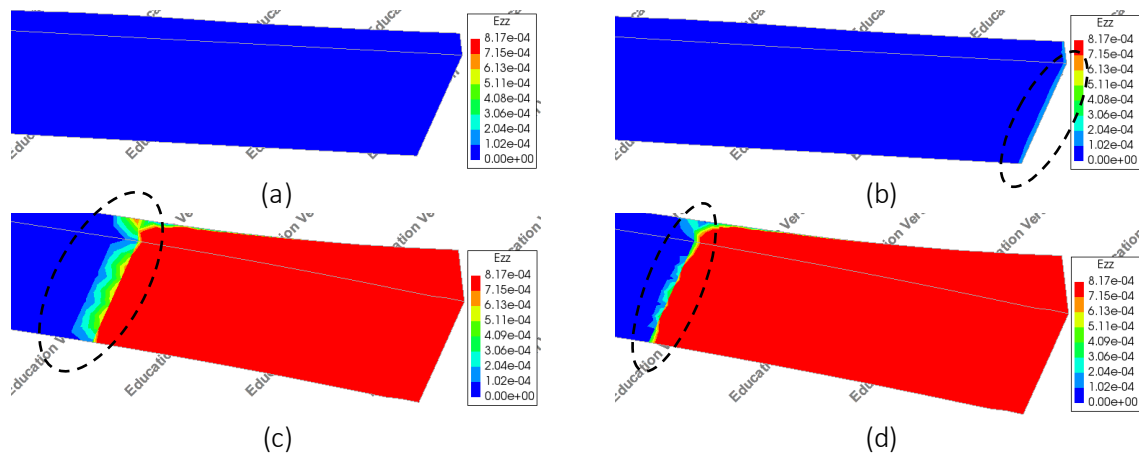


Figure 5.15 – Strain E_{zz} of the elements at the level of the coupling reinforcement of model 3D-PB (a) at load stage 1, (b) right after load stage 2, (c) at load stage 4, (d) at failure stage

At the beginning of this analysis, a stress concentration in longitudinal direction also occurs as in the model with smooth interface. This stress concentration is also reflected in a peak of tensile and shear stresses at the joint as in model 3D-SI. However, since in this model there is no Coulomb friction interface model and the horizontal crack is modelled with the continuum element itself (smeared crack), the cracks are governed only by the concrete tensile strength. Therefore, there is no interest to the shear stress along the coupling reinforcement.

When the load reaches load stage 1, the coupling reinforcement starts to take the tensile stress from the surrounding cracked concrete matrix at the joint. As a result, stress becomes concentrated in transverse direction (width of specimen) around the coupling reinforcement at the joint. This situation can be seen in Figure 5.14. Although it is not yet observed at load stage 1 in figure (a), as the load increases and reaches load stage 2, it becomes visible that there are stress concentrations around the coupling reinforcement in the later load stages as indicated by black dashed circles in figure (b), (c), and (d). Beside the stress concentration, Figure 5.15 shows a non-uniform horizontal crack propagation across the width of the specimen as indicated by the black dashed line in figure (b), (c), and (d). In that figure, the concrete crack strain (the cracked concrete element) is in red. It is worth to note that prior to load stage 1, when the flexural crack has not occurred yet, there is only stress concentration in longitudinal direction at the joint, while the stress distribution in transverse direction is evenly distributed. However, after the flexural crack occurs, the stress concentration in transverse direction starts to develop in addition to the stress concentration in longitudinal direction. As the load increases

further, the stress concentration and horizontal crack patterns shift further from the joint to the end of coupling reinforcement.

As the load increases and reaches load stage 3, the tensile stress component in vertical direction at the joint reaches the concrete tensile strength. As a result, a horizontal crack starts to develop at the joint as shown in Figure 5.12(b). As the load increases further reaches load stage 4, the horizontal crack propagates along the coupling reinforcement as shown in Figure 5.12(c), instead of along the interface as happened in the model with smooth interface (2D-SI) as described in chapter 5.1.1.1. The difference in the horizontal crack propagation level is caused by the absence of the weak Coulomb friction interface in the model with the perfect bonded interface. At the failure stage, the horizontal crack reaches the end of coupling reinforcement and the flexural crack at the end of coupling reinforcement reaches the top of the cast-in-situ layer.

As observed in Figure 5.14 and Figure 5.15, there are non-uniform stress distribution and horizontal crack propagation in transverse direction. In compared to the 2D model (2D-PB), by using a plane stress element in the specimen, the stress distribution and the horizontal crack propagation across the width are assumed to be uniform. Thus, with a perfect bonded interface, there is a different interface behaviour between 2D and 3D model. From the load-displacement graph as shown in Figure 5.11, this 3D model (3D-PB) has 19% higher load capacity compared to the 2D model. In contrast to the models with the smooth interface in chapter 5.1.1.1 which has the the same load capacity and the same interface behaviour, the models with the perfect bonded interface in this discussion have a different load capacity and a different interface behaviour. The difference in the interface behaviour could be the cause of the load capacity difference. However, there is not enough observation which can be used for the analysis of this relationship. Further analysis about the influence of the interface behaviour to the capacity is discussed further in chapter 5.1.2.2.

5.1.2. Single lap splice setup

In this section, models with a single lap splice setup (one coupling reinforcement and one bottom reinforcement) are analysed. A reduction in the number of lap splice across the width is meant to increase the spacing (transverse distance) between lap splices while maintaining the total area of the reinforcements. With an increase of spacing, the influence of the lap splice spacing can be observed. In the setup of the experiment Sample 1 [1], there are three lap splices consisting of three 8 mm diameter bottom reinforcements in the precast layer and three 8 mm diameter connecting reinforcements in the cast-in-situ layer. By reducing the number of lap splices, the diameter of bottom and coupling reinforcements are increased to 13.86 mm and the effective spacing between each lap splice becomes 150 mm (equal to the width of the specimen). It should be noted that this single lap splice setup is still below the maximum transverse distance permitted by Eurocode as explained in chapter 2.5.2. Ideally, a further spacing larger than the limit value is better for the analysis of the spacing influence. However, this single lap splice setup is chosen due to the limited computational resource which is available for the research.

This chapter consists of two models with different type of concrete-to-concrete interface, a model with a smooth interface (3D-SI-1L) and a model with a perfect bonded interface (3D-PB-1L). The reinforcement and interface setup of both models are indicated in Figure 5.16 and Figure 5.17.

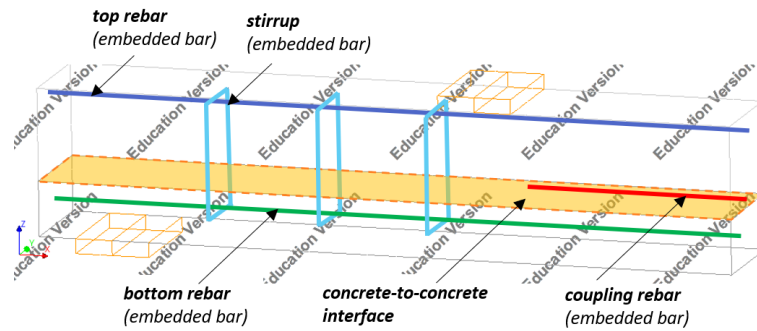


Figure 5.16 – Reinforcement setup and concrete-to-concrete interface of model with a smooth interface (3D-SI-1L)

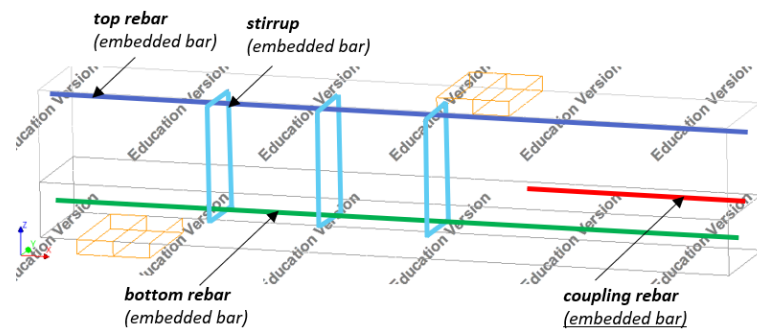


Figure 5.17 – Reinforcement setup of model with a perfect bonded interface (3D-PB-1L)

5.1.2.1. Smooth interface

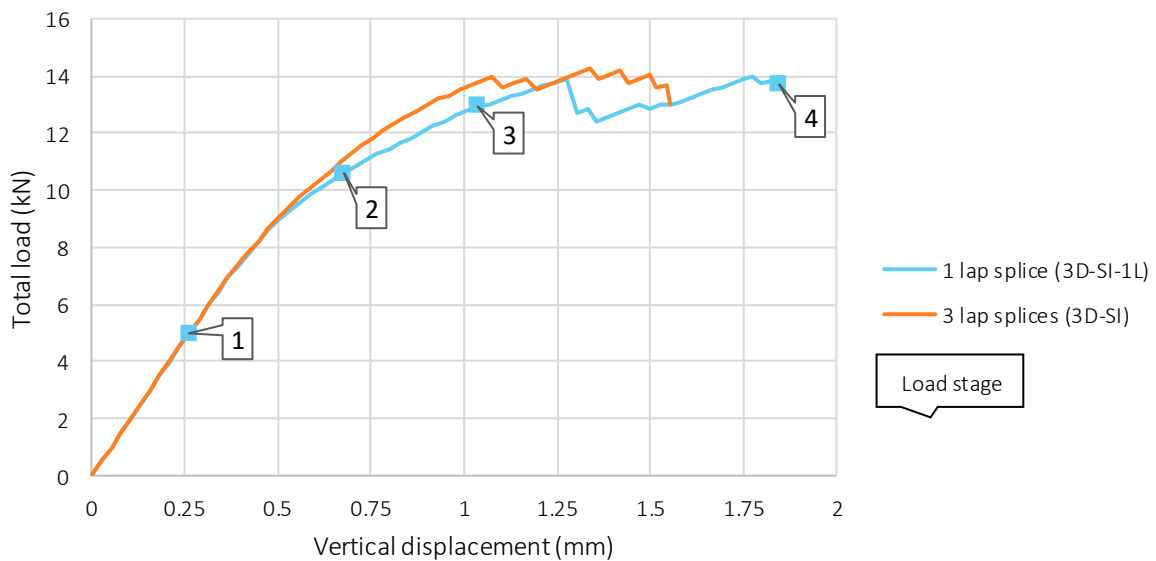


Figure 5.18 – Load-displacement graph of unreinforced interface model (smooth interface) with single lap splice setup (3D-SI-1L) and experimental setup (3D-SI)

In Figure 5.18, the load-displacement graph of the model with single lap splice setup (3D-SI-1L) is shown. Although there is a slightly different gradient after 0.68 mm of vertical displacement, the maximum vertical load of this model, which is 14.00 kN, is similar to the model with the experimental setup using three lap splices. In that figure, the damage development of this model is marked at four load stages prior to the failure. The damage development of this model can be observed in Figure 5.19. Load stage 1 is at the onset of a flexural crack at the joint, load stage 2 is at the start of an observed uneven stress distribution in transverse direction, load stage 3 is right before the start of horizontal crack at the joint, and load stage 4 is right before the failure. This model fails with the same mechanism as the model with

the experimental lap splice setup when the horizontal crack along the concrete-to-concrete interface (delamination) reaches the end of coupling reinforcement and the flexural crack at the end of coupling reinforcement reaches the top of the cast-in-situ layer. Figure 5.20 shows the interface stresses development at four node locations which is indicated in Figure 5.3. That figure is also marked with the four load stages which have been described before.

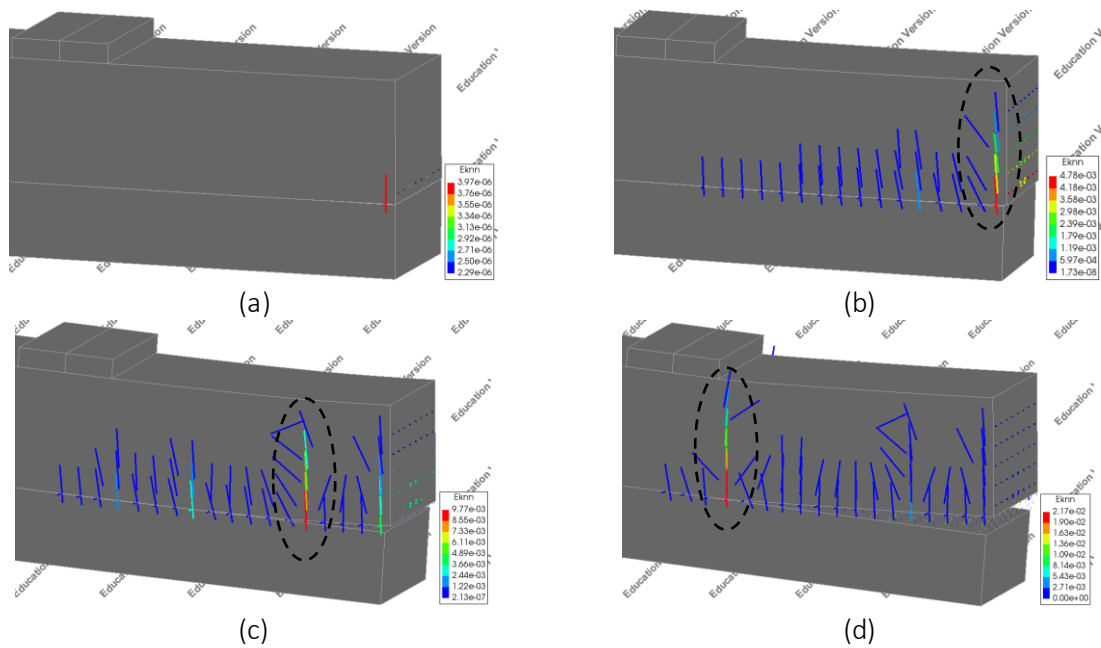


Figure 5.19 – Crack strain on the side of model 3D-SI-1L
 (a) at load stage 1, (b) at load stage 3, (c) at load stage 4, (d) at failure stage

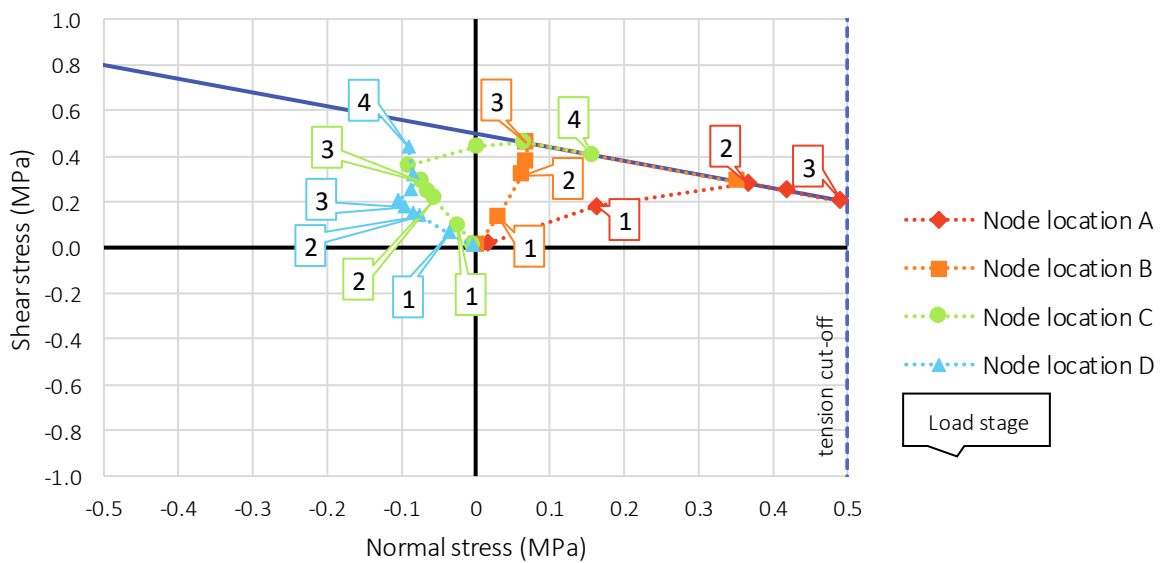


Figure 5.20 – Interface stresses development of model 3D-SI-1L at four nodes location

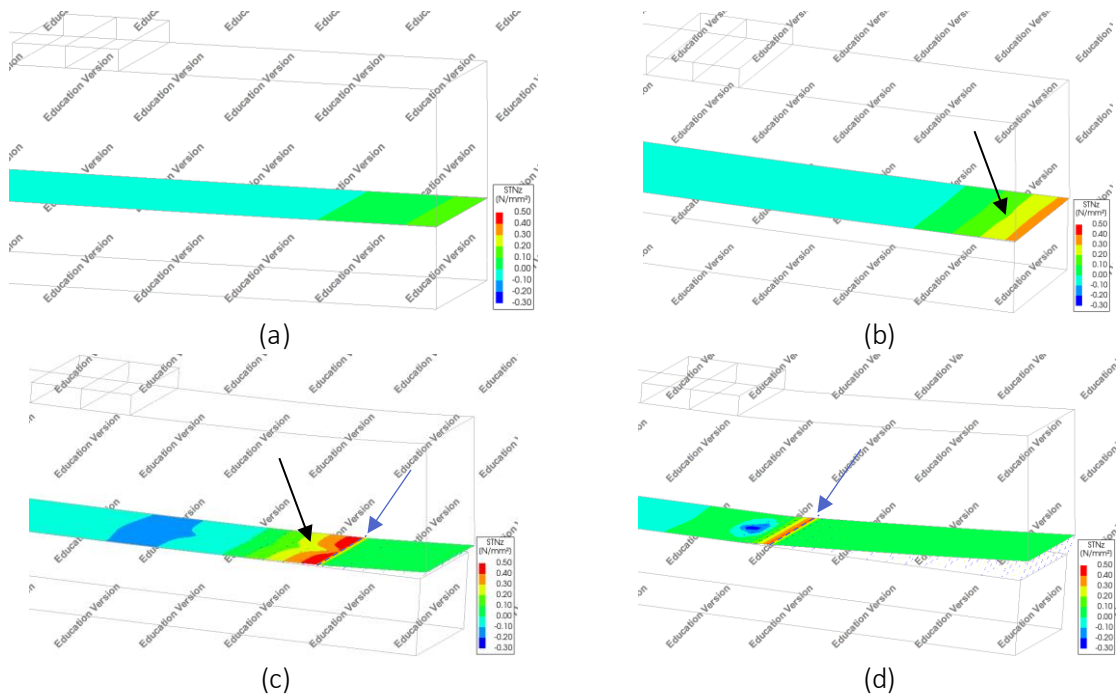


Figure 5.21 – Interface normal stress STN_z development of model 3D-SI-1L
 (a) at load stage 1, (b) right after load stage 2, (c) at load stage 4, (d) at failure stage

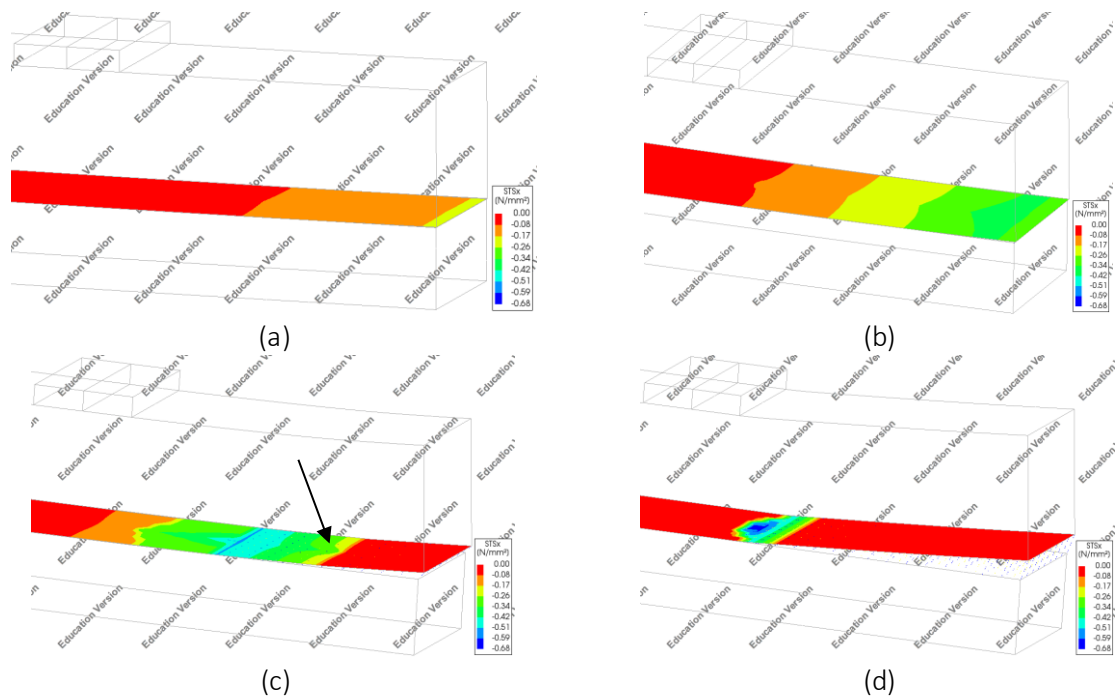


Figure 5.22 – Interface shear stress STS_x development of model 3D-SI-1L
 (a) at load stage 1, (b) right after load stage 2, (c) at load stage 4, (d) at failure stage

At the beginning of the analysis, a stress concentration around the joint in longitudinal direction, which occurs in the model with experimental lap splice setup (3D-SI), also occurs in this model as indicated with a black dotted circle in Figure 5.23(a). This stress concentration is also reflected in a peak of tensile and shear stresses at the joint as in model 3D-SI. When the load reaches load stage 1, the coupling reinforcement starts to take the tensile stress from the surrounding cracked concrete matrix at the joint. As a result, stress becomes concentrated in transverse direction (width of specimen) around the coupling reinforcement at the joint. This situation can be seen in Figure 5.21 and Figure 5.22. Although it is not yet observed at load stage 1 in figure (a), as the load increases and reaches load stage 2 and

further, it becomes visible that there are stress concentrations around the coupling reinforcement as indicated by the black arrows in figure (b) and (c). This stress concentration patterns shift further from the joint to the end of coupling reinforcement as the load increases.

In Figure 5.20, the similar interface stresses development as the model with three lap splices (3D-SI) are shown. This figure indicates that the tensile stress at node A and node B increases from load stage 1 to load stage 3, while the compressive stress at node C and node D also increases at the same time, similar to the model with the experimental lap splice setup (3D-SI). As the load reaches load stage 3, the tensile stress at node A (the joint) reaches the interface tensile strength (cut-off limit), so that the delamination of the interface starts to occur at the joint (see Figure 5.19(b)).

As the load increases and reaches load stage 4, the horizontal crack grows along the interface as shown in Figure 5.19(c). The peak of the tensile stress shifts towards end of coupling reinforcement as can be seen in Figure 5.21. This shift can also be observed in Figure 5.20 as the stress development of point C and D changes its direction towards the x-axis positive direction after load stage 3. This is following the shift of shear stress peak in the same direction as can be seen in Figure 5.22. When failure occurs, the delamination (horizontal crack at interface level) reaches the end of coupling reinforcement and the large flexural crack reaches the top of the cast-in-situ layer.

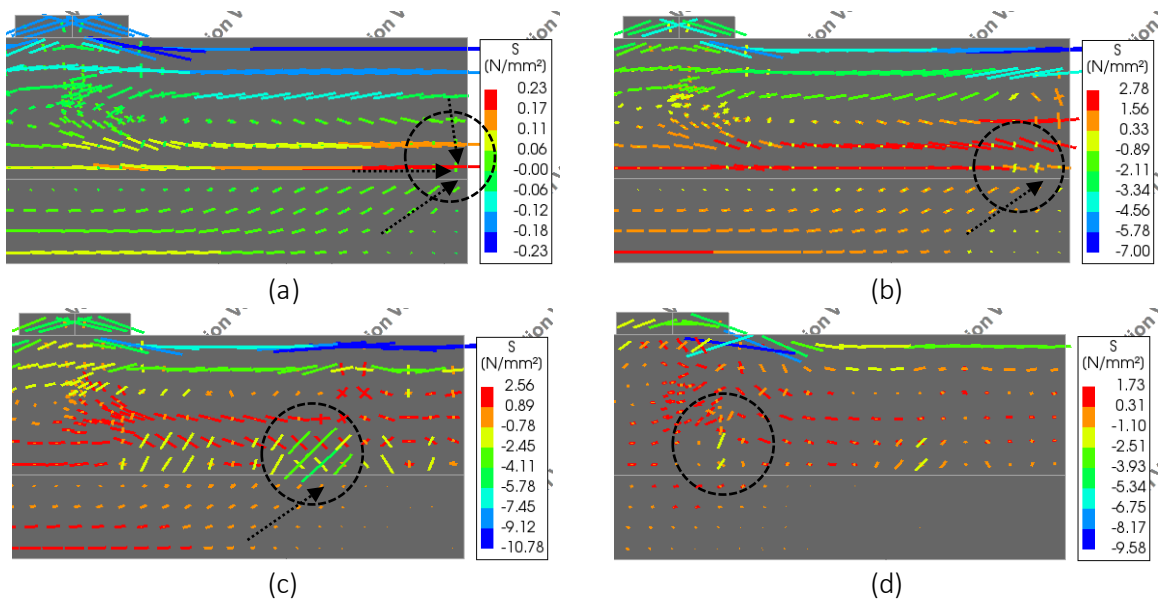


Figure 5.23 – In-plane principal stress at mid-section of model 3D-SI-1L
 (a) at load step 1, (b) right after load stage 2, (c) at load stage 4, (d) at failure stage

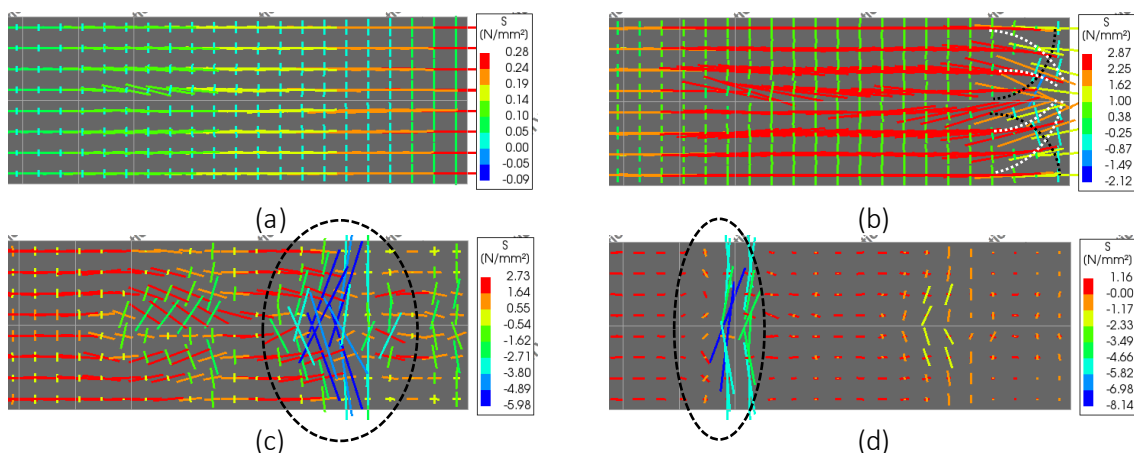


Figure 5.24 – In-plane principal stress at the top side of interface of model 3D-SI-1L
 (a) at load step 1, (b) right after load stage 2, (c) at load stage 4, (d) at failure stage

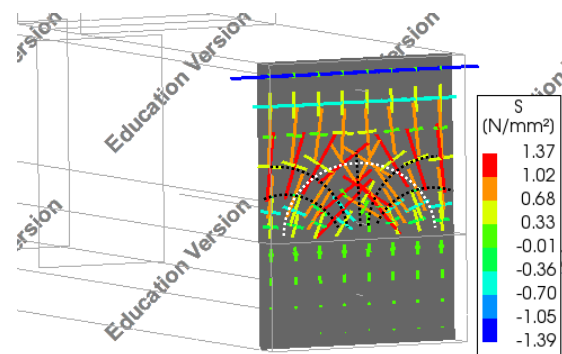


Figure 5.25 – In-plane principal stress at the location of stress concentration in transverse direction right after load stage 2 of model 3D-SI-1L

As discussed in the previous paragraphs, when the load reaches load stage 1, the coupling reinforcement starts to take the tensile stress from the surrounding cracked concrete matrix at the joint. However, the stress concentration around the coupling reinforcement which indicates this situation is not yet observed until load stage 2. This phenomenon is supported by Figure 5.25. This figure shows two patterns of principal stress direction, which are a radial compressive stress (black dotted line) and a circumferential tensile stress (white dotted lines). Although these patterns only occur in the cast-in-situ layer due to the use of Coulomb friction interface, these patterns can be recognized as the stress pattern of reinforcement bond transfer in Figure 2.2 which is caused by the transfer of tensile load between the lap splices. The stress patterns can also be seen in Figure 5.23(b) as a vertical compressive stress along the top part of the concrete-to-concrete interface, while in Figure 5.24(b), they can be seen as the patterns which are also marked by black and white dotted lines.

As shown in Figure 5.23(c) and Figure 5.24(c), the location of these stress patterns at load stage 4 have been shifted from their previous location at load stage 2 as indicated in Figure 5.23(b) and Figure 5.24(b). It happens since at load stage 4, the interface delamination has propagated to the same location as indicated by black dashed circle in Figure 5.19(c), thus the end of the tensile force transfer is also at that same location as indicated by black dash arrow in Figure 5.23(c). Moreover, the growth of the interface delamination is always followed by the occurrence of a large flexural crack at the end of the delamination as can be seen in Figure 5.19(c). With a flexural crack at the cast-in-situ layer, the coupling reinforcement starts to take the tensile stress from the surrounding cracked concrete matrix at the joint which is resulted to the presence of the stress concentration patterns at that location.

As discussed in chapter 5.1.1.1, the model with experimental lap splice setup (3D-SI) has no observed stress concentration across the width of the specimen, while this model with a single lap splice setup (3D-SI-1L) has the stress concentration. Although both models have a different stress distribution in transverse direction, they have the same interface delamination propagation. Both models have a uniform horizontal crack propagation along the interface in transverse direction. This phenomenon could be related to the properties of the Coulomb friction model for the smooth interface. However, it needs a further study to investigate the governing parameters which cause this phenomenon.

Finally, the similar uniform horizontal crack propagation between model 3D-SI (experimental lap splice setup) and model 3D-SI-1L (single lap splice setup) could be the cause of the similar load capacity of both models. With the same uncracked interface area, both models have the same number of elements which can transfer the tensile force from the precast layer to the cast-in-situ layer.

5.1.2.2. Perfect bonded interface

In Figure 5.26, the load-displacement graph of the model with perfect bonded interface and single lap splice (3D-PB-1L) is shown. The maximum vertical load of this model is 24.62 kN which is 10% higher than the model with three lap splices setup (3D-PB). In that figure, the damage development of this model is marked at four load stages prior to the failure. The damage development of this model can be

observed in Figure 5.27. Load stage 1 is at the onset of a flexural crack at the joint, load stage 2 is at the start of an observed uneven stress distribution in transverse direction, load stage 3 is right before the start of horizontal crack at the joint, and load stage 4 is right before the failure. This model fails when the horizontal crack along the coupling reinforcement reaches the end of that reinforcement and the flexural crack at the end of that reinforcement reaches the top of the cast-in-situ layer.

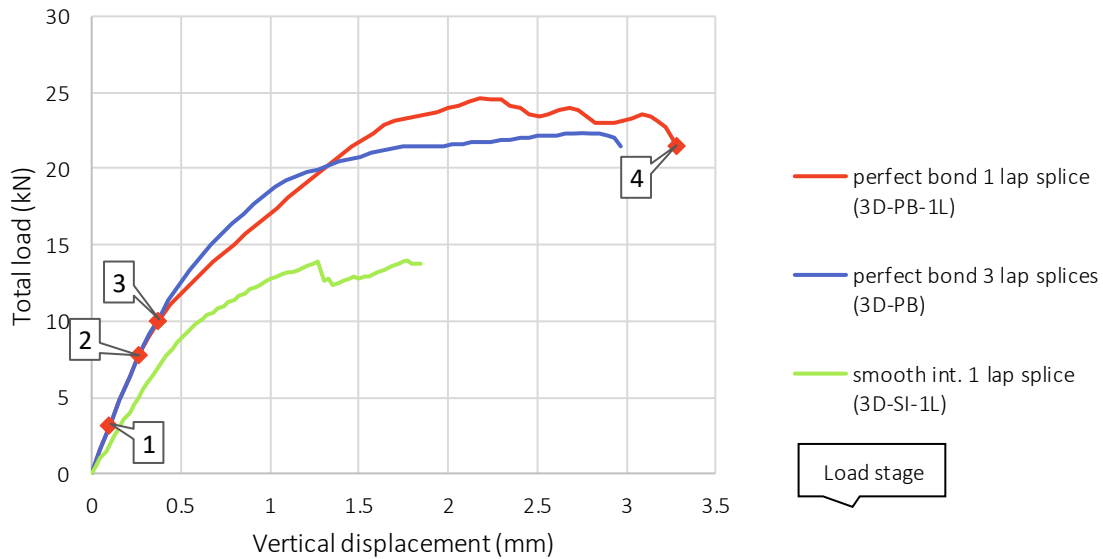


Figure 5.26 – Load-displacement graph of unreinforced interface model (perfect bonded interface) with single lap splice setup (3D-PB-1L) and experimental setup (3D-PB)

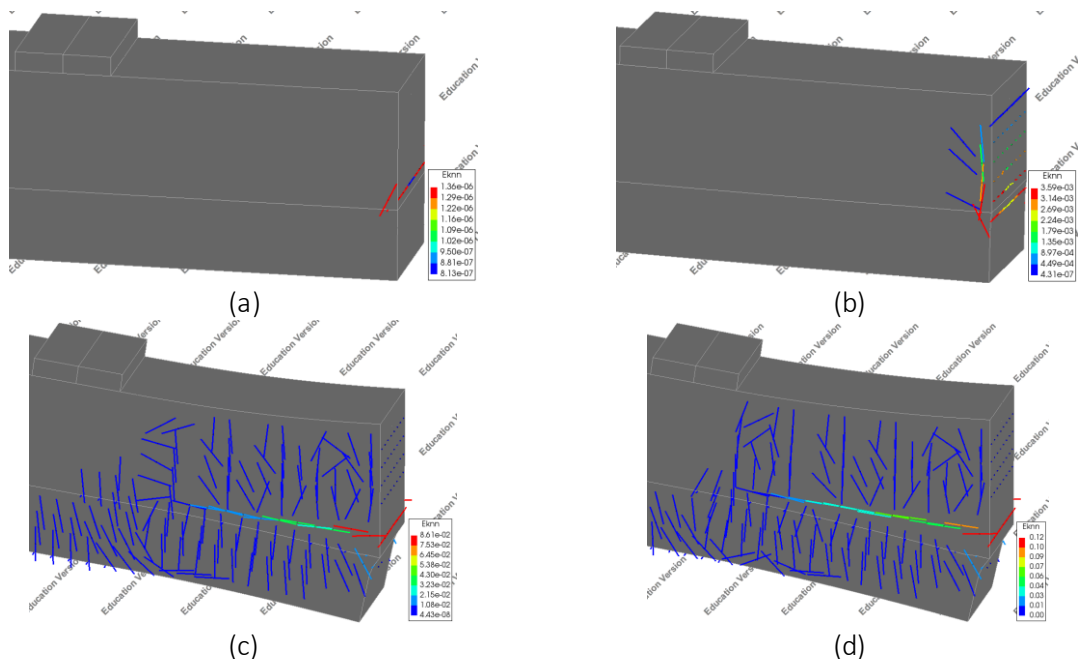


Figure 5.27 – Crack strain on the side of model 3D-PB-1L (a) at load stage 1, (b) a few load steps after load stage 3, (c) at load stage 4, (d) at failure stage

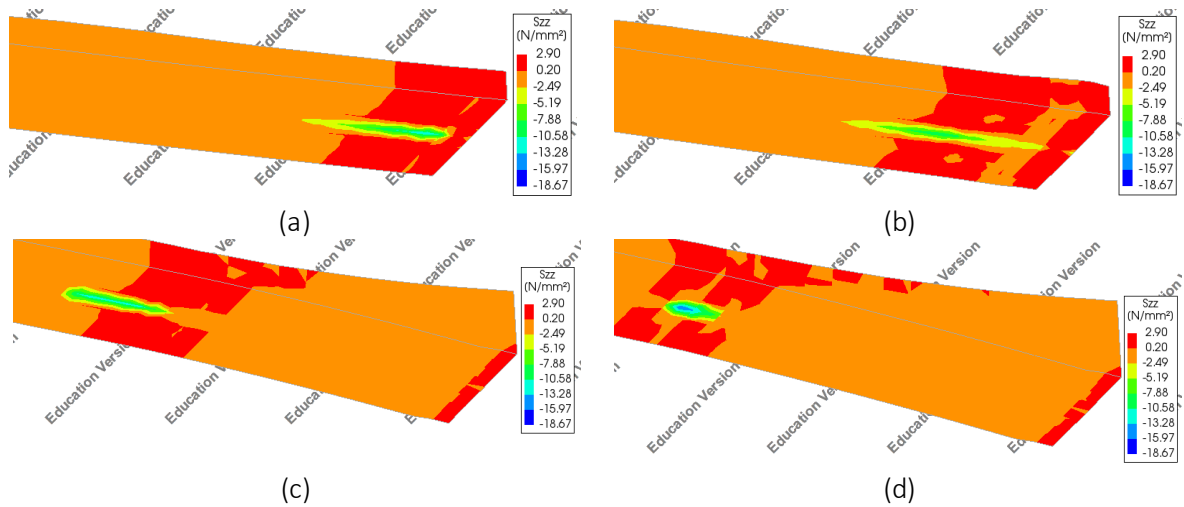


Figure 5.28 – Stress S_{zz} of the elements at the level of coupling reinforcement of model 3D-PB-1L (a) at $P = 20$ kN, (b) at $P = 23.5$ kN, (c) at load stage 4, (d) at failure

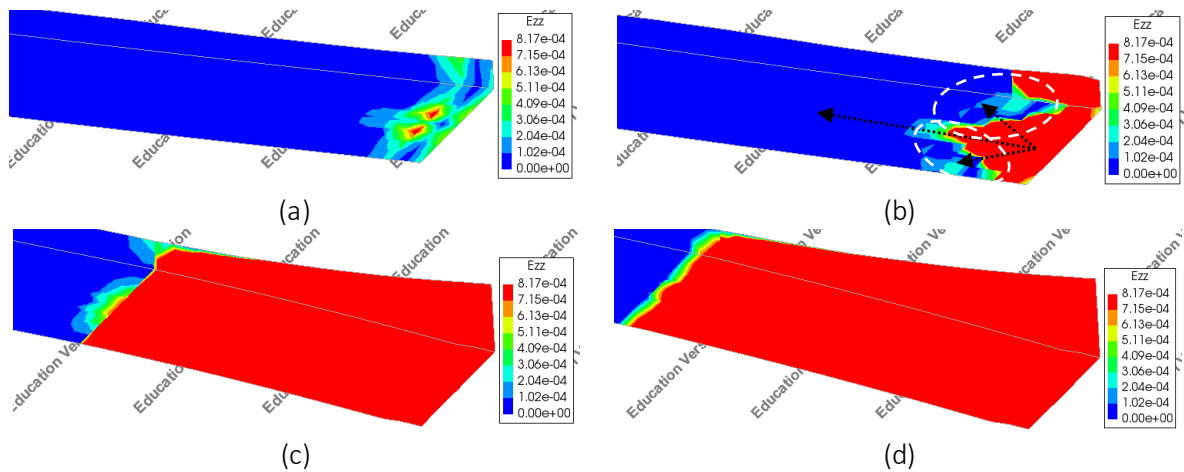


Figure 5.29 – Stress E_{zz} of the elements at the level of coupling reinforcement of model 3D-PB-1L (a) at $P = 20$ kN, (b) at $P = 23.5$ kN, (c) at load stage 4, (d) at failure

At the beginning of this analysis, a stress concentration in longitudinal direction also occurs as in the model with smooth interface. When the load reaches load stage 1, the coupling reinforcement starts to take the tensile stress from the surrounding cracked concrete matrix at the joint. As a result, from load stage 2, there is a similar stress concentration around the coupling reinforcement as the one in the model with three lap splices setup, which can be seen in Figure 5.28. A non-uniform horizontal crack propagation across the width of the specimen also occurs in this model as shown in Figure 5.29. As the load increases further, the stress concentration and horizontal crack patterns shift further from the joint to the end of coupling reinforcement.

As the load increases and reaches load stage 3, the tensile stress component in vertical direction at the joint reaches the concrete tensile strength and resulted in a horizontal crack at the joint as shown in Figure 5.27(b). As the load reaches load stage 4, the horizontal crack propagates along the coupling reinforcement as shown in Figure 5.12(c). At the failure stage, the horizontal crack reaches the end of coupling reinforcement and the flexural crack at the end of coupling reinforcement reaches the top of the cast-in-situ layer. The failure mechanism of this model as described above is similar to the failure mechanism of model with experimental lap splice setup (3D-PB).

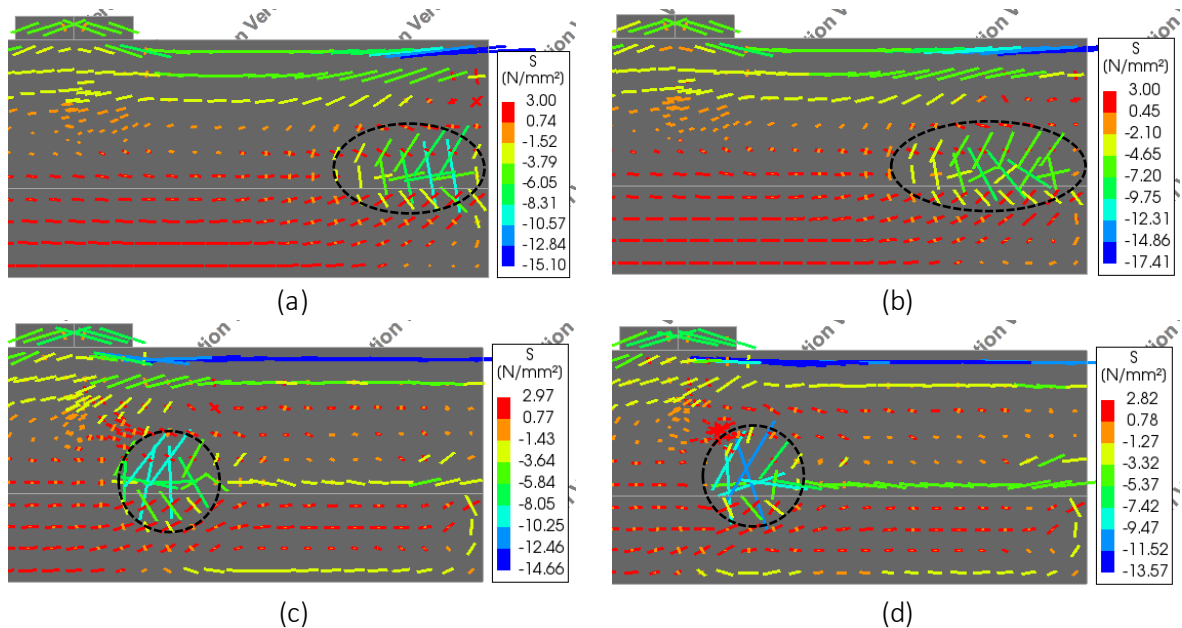


Figure 5.30 – In-plane principal stress at mid-section of model 3D-PB-1L
 (a) at $P = 20$ kN, (b) at $P = 23.5$ kN, (c) at load stage 4, (d) at failure

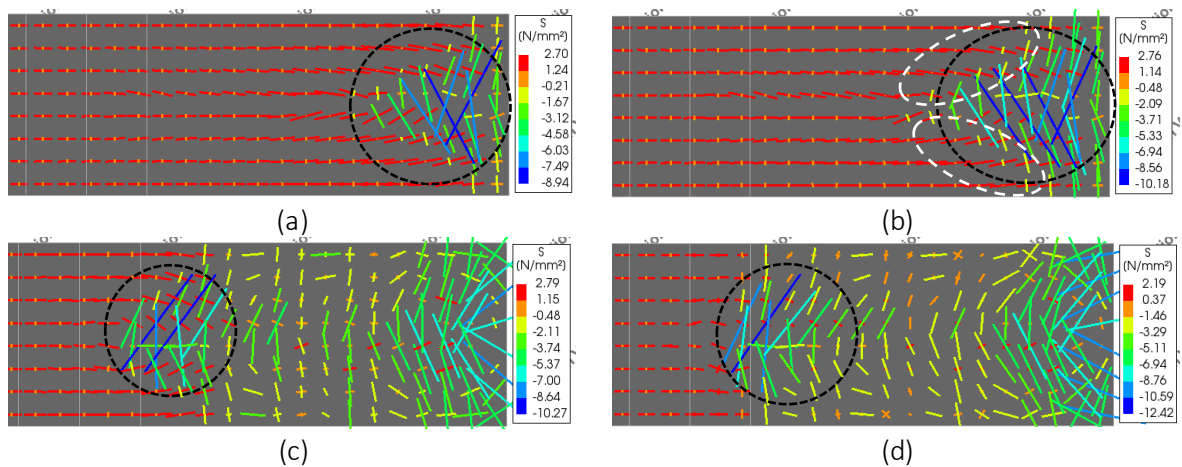


Figure 5.31 – In-plane principal stress at level of coupling reinforcement of model 3D-PB-1L
 (a) at $P = 20$ kN, (b) at $P = 23.5$ kN, (c) at load stage 4, (d) at failure

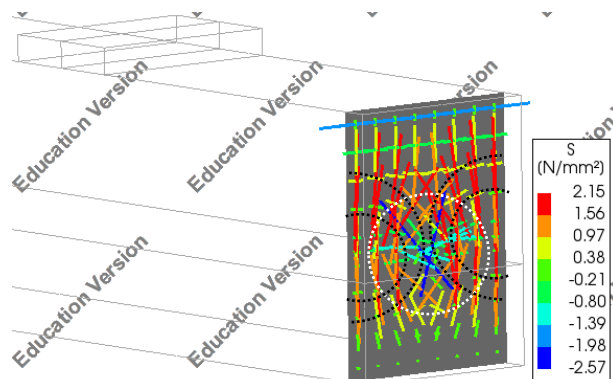


Figure 5.32 – Reinforcement bond transfer stress patterns in transverse direction
 at a few load steps after load stage 2 (load step 12) in model 3D-PB-1L

As observed in Figure 5.28 and Figure 5.29, there is a non-uniform stress distribution and horizontal crack propagation in transverse direction. As explained in chapter 5.1.2.1, the stress concentration is related to the principal stress pattern which are shown in Figure 5.30, Figure 5.31, and Figure 5.32. This

pattern is the stress pattern of reinforcement bond transfer which is caused by the transfer of tensile load between the bottom reinforcement in precast layer and coupling reinforcement in cast-in-situ layer. Although this model has a similar principal stress pattern as the model with smooth interface (3D-SI-1L), in model with smooth interface, both radial compressive stress and circumferential tensile stress only occur in the cast-in-situ layer due to the use of the Coulomb friction model for the interface, while in this model, as shown in Figure 5.32, the pattern occurs in both concrete layers.

In compared to the model with perfect bonded interface with experimental lap splices setup (3D-PB-1L) in chapter 5.1.1.2, this model has more higher stress concentration and more concentrated horizontal crack propagation around the coupling reinforcement. This more concentrated horizontal crack propagation (Figure 5.29(b)) is caused by the smaller number of lap splice used in this model, compared to the model with three lap splices. In the other hand, the more uniform crack propagation in the model with three lap splices (Figure 5.15(c)) could be caused by the larger number of lap splices used in the model which causes a smaller spacing between the lap splices. With smaller lap splice spacing, the concentrated horizontal propagation of each lap splice is overlapping each other, thus creating more uniform crack propagation.

The difference in this horizontal crack propagation is the most plausible cause of the difference in their load capacity. In Figure 5.29(b), dotted black arrows indicating the horizontal crack propagation direction. The crack starts from the joint at the mid-section area, which is the location of the coupling reinforcement, and continues to grow to two directions, towards the rest of the width of the model and towards the end of coupling reinforcement. Since the crack is started from the area around coupling reinforcement, the area which are marked with white dashed circles in that figure are still intact or uncracked. These uncracked area can transfer the tensile force from the precast layer to the cast-in-situ layer as indicated by white dashed circles in Figure 5.31(b). It is different with model with three lap splices (3D-PB). With more uniform horizontal crack propagation, there are less uncracked elements which can transfer the tensile force from the precast layer to the cast-in-situ layer. Therefore, the model with single lap splice has a higher load capacity compared to the model with three lap splice. This is also the case when comparing the 3D model with three lap splices (3D-PB) and the 2D model (2D-PB). The latter has lower capacity since in 2D model, the crack is assumed to be evenly distributed across its width, while model 3D-PB has its advantage from the slightly uncracked area across its width.

From this study of lap splice spacing, the unreinforced interface beam with a perfect bonded interface has a different capacity when using a different lap splice spacing. An additional analysis is added to understand whether there is an influence from the different concrete type used in the precast layer as a substitute of SHCC. Model 3D-PB-1L-RC is made with both layers using the same regular concrete as described in Table 3.7.

In Figure 5.33, the load-displacement graph of model 3D-PB-1L-RC is shown. This model has perfect bonded interface, same regular concrete properties in the precast and the cast-in-situ layer, and single lap splice. The maximum vertical load of this model is 29.88 kN which is 34% higher than the model with SHCC-concrete configuration (3D-PB-1L). In that figure, the damage development of this model is marked at six load stages prior to the failure. Load stage 1 is at the onset of a flexural crack at the joint, load stage 2 is at the start of an observed uneven stress distribution in transverse direction, load stage 3 is right before the start of horizontal crack at the joint, and load stage 4 is right before the failure. The other 2 load stages, which are load stage 3A and 3B, are the additional load stages to help the analysis. This model fails the same way as model with SHCC-concrete configuration, which is when the horizontal crack along the coupling reinforcement reaches the end of that reinforcement and the flexural crack at the end of that reinforcement reaches the top of the cast-in-situ layer.

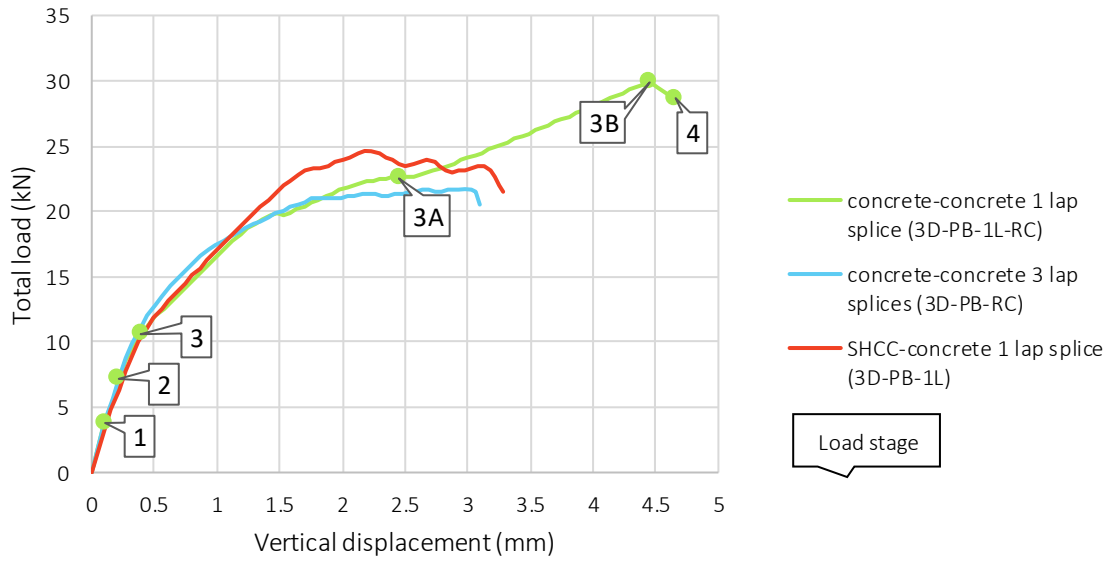


Figure 5.33 – Load-displacement graph of unreinforced interface model (3D-PB and 3D-PB-1L) with perfect bonded interface and concrete in both layers

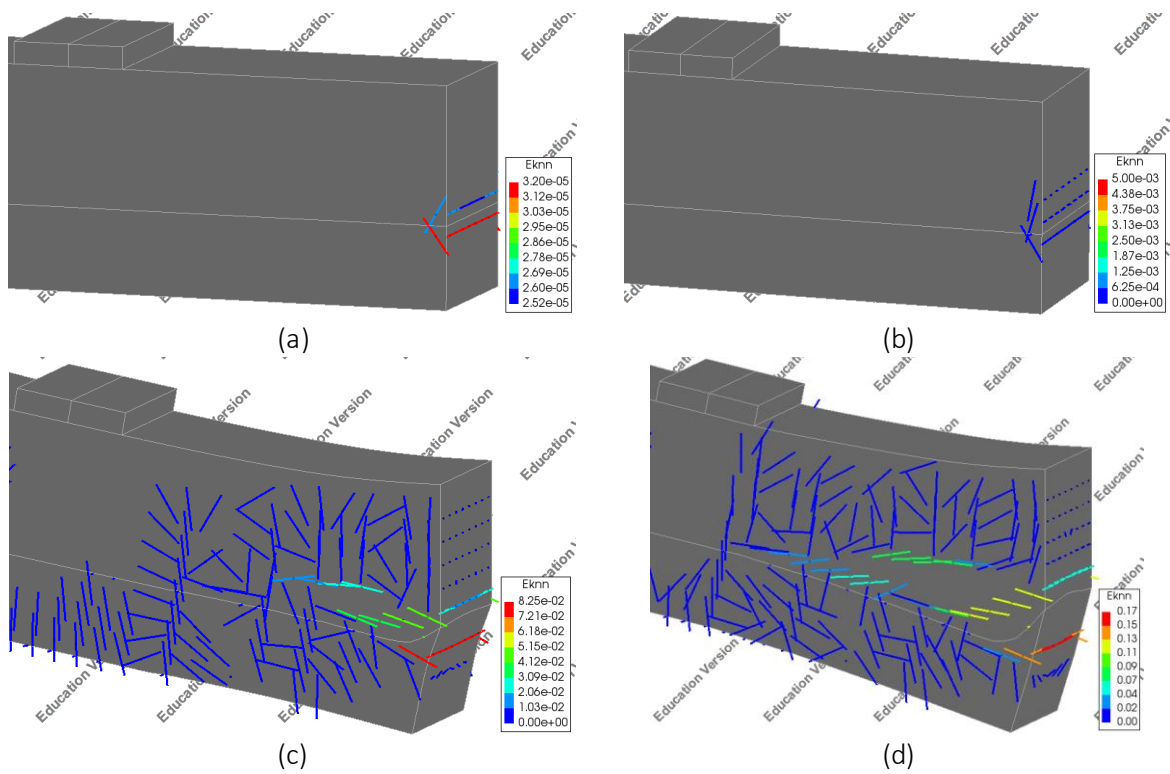


Figure 5.34 – Crack strain on the side of model 3D-PB-1L-RC (a) at load stage 1, (b) right after load stage 2, (c) at load stage 4, (d) at failure stage

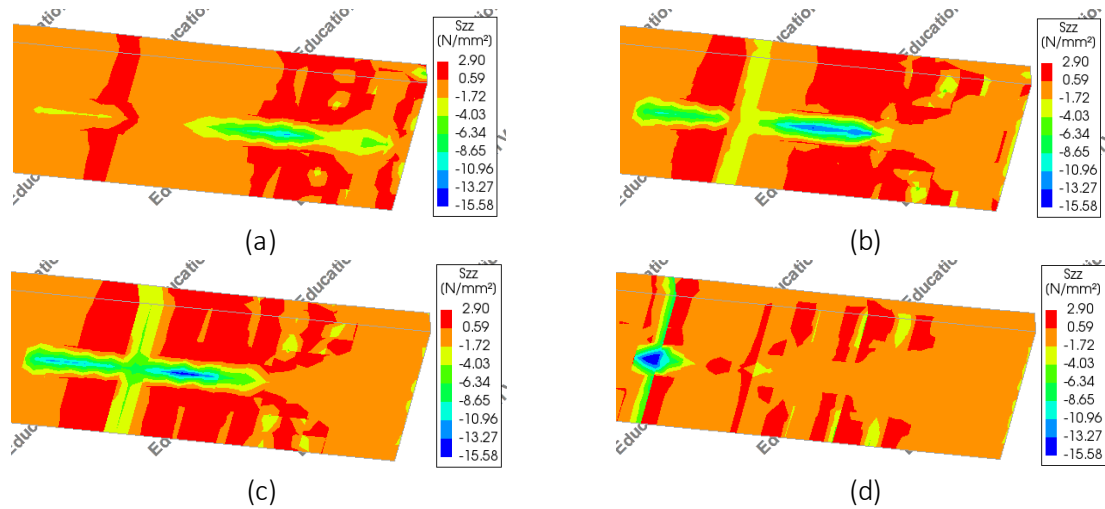


Figure 5.35 – Stress S_{zz} of the elements at the level of coupling reinforcement of model 3D-PB-1L-RC (a) at load stage 3A, (b) at load stage 3B, (c) at load stage 4, (d) at failure stage

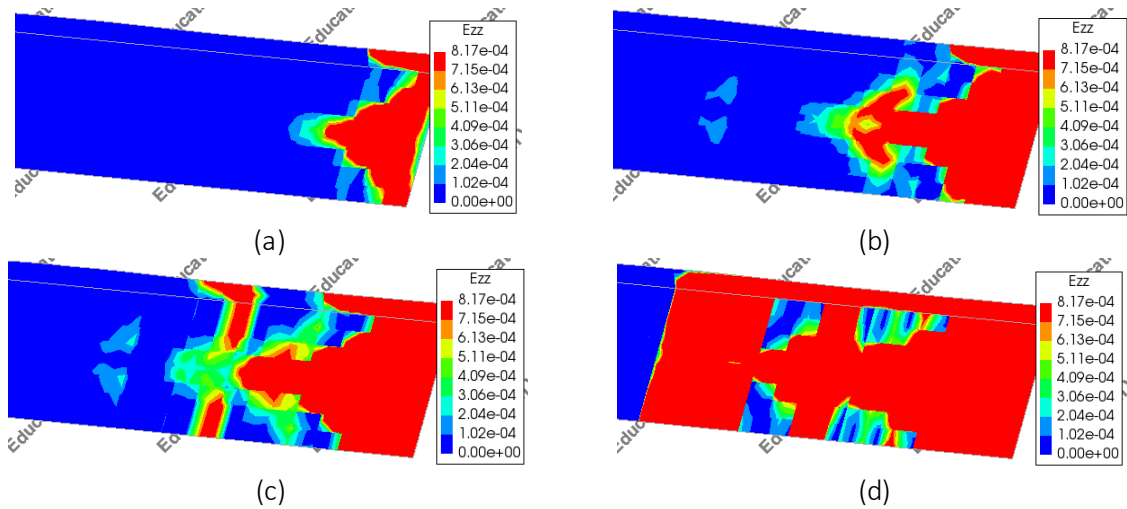


Figure 5.36 – Strain E_{zz} of the elements at the level of coupling reinforcement of model 3D-PB-1L-RC (a) at load stage 3A, (b) at load stage 3B, (c) at load stage 4, (d) at failure stage

This model has a similar damage development from load stage 1 to load stage 3, compared to model with SHCC-concrete configuration (3D-PB-1L). As can be seen in Figure 5.33, the equilibrium path of those load stages coincides with the one from model 3D-PB-1L. At the beginning of this analysis, a stress concentration in longitudinal direction occurs. When the load reaches load stage 1, the coupling reinforcement starts to take the tensile stress from the surrounding cracked concrete matrix at the joint. At load stage 2, the stress concentration and non-uniform horizontal crack propagation become distinguishable. As the load increases and reaches load stage 3, the tensile stress component in vertical direction at the joint reaches the concrete tensile strength and resulted in a horizontal crack at the joint.

However, as the load increases and approaching load stage 3A, the equilibrium path of this model starts to differ and its structural stiffness increases. Between load stage 3A and 3B, as shown in Figure 3.36(a) and (b), there is small increase of horizontal crack propagation although the number of load increments in between this load stages is about 44% of the total load increment from the beginning of the analysis until the failure stage. The cause of this behaviour is not clear yet. However, it is clear that between load stage 3A and 3B, the horizontal crack does not propagate into the transverse direction. It only grows in the longitudinal direction. As a result, in Figure 3.36(b), there is a narrow horizontal crack pattern around the coupling reinforcement. By having a narrow crack pattern, there are a lot of elements that can transfer the tensile force from the precast layer to the cast-in-situ layer. This could be the reason of the higher load capacity in the model with concrete-concrete configuration.

5.2. Reinforced interface beams

In the first part of this section, the results and analysis of the models which represent the experimental setup of Sample 7 [1] are discussed. In the second part, to understand the influence of stirrup spacing on the interface behaviour, the number of the stirrup's legs are reduced from two to one leg or become single vertical stirrup while maintaining the total area of the stirrup legs. By reducing the number of the stirrup's legs across the width of the model, the effective spacing between stirrups increases.

5.2.1. Rectangular stirrup setup

This chapter also consists of two types of concrete-to-concrete interface, the smooth interface and the perfect bonded interface. The model with smooth interface is model 3D-SI-SJ, which finite element model, reinforcement setup, and the numerical setup are presented in chapter 3.2. The model with the second type of interface, model 3D-PB-SJ which has the same numerical setup as model 3D-SI-SJ. However, instead of using Coulomb friction interface, this model uses a rigid connection to connect the precast and cast-in-situ layer. It should be noted since the “embedded bar” reinforcement type is used for coupling reinforcement, the possibility of pull-out failure of stirrup is not included in the analysis.

5.2.1.1. Smooth interface

In Figure 5.37, the load-displacement graph of model 3D-SI-SJ is shown. The maximum vertical load of the model is 28.96 kN at the end of the analysis. In that figure, this model is compared with the unreinforced interface model (3D-SI) and the 2D version of this model (2D-SI-SJ). There is also an analytical solution for yielding of coupling reinforcement in the graph. The calculation of this solution is provided in the appendix. In that figure, the damage development of this model is marked at three load stages prior to the failure, so the interface behaviour can be analysed step-by-step. Load stage 1 is at the onset of the flexural crack at the joint and the start of an observed uneven stress distribution in transverse direction, load stage 2 is right before the start of the delamination at the joint, and load stage 3 is at the end of the analysis. As described in chapter 3.3.2, the specimen in this model has not failed yet at the end of the analysis. If the prescribed displacement is increased, the load-displacement graph will reach the yielding of coupling reinforcement though in a really high displacement around 20 mm. For the purpose of this analysis, the load-displacement graph of this model is only presented as shown in Figure 5.37, which is until 4 mm of prescribed displacement.

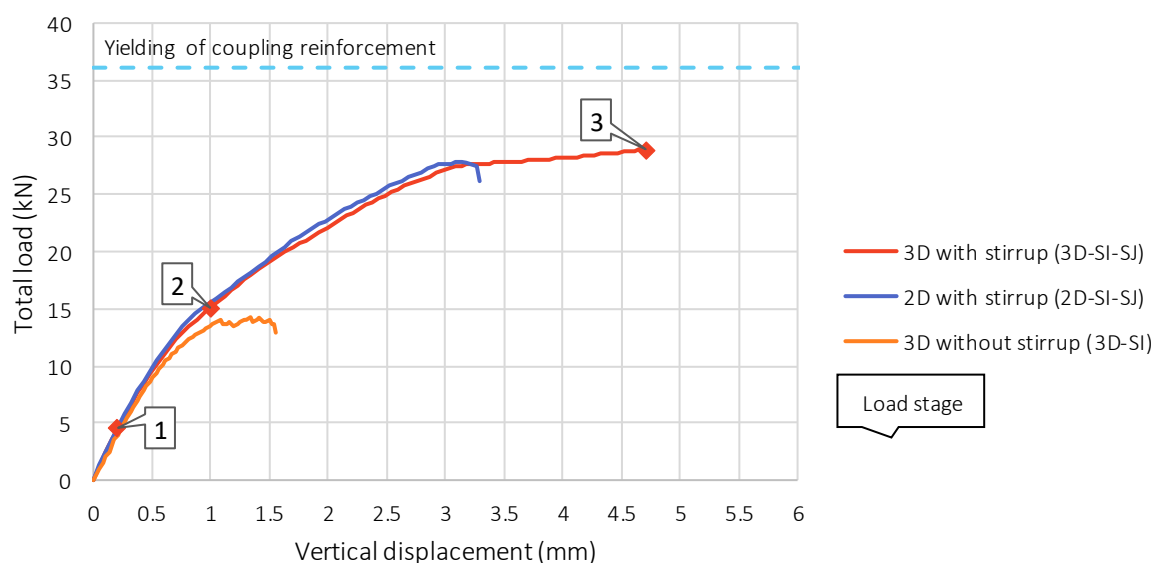


Figure 5.37 – Load-displacement graph of reinforced interface model with smooth interface (2D-SI-SJ and 3D-SI-SJ)

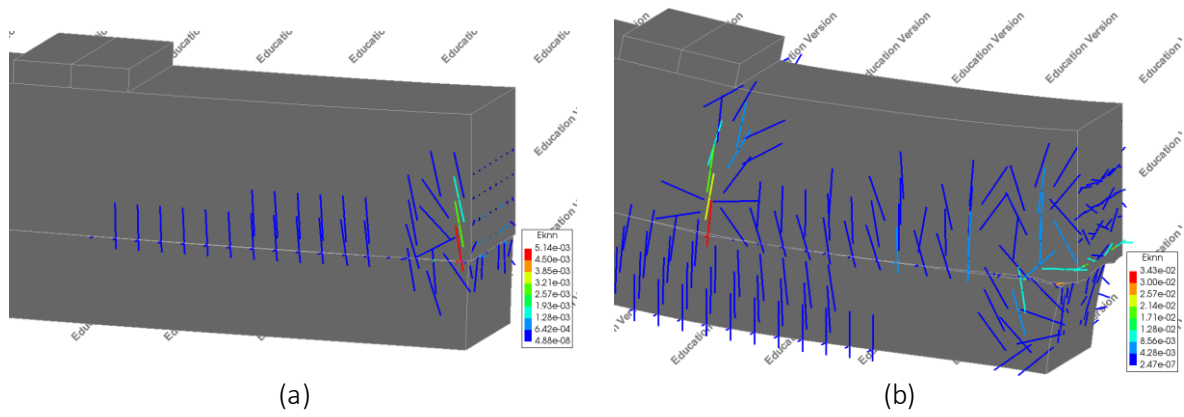


Figure 5.38 – Crack strain on the side of model 3D-SI-SJ (a) right after load stage 2, (b) at load stage 3

Figure 5.39 shows the interface stresses development at four node locations which is indicated in Figure 5.3. That figure is also marked with the three load stages which have been described before.

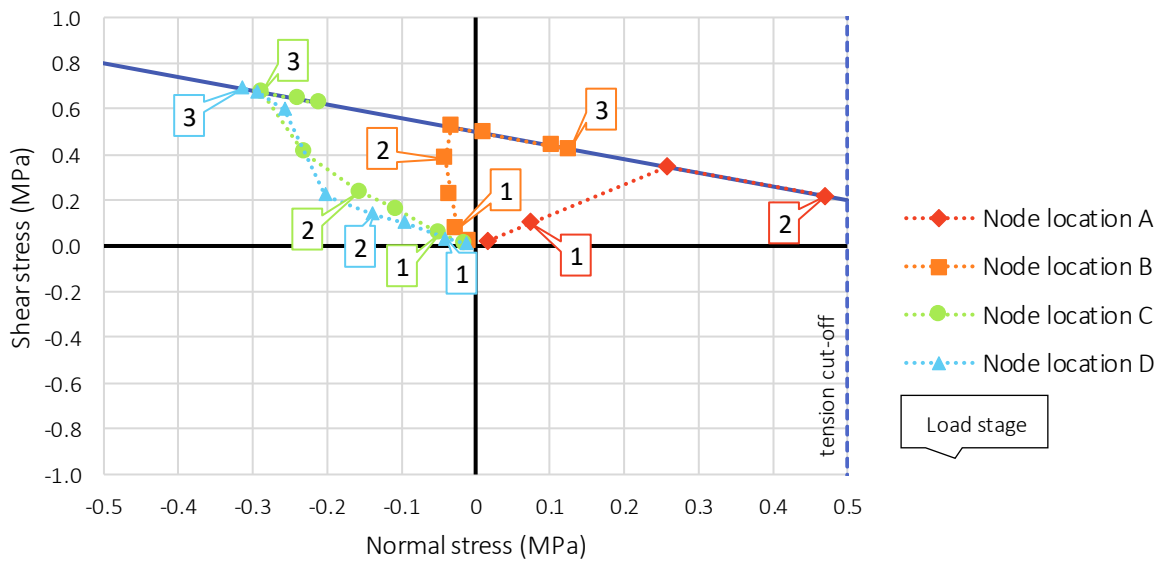


Figure 5.39 – Interface stresses development of model 3D-SI-SJ at four nodes location

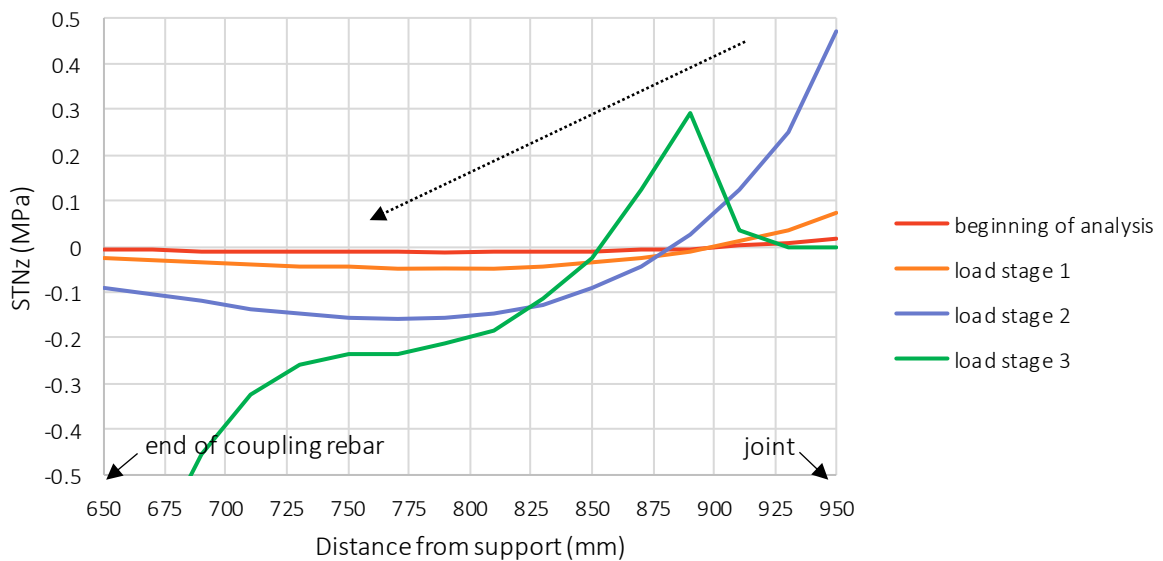


Figure 5.40 – Interface normal stress at the mid-section of model 3D-SI-SJ at different load stages

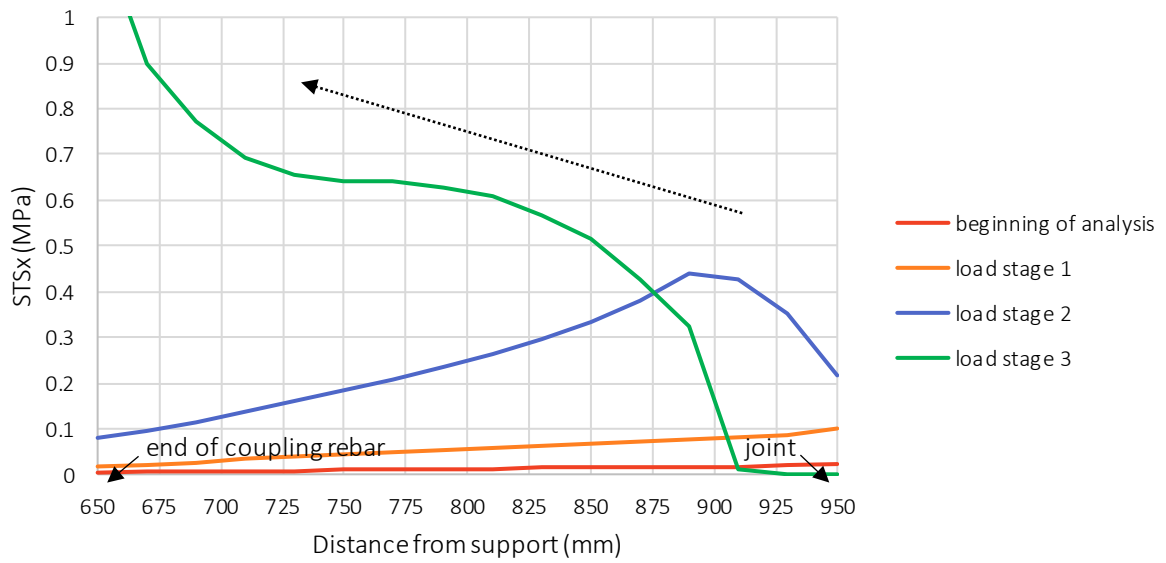


Figure 5.41 – Interface shear stress at the mid-section of model 3D-SI-SJ at different load stages

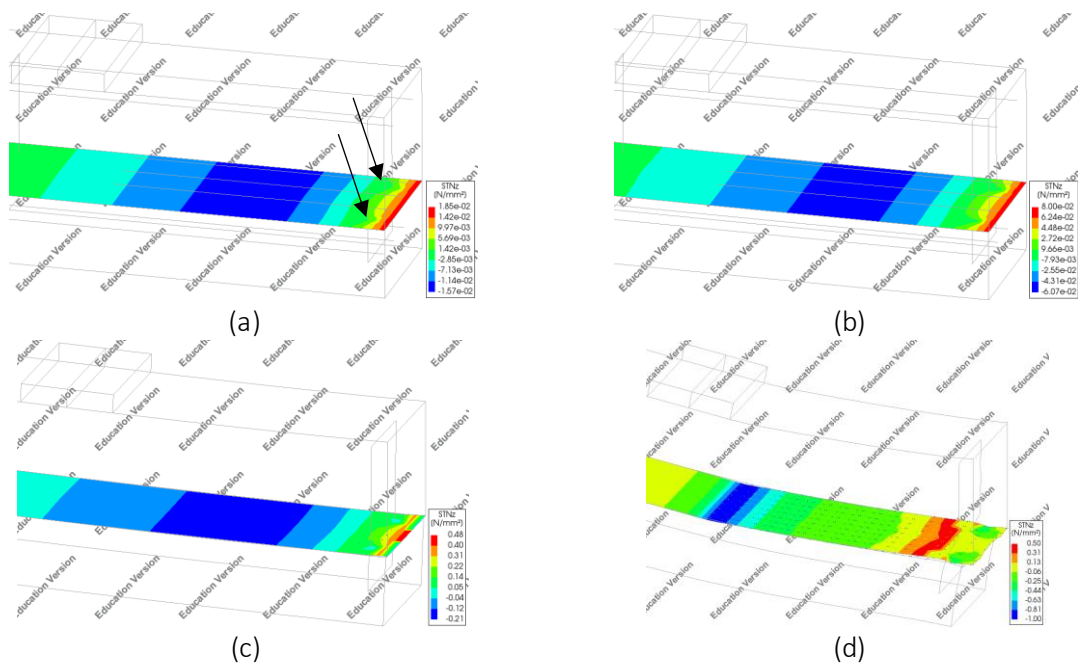


Figure 5.42 – Interface normal stress STN_z development of model 3D-SI-SJ (a) at the beginning of analysis, (b) at load stage 1, (c) right after load stage 2, (d) at load stage 3

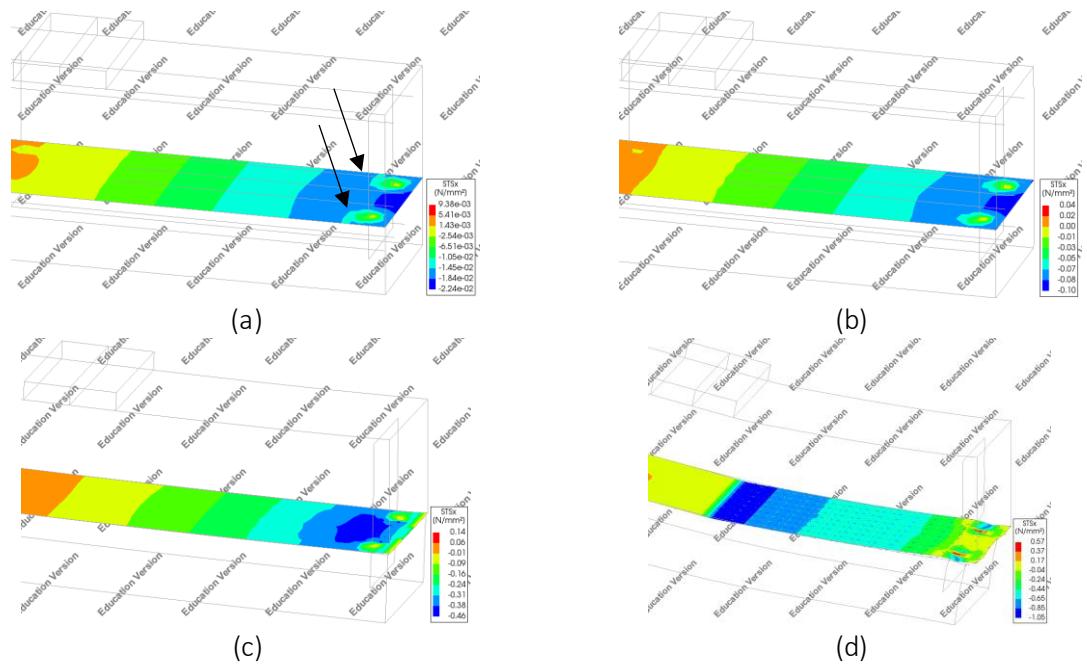


Figure 5.43 – Interface shear stress ST_x development of model 3D-SI-SJ
 (a) at the beginning of analysis, (b) at load stage 1, (c) right after load stage 2, (d) at load stage 3

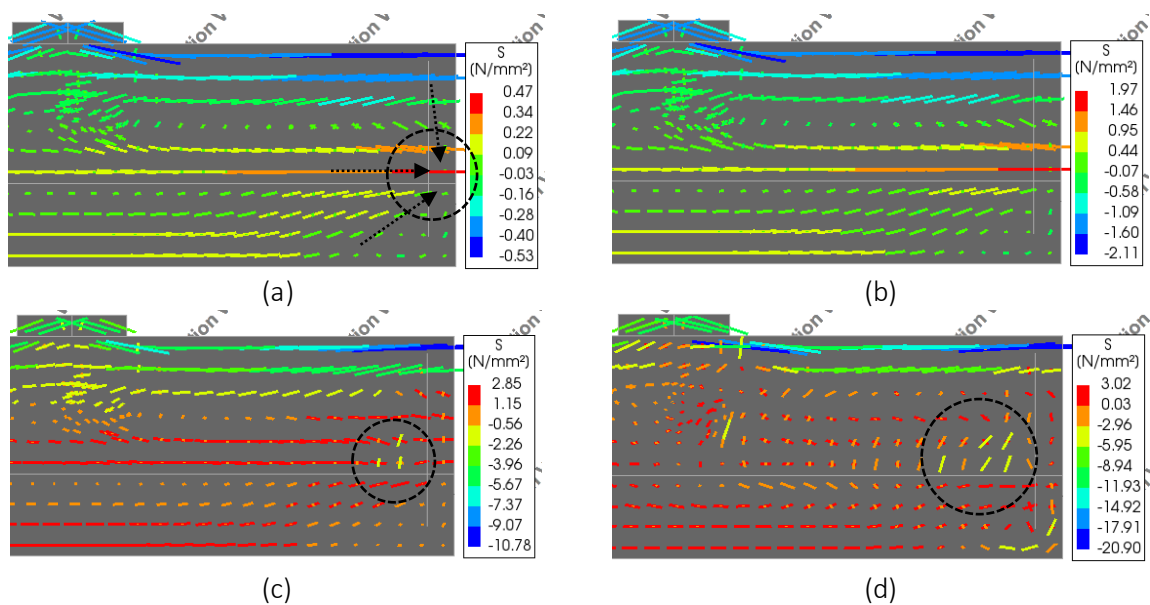


Figure 5.44 – In-plane principal stress at mid-section of model 3D-SI-SJ
 (a) at the beginning of analysis, (b) at load stage 1, (c) right after load stage 2, (d) at load stage 3

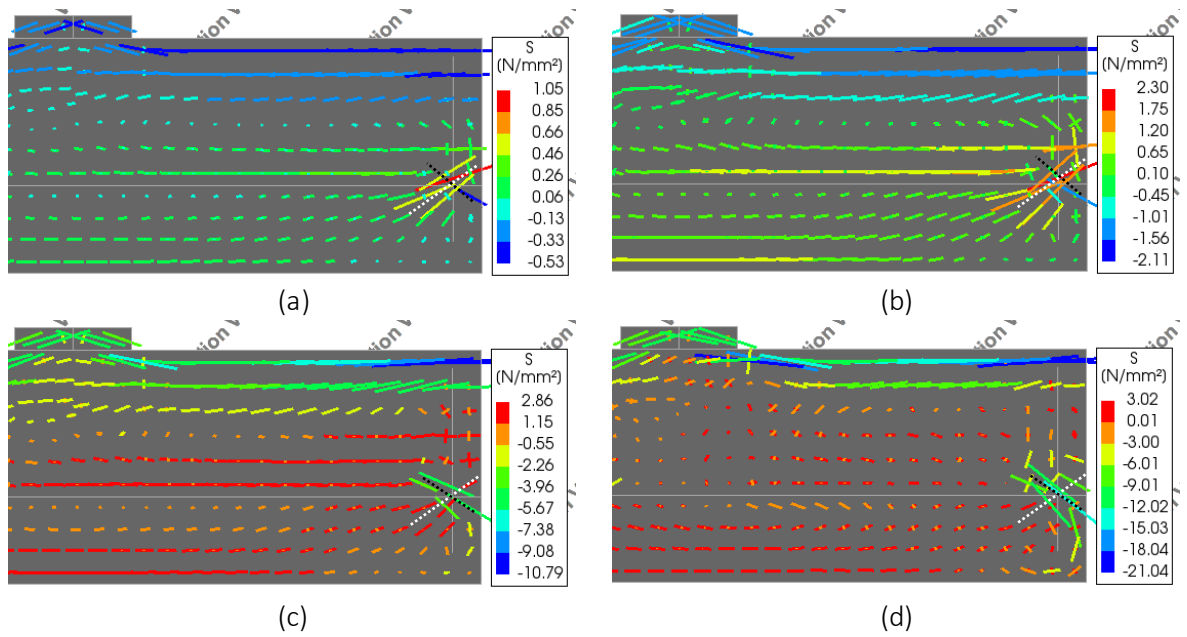


Figure 5.45 – In-plane principal stress at the stirrup section of model 3D-SI-SJ (a) at the beginning of analysis, (b) at load stage 1, (c) right after load stage 2, (d) at load stage 3

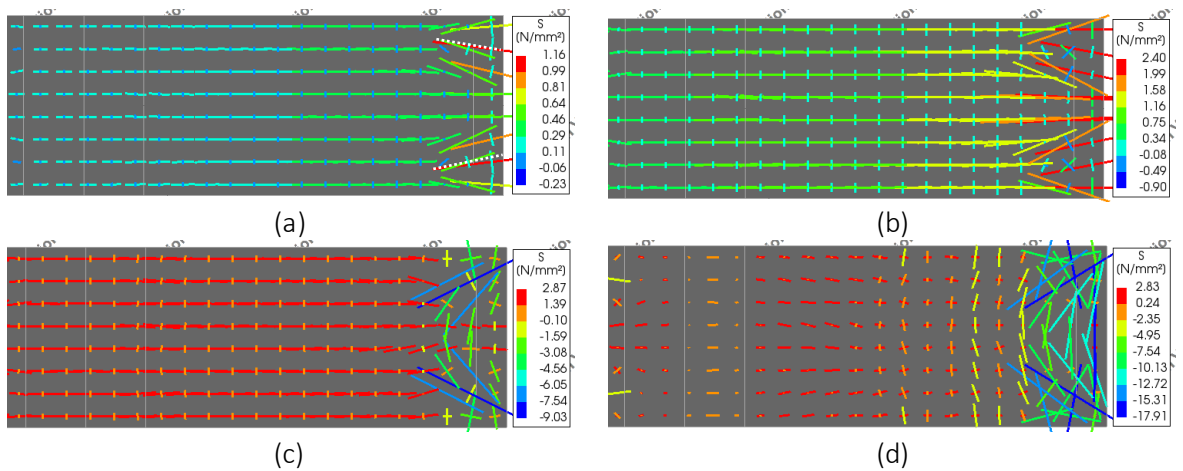


Figure 5.46 – In-plane principal stress at the top side of interface of model 3D-SI-SJ (a) at the beginning of analysis, (b) at load stage 1, (c) right after load stage 2, (d) at load stage 3

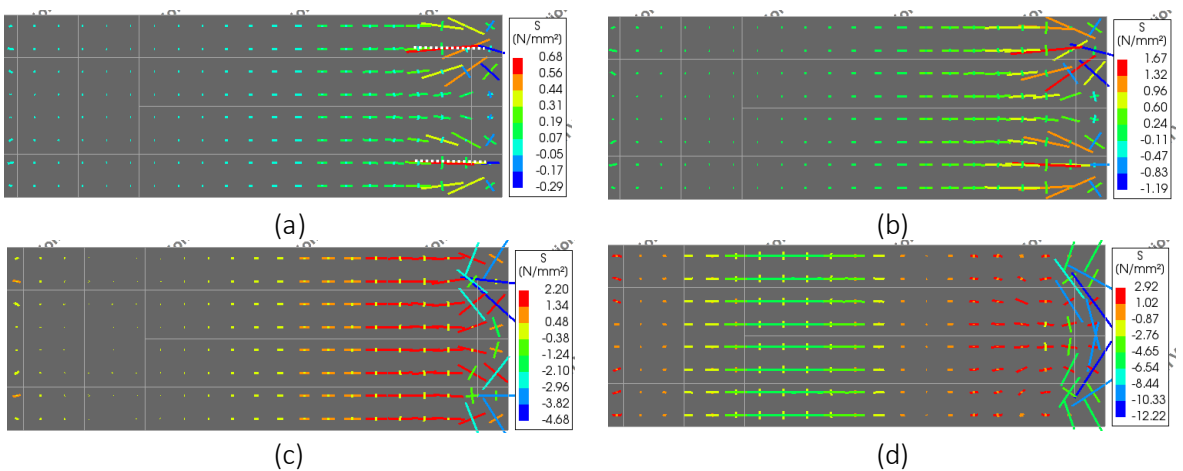


Figure 5.47 – In-plane principal stress at the bottom side of interface of model 3D-SI-SJ (a) at the beginning of analysis, (b) at load stage 1, (c) right after load stage 2, (d) at load stage 3

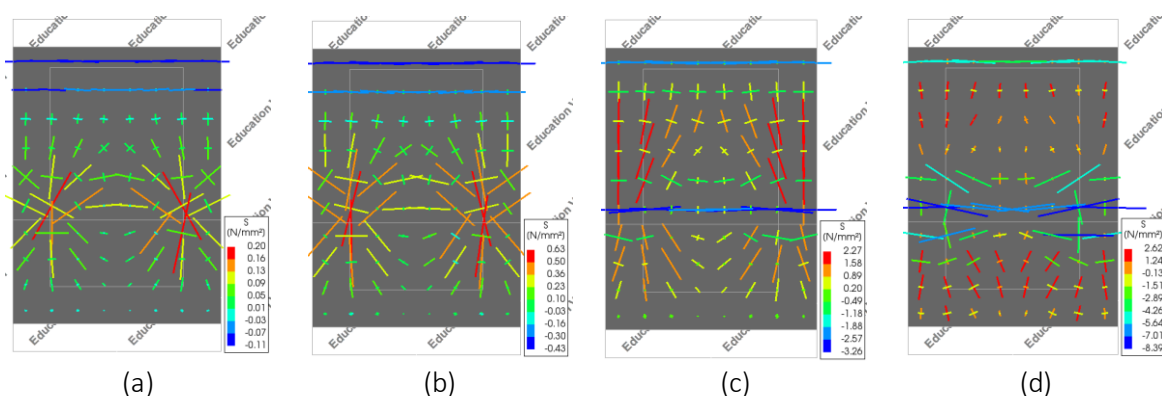


Figure 5.48 – In-plane principal stress at the stirrup location of model 3D-SI-SJ

(a) at the beginning of analysis, (b) at load stage 1, (c) right after load stage 2, (d) at load stage 3

At the beginning of the analysis, similar to the unreinforced interface model (3D-SI), a stress concentration in longitudinal direction develops at the joint as indicated with a black dotted circle in Figure 5.44(a). This stress concentration is also reflected in a peak of tensile and shear stresses at the joint as in model 3D-SI, which can be seen in Figure 5.40 and Figure 5.41. However, due to the presence of stirrup, the normal and shear stresses concentration has occurred from the beginning of the analysis as indicated by black arrows in Figure 5.42(a) and Figure 5.43(a). It is related to the dowel action which can be observed from the in-plane principal stress in Figure 5.45(a), Figure 5.46(a), and Figure 5.47(a) with the tensile ties (white dotted line) and compression strut (black dotted line) at the location of the stirrup. The presence of the dowel action from the beginning of analysis means the stirrup has been utilized to transfer of the tensile force from the precast layer to the cast-in-situ layer from the beginning of analysis. When the load reaches load stage 1, the coupling reinforcement starts to take the tensile stress from the surrounding cracked concrete matrix at the joint. As a result, from load stage 2, the stress pattern of reinforcement bond transfer can be in Figure 5.44(c) and (d).

Figure 5.39 shows that as the load increases and reaches load stage 2, the node at location A has an increase of tensile and shear stresses, while the node at location B, C, and D have an increase of compressive and shear stress. The difference which occurs in this figure, compared to the interface stresses development in unreinforced interface model (3D-SI), is the failure of the joint (location A) is not governed by the interface tensile strength (cut-off limit). Moreover, the number of load increments between load stage 2 (when the delamination occurs) and the maximum load is considerably larger, compared to model 3D-SI. Therefore, both differences explain why the interface tensile strength does not influence much to the capacity of the reinforced interface models.

As the load increases further, the peak of tensile stress shifts towards the end of coupling reinforcement as can be seen in Figure 5.40. This is following the shift of shear stress peak towards the same direction as can be seen in Figure 5.41. Similar to the unreinforced interface model (3D-SI), there is a decrease of the tensile stress peak value and the increase of the shear stress peak value as they shift. However, as can be seen in Figure 5.40, the tensile stress peak stops at around 890 mm, which is in accordance to Figure 5.42 (d) since the interface delamination stops there. Consequently, at load stage 3 (the end of the analysis), the concrete-to-concrete interface is not fully cracked until the end of coupling reinforcement (just barely passing the position of the stirrup). These uncracked interface elements maintain the ability to transfer the tensile force from the precast layer into the cast-in-situ layer, from the early load stage until load stage 3. As a result, this model could reach 103% higher load capacity at the end of this analysis compared to unreinforced interface model.

Most of the interface elements between the end of coupling reinforcement and stirrup are not only uncracked, but also in compression as shown in Figure 5.40. This high compressive interface area thus could provide higher transfer of tensile force from the precast layer to cast-in-situ layer through

interface shear stress as can be observed in Figure 5.41. This high shear stress area is the cause of the high influence of the cohesion parameter in the sensitivity study of reinforced interface models.

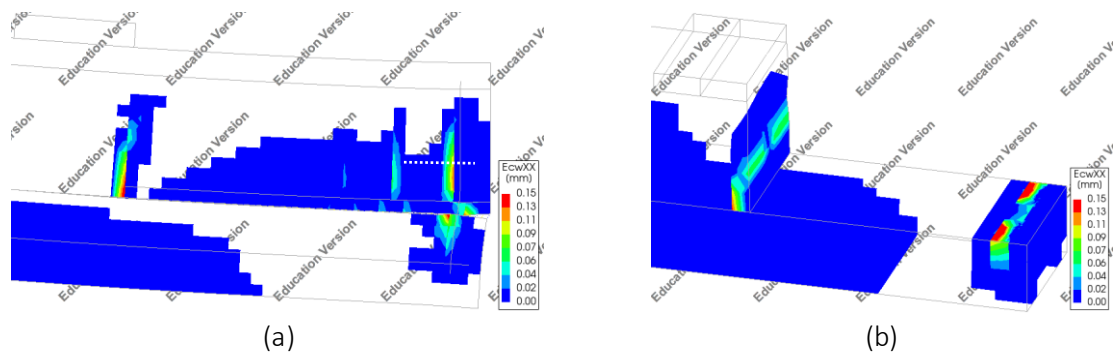


Figure 5.49 – Crack-width E_{cwXX} of (a) model 2D-SI-SJ and (b) model 3D-SI-SJ at 3.0 mm displacement

This model has a different failure mechanism compared to the 2D version of this model (2D-SI-SJ). The 2D model fails with a large crack at the end of coupling reinforcement and at the stirrup in precast layer. However, the 3D model (3D-SI-SJ) can continue to reach the yielding, although with a decreased structural stiffness after around 3.2 mm of vertical displacement. The reason to this difference is due to the assumed uniform crack along the width of the specimen in 2D model, while in 3D model, the crack is localized around the stirrup as shown in Figure 5.49. With a more localized crack, there are more capacity to transfer the tensile force from the precast layer to the cast-in-situ layer.

As described at the beginning of the discussion, this model can reach the yielding of coupling reinforcement, although in a really high displacement, around 20 mm. However, it should be noted that it can happen since the pull-out failure of stirrup is excluded in this model. In real situation, 20 mm of displacement is really high and the pull-out failure could be governing before this specimen reaches the yielding of coupling reinforcement.

5.2.1.2. Perfect bonded interface

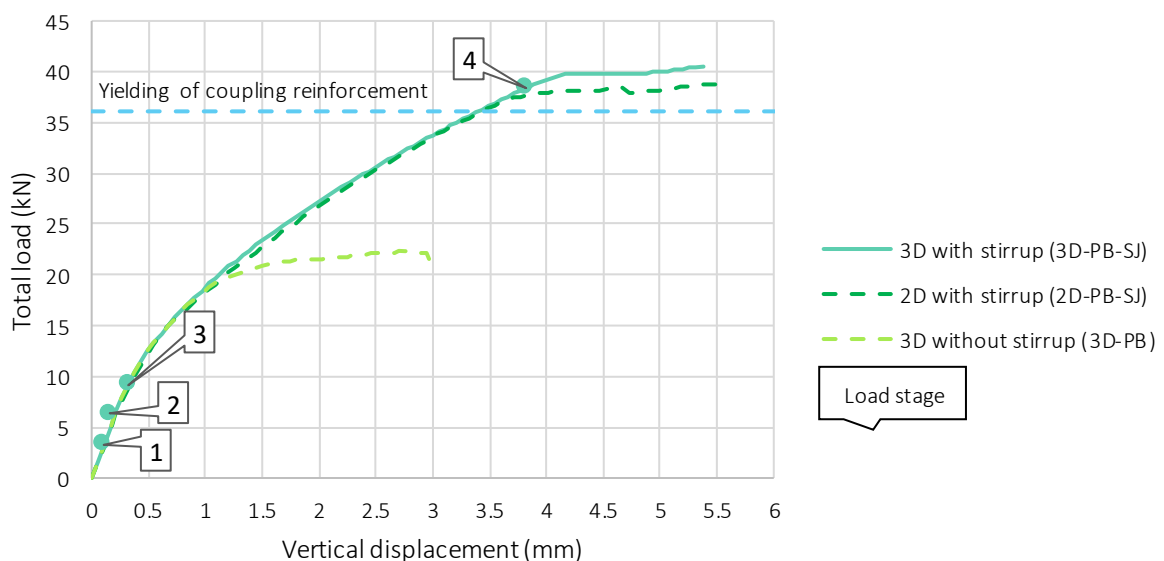


Figure 5.50 – Load-displacement graph of reinforced interface model with perfect bonded interface (2D-PB-SJ and 3D-PB-SJ)

In Figure 5.50, the load-displacement graph of reinforced interface model with perfect bonded interface (3D-PB-SJ) is shown. The maximum vertical load of this model is 40.50 kN. In that figure, the damage development of this model is marked at four load stages prior to the failure. Load stage 1 is at the onset

of a flexural crack at the joint, load stage 2 is at the start of an observed uneven stress distribution in transverse direction, load stage 3 is right before the start of horizontal crack at the joint, and load stage 4 is when the coupling reinforcement reaches its yielding strength.

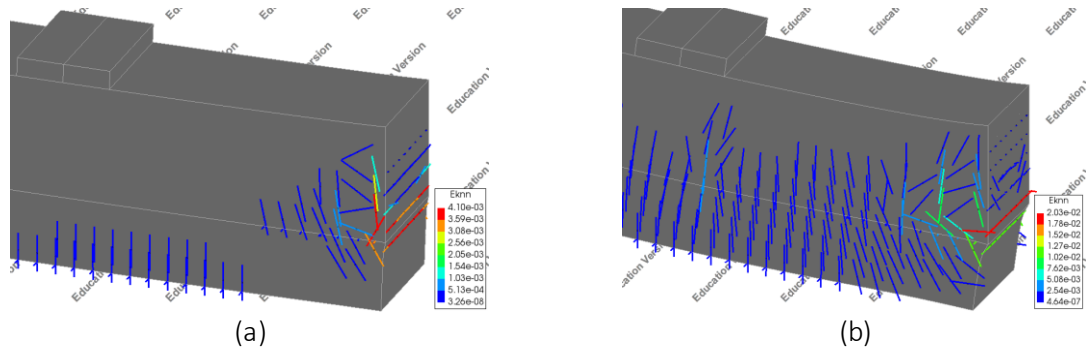


Figure 5.51 – Crack strain on the side of model 3D-PB-SJ (a) at $P = 20$ kN, (b) at load stage 4

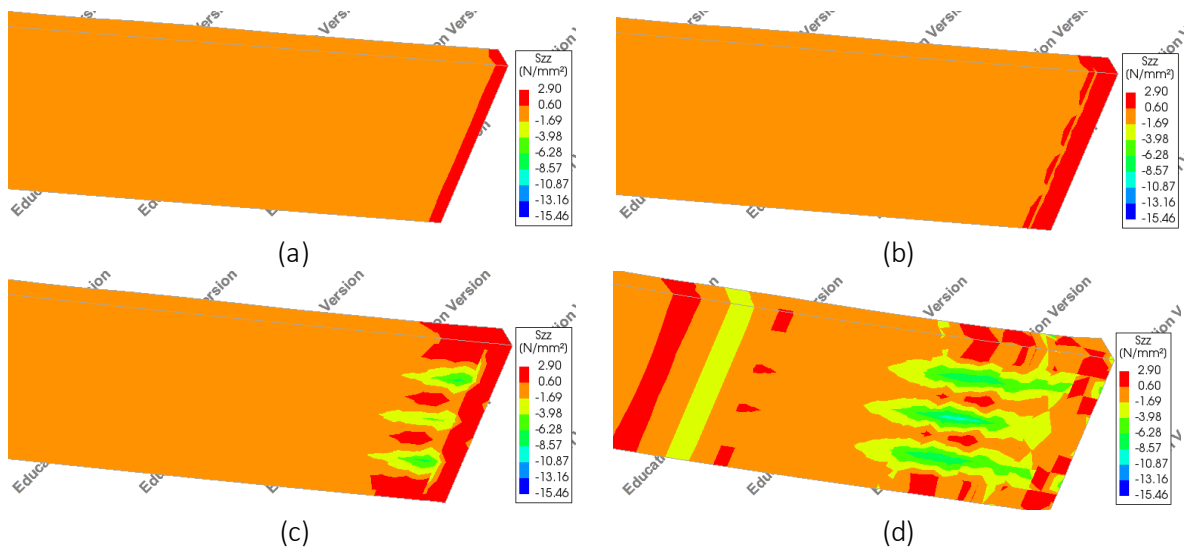


Figure 5.52 – Stress S_{zz} of the elements at the level of coupling reinforcement of model 3D-PB-SJ (a) at load stage 1, (b) right after load stage 2 (c) at $P = 20$ kN, (d) at load stage 4

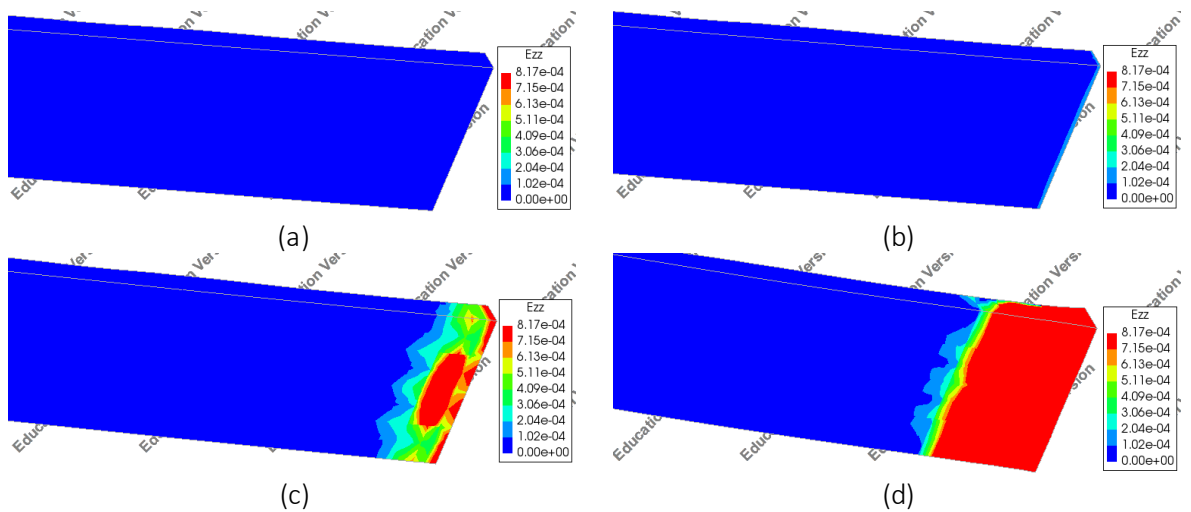


Figure 5.53 – Strain E_{zz} of the elements at the level of coupling reinforcement of model 3D-PB-SJ (a) at load stage 1, (b) right after load stage 2 (c) at $P = 20$ kN, (d) at load stage 4

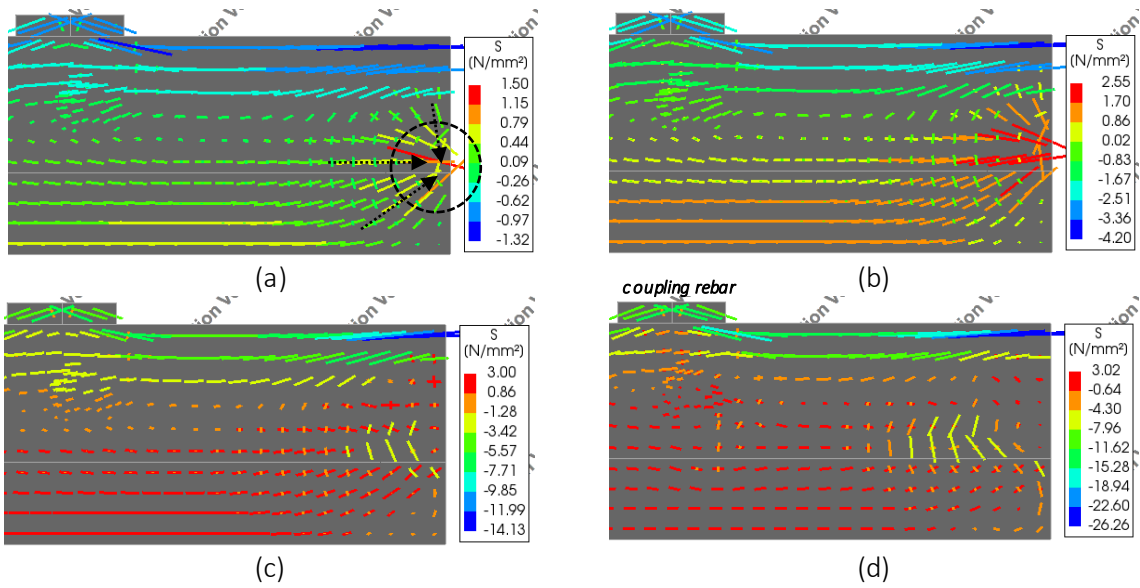


Figure 5.54 – In-plane principal stress at mid-section of model 3D-PB-SJ (a) at load stage 1, (b) right after load stage 3, (c) at $P = 20$ kN, (d) at load stage 4

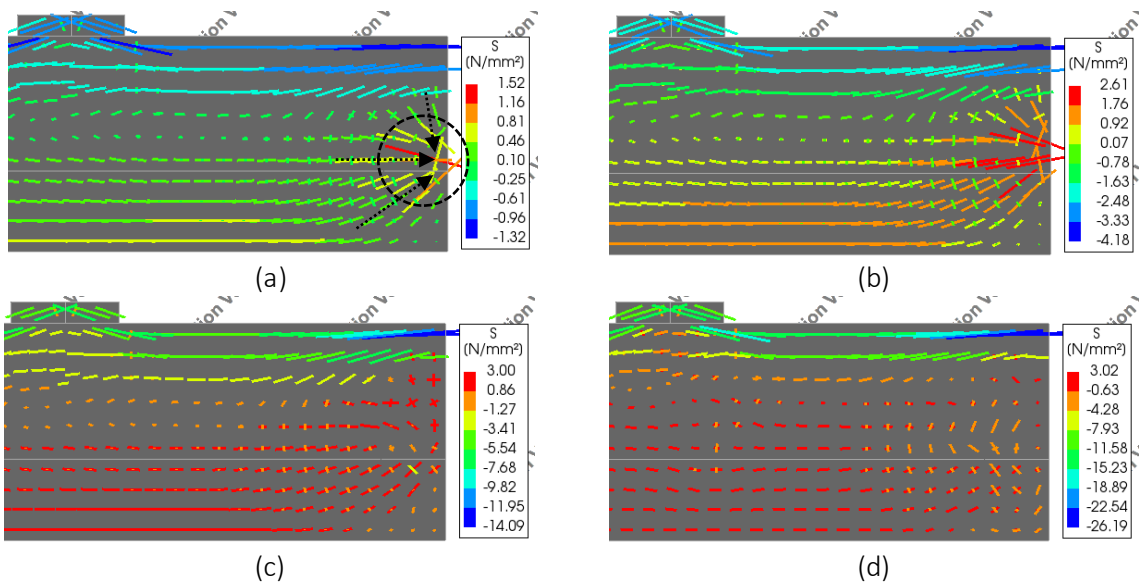


Figure 5.55 – In-plane principal stress at the stirrup section of model 3D-PB-SJ (a) at load stage 1, (b) right after load stage 3, (c) at $P = 20$ kN, (d) at load stage 4

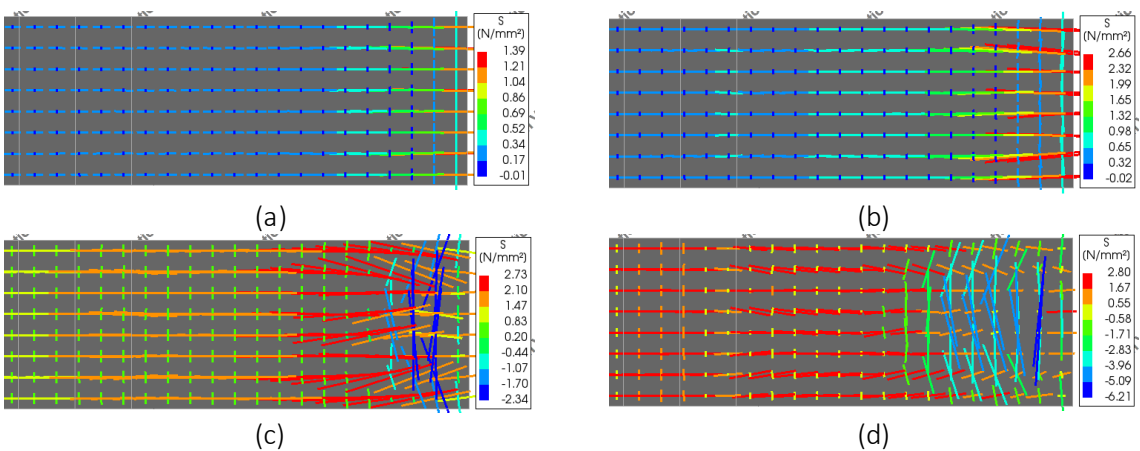


Figure 5.56 – In-plane principal stress at level of coupling reinforcement of model 3D-PB-SJ (a) at load stage 1, (b) right after load stage 3, (c) at $P = 20$ kN, (d) at load stage 4

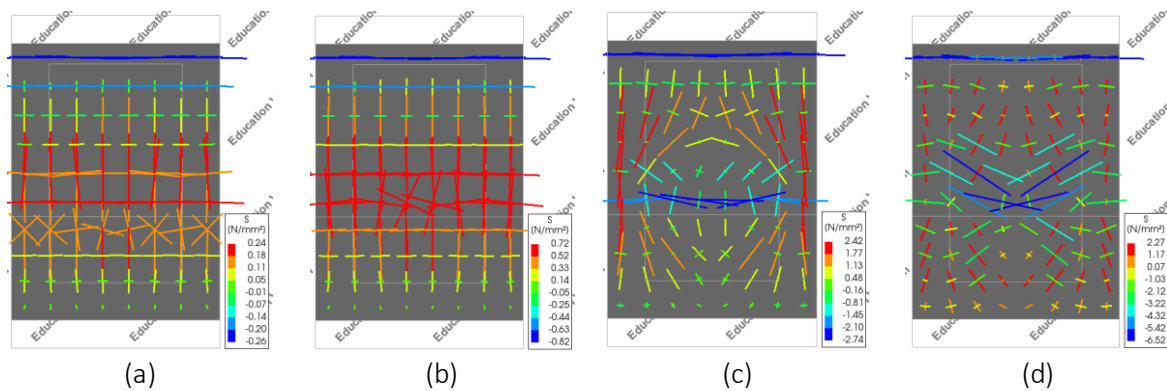


Figure 5.57 – In-plane principal stress at the stirrup location of model 3D-PB-SJ (a) at load stage 1, (b) right after load stage 3, (c) at $P = 20$ kN, (d) at load stage 4

At the beginning of the analysis, a stress concentration in longitudinal direction develops at the joint as indicated with a black dotted circles in Figure 5.54(a) and Figure 5.55(a). This stress concentration is also reflected in a peak of tensile and shear stresses at the joint as in model 3D-SI-SJ. Since in this model there is no Coulomb friction interface model and the horizontal crack is modelled with the continuum element itself (smeared crack), the cracks are governed only by the concrete tensile strength. Therefore, there is no interest to the shear stress along the coupling reinforcement.

When the load reaches load stage 1, the coupling reinforcement starts to take the tensile stress from the surrounding cracked concrete matrix at the joint. As a result, from load stage 2, there is a stress concentration around the coupling reinforcement, which can be seen in Figure 5.52(b). A non-uniform horizontal crack propagation across the width of the specimen also occurs in this model as shown in Figure 5.53(b). As the load increases further, the stress concentration and horizontal crack patterns shift further from the joint to the end of coupling reinforcement.

As the load increases and reaches load stage 3, the tensile stress component in vertical direction at the joint reaches the concrete tensile strength and resulted in a horizontal crack at the joint. As the load increases further, the horizontal crack propagates along the coupling reinforcement as shown in Figure 5.51(a). However, as the load reaches load stage 4, different from the unreinforced interface model (3D-PB), the horizontal crack propagation stops at around the stirrup location, as shown in Figure 5.53(d). Even, when Figure 5.51(b) is observed, the horizontal crack propagation does not only stop, but a lot of flexural cracks continuously propagate from the precast layer into the cast-in-situ layer. This structure behaves like a homogeneous structure. These uncracked concrete elements across the interface maintain the ability to transfer the tensile force from the precast layer into the cast-in-situ layer, from the early load stage until the structure reaches the yielding of coupling reinforcement. As a result, with this failure mechanism, this model has 81% increase of load capacity compared to the unreinforced interface model (3D-PB).

It is important to highlight that there is no dowel action observed in Figure 5.54 and especially in Figure 5.55, where the cutting plane intersect the position of the stirrup. It happens since in the model with perfect bonded interface, shear deformation around the stirrup is very small, while in the model with Coulomb friction interface, due to its weak shear properties, there is a large deformation which is even visible in Figure 5.38(b).

5.2.2. Single leg stirrup setup

Models with single leg stirrup setup are meant to increase the transverse distance between the stirrup while maintaining the total area of the stirrup crossing the interface. With the increase of distance, the influence of transverse distance can be observed. In experimental setup, the 6 mm diameter rectangular 2-leg stirrup is used for the connecting reinforcement. By changing the stirrup setup from rectangular shape into single vertical stirrup, the diameter of the single stirrup is increased into 8.49 mm and the effective transverse distance between each stirrup becomes 150 mm (equal to width of model). Similar to the setup of lap splice, ideally, further spacing is better to see its influence. However, this setup is chosen due to the limited computational resource available for the research.

This chapter also consists of two types of concrete-to-concrete interface, the untreated (smooth) interface and perfect bonded interface. The reinforcement and interface setup of model 3D-SI-SJ-1L and 3D-PB-SJ-1L are provided in Figure 5.58 and Figure 5.59.

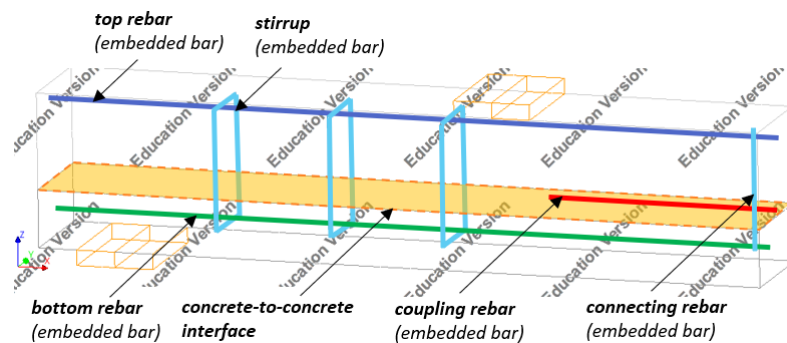


Figure 5.58 – Reinforcement setup and concrete-to-concrete interface of model with smooth interface (3D-SI-SJ-1L)

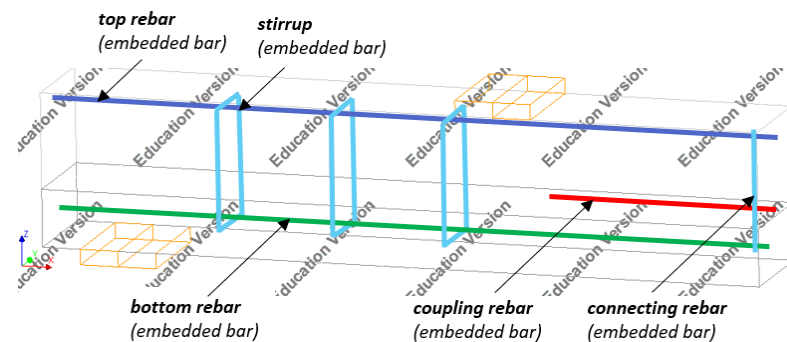


Figure 5.59 – Reinforcement setup of model with perfect bonded interface (3D-PB-SJ-1L)

5.2.2.1. Smooth interface

In Figure 5.60, the load-displacement graph of model 3D-SI-SJ-1L is shown. The maximum vertical load of the model is 23.74 kN at the end of the analysis, which is slightly lower compared to the model with experimental stirrup setup (3D-SI-SJ). In that figure, the damage development of this model is marked at three load stages prior to the failure. Load stage 1 is at the onset of the flexural crack at the joint and the start of an observed uneven stress distribution in transverse direction, load stage 2 is right before the start of the delamination at the joint, and load stage 3 is at the end of the analysis. Similar to model 3D-SI-SJ, the specimen in this model has not failed yet at the end of the analysis. If the prescribed displacement is increased, the load-displacement graph will reach the yielding of coupling reinforcement though in a really high displacement. For the purpose of this analysis, the load-displacement graph of this model is only presented as shown in Figure 5.60, which is until 4 mm of prescribed displacement.

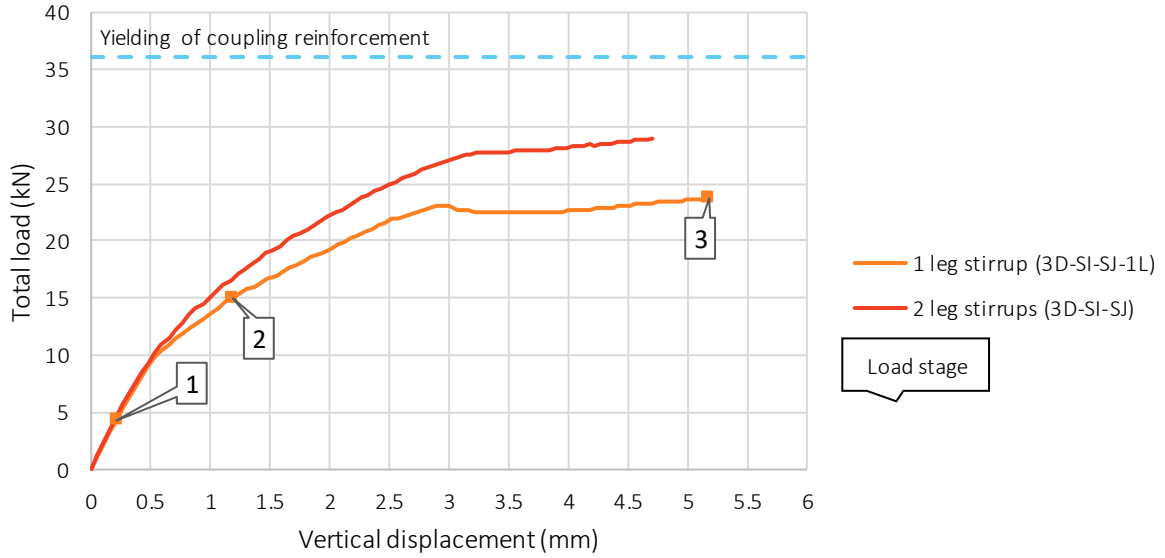


Figure 5.60 – Load-displacement graph of reinforced interface model with smooth interface and single leg stirrup (3D-SI-SJ-1L)

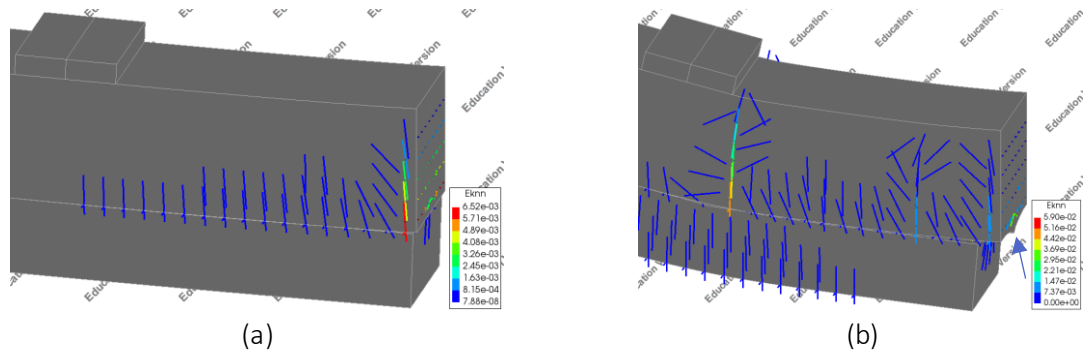


Figure 5.61 – Crackstrain on the side of model 3D-SI-SJ-1L
(a) right after load stage 2, (b) at load stage 3

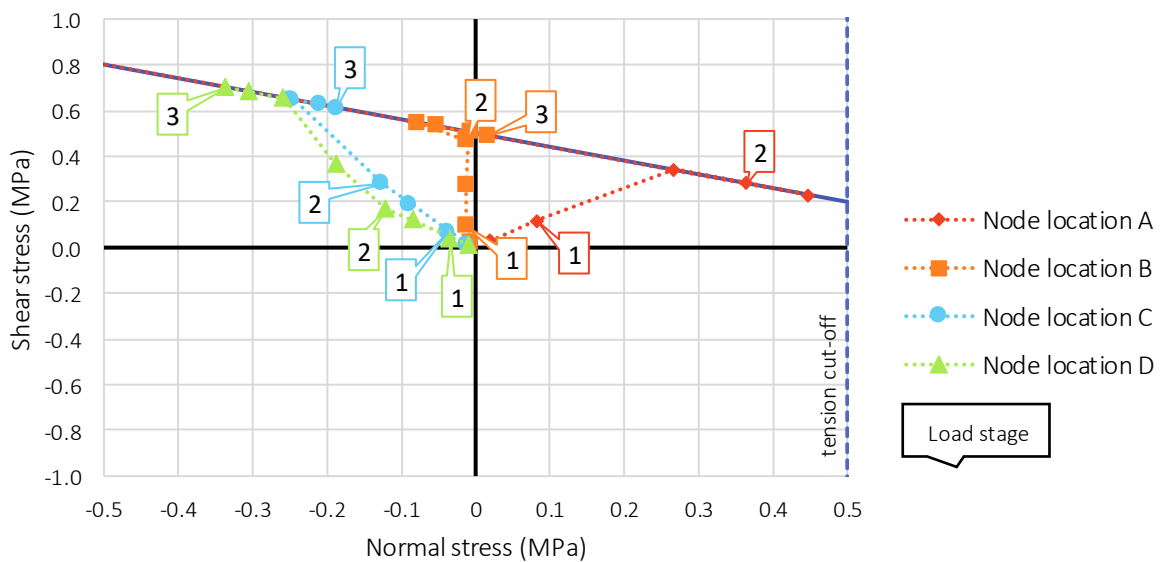


Figure 5.62 – Interface stresses development of model 3D-SI-1L at four nodes location

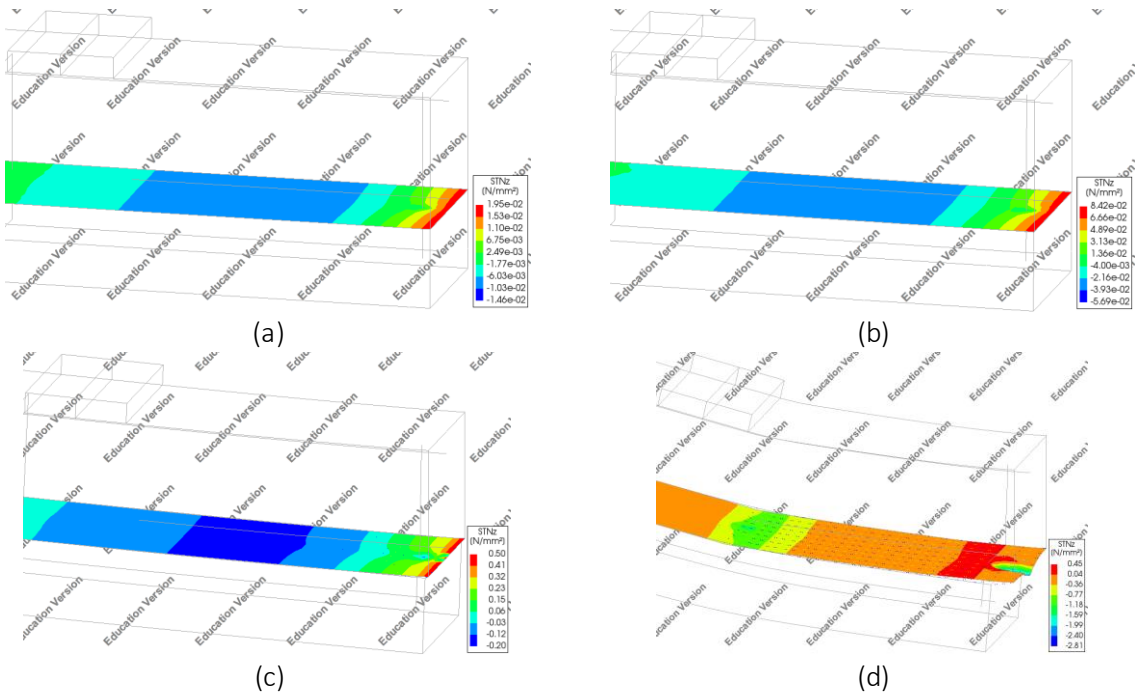


Figure 5.63 – Interface normal stress STN_z development of model 3D-SI-SJ-1L
 (a) at the beginning of analysis, (b) at load stage 1, (c) right after load stage 2, (d) at load stage 3

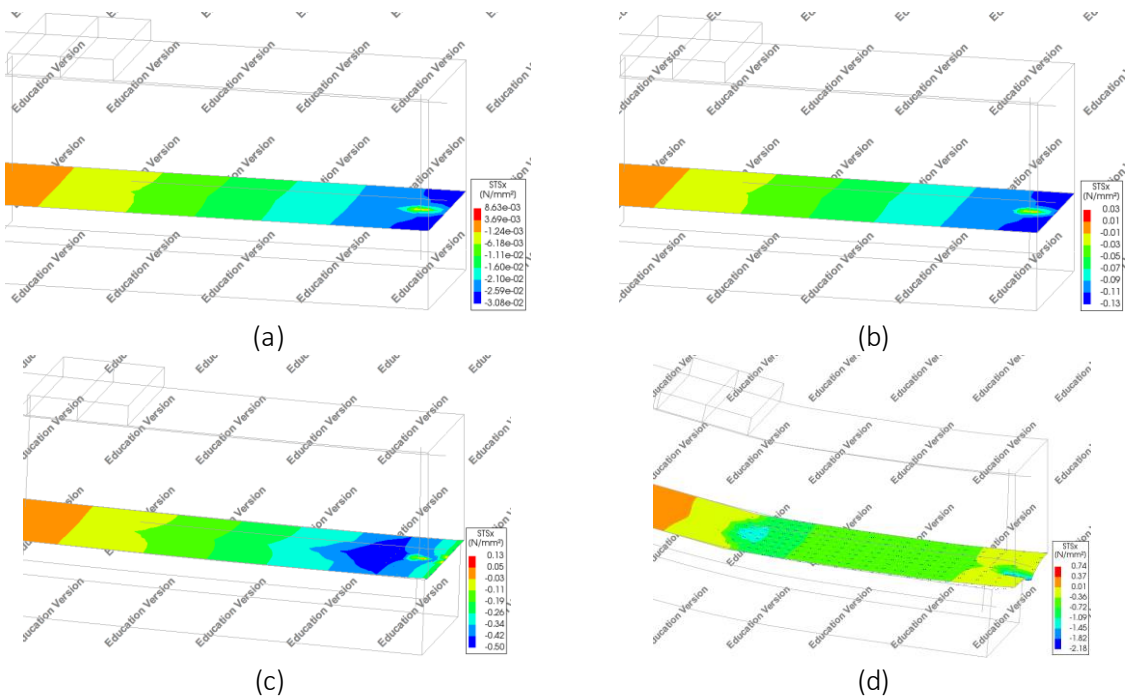


Figure 5.64 – Interface shear stress STS_x development of model 3D-SI-SJ-1L
 (a) at the beginning of analysis, (b) at load stage 1, (c) right after load stage 2, (d) at load stage 3

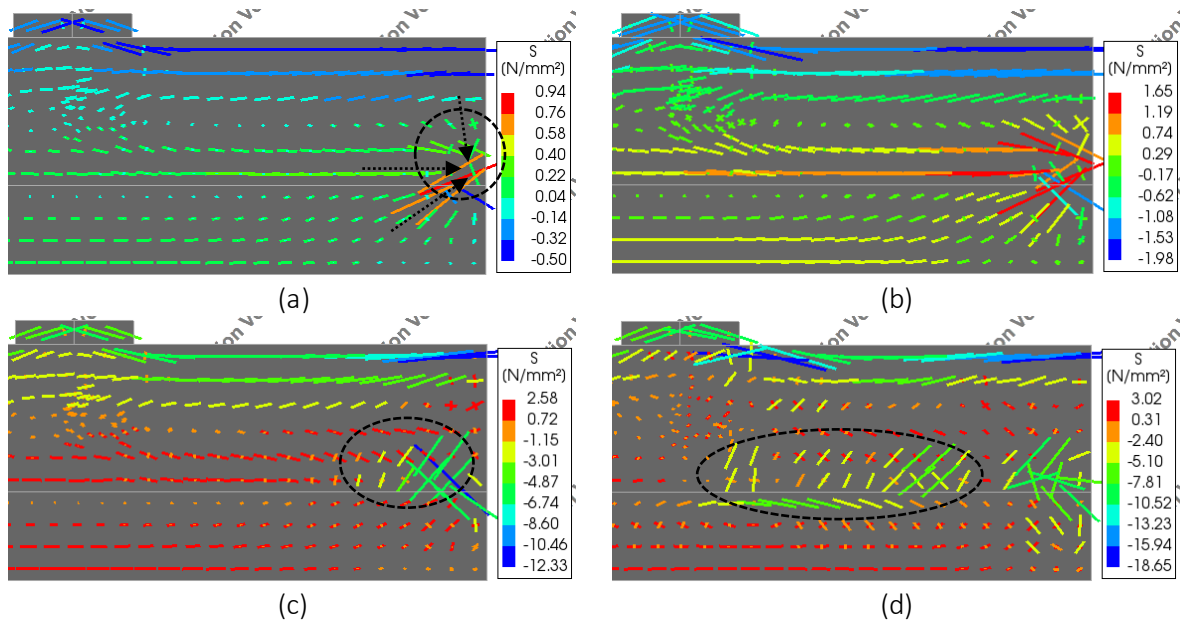


Figure 5.65 – In-plane principal stress at mid-section of model 3D-SI-SJ-1L
 (a) at the beginning of analysis, (b) at load stage 1, (c) right after load stage 2, (d) at load stage 3

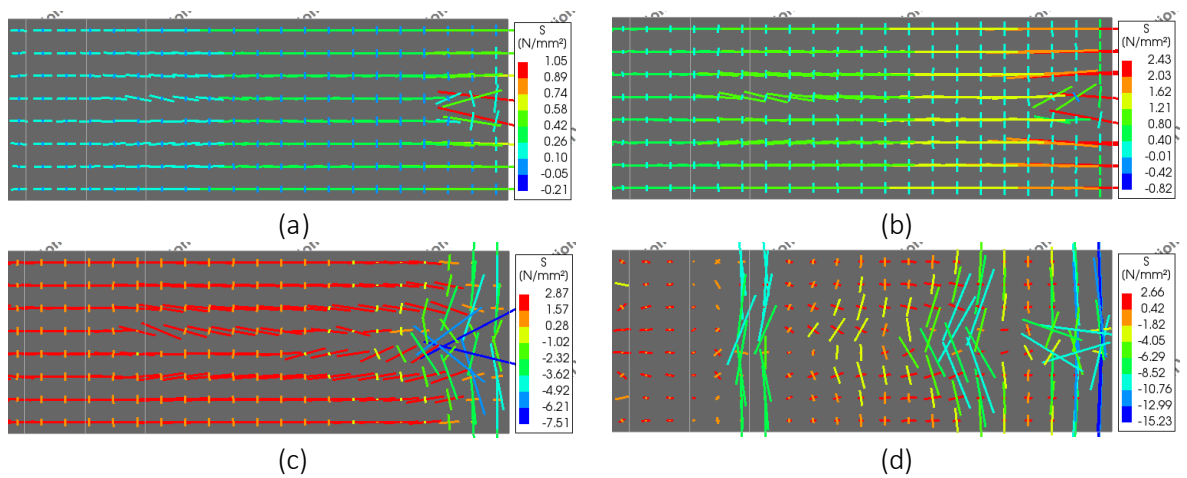


Figure 5.66 – In-plane principal stress at the top side of interface of model 3D-SI-SJ-1L
 (a) at the beginning of analysis, (b) at load stage 1, (c) right after load stage 2, (d) at load stage 3

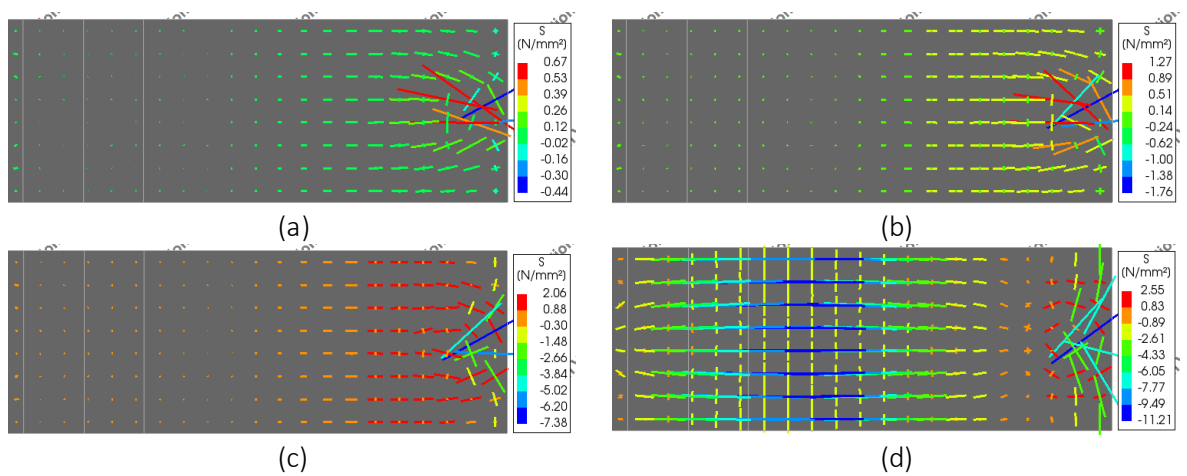


Figure 5.67 – In-plane principal stress at the bottom side of interface of model 3D-SI-SJ-1L
 (a) at the beginning of analysis, (b) at load stage 1, (c) right after load stage 2, (d) at load stage 3

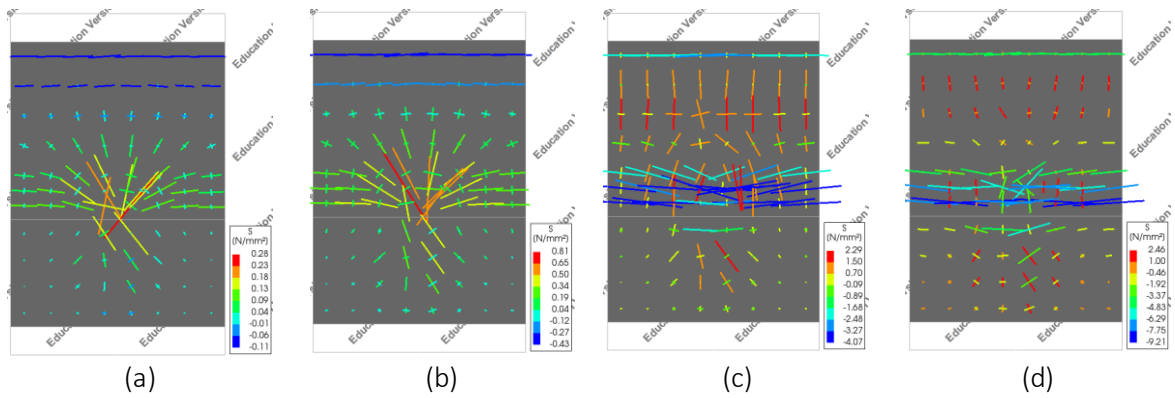


Figure 5.68 – In-plane principal stress at the stirrup location of model 3D-SI-SJ-1L (a) at the beginning of analysis, (b) at load stage 1, (c) right after load stage 2, (d) at load stage 3

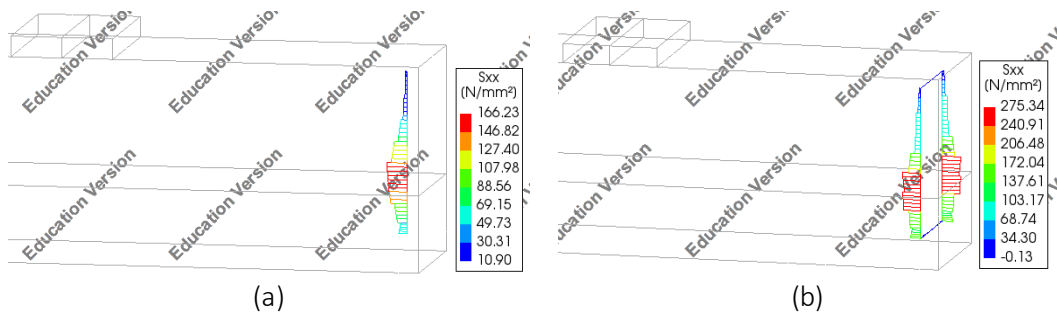


Figure 5.69 – Sxx of connecting reinforcement of (a) model 3D-SI-SJ (b) model 3D-SI-SJ-1L at 4 mm vertical displacement

At the beginning of the analysis, a stress concentration in longitudinal direction develops at the joint as indicated with a black dashed circles in Figure 5.65(a). This stress concentration is also reflected in a peak of tensile and shear stresses at the joint as in model 3D-SI-SJ. The normal and shear stresses concentration, which is caused by the presence of stirrup, occur from the beginning of the analysis as shown in Figure 5.63(a) and Figure 5.64(a). The related dowel action can be observed from the in-plane principal stress in Figure 5.65(a), Figure 5.66(a), and Figure 5.68(a). When the load reaches load stage 1, the coupling reinforcement starts to take the tensile stress from the surrounding cracked concrete matrix at the joint. As a result, from load stage 2, the stress pattern of reinforcement bond transfer can be in Figure 5.65 (c) and (d).

As the load increases further, the horizontal crack grows along the interface. As it reaches load stage 3, the interface delamination stops around the stirrup which can be seen in Figure 5.63(d). Consequently, at load stage 3 (the end of the analysis), the concrete-to-concrete interface is not fully cracked until the end of coupling reinforcement (just barely passing the position of the stirrup). These uncracked interface elements maintain the ability to transfer the tensile force from the precast layer into the cast-in-situ layer, from the early load stage until load stage 3. As a result, this model could reach 67% higher load capacity at the end of this analysis compared to unreinforced interface model.

As shown in Figure 5.60, the load capacity of this model is lower than the model with two leg stirrups (3D-SI-SJ). It happens because in the model with single leg stirrup, as can be seen Figure 5.67, the total area which can distribute the stress to the stirrup is smaller than the one in Figure 5.47. As a result, the stress in the stirrup of model with single leg stirrup (Figure 5.69(a)) is lower than the stress in the stirrup of the model with experimental stirrup setup (Figure 5.69(b)). The lower the stress in the stirrup, the lower the tensile stress which could be transferred from the precast layer to the cast-in-situ layer, thus the lower the maximum load.

5.2.2.2. Perfect bonded interface

In Figure 5.70, the load-displacement graph of reinforced interface model with perfect bonded interface and single leg stirrup (3D-PB-SJ-1L) is shown. The maximum vertical load of this model is 39.64 kN, which is similar to the model with the experimental stirrup setup (3D-PB-SJ). In that figure, the damage development of this model is marked at four load stages prior to the failure. Load stage 1 is at the onset of a flexural crack at the joint, load stage 2 is at the start of an observed uneven stress distribution in transverse direction, load stage 3 is right before the start of horizontal crack at the joint, and load stage 4 is when the coupling reinforcement reaches its yielding strength.

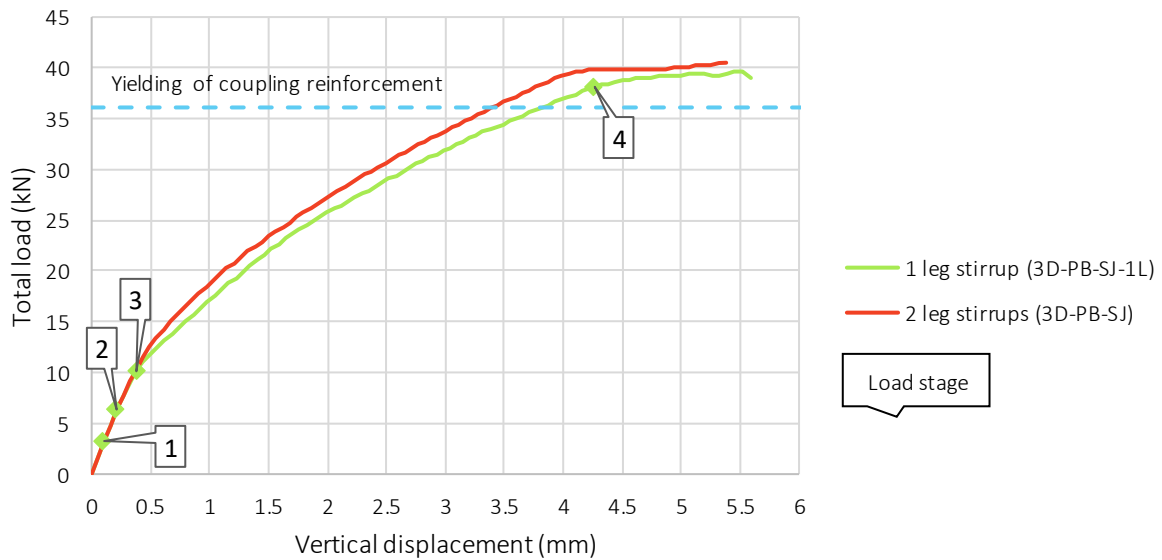


Figure 5.70 – Load-displacement graph of reinforced interface model with perfect bonded interface and single leg stirrup (3D-PB-SJ-1L)

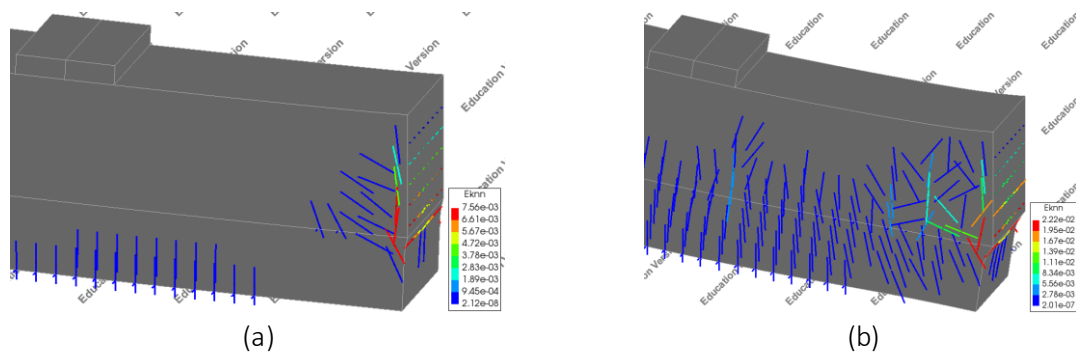


Figure 5.71 – Crack strain on the side of model 3D-PB-SJ-1L (a) at P = 20 kN, (b) at load stage 4

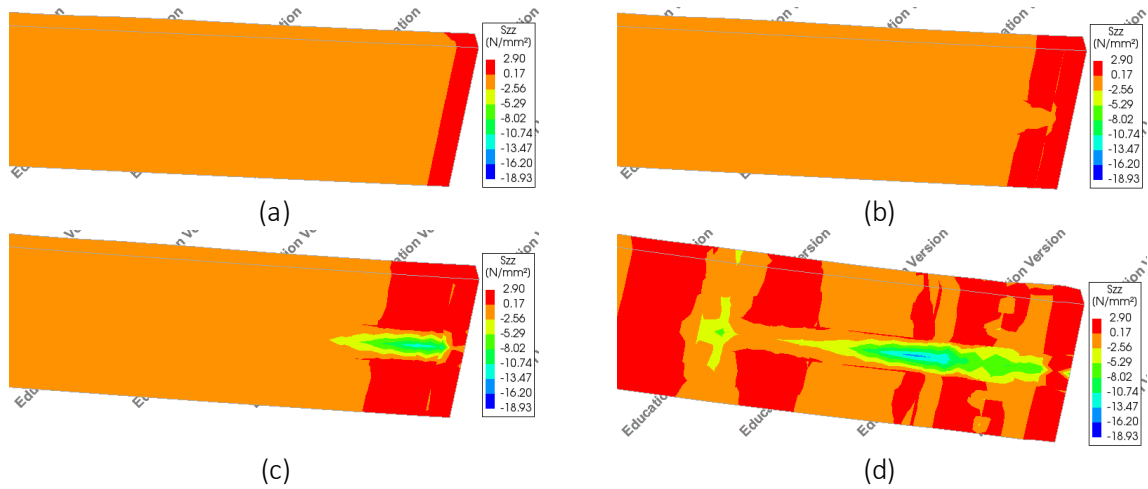


Figure 5.72 – Stress S_{zz} of the elements at the level of coupling reinforcement of model 3D-PB-SJ-1L (a) at load stage 1, (b) right after load stage 3 (b) at $P = 20$ kN, (b) at load stage 4

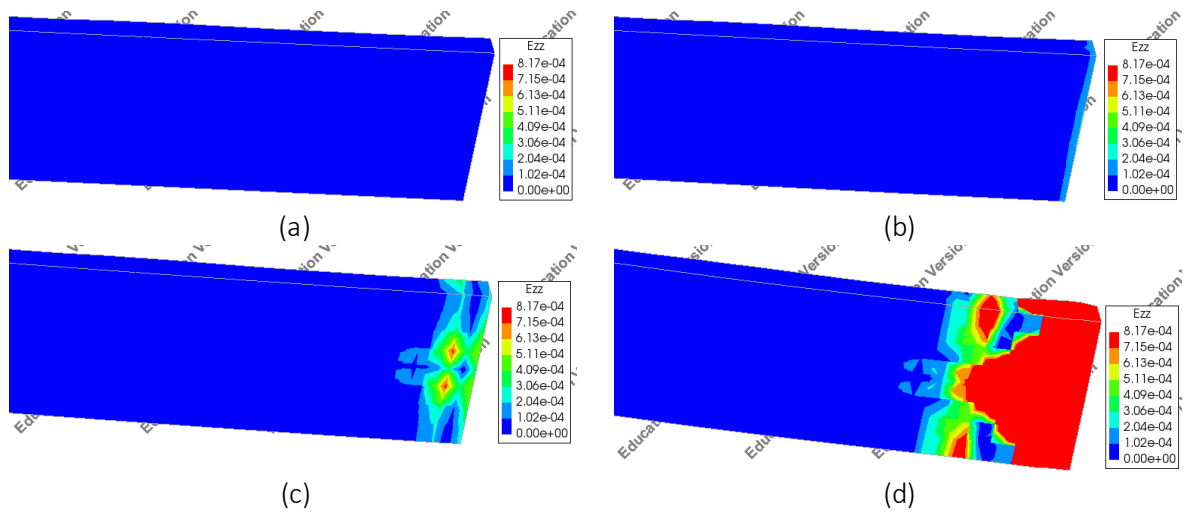


Figure 5.73 – Strain E_{zz} of the elements at the level of coupling reinforcement of model 3D-PB-SJ-1L (a) at load stage 1, (b) right after load stage 3 (b) at $P = 20$ kN, (b) at load stage 4

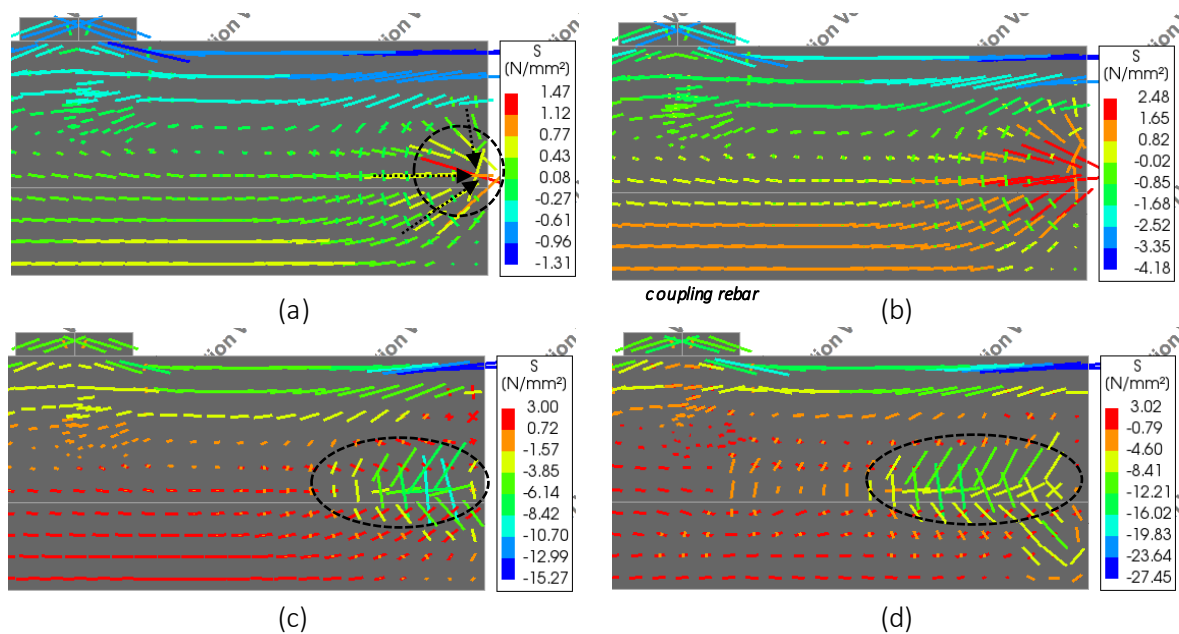


Figure 5.74 – In-plane principal stress at mid-section of model 3D-PB-SJ-1L (a) at load stage 1, (b) right after load stage 3, (c) at $P = 20$ kN, (d) at load stage 4

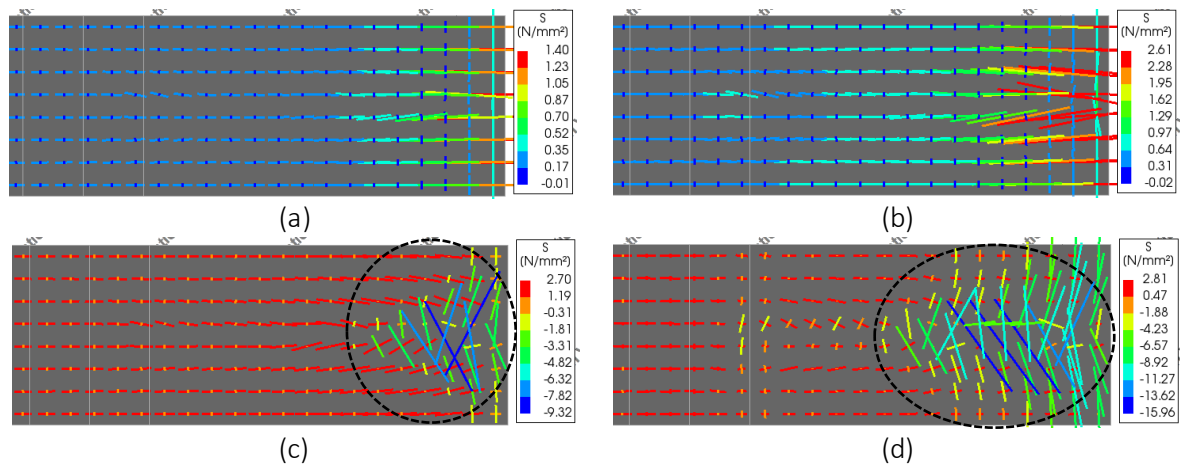


Figure 5.75 – In-plane principal stress at level of coupling reinforcement of model 3D-PB-SJ-1L (a) at load stage 1, (b) right after load stage 3, (c) at $P = 20$ kN, (d) at load stage 4

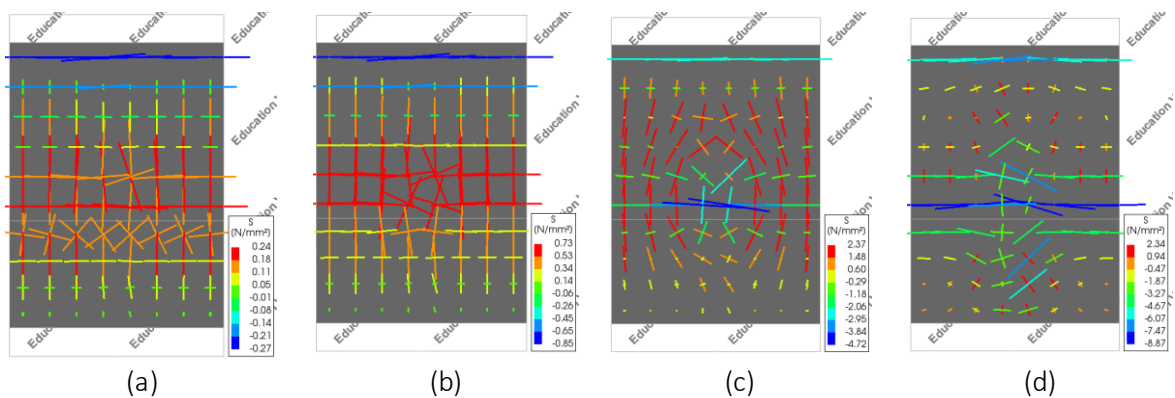


Figure 5.76 – In-plane principal stress at the stirrup location of model 3D-PB-SJ-1L (a) at load stage 1, (b) right after load stage 3, (c) at $P = 20$ kN, (d) at load stage 4

At the beginning of the analysis, a stress concentration in longitudinal direction develops at the joint as indicated with a black dashed circles in Figure 5.74(a). This stress concentration is also reflected in a peak of tensile stress at the joint as can be observed in Figure 5.72(a). When the load reaches load stage 1, the coupling reinforcement starts to take the tensile stress from the surrounding cracked concrete matrix at the joint. As a result, from load stage 2, there is a stress concentration around the coupling reinforcement, which can be seen in Figure 5.72(b). A non-uniform horizontal crack propagation across the width of the specimen also occurs in this model as shown in Figure 5.73(b). As the load increases further, the stress concentration and horizontal crack patterns shift further from the joint to the end of coupling reinforcement.

As the load increases and reaches load stage 3, the tensile stress component in vertical direction at the joint reaches the concrete tensile strength and resulted in a horizontal crack at the joint. As the load increases further, the horizontal crack propagates along the coupling reinforcement as shown in Figure 5.71(a). However, as the load reaches load stage 4, similar to the model with experimental stirrup setup, the horizontal crack propagation stops at around the stirrup location, as shown in Figure 5.73(d). These uncracked concrete elements across the interface maintain the ability to transfer the tensile force from the precast layer into the cast-in-situ layer, from the early load stage until the structure reaches the yielding of coupling reinforcement.

In Figure 5.73(d), the horizontal crack propagation is concentrated around the coupling reinforcement location. The same behaviour can be found in the unreinforced model with perfect bonded interface and single lap splice (3D-PB-1L), as shown in Figure 5.29(b). In that model, this cracking behaviour increases the capacity of the structure, in compared to the model with three lap splices (3D-PB).

However, in this model with single leg stirrup, this concentrated horizontal crack propagation is not reflected in a higher load at a given vertical displacement, in compared to the model with 2 stirrup legs (3D-PB-SJ). It might be caused by the presence of the stirrup which provides an alternative way to transfer the tensile force from the precast layer to the cast-in-situ layer. So, even this concentrated horizontal crack propagation has more uncracked elements around the cracking pattern, the stirrup is more governing in this situation.

5.3. Laterally restrained beams

In the third part of the numerical study, the unreinforced interface models which are discussed in chapter 5.1.1 are restrained in lateral direction in order to understand the influence of the lateral restraint on the behaviour of the structure. This restraint is modelled as full height translational restraint in x-direction of 2D model at the location of the boundary to introduce infinitely stiff restraint.

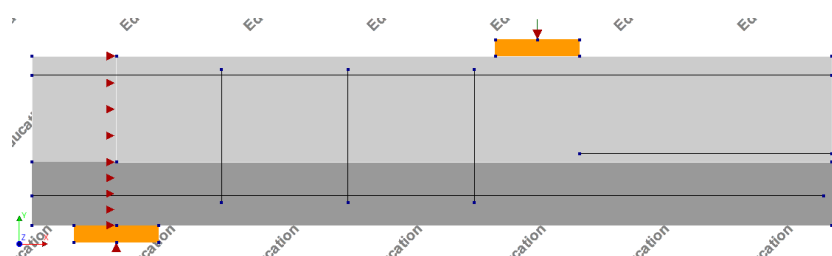


Figure 5.77 – Finite element model of laterally restraint unreinforced beam with a perfect bonded interface (2D-PB-RC-FR)

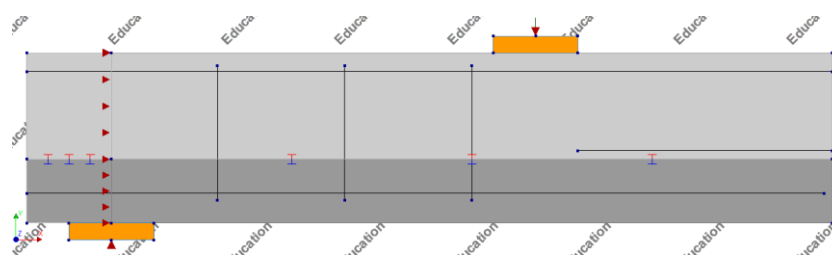


Figure 5.78 – Finite element model of laterally restraint unreinforced beam with a smooth interface (2D-SI-RC-FR)

As explained in the opening of this chapter, there are two types of the concrete-to-concrete interface included in each analyses. However, different from the previous analyses, in this chapter, the analysis of model with perfect bonded interface is presented first and followed by the analysis of model with smooth interface. This is done since the floor structure which is described in the literature reference in chapter 2.4 is a homogeneous concrete floor. Therefore, it is better to first study the behaviour of the structure with perfect bonded interface and analysing it with the available reference, then introduce a Coulomb friction interface to the model. Moreover, all of the models in this chapter use the same type of regular concrete as described in Table 3.7 for all of the layers, instead of using SHCC for the precast layer. The other numerical setup is applied to the models as described in chapter 3.2.

5.3.1. Perfect bonded interface

In Figure 5.79, the load-displacement graph of the laterally restrained model (2D-PB-RC-FR) is shown with the maximum load at 283.85 kN. The graph includes the comparison to the simply supported model (2D-PB-RC) which has the same numerical setup with model 2D-PB but with regular concrete used in both concrete layers so it could be compared with model 2D-PB-RC-FR. As a comparison, the model with lateral restraint has 14.5 times higher load capacity than the model without lateral restraint. There are two analytical solutions for the failure mechanism of this structure. Due to the lateral restraint at the support locations, this structure has a degree of statically indeterminate (n) equal to 2, thus it has three

hinge for the mechanism. The orange dashed line represents the total load when the moment at the support equal to plastic moment of the section at the support while the red dashed line represents the total load when the moment at the joint equals to the plastic moment of the section at the joint. The calculation of the value of these loads are provided in the appendix.

In that figure, the damage development of this model is marked at six load stages prior to the failure, so the interface behaviour can be analysed step-by-step. The damage development at each load stage can be observed in Figure 5.81. Load stage 1 is at the onset of a flexural crack at the top of cast-in-situ layer near the support and at the joint, load stage 2 is when the top reinforcement at the support reaches the yield strength, load stage 3 is when the section at the support has become fully plastic and starts the plastic rotation, load stage 4 is at the start of concrete crushing, load stage 5 is when the bottom part of the section at support has fully crushed, and load stage 6 is at the failure when a flexural crack at the end of the coupling reinforcement reaches the top of the cast-in-situ layer.

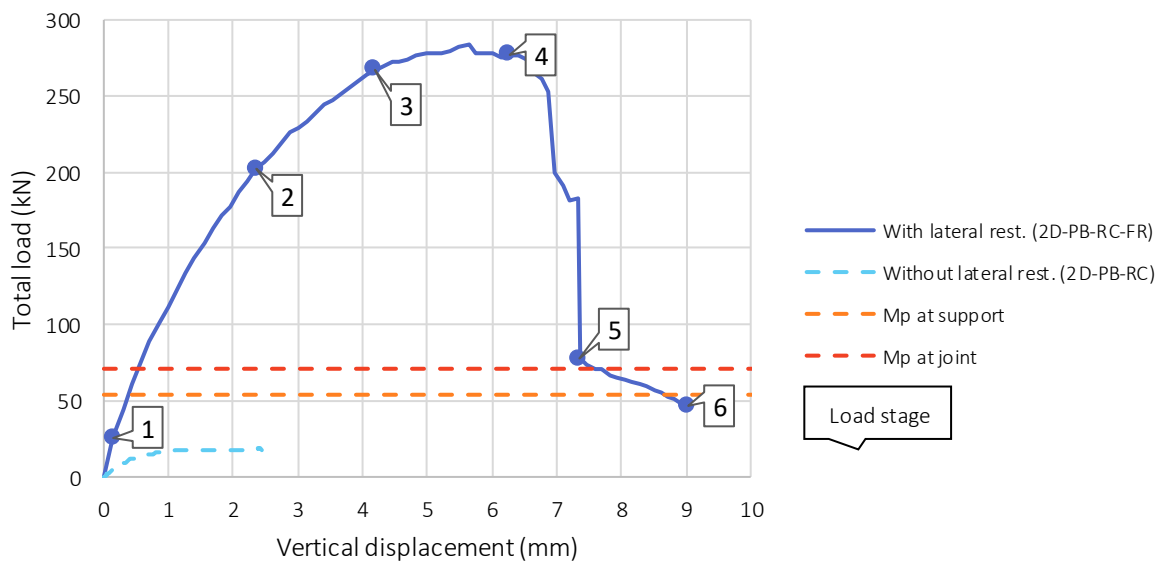


Figure 5.79 – Load-displacement graph of laterally restrained unreinforced interface model with perfect bonded interface (2D-PB-RC-FR)

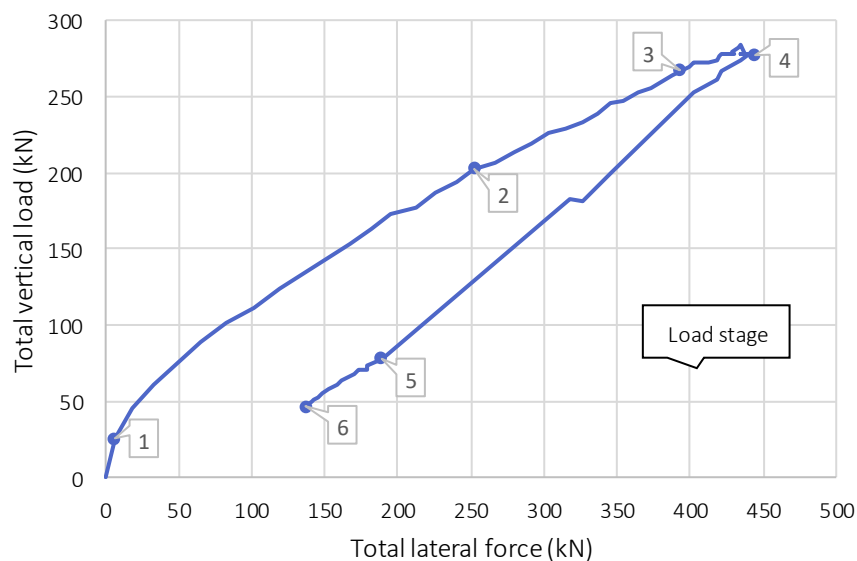


Figure 5.80 – Total load-total lateral force graph of laterally restrained unreinforced interface model with perfect bonded interface (2D-PB-RC-FR)

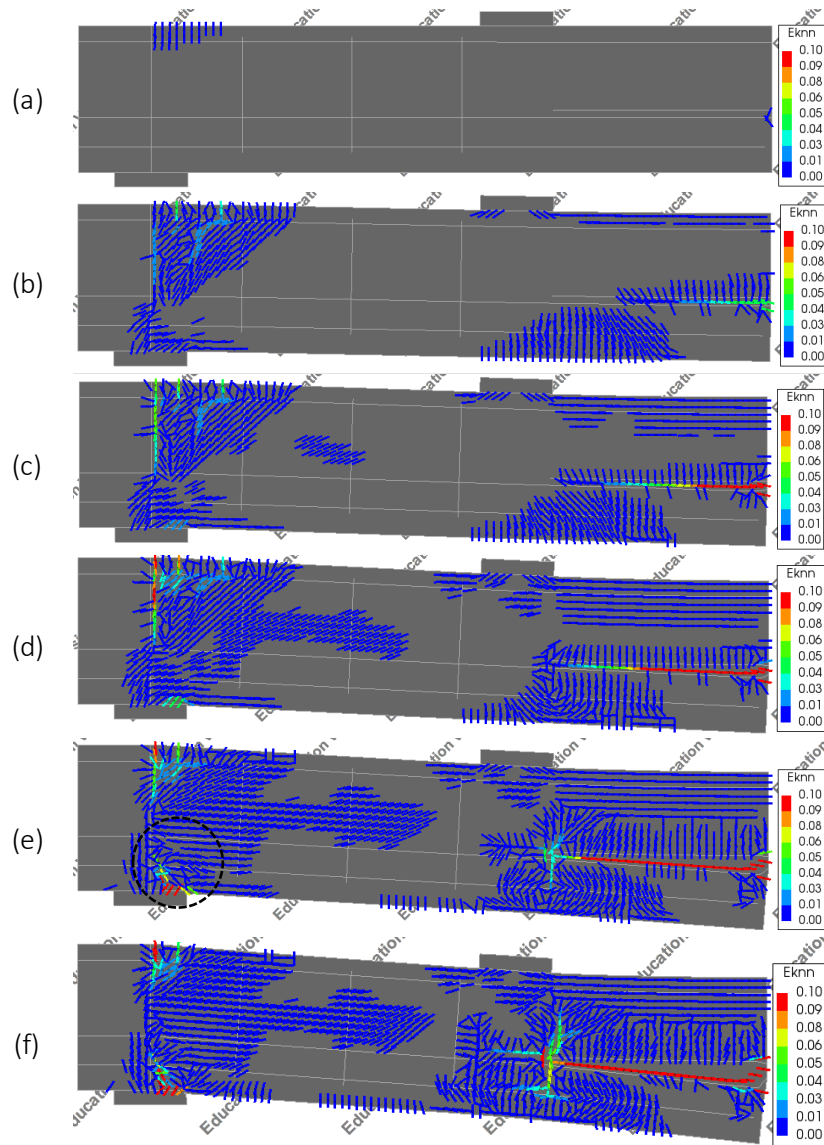


Figure 5.81 – Crack strain of model 2D-PB-RC-FR at load stage (a) 1, (b) 3, (c) 3, (d) 4, (e) 5, (f) 6

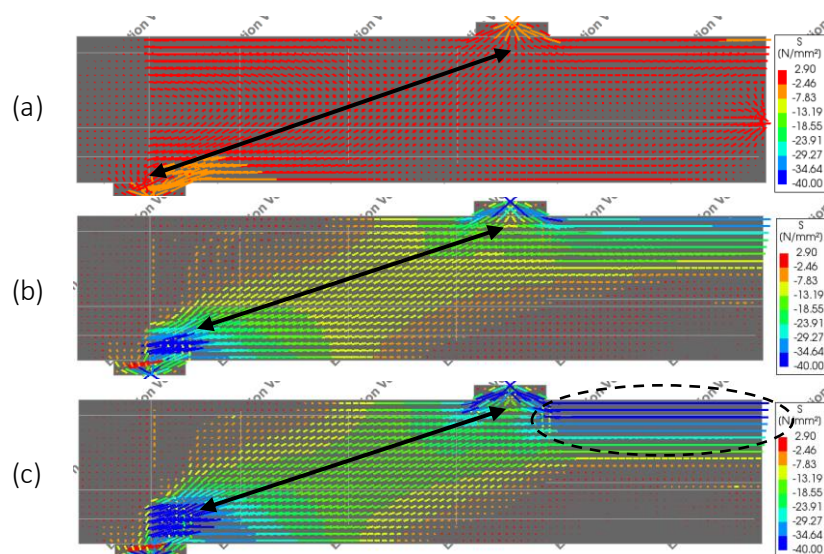


Figure 5.82 – In-plane principal stress of model 2D-PB-RC-FR at load stage (a) 1, (b) 2, (c) 3

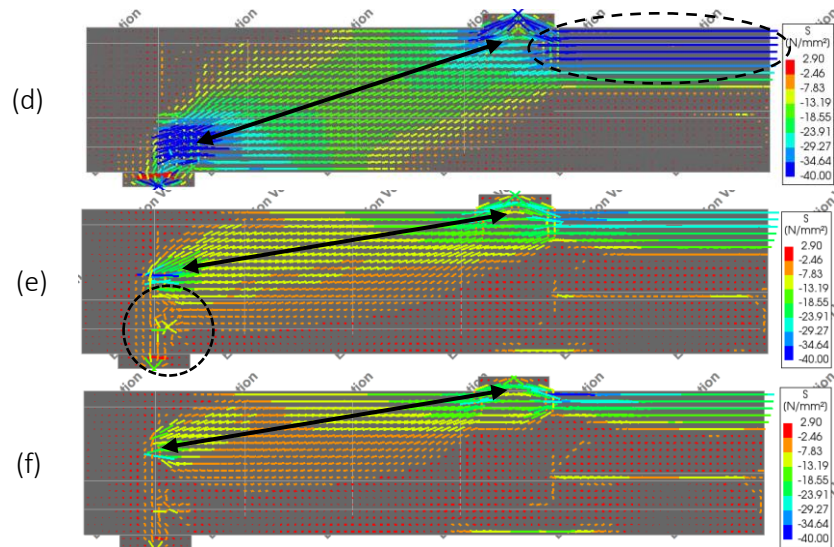


Figure 5.82 (cont.) – In-plane principal stress of model 2D-PB-RC-FR at load stage (d) 4, (e) 5, (f) 6

From Figure 5.81(a), it can be seen that at load stage 1, cracks occur at the top part of cast-in-situ layer near the support and at the joint. As explained in chapter 2.4.1, the compressive membrane action starts to develop after the occurrence of a flexural crack, which is at load stage 1. The start of the compressive membrane action development can be observed in Figure 5.80, as the total lateral (horizontal) force rapidly increases after the load stage 1. This rapid increase is the effect of the presence of compressive membrane action, in addition to the fix boundary (full height lateral restraint) action, due to the bending moment at support. This bending moment occurs since the full height lateral also works as a rotational restraint. This behaviour is in accordance with the result from [31]. In Figure 5.82(a), the strut of compressive stress occurs from the top part of cast-in-situ layer near the loading pad to the bottom part of precast layer at the lateral restraint.

As the load increases, the horizontal crack starts to develop from the joint and more flexural cracks are developed at the top part of the support until the top reinforcements reaches their yield strength at the load stage 2 as shown in Figure 5.81(b). When the load increases further, more part of the concrete at the bottom part of support reaches its compressive strength as can be seen in Figure 5.82(c). The load stage 3 then reached when all of the compressive region at the support reaches the compressive strength or become fully plastic. After reaching the third load stage, the plastic hinge starts to rotate and the load increases further. However, due to the lack of the rotation capacity in the compressive part of the concrete, the concrete starts to crush at load stage 4 until it is fully crushed at the load stage 5 as indicated by the dashed black circles in Figure 5.81(e) and Figure 5.82(e). The concrete crush decreases a lot of the capacity between load stage 4 and 5 (see Figure 5.79), since the compressive strut is shifted upwards (see Figure 5.82(f)) and less lateral force works in the structure as shown in Figure 5.80. The load keeps dropping as the displacement increases until it reaches the failure stage when a flexural crack at the end of the coupling reinforcement reaches the top of the cast-in-situ layer.

As described from the observation, this model has a different failure mechanism compared to the reference model (2D-PB-RC) which has no lateral restraint. However, it has a similar final stage of the failure mechanism, which is the flexural crack at the end of coupling reinforcement, though at a really large vertical displacement compared to the unrestrained model. Although at load stage 3, the horizontal crack along the coupling reinforcement has reached the end of that reinforcement as shown in Figure 5.81(c), the flexural crack propagation at the end of coupling reinforcement can be prevented from occurring earlier due to the high compressive stress at the top part of the cast-in-situ layer as indicated by the black dashed circles in Figure 5.82(c) and (d). As this high compressive stress is reduced due to the crush of the concrete section at load stage 5, the propagation of the flexural crack at the end of coupling can be started as shown in Figure 5.81(e).

Due to the concrete crushing, the ideal failure mechanism of the indeterminate structure with moment at the mid-span equal to plastic moment could not be reached. However, even this failure cannot be reached, this model with lateral restraint increases the load capacity by almost 4 times, compared to the collapse load. This increase of load capacity is in accordance with a research by Ockleston [2] which found an increase of load capacity by 1.60 to 8.25 times on a concrete slab with lateral restraint compared to the yield line theory.

5.3.2. Smooth interface

In Figure 5.83, the load-displacement graph of the laterally restrained model with smooth interface (2D-SI-RC-FR) is shown with the maximum load at 149.67 kN. The graph includes the comparison to the simply supported model (2D-SI-RC) which has the same numerical setup with model 2D-SI but with regular concrete used in both concrete layers so it could be compared with model 2D-PB-RC-FR. As a comparison, the model with lateral restraint has 10 times higher load capacity than the model without lateral restraint. The two analytical solutions for the failure mechanism of this indeterminate structure are also provided in the graph. The orange dashed line represents the total load when the moment at the support equal to plastic moment of the section at the support while the red dashed line represents the total load when the moment at the joint equals to the plastic moment of the section at the joint.

In that figure, the damage development of this model is marked at six load stages prior to the failure. The damage development at each load stage can be observed in Figure 5.85. Load stage 1 is the onset of the flexural crack at the top part of cast-in-situ layer near the support and at the joint, load stage 2 is the onset of the interface delamination at the joint, load stage 3 is when the top reinforcement at the support reaches the yield strength, load stage 4 is when the cast-in-situ layer section at the support has become fully plastic and starts the plastic rotation, load stage 5 is at the start of the concrete crushing at the bottom part of the cast-in-situ layer, and load stage 6 is at the failure when the concrete becomes fully crushed and followed with a flexural crack at the end of coupling reinforcement reaches the top of cast-in-situ layer.

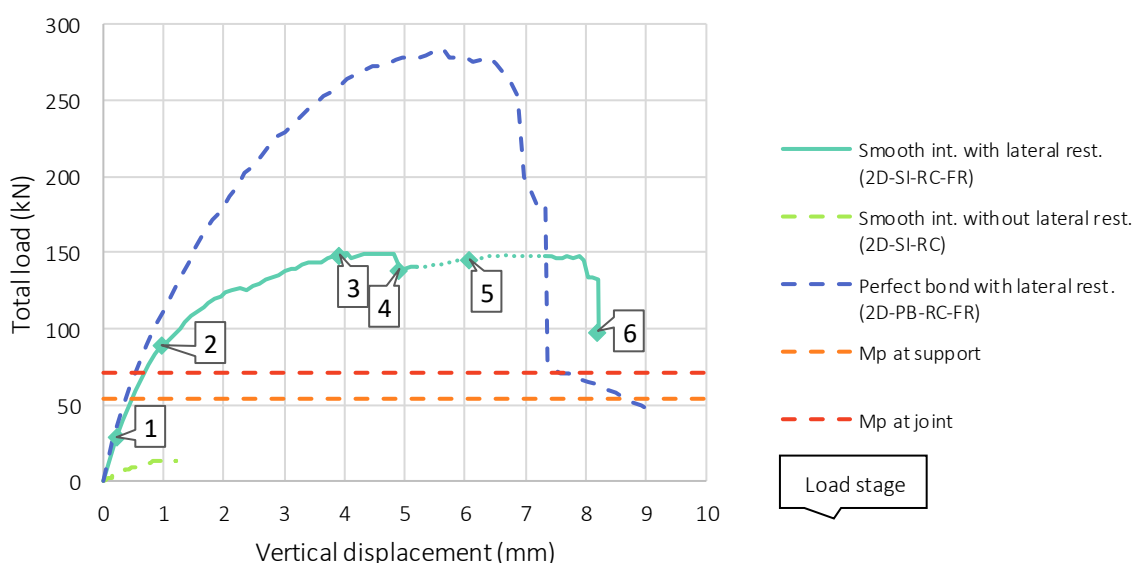


Figure 5.83 – Load-displacement graph of laterally restrained unreinforced interface model with smooth interface (2D-SI-RC-FR)

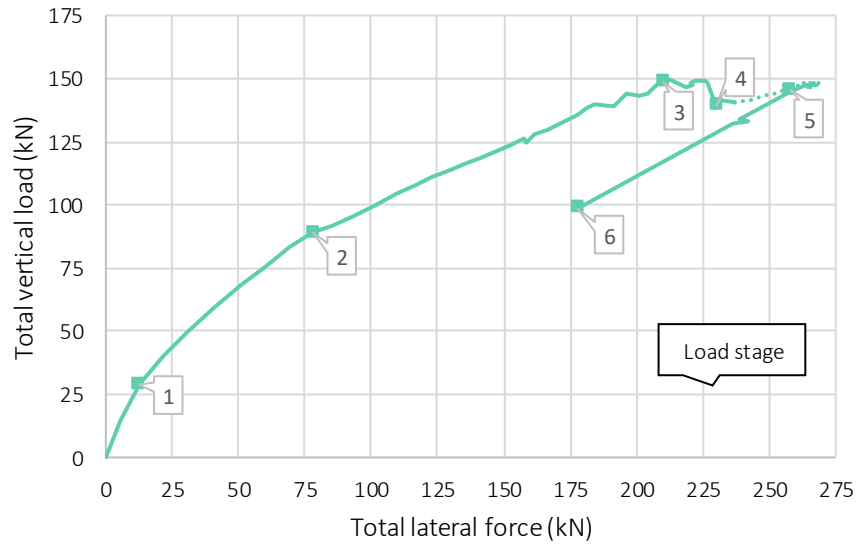


Figure 5.84 – Total load-total lateral force of laterally restrained unreinforced interface model with smooth interface (2D-SI-RC-FR)

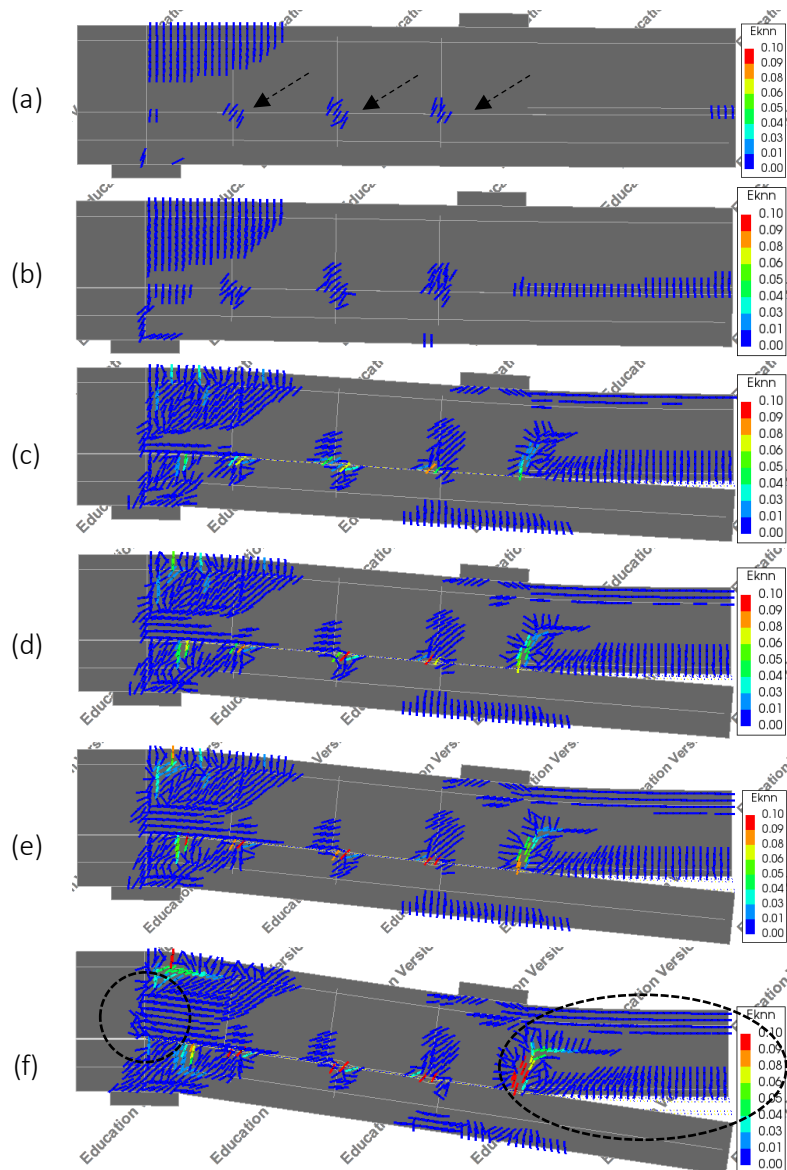


Figure 5.85 – Crack strain of model 2D-SI-RC-FR at load stage (a) 1, (b) 3, (c) 3, (d) 4, (e) 5, (f) 6

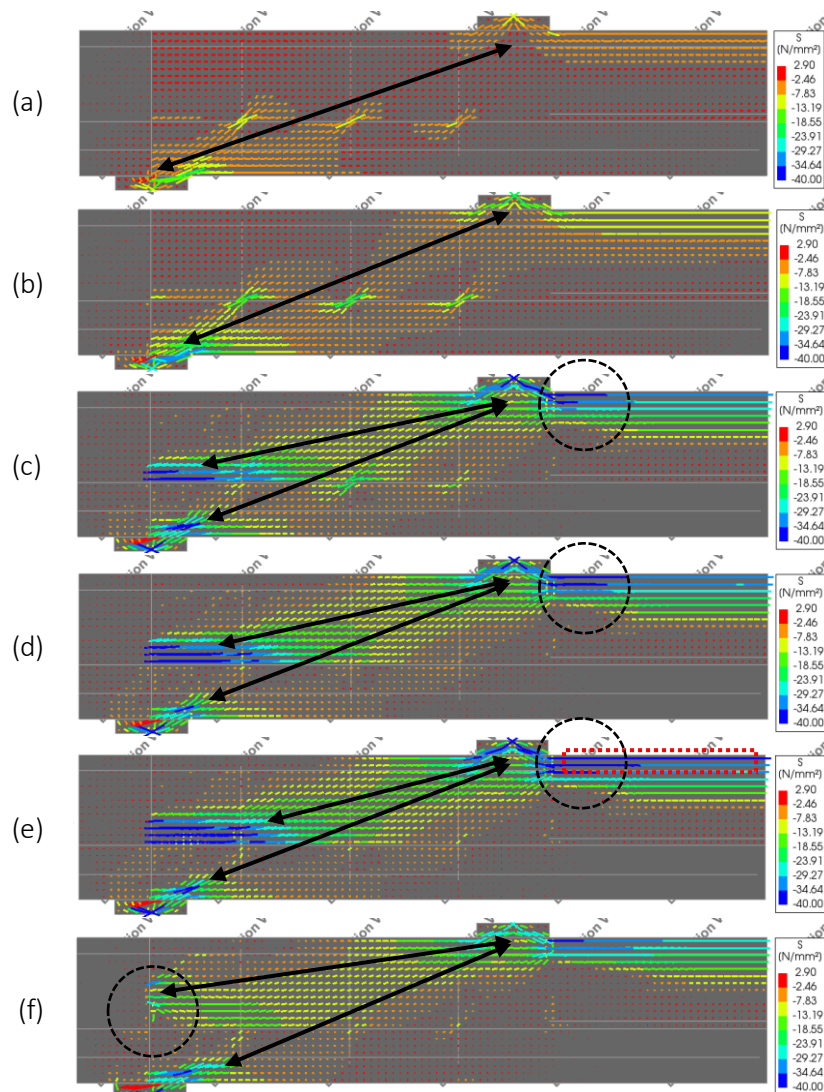


Figure 5.86 – In-plane principal stress of model 2D-SI-RC-FR at load stage (a) 1, (b) 2, (c) 3, (d) 4, (e) 5, (f) 6

Similar to the model with a perfect bonded interface, at load stage 1, cracks have appeared at the top part of the cast-in-situ layer near the support and at the joint as shown in Figure 5.85(a). However, due to the use of Coulomb friction model which can simulate the slip between the concrete layers, there are some dowel cracks which occur around the intersection of shear reinforcements and the interface as indicated by black dashed arrows in that figure. Due to the development of flexural crack at the joint, compressive membrane action starts to develop from load stage 1 which is reflected from the rapid increase of lateral force after load stage 1 as shown in Figure 5.84. The occurrence of compressive stress strut at load stage 1 can be observed in Figure 5.86(a).

When the load reaches load stage 2, the interface starts to crack at the joint, and as can be seen in Figure 5.86(b), the dowel action becomes more prominent to transfer the compressive stress from the cast-in-situ layer to the precast layer. As the load increases, more flexural cracks are developed at the top part of the support until the top reinforcement reaches the yield strength at the load stage 3 as shown in Figure 5.85(c). This figure also shows that at this load stage, the interface delamination has reached the end of coupling reinforcement. Moreover, between load stage 2 and 3, the interface shear displacement increases which creates two compression zones in both concrete layers near the lateral restraint as shown in Figure 5.86(c). At load stage 4, the compression area in the cast-in-situ layer reaches the start of plastic rotation.

After load stage 4, DIANA could not give a convergence result. This result is caused by unstable elements which are marked with the red dotted line in Figure 5.86(e). Several modification such as a smaller load increment and a higher number of iterations have been done, but the results still have non-convergence result in the range of the load increments which are marked with dotted line in Figure 5.83 and Figure 5.84. Therefore, the result after load stage 4 is not reliable to be analysed. However, since the elements which caused the error is not affecting the global behaviour of the structure, the convergence result after the non-convergence one could give an idea about the failure of the structure.

Due to the lack of rotation capacity, at load stage 5, the concrete matrix in the cast-in-situ layer starts to crush. The concrete crush decreases the load capacity between load stage 5 and 6 since less lateral force works in the structure as shown in Figure 5.84. As the displacement increases, the structure fails at load stage 6 when the concrete matrix at the bottom part of the cast-in-situ layer at the support is fully crushed. At the same time, the flexural crack at the end of coupling reinforcement reaches the top of the cast-in-situ layer.

This model has a different failure mechanism compared to the reference model (2D-SI-RC) which has no lateral restraint as described above. However, it has a similar final stage of the failure mechanism, which is the flexural crack at the end of coupling reinforcement, though at a really large vertical displacement compared to the unrestrained model. Similar to the laterally restrained model with perfect bonded interface (2D-PB-RC-FR) in chapter 5.3.1, the propagation of the flexural crack at the end of coupling reinforcement is also hindered due to the high compressive stress at the top part of the cast-in-situ layer as indicated by the black dashed circles in Figure 5.86 (c), (d), and (e).

Due to the concrete crushing, this model also could not reach the plastic moment at the mid-span. However, even this failure cannot be reached, this model increases the load capacity by more than 2 times, compared to the collapse load. This increase of capacity is lower than the laterally restrained model with perfect bonded interface since this model with smooth interface has shorter compression area at the bottom part of the cast-in-situ layer at the support. In practice, with different surface quality of the concrete-to-concrete interface and different stiffness or lateral restraint, the capacity of the structure can be estimated with the simulation of a laterally restraint structure with perfect bonded interface as an upper limit and a simply supported structure with smooth interface as a lower limit.

It is important to highlight that the laterally restrained models with perfect bonded interface (2D-PB-RC-FR) and smooth interface (2D-SI-RC-FR) assume a good anchoring of top reinforcement to the lateral restraint, thus the possibility of pull-out failure of this reinforcement is not considered. In the real situation, it could be one of the decisive failure mechanism which lower the additional capacity provided by the compression membrane action.

| 6 | CONCLUDING REMARKS

6.1. Conclusions

In order to study the influence of interface behaviour on the capacity of composite structures, two composite SHCC-concrete beam specimens from an experimental research by Harrass [1] were used in this numerical study. Sample 1 is an unreinforced interface beam, while Sample 7 is a reinforced interface beam using rectangular stirrup which crosses the interface near the joint. By using DIANA 10.4 finite element analysis software, this study is able to simulate both specimens in 2D and 3D numerical models. In these models, Coulomb friction interface is used to simulate the concrete-to-concrete interface and CEB-FIB 2010 bond-slip function is applied to simulate the slip of reinforcement. The cohesion and the friction angle used for the Coulomb friction interface are in accordance with the *fib* model code for concrete structures 2010 [13]. The numerical models represented Sample 1 failed with a horizontal crack along the interface and a flexural crack at the end of coupling reinforcement reaches the top of the cast-in-situ layer, while the numerical models represented Sample 7 failed with a horizontal crack along the interface, a flexural crack at the end of coupling reinforcement, and a crack at the stirrup location in precast layer. In the verification process, it is found that the use of reinforcement bond-slip function does not influence much of the load and displacement capacity of the specimens, while the failure mechanism remains unchanged. Therefore, the reinforcement bond-slip function is chosen not to be used for the rest of the study. As a result, pull-out failure of the stirrup is excluded for the rest of the study.

The interface parameters of models with unreinforced and reinforced interface are varied in sensitivity study. There are four parameters which are studied in each analyses, the interface stiffness, interface tensile strength, cohesion, and friction angle. The range of each parameter used in these studies is in accordance with the values which are suggested by the Eurocode 2 [9], *fib* model code for concrete structures 2010 [13], and commonly used in the recent numerical research [1], [26], [27]. It is observed that interface stiffness and interface tensile strength are the governing parameters of models with unreinforced interface. Within the range of those parameters, the load capacity is increased and decreased by more than 50% in compared to the reference model verified by Sample 1. The influences of these parameters are related to the observation that the start of horizontal crack at the joint occurs due to the exceedance of interface tensile strength (cut-off limit) and the maximum load is reached in just a few load steps after this crack onset. By adding a rectangular stirrup near the joint of unreinforced interface model, the model with reinforced interface has a different governing parameter, the cohesion, and the variability of the results decrease. Within the range of the cohesion, the load capacity is increased and decreased up to 30% in compared to the reference model verified by Sample 7. This influence is related to the high shear stress of the uncracked area between the stirrup and the end of coupling reinforcement which could keep transferring the tensile force from the precast layer to cast-in-situ layer through shear stress. In conclusion, different interface parameters can result in different capacity of the structure. Therefore, it is important to include different interface types to study the interface behaviour. Two types of interfaces are chosen, which is known as “smooth interface” which

uses the interface parameters verified by Sample 1 and “perfect bonded interface” which uses a rigid connection between two concrete layers elements.

The influence of lap splices spacing is studied by varying the number of lap splices (coupling reinforcement and bottom reinforcement), 1 and 3, which have an equal area. This is done by using the unreinforced interface model, which has been verified with Sample 1.

- With a perfect bonded interface, models with both lap splice setups have the same failure mechanism, which is the horizontal crack along coupling reinforcement and a flexural crack at the end of coupling reinforcement. However, model with single lap splice has higher load capacity by more than 10% in compared to model with three lap splices. From the observation, model with single lap splice has higher stress concentration and more concentrated horizontal crack propagation around the coupling reinforcement, compared to the model with three lap splices. This more concentrated horizontal crack propagation is caused by the use of a smaller number of lap splice, while the more uniform crack propagation of model with three lap splices, might be caused by the presence of more lap splices with closer spacing, compared to model with single lap splice. This difference in horizontal crack propagation across the width could be the cause of the difference in the load capacity, since more uncracked elements could provide more tensile force transfer from precast layer to cast-in-situ layer.
- With a smooth interface, models with both lap splice setups have the same failure mechanism, which is the horizontal crack along the interface and a flexural crack at the end of coupling reinforcement. Both models have a similar load and displacement capacity. From the observation, the model with a single lap splice has a stress concentration around the coupling reinforcement, while the model with three lap splices has a uniform stress distribution across the width. However, both models have a uniform interface delamination across the width. This similarity in crack propagation in transverse direction could be the cause of the similarity in the load capacity, since with similar crack propagation, there is a similar number of uncracked elements, which could transfer the tensile force from precast layer to cast-in-situ layer. The phenomenon where the model with single lap splice has concentrated stress distribution while the interface delamination is uniform across the width, might be related to the properties of the Coulomb friction model for the smooth interface. However, it needs a further study to investigate which parameter affecting this phenomenon.

The influence of stirrup spacing is studied by varying the number of stirrup legs, 1 and 2, which have an equal area. This is done by using the reinforced interface model, which has been verified with Sample 7

- With a perfect bonded interface, models with both stirrup setups could reach the desired failure mechanism, which is yielding of coupling reinforcement. This failure mechanism governs since horizontal crack propagation stops due to the presence of stirrups. Despite of the similar failure, model with two legs stirrup has slightly higher structural stiffness compared to model with single leg stirrup. It could be caused by higher tensile force which is transferred through stirrups in model with two legs stirrup in compared to model with single leg stirrup. This higher tensile force might be resulted by the more distributed stirrup across the width of the beam.
- With a smooth interface, models with both stirrup setups could also reach the desired failure mechanism, which is yielding of coupling reinforcement. However, it could only be reached in really high deflection of the beam. It should also be noted that this failure is governing since pull-out failure of the stirrups is excluded from the model without reinforcement bond-slip function. Model with two legs stirrup also has slightly higher structural stiffness compared to model with single leg stirrup. It could also be caused by the same reason in model with perfect bonded interface.

The influence of lateral restraint is studied by comparing the full height laterally restrained unreinforced interface model with the simply supported one which has been verified with Sample 1.

- With a perfect bonded interface, the model with lateral restraint has a higher load by more than 14 times and a higher displacement capacity by more than 2.5 times, compared to the simply supported model. In compared to the collapse load, the model with lateral restraint has a higher load capacity by almost 4 times, although it does not reach the yielding of the coupling reinforcement. With a smooth interface, the model with lateral restraint has a higher load capacity by more than 10 times and a displacement capacity by more than 5.5 times, compared to the simply supported model. In compared to the collapse load, the model with lateral restraint has a higher load capacity by more than 2 times, although it also does not reach the yielding of the coupling reinforcement.
- These increase of load capacity in compared to the collapse load is in accordance with a research by Ockleston [2] which found an increase of load capacity by 1.60 to 8.25 times on a concrete slab with lateral restraint compared to the yield line theory. Part of the increase of the load capacity is resulted by the fix boundary action due to the bending moment at the support. It is observed that the compressive membrane action starts to develop and contributes to the increase of load capacity after the first flexural crack, as the horizontal force at the support rapidly increases after that crack.
- The laterally restrained model with perfect bonded interface also has a different failure mechanism compared to the simply supported model, although it also has a similar final stage of the failure mechanism. It fails with a horizontal crack along the coupling reinforcement until the end of this reinforcement, followed by the crush of the concrete in the precast layer at the support and ended with the flexural crack at the end of the coupling reinforcement reaches the top of the cast-in-situ layer. The laterally restrained model with smooth interface has a different failure mechanism compared to the simply supported model, although it has a similar final stage of the failure mechanism. It fails with an interface delamination until the end of coupling reinforcement, followed by the crush of the concrete at the bottom of the cast-in-situ layer at the support and ended with the flexural crack at the end of the coupling reinforcement reaches the top of the cast-in-situ layer. The laterally restrained models with both concrete interface have a delayed growth of the flexural crack at the end of coupling reinforcement since the high compressive stress at the top part of the cast-in-situ layer prevents the crack propagation. However, when the concrete crushes at the support due to the limited rotation capacity of the concrete, the compressive stress drops, causing the flexural crack propagation reaching the top of the cast-in-situ layer.

In conclusion, from the study of lap splices and stirrups spacing, it is found that the interface behaviour influences the failure and capacity of composite SHCC-concrete beam. The degree of its influence is depending on the lap splice spacing, the presence of stirrup near the joint, the spacing of stirrup, and the interface type. It is also concluded that compressive membrane action in addition to fix bending action, which occurs due to the lateral restraint, increases the capacity of the structure. This increase depends on the interface type and rotation capacity of the concrete. In practice, the increase of the load capacity in laterally restrained composite floors depends on the surface quality of the concrete-to-concrete interface and the stiffness of the lateral restraint, which is commonly induced by the connection with the walls or the adjacent floors. The capacity can be estimated with the simulation of a laterally restraint structure with perfect bonded interface as an upper limit and a simply supported structure with smooth interface as a lower limit. It should be noted that the pull-out failure of stirrup is excluded from this research. In the real situation, this failure mechanism could be the governing one. A wider range of the influencing parameters are needed in future studies to get a more robust results which are beneficial for a more general conclusions. However, the series of experimental research based on this study are essential to provide a verification on the results of this numerical study.

6.2. Recommendation

There are a lot of things that could be added, completed, and verified in order to reach more binding and general conclusion.

1. Experimental research on the same topic of this numerical study is essential to provide a verification on the result of this study. At the same time as the writing of this thesis, there is an ongoing research in TU Eindhoven in regard to the influence of lattice girder spacing at short-end joint. However, this experiment could not be used as a verification of this numerical study since this study focus at the long-end joint.
2. Various reference models could be used in sensitivity study of interface parameters to investigate the presence of geometrical influence on the governing interface parameters.
3. With more variety of number of lap splices and their spacing, the boundary between evenly distributed and more concentrated horizontal crack propagation could be obtained.
4. As the interface behaviour is influenced by the spacing of lap splices, another study should be done to investigate whether the effect of eccentricity between the coupling and tensile reinforcements has a significant influence on the interface behaviour
5. More computational resource is needed to model the specimen with larger width which could be beneficial for recommendation number 3 and 4.
6. This research has been able to simulate the failure in delamination. However, the pull out failure has not been able to be simulated in the numerical model. Another study should be done to understand the suitable approach to numerically model the pull-out failure of the stirrup crossing the interface near the joint.
7. In the study, it was found that the unreinforced interface beam with smooth interface could have a uniform horizontal crack propagation across the width of the specimen although its interface stress distribution is non-uniform. This phenomenon should be studied further to see the influence of each parameter of Coulomb friction interface to this phenomenon.
8. More studies with different dimension, reinforcement setup, and material properties should be performed to strengthen the conclusion of this study and its applicability to a general case of composite plank floor.

REFERENCES

- [1] O. Harrass, "Interfacial behavior of hybrid SHCC-Concrete beams with a joint at midspan," Technische Universiteit Delft, Delft, 2020.
- [2] A. Ockleston, "Arching action In reinforced concrete slabs," *Structural Engineer*, vol. 36, pp. 197-201, 1958.
- [3] H. Borsje and G. Dieteren, "Rapport R11127, Onderzoek naar de technische oorzaak van de gedeeltelijke instorting van de in aanbouw zijnde parkeergarage P1 Eindhoven Airport," TNO, Delft, 2017.
- [4] Adviesbureau Hageman, "Rapport 9663-1-0, Bezwijken parkeergarage Eindhoven Airport, Analyse naar de oorzak," Adviesbureau Hageman, Rijswijk, 2017.
- [5] J. Vambersky, J. Walraven, T. Salet, H. Vrijling, D. Hordjik and T. Vrouwenfelder, "De breedplaatvloerenproblematiek uitgelicht," *Cement*, vol. 4, pp. 42-51, 2020.
- [6] TU/e Bouwkunde Structures Laboratory Eindhoven, "Meetrapport betreffende 4-puntsbuigproeven van BAM-Cobiax breedplaatproefstukken," TU/e Bouwkunde Structures Laboratory Eindhoven, Eindhoven, 2018.
- [7] TU/e Bouwkunde Structures Laboratory Eindhoven, "Meetrapport 4-puntsbuigproeven voor het Betonhuis test breedplaatproefstukken," TU/e Bouwkunde Structures Laboratory Eindhoven, Eindhoven, 2018.
- [8] S. N. Wijte, "Stappenplan beoordeling bestaande gebouwen met breedplaatvloeren," Adviesbureau Hageman, Rijswijk, 2019.
- [9] Nederlands Normalisatie-instituut, NEN-EN 1992-1-1+C2, Eurocode 2: Ontwerpen berekening van betonconstructies – Deel 1-1: Algemene regels en regels voor gebouwen, Delft, 2011.
- [10] T. Joustra, M. v. Asselt and S. Zouridis, "Bouwen aan constructieve veiligheid - Lessen uit instorting parkeergebouw Eindhoven Airport," De Onderzoeksraad voor Veiligheid, Den Haag, 2018.
- [11] Nederlands Normalisatie-instituut, NEN-EN 13747+A2, Vooraf vervaardigde betonproducten Breedplaatvloeren, Delft, 2010.
- [12] S. Wijte and G. Dieteren, "Achtergronden nieuwbouwregels detaillering breedplaatvloeren," *Cement*, vol. 4, pp. 60-71, 2020.
- [13] fédération internationale du béton, fib Model Code for Concrete Structures 2010, Lausanne: Enst & Sohn, 2013.
- [14] J. K. Wight and J. G. MacGregor, Reinforced concrete: mechanics and design, 6th ed., New Jersey: Pearson, 2012.
- [15] L. Croes, "Behaviour of unreinforced concrete-to-concrete interfaces under shear loading," Eindhoven University of Technology, Eindhoven, 2019.
- [16] N. Randl, "Design recommendations for interface shear transfer in fib Model Code 2010," *Structural Concrete*, vol. 14, no. 3, pp. 230-241, 2013.

- [17] R. Park and W. L. Gamble, Reinforced Concrete Slab, 2nd ed., New York: John Wiley & Sons, Inc., 2000.
- [18] G. Rankin, "Arching action strength enhancement in laterally-restrained slab strips," *Structures & Buildings*, vol. 122, pp. 461-467, 1997.
- [19] S. N. Wijte, "Rapport 9780-1-0, Onderzoek constructieve veiligheid breedplaatvloeren in bestaande utiliteitgebouwen, Voorstellen voor en achtergronden bij rekenregels voor beoordeling van bestaande bouw," Adviesbureau Hageman, Rijswijk, 2019.
- [20] TGB Betonconstructies, "VARCE 13 - Detaillering aansluitvlak breedplaatvloeren (2)," *Cement*, vol. 4, pp. 54-58, 2020.
- [21] T. Gudmand-Høyer, "Note on the moment capacity in a Bubble deck joint," Danmarks Tekniske Universitet, Kongens Lyngby, 2003.
- [22] K. Lundgren, "Analyses of a lap splice in a lattice girder system," Chalmers University of Technology, Göteborg, 2003.
- [23] J. Stehle, A. Kanellopoulos and B. L. Karihaloo, "Performance of joints in reinforced concrete slabs for two-way spanning action," *Structures and buildings*, vol. 163, pp. 197-209, 2011.
- [24] J. K. Weglarzy, "Untersuchungen zum Tragstoß von nachträglich mit Ortbeton ergänzten zweiachsig gespannten Stahlbeton-Fertigteileplatten," Universität Siegen, Siegen, 2014.
- [25] K. Lundgren, J. Helgesson and R. Sylvén, "Joints in lattice girder structures," Chalmers University of Technology, Göteborg, 2005.
- [26] M. Verbaten and K. Riemens, "Proof of concept Bubbledeck o.b.v. proeven Eindhoven," abt, Arnhem, 2018.
- [27] W. H. Bouwsema, "The pull-out and shear resistance of a lattice girder from a precast concrete floor plate during a 4-point bending test," Eindhoven University of Technology, Eindhoven, 2021.
- [28] M. A. Hendriks and M. A. Roosen, "Guidelines for Nonlinear Finite Element Analysis of Concrete Structures," Rijkswaterstaat Centre for Infrastructure, Report RTD:1016-1:2019, 2019.
- [29] DIANA FEA BV, DIANA Documentation release 10.4, Delft: DIANA FEA BV, 2020.
- [30] C. Zanotti and N. Randl, "Are concrete-concrete bond test comparable?," *Cement and Concrete Composites*, vol. 99, pp. 80-88, 2019.
- [31] S. Amir, "Compressive Membrane Action in Prestressed Concrete Deck Slabs," Technische Universiteit Delft, Delft, 2014.

|A1| MODEL VARIATIONS

In Table A1.1, a list of all models used in this numerical research is provided. It indicates the variation of parameters which are used in each model of each study. There are some notes related to the information in the table:

1. Interface type:
 - Smooth interface: see details in Table 3.11
 - Perfect bonded interface uses a rigid connection to connect the elements of precast and cast-in-situ layers (chapter 4.3)
2. Reinforcement bond-slip function:
 - Yes: coupling reinforcement and stirrup near the joint use CEB-FIB 2010 bond-slip function. See details in Table 3.9
 - No: coupling reinforcement and stirrup near the joint use embedded bar type
3. Lapsplice:
 - Containing the number and equivalent diameter of coupling and bottom reinforcements used in the models
4. Stirrup near the joint:
 - Rectangular stirrup uses the same geometrical properties of stirrup in Sample 7 (chapter 3.1.3)
 - Single leg stirrup uses one vertical stirrup near the joint with equivalent diameter so that the total reinforcement area remains the same as the experiment (Sample 7)

Table A1.1 – List of models used in this research along with their variations

Study	Model name	Interface type	Bond-slip	Lap splice	Stirrup near joint	Precast layer	Interface stiffness (N/mm ³)	Interface tensile strength (MPa)	Cohesion (MPa)	Friction angle (rad)
Numerical model verification	2D-SI	smooth	No	1 D14	No	SHCC	10	0.5	0.5	0.54
	2D-SI-BS	smooth	Yes	1 D14	No	SHCC	10	0.5	0.5	0.54
	3D-SI	smooth	No	3 D8	No	SHCC	10	0.5	0.5	0.54
	3D-SI-BS	smooth	Yes	3 D8	No	SHCC	10	0.5	0.5	0.54
	2D-SI-SJ	smooth	No	1 D14	single leg	SHCC	10	0.5	0.5	0.54
	2D-SI-SJ-BS	smooth	Yes	1 D14	single leg	SHCC	10	0.5	0.5	0.54
	3D-SI-SJ	smooth	No	3 D8	rectangular	SHCC	10	0.5	0.5	0.54
	3D-SI-SJ-BS	smooth	Yes	3 D8	rectangular	SHCC	10	0.5	0.5	0.54
Sensitivity study of interface parameter	2D-SI-IS1000	smooth	No	1 D14	No	SHCC	1000	0.5	0.5	0.54
	2D-SI-IS500	smooth	No	1 D14	No	SHCC	500	0.5	0.5	0.54
	2D-SI-IS150	smooth	No	1 D14	No	SHCC	150	0.5	0.5	0.54
	2D-SI-IS100	smooth	No	1 D14	No	SHCC	100	0.5	0.5	0.54
	2D-SI-IS50	smooth	No	1 D14	No	SHCC	50	0.5	0.5	0.54
	2D-SI-IS20	smooth	No	1 D14	No	SHCC	20	0.5	0.5	0.54
	2D-SI-IS15	smooth	No	1 D14	No	SHCC	15	0.5	0.5	0.54
	2D-SI-IS5	smooth	No	1 D14	No	SHCC	5	0.5	0.5	0.54
	2D-SI-ITS1	smooth	No	1 D14	No	SHCC	10	1.0	0.5	0.54
	2D-SI-ITS0.9	smooth	No	1 D14	No	SHCC	10	0.9	0.5	0.54
	2D-SI-ITS0.8	smooth	No	1 D14	No	SHCC	10	0.8	0.5	0.54
	2D-SI-ITS0.7	smooth	No	1 D14	No	SHCC	10	0.7	0.5	0.54
	2D-SI-ITS0.6	smooth	No	1 D14	No	SHCC	10	0.6	0.5	0.54
	2D-SI-ITS0.4	smooth	No	1 D14	No	SHCC	10	0.4	0.5	0.54
	2D-SI-ITS0.3	smooth	No	1 D14	No	SHCC	10	0.3	0.5	0.54
	2D-SI-ITS0.2	smooth	No	1 D14	No	SHCC	10	0.2	0.5	0.54
	2D-SI-ITS0.1	smooth	No	1 D14	No	SHCC	10	0.1	0.5	0.54
	2D-SI-C1	smooth	No	1 D14	No	SHCC	10	0.5	1.0	0.54
	2D-SI-C0.9	smooth	No	1 D14	No	SHCC	10	0.5	0.9	0.54
	2D-SI-C0.8	smooth	No	1 D14	No	SHCC	10	0.5	0.8	0.54
2D-SI-C0.7	smooth	No	1 D14	No	SHCC	10	0.5	0.7	0.54	

Study	Model name	Interface type	Bond-slip	Lap splice	Stirrup near joint	Precast layer	Interface stiffness (N/mm ³)	Interface tensile strength (MPa)	Cohesion (MPa)	Friction angle (rad)
	2D-SI-C0.6	smooth	No	1 D14	No	SHCC	10	0.5	0.6	0.54
	2D-SI-C0.4	smooth	No	1 D14	No	SHCC	10	0.5	0.4	0.54
	2D-SI-C0.3	smooth	No	1 D14	No	SHCC	10	0.5	0.3	0.54
	2D-SI-C0.2	smooth	No	1 D14	No	SHCC	10	0.5	0.2	0.54
	2D-SI-C0.1	smooth	No	1 D14	No	SHCC	10	0.5	0.1	0.54
	2D-SI-FA1	smooth	No	1 D14	No	SHCC	10	0.5	0.5	1.0
	2D-SI-FA0.9	smooth	No	1 D14	No	SHCC	10	0.5	0.5	0.9
	2D-SI-FA0.8	smooth	No	1 D14	No	SHCC	10	0.5	0.5	0.8
	2D-SI-FA0.7	smooth	No	1 D14	No	SHCC	10	0.5	0.5	0.7
	2D-SI-FA0.4	smooth	No	1 D14	No	SHCC	10	0.5	0.5	0.4
	2D-SI-FA0.3	smooth	No	1 D14	No	SHCC	10	0.5	0.5	0.3
	2D-SI-FA0.2	smooth	No	1 D14	No	SHCC	10	0.5	0.5	0.2
	2D-SI-FA0.1	smooth	No	1 D14	No	SHCC	10	0.5	0.5	0.1
	2D-SI-SJ-IS1000	smooth	No	1 D14	single leg	SHCC	1000	0.5	0.5	0.54
	2D-SI-SJ-IS500	smooth	No	1 D14	single leg	SHCC	500	0.5	0.5	0.54
	2D-SI-SJ-IS150	smooth	No	1 D14	single leg	SHCC	150	0.5	0.5	0.54
	2D-SI-SJ-IS100	smooth	No	1 D14	single leg	SHCC	100	0.5	0.5	0.54
	2D-SI-SJ-IS50	smooth	No	1 D14	single leg	SHCC	50	0.5	0.5	0.54
	2D-SI-SJ-IS20	smooth	No	1 D14	single leg	SHCC	20	0.5	0.5	0.54
	2D-SI-SJ-IS15	smooth	No	1 D14	single leg	SHCC	15	0.5	0.5	0.54
	2D-SI-SJ-IS5	smooth	No	1 D14	single leg	SHCC	5	0.5	0.5	0.54
	2D-SI-SJ-ITS1	smooth	No	1 D14	single leg	SHCC	10	1.0	0.5	0.54
	2D-SI-SJ-ITS0.9	smooth	No	1 D14	single leg	SHCC	10	0.9	0.5	0.54
	2D-SI-SJ-ITS0.8	smooth	No	1 D14	single leg	SHCC	10	0.8	0.5	0.54
	2D-SI-SJ-ITS0.7	smooth	No	1 D14	single leg	SHCC	10	0.7	0.5	0.54
	2D-SI-SJ-ITS0.6	smooth	No	1 D14	single leg	SHCC	10	0.6	0.5	0.54
	2D-SI-SJ-ITS0.4	smooth	No	1 D14	single leg	SHCC	10	0.4	0.5	0.54
	2D-SI-SJ-ITS0.3	smooth	No	1 D14	single leg	SHCC	10	0.3	0.5	0.54
	2D-SI-SJ-ITS0.2	smooth	No	1 D14	single leg	SHCC	10	0.2	0.5	0.54
	2D-SI-SJ-ITS0.1	smooth	No	1 D14	single leg	SHCC	10	0.1	0.5	0.54

Study	Model name	Interface type	Bond -slip	Lap splice	Stirrup near joint	Precast layer	Interface stiffness (N/mm ³)	Interface tensile strength (MPa)	Cohesion (MPa)	Friction angle (rad)
	2D-SI-SJ-C1	smooth	No	1 D14	single leg	SHCC	10	0.5	1.0	0.54
	2D-SI-SJ-C0.9	smooth	No	1 D14	single leg	SHCC	10	0.5	0.9	0.54
	2D-SI-SJ-C0.8	smooth	No	1 D14	single leg	SHCC	10	0.5	0.8	0.54
	2D-SI-SJ-C0.7	smooth	No	1 D14	single leg	SHCC	10	0.5	0.7	0.54
	2D-SI-SJ-C0.6	smooth	No	1 D14	single leg	SHCC	10	0.5	0.6	0.54
	2D-SI-SJ-C0.4	smooth	No	1 D14	single leg	SHCC	10	0.5	0.4	0.54
	2D-SI-SJ-C0.3	smooth	No	1 D14	single leg	SHCC	10	0.5	0.3	0.54
	2D-SI-SJ-C0.2	smooth	No	1 D14	single leg	SHCC	10	0.5	0.2	0.54
	2D-SI-SJ-C0.1	smooth	No	1 D14	single leg	SHCC	10	0.5	0.1	0.54
	2D-SI-SJ-FA1	smooth	No	1 D14	single leg	SHCC	10	0.5	0.5	1.0
	2D-SI-SJ-FA0.9	smooth	No	1 D14	single leg	SHCC	10	0.5	0.5	0.9
	2D-SI-SJ-FA0.8	smooth	No	1 D14	single leg	SHCC	10	0.5	0.5	0.8
	2D-SI-SJ-FA0.7	smooth	No	1 D14	single leg	SHCC	10	0.5	0.5	0.7
	2D-SI-SJ-FA0.4	smooth	No	1 D14	single leg	SHCC	10	0.5	0.5	0.4
	2D-SI-SJ-FA0.3	smooth	No	1 D14	single leg	SHCC	10	0.5	0.5	0.3
	2D-SI-SJ-FA0.2	smooth	No	1 D14	single leg	SHCC	10	0.5	0.5	0.2
2D-SI-SJ-FA0.1	smooth	No	1 D14	single leg	SHCC	10	0.5	0.5	0.1	
Lap splice spacing	3D-SI	smooth	No	3 D8	No	SHCC	10	0.5	0.5	0.54
	3D-PB	perfect bond	No	3 D8	No	SHCC	rigid connection			
	3D-SI-1L	smooth	No	1 D14	No	SHCC	10	0.5	0.5	0.54
	3D-PB-1L	perfect bond	No	1 D14	No	SHCC	rigid connection			
	3D-PB-RC	perfect bond	No	3 D8	No	concrete	rigid connection			
	3D-PB-1L-RC	perfect bond	No	1 D14	No	concrete	rigid connection			
Stirrup spacing	3D-SI-SJ	smooth	No	3 D8	rectangular	SHCC	10	0.5	0.5	0.54
	3D-PB-SJ	perfect bond	No	3 D8	rectangular	SHCC	rigid connection			
	3D-SI-SJ-1L	smooth	No	1 D14	single leg	SHCC	10	0.5	0.5	0.54
	3D-PB-SJ-1L	perfect bond	No	1 D14	single leg	SHCC	rigid connection			
Lateral restraint	2D-SI-RC-FR	smooth	No	1 D14	No	concrete	10	0.5	0.5	0.54
	2D-PB-RC-FR	perfect bond	No	1 D14	No	concrete	rigid connection			

|A2| ANALYTICAL SOLUTIONS

1. Failure mechanism of simply supported structure (yielding of coupling reinforcement)

$$\alpha = 0.75$$

$$\beta = 0.39$$

$$T_{coup} = A_c f_{ym}$$

$$x_{u,coup} = \frac{T_{coup}}{\alpha b f_{cm}}$$

$$d_{coup} = h_c - c_c - 0.5d_c$$

$$M_{u,coup} = T_{coup} (d_{coup} - \beta x_{u,coup}) = 9.02 \text{ kNm}$$

$$P_{u,coup} = \frac{2M_{u,coup}}{e_l - e_b} = 36.10 \text{ kN}$$

2. Failure mechanism of laterally restrained structure (yielding of top reinforcement and yielding of coupling reinforcement)

Maple script

restart;

ode1 := 0 = diff(w1(x), x \$ 4); ode2 := 0 = diff(w2(x), x \$ 4);

sol := dsolve({ode1, ode2}, {w1(x), w2(x)}); assign(sol);

w1 := w1(x); w2 := w2(x);

phi1 := -diff(w1, x); kappa1 := diff(phi1, x); M1 := EI*kappa1; V1 := diff(M1, x);

phi2 := -diff(w2, x); kappa2 := diff(phi2, x); M2 := EI*kappa2; V2 := diff(M2, x);

x := 0; eq1 := w1 = 0; eq2 := phi1 = 0;

x := l1; eq3 := w1 = w2; eq4 := phi1 = phi2; eq5 := M1 = M2; eq6 := V1 = F;

x := l1 + l2; eq7 := phi2 = 0; eq8 := V2 = 0;

sol := solve({eq1, eq2, eq3, eq4, eq5, eq6, eq7, eq8}, {_C1, _C2, _C3, _C4, _C5, _C6, _C7, _C8});
assign(sol);

$$T_{comp} = A_v f_{ym}$$

$$x_{u,comp} = \frac{T_{comp}}{\alpha b f_{cm}}$$

$$d_{comp} = 177 \text{ mm}$$

$$M_{u,comp} = T_{comp} (d_{comp} - \beta x_{u,comp}) = 9.52 \text{ kNm}$$

$$l_1 = e_l - e_b$$

$$l_2 = 0.5L_0 - l_1$$

$$x = \frac{l_1 + 2l_2}{2(l_1 + l_2)}$$

$$P_{u,comp} = \frac{2M_{u,comp}}{l_1 x} = 53.96 \text{ kN}$$

$$M_{mid} = \frac{0.5P_u}{l_1(1-x)} = 3.97 \text{ kNm}$$

Yielding of top reinforcement

$$M_{u,end,1} = M_{u,comp} = 9.52 \text{ kNm}$$

$$M_{u,mid,1} = 0.5M_{u,end,1} = 4.76 \text{ kNm}$$

$$P_{u,1} = P_{u,comp} = 53.96 \text{ kN}$$

Collapse load

$$M_{u,mid,2} = M_{u,comp} = 9.02 \text{ kNm}$$

$$\Delta M_{u,mid,2} = M_{u,mid,2} - M_{u,mid,1} = 4.26 \text{ kNm}$$

$$\Delta P_{u,2} = \frac{2\Delta M_{u,mid,2}}{e_l - e_b} = 17.06 \text{ kN}$$

$$P_{u,total} = P_{u,1} + P_{u,2} = 71.01 \text{ kN}$$

|A3| CONVERGENCE BEHAVIOUR OF REFERENCE MODELS

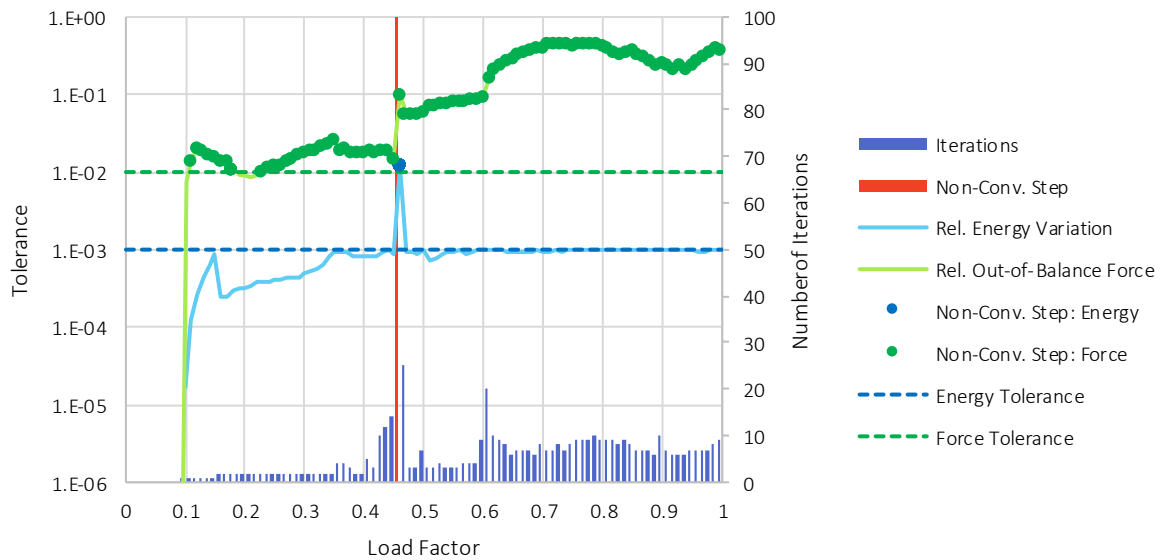


Figure A2.1 – Convergence behaviour of model 2D-SI

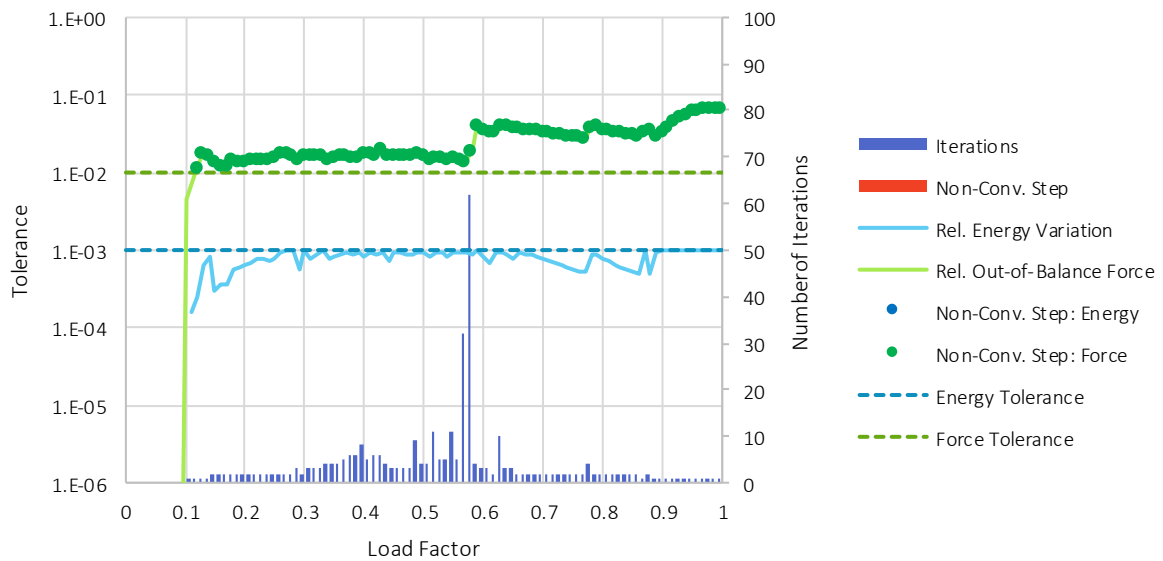


Figure A2.2 – Convergence behaviour of model 3D-SI

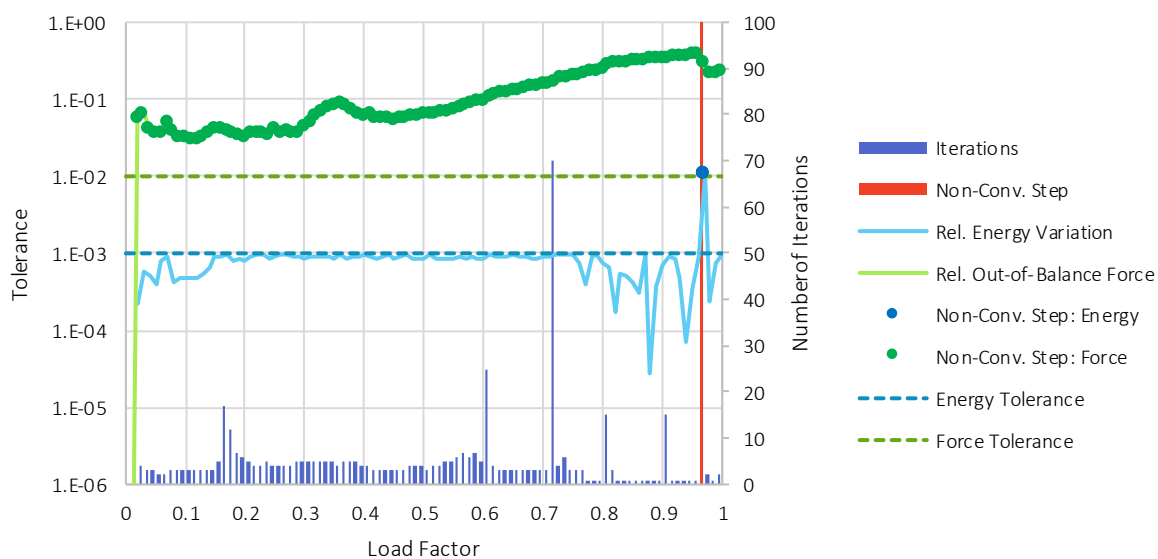


Figure A2.3 – Convergence behaviour of model 2D-SI-SJ

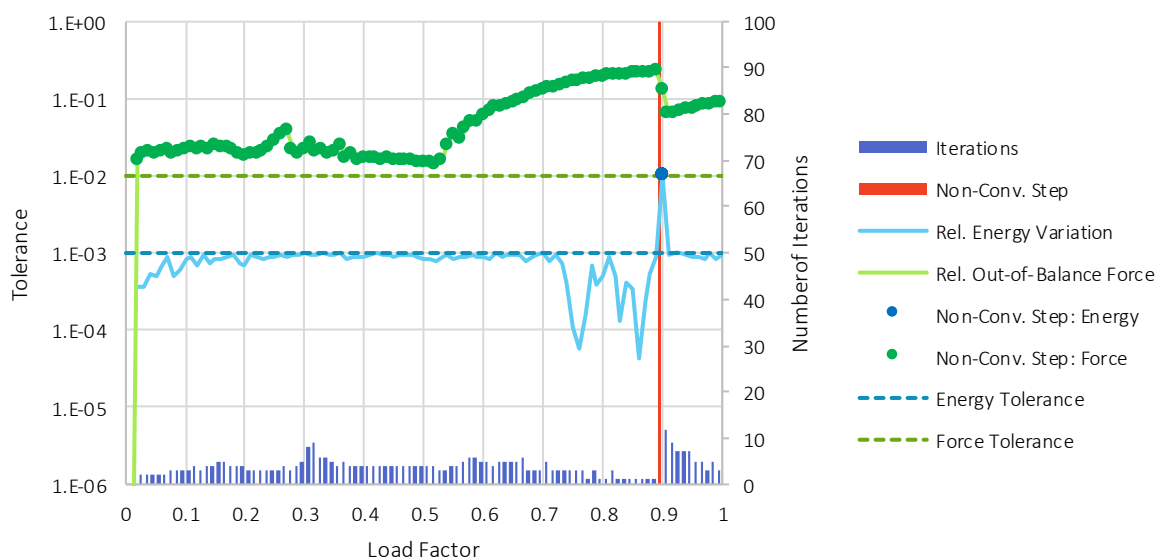


Figure A2.4 – Convergence behaviour of model 3D-SI-SJ